

PARTICLE SHAPE AND STIFFNESS
- EFFECTS ON SOIL BEHAVIOR -

A Thesis
Presented to
The Academic Faculty

by

Jake Dodds

In Partial Fulfillment
Of the Requirements for the Degree
Master of Science in Civil Engineering

Georgia Institute of Technology
November 2003

PARTICLE SHAPE AND STIFFNESS
- EFFECTS ON SOIL BEHAVIOR -

Approved by:

Dr. Carlos Santamarina, Advisor

Dr. Paul Mayne

Dr. Glenn Rix

Date Approved: January 6, 2004

ACKNOWLEDGEMENT

I would like to first thank my advisor Dr. Carlos Santamarina for his thoughtful guidance and his insistence on excellence. Guillermo Narsillio, Tae Sup Yun and Hyunki Kim spent hours discussing the meaning of results and offering suggestions and insights. Franco Fransica, Jose Alvarelllos, Angel Polomino and Jong Sub Lee shared their knowledge of experimental practices and particulate material behavior. Several teachers including Dr. Santamarina, Dr. Frost, Dr. Mayne and Dr. Sacks provided a foundation for this research through well prepared and insightful courses.

Most importantly, I would like to thank my dear wife for her unconditional love and continuous support for me and our family, which allowed me to devote so much of my time and energy to this work.

Support for this research was provided through endowed funds contributed by Vulcan Materials and other Georgia mining companies.

TABLE OF CONTENTS

Thesis Approval	ii
Acknowledgement	iii
Table of Contents	iv
List of Tables	vi
List of Figures	viii
List of Mathgrams	xiv
List of Symbols	xv
Summary	xvii
Chapter I Introduction	1
Chapter II Particle Shape— Literature Review	2
2.1 Introduction	2
2.2 Sand Particle Shape	2
2.3 Clay Particle Shape	9
2.4 Characterization	11
2.5 Affects of Particle Shape on Soil Behavior	19
2.6 Other Affects of Shape	26
2.7 Conclusions	33
Chapter III Crushed and Natural Sands	34
3.1 Introduction	34
3.2 Microscale Analysis	34
3.3 Macroscale Analysis	42
3.4 Conclusions	74
Chapter IV Shape Based Segregation	79
4.1 Introduction	79
4.2 Literature Review	79
4.3 Fundamental Study	82
4.4 Sands	86
4.5 Conclusions	89
Chapter V Mixtures of Rigid and Soft Particles	91
5.1 Introduction	91
5.2 Brief Review of V_s and G_{max}	94
5.3 Rubber-Sand Mixtures—Literature Review	94
5.4 Experimental Design	98
5.5 Stiffness Results and Analysis	101
5.6 Analysis	108
5.7 Photoelastic Study	112

5.8 Conclusions	119
Chapter VI Conclusions	121
Appendix A	123
References	169

LIST OF TABLES

Table 3.1	Tests and standards. Modifications are discussed in the text.	36
Table 3.2	Instruments and settings used to determine shear wave velocity. Settings are constant unless otherwise noted. Figure 3.13 is a simple schematic of the experimental setup, which shows how each instrument is used.	55
Table 3.3	One-to-one correlation among soil index properties and critical state parameters – Trends (Cho and Santamarina 2003).	60
Table 3.4	Values used to establish the uncertainty in critical state parameters determined using the simplified method. Typical values are used, they do not represent the results of a single test.	65
Table 3.5	Experimental results – Complete Dataset for specimens used in at least one macroscale test (Critical state friction angle, critical state parameters, shear wave velocity, mortar strength and workability). The table is in two parts; gradation, shape and void ratio results are listed on the first page and critical state, shear wave velocity, mortar and other results are listed on the second page.	77
Table 5.1	Basic properties of rubber from pneumatic tires and Quartz (Beatty 1980, Santamarina et al. 2001).	92
Table 5.2	Theoretical shear wave velocity exponent β values for different contact types (Santamarina et al. 2001).	93
Table 5.3	Mechanical properties of rubber-sand mixtures. $D_{\text{rigid}} / D_{\text{soft}}$ is roughly 0.1. Permeability values are determined at 150 kPa. Modulus of elasticity, friction angle and cohesion intercept values are determined from consolidated drained triaxial tests (Masad et al. 1996).	96
Table 5.4	Compilation of data from several studies which measure water contaminant levels near tire shred fill sites (Liu et al. 2000). Numbers in bold represent higher than maximum contaminant levels. Only Fe and Mg levels were observed above maximum contaminant levels. Standards for these minerals are aesthetic rather than health related.	97
Table 5.5	Salient ratios --- Significance.	99
Table 5.6	Instruments and settings used to determine shear wave velocity. Settings are constant unless otherwise noted. Figure 3.13 is a simple schematic of the experimental setup, which shows how each instrument is used.	102

Table 5.7

Photoelastic results. Rigid particles which do not cause visible force in neighboring photoelastic particles (no force), and rigid particles visibly stressed are used to quantify the nature of force chains. Greater numbers of un-stressed rigid particles, and fewer numbers of load transferring soft particles implies that the load is primarily transferred by a small number of large rigid force chains. In contrast, less un-stressed rigid particles and more load transferring soft particles implies a diffused load which is transferred through many small chains. Packings in which soft particles are uniformly spaced are termed ordered, other packings are termed disordered.

120

LIST OF FIGURES

Figure 2.1	Sand surface features and the environments that produce them. Darker boxes indicate greater prevalence (Margolis and Krinsley, 1974).	5
Figure 2.2	Mechanical weathering of quartz sands. (a) Conchoidal fracture, (b) v-shaped grooves, (c) upturned cleavage plates and (d) flat particle separated from a sand grain along a cleavage plane (Margolis and Krinsley 1974).	7
Figure 2.3	Schematic diagram of (left) Halloysite 10 A and (right) halloysite 7 A or kaolinite unit structure (Mitchell 1993).	10
Figure 2.4	SEM images of kaolin (left) and halloysite particles (Mitchell 1993).	10
Figure 2.5	Diagram showing independence of form, roundness and roughness (Barrett 1980).	12
Figure 2.6	Fourier representation of shape using different numbers of harmonics (Garboczi 2002).	16
Figure 2.7	Fractal analysis of sand grains (Hyslip and Vallejo 1997).	17
Figure 2.8	Fractal dimension versus sand roughness. Six sand samples (sand types 1-6) are examined ranging from rough (sand type 1) to smooth (sand type 6). (Hyslip and Vallejo 1997).	17
Figure 2.9	Coefficient of wall friction for (left) smooth particles and (right) rough particles interacting with a smooth wall (Abou-Chakra and Tuzun 1999).	22
Figure 2.10	Surface roughness and rotational frustration (Duran 2000).	22
Figure 2.11	Effect of shape on shear band formation. C lines represents angular particles while M and F lines represent sub-angular to sub-rounded and smooth particles (Alshibli and Sture 2000). Notice that the drop in the principal stress ratio occurs at greater axial strains and is less marked in angular particles.	23
Figure 2.12	Effect of eccentricity on soil behavior. (a) Friction angle, (b) packing fraction, (c) coordination number and (d) peak dilation rate (Rothenburg and Bathurst 1993).	25
Figure 2.13	Friction angle versus bedding plane inclination angle in sands (Oda 1999).	27
Figure 2.14	Undrained shear strength versus bedding plane inclination angle of clays (Oda 1999).	27
Figure 2.15	Influence of surface roughness on small strain stiffness (Santamarina and Cascante 1998).	29

Figure 2.16	Evolution of structure of vibrated rod shaped particles with time. (a) initial fabric, (b) final arrangement, (c-f) pictures taken by stopping the test and carefully removing the top half of the particles at different stages of particle alignment (Villarruel et al. 2000).	29
Figure 2.17	Particle shape and van der Waals interaction forces (Tadmor 2001).	31
Figure 2.18	Flow of rough (a – d) and smooth (e-f) sand through a funnel like device. Dark regions correspond to low density. Arching in the rough sand leads to concentrations of low and high density (Baxter and Behringer 1989).	32
Figure 3.1	Quarry locations, 43 samples are tested from 32 quarries operated by five producers.	35
Figure 3.2	Chart used to characterize sphericity and roundness of particles (Krumbein and Sloss 1963).	37
Figure 3.3	Correlation between numerical roundness values and verbal descriptions used to classify particles (right). Roundness is defined as the radius of curvature of the corners divided by the radius of the maximum inscribed circle (left) (Powers, 1953).	37
Figure 3.4	Shape of different sized particles from the same granite quarry. Smaller particles (left) tend to have planar faces and sharp corners, while larger particles (right) are more rough with less sharp corners.	39
Figure 3.5	Shape extremes encountered in this study. The angular sand on the left is a crushed aggregate from Georgia, while the rounded sample on the right is a natural sand from Margaret River Australia.	39
Figure 3.6	Grain Size distributions of sands used in this study. M10, M810 etc. are blend names used by the crushed stone industry, other refers to manufactured sands for which blend type is unknown or not standard. Most of the manufactured sands fall into two grain size distribution categories with lower or higher fines contents. Lower fines sands include 10FM, 10SM, W10 and AW10, while higher fines sands include M10 and M810 blends. Particles of a single natural sand show little size variation, but grain size does vary between specimens.	41
Figure 3.7	Maximum void ratio determined by raining sand into a mold (ASTM D 4254 method A) versus e_{\max} determined by inverting a graduated cylinder then quickly returning it to upright (ASTM D 4254 method C). There is a correlation between the values obtained from each method. Maximum void ratios determined from test method A are generally higher than those from test method C.	44

Figure 3.8	The value of e_{\max} as a function of coefficient of uniformity, C_u . Lines represent empirical relations between roundness R , e_{\max} and c_u (Youd, 1973). Youd roundness values are different from those used in this study (Figure 3.7). Nineteen of 27 crushed sand e_{\max} values fall between the 0.20 and 0.25 roundness lines. Natural sand e_{\max} values are much more variable.	45
Figure 3.9	Relationship between roundness values determined using the chart in Figure 3.2, and roundness values predicted from e_{\max} and c_u values using the empirical relations of Youd (1973).	46
Figure 3.10	Use of Hele-Shaw cell to determine angle of repose (planar). The cell is rotated past 45° then returned to the upright position. The repose angle is determined in the center of the slope.	46
Figure 3.11	The Helle-Shaw cell (planar) angle of repose used to approximate the critical state friction angle versus angles of repose of a sand pile (convex), the cavity formed when sand drains from the center of a sand pile (concave) and the critical state friction angle from triaxial tests. Angles from highest to lowest are concave, planar, convex and triaxial. The same four samples are tested for planar, convex and concave (Narsillio, 2003) angles. Triaxial results are taken from Cho (2001).	50
Figure 3.12	Critical state friction angle as a function of particle roundness. Because crushed sand shapes vary little between specimens, a typical roundness value for granite and calcareous sands is used. Lines represent the range of roundness and friction angles within which most samples fall.	51
Figure 3.13	Simple schematic of shear wave velocity experimental setup. Diagram displays signal travel direction and instrument settings. Table 3.2 also displays instrumental settings.	53
Figure 3.14	Shear wave parameter α as a function of mean crushed granite grain size D_{50} .	56
Figure 3.15	Shear wave parameter β as a function of crushed granite grain size and fines content.	57
Figure 3.16	Shear wave parameter α as a function of natural sand roundness and roughness. Lines represent the two dimensional face of a three dimensional plane.	57
Figure 3.17	The Relationship between shear wave velocity parameters α and β . The line represents the relationship between α and β experimentally observed by Santamarina et al. (2001).	58
Figure 3.18	Simplified critical state apparatus. (a) Description of parts, (b) apparatus prior to applied load and (c) apparatus following applied load. Vacuum pressures of 5, 10, 20, 30, 45 and 60 are applied. Load magnitude is not measured; sands are loaded until strains reach about 40%. All samples are dilative during shear.	62

Figure 3.19	Critical state parameter λ as a function of Γ for natural sands. Numbers next to symbols represent the specimen critical state friction angle.	67
Figure 3.20	Localization identified by comparing local and global strains. Test 7 which exhibits the greatest localization is performed on a loose sand at a confining pressure within the range used in this study. The strain level for localization is much lower than the strain level used in performing simplified critical state tests. (Klotz and Coop, 2002).	67
Figure 3.21	Schedule followed in performing the flow test and preparing cubical samples for strength testing. Details in the text.	71
Figure 3.22	Strength and workability of natural sand mortars. (top left) Flow as a function of particle size and roundness, (top right) strength as a function of particle size and sphericity and (bottom) strength as a function of flow value.	72
Figure 3.23	Strength and workability of crushed granites. (top left) Flow as a function of fines content, (top right) strength as a function of fines content and (bottom) strength as a function of flow value.	73
Figure 3.24	Strength and workability of all specimens. (top left) Flow as a function of particle size (top right) strength as a function of fines content and (bottom) strength as a function of flow value	76
Figure 4.1	Segregation of disk (split peas) and rod (rice) shaped particles. The lines represent the surface heights along the length of the glass cylinder. Notice the peaks in the rice sections and valley in the pea sections (Khosropour et al., 2000).	80
Figure 4.2	Profile view of lead particles. Original round shape (left), Particles flattened using 1.5 mm spacers (middle), and particles flattened using 1.2 mm spacers.	80
Figure 4.3	Method used to investigate rolling and sliding tendencies of different particles. A planar paper covered Plexiglas sheet is rotated from the horizontal and particle motions are recorded.	83
Figure 4.4	Spherical and flattened particles are segregated by tilting the transparent box at 45°.	83
		85

Figure 4.5	Segregation of round (black) and flat (white) lead particles. Photos are in sets with the photo on the left representing the profile view and the photo on the right representing the plan view as each layer is removed. The particle mixture is 3 parts round to 1 part flat. The mixture is vibrated at a frequency of 3 Hz and an amplitude of 50 mm for 3 minutes. During vibration the top half of the particles are in motion while the bottom section remains static relative to the container. The spherical particles are 2.3 mm in diameter. The long axis to short axis ratio of the flat particles is about 2. The container is LxWxH 41x41x48 mm.	
Figure 4.6	Mixture of round and angular particles segregated by horizontal vibration at an amplitude of 15 mm and a frequency of 3 Hz. Vibrational direction is switched periodically from right to left in the figure to top to bottom.	87
Figure 4.7	Sands segregated through horizontal and vertical vibration. Georgia crushed granite (left) and Ottawa sand (right). Particles all pass the #20 sieve and are retained on the #40 sieve.	88
Figure 4.8	Segregation of angular (lighter color) and round (darker color) particles during convective flow. The ratio of round to angular particles is 10:1. Vertical vibration is applied at 122 Hz using a modified 4 inch speaker. An HP model 200 Oscilloscope is used to create the signal at an amplitude of 15 volts. A Krohn-Hite model 7500 amplifier is used to amplify the signal with the gain set at 15. During vibration the sand container is allowed to move so that the center of the speaker is about 10 mm from the center of the base of the container.	88
Figure 5.1	Photograph of a crumb rubber (left) and Ottawa sand (right) particles. Photographs are of particles of the same composition, but larger size than the particles used in this study.	92
Figure 5.2	Grain size distribution of Ottawa sand and rubber particles determined using sieve analysis.	93
Figure 5.3	Gmax of sand-rubber mixtures tested in the resonant column device (Feng and Sutter 2000). Gmax is divided by a number that is a function of the overconsolidation ratio OCR, a parameter related to the soil index k , and the confining pressure raised to the 0.5 power. A similar plot could be created by solving for A in equation 5.2 assuming b equals 0.5, and plotting the value against the % rubber or sand (see Figure 1.5), $D_{\text{rigid}} / D_{\text{soft}}$ is roughly 0.2.	96
Figure 5.4	Sketch of oedometer used to determine stiffness. Cap and baseplate are fitted with bender elements.	103
Figure 5.5	Strain as a function of vertical effective stress.	104

Figure 5.6	Shear wave signals collected at different confining pressures. Amplitudes are normalized with respect to the peak amplitude to create the plot. (+) markers indicate the arrival times used to calculate shear wave velocity. Signals are for 100% sand (left) and 60% sand 40% rubber (right).	105
Figure 5.7	Selected plot of G_{max} vs. vertical effective stress plotted in log-log form. The lines in the plot represent G_{max} as calculated from the equation $G_{max} = A\sigma^b$, where A and b are determined experimentally.	106
Figure 5.8	G_{max} as a function of vertical effective stress during loading for each sand fraction.	107
Figure 5.9	A -coefficient and b -exponent used to model small strain stiffness; plotted as a function of sand fraction.	109
Figure 5.10	Constraint modulus as a function of confining pressure for several rigid-soft mixtures. M^* is calculated at each stress increment by dividing the average stress by the strain over the loading increment.	111
Figure 5.11	G_{max} at different loading levels. Near the percolation threshold the change in G_{max} with stress follows a power relationship. As stress increases soft particles deform allowing rigid particles to move closer to one another and form a percolating network at lower sand fractions.	111
Figure 5.12	Porosity of a binary mixture of large and small particles as a function of volume fraction of small particles (Guyon, Oger and Plona 1987).	111
Figure 5.13	Increase in sand particle contact with increasing effective stress.	113
Figure 5.14	Skeletal void ratio as a function of effective stress for several sand fractions.	114
Figure 5.15	First two layers of a disordered (left) and ordered (right) packing. Particles are more evenly spaced in an ordered packing.	116
Figure 5.16	Simple Schematic of the photoelastic setup. The Load is applied using a Bellofram air cylinder mounted on a load frame. The Load magnitude is determined using a Fairchild guage. Photoelastic disks represent stiff particles while rubber disks represent soft particles.	116
Figure 5.17	Typical photoelastic results. Soft particles appears as dark circles (above). Mixture of 29 soft and 119 rigid particles. Notice the high number of particles with no dark lines caused by stress. Several large chains carry most of the load while many particles do not contribute. (below) Mixture of 56 soft and 119 rigid particles. Notice the high number of dark (soft) particles causing stress in their rigid neighbors. The high number of soft particles leaves few paths made of rigid particles only. This causes a more even distribution of load among particles and fewer vertical force chains.	117

LIST OF MATHGRAMS

Mathgram 3.1	Error analysis of simplified critical state test. Assumed values are listed first, followed by equations, calculations and results	66
--------------	--	----

LIST OF SYMBOLS

A	Coefficient in the G_{\max} - σ relationship
a	Long axis of ellipse
AF	Angularity factor
a_n	Fourier coefficient
A_s	Surface area
A_t	Tubing cross sectional area
A_{tt}	Interparticle attractive force
α	Shear wave velocity parameter, V_s at 1 kPa
B	Particle intermediate axis
b	Exponent in the G_{\max} - σ relationship
b_n	Fourier coefficient
β	Shear wave velocity parameter, exponent
c	Percolation proportionality constant
Γ	Critical state intercept in the e-p' space
γ_w	Unit weight of water
d	Oedometer cell base diameter
D_R	Fractal dimension
D_{rigid}	Sand particle diameter
D_{50}	Mean grain size diameter
D_{soft}	Rubber particle diameter
δ	Dilatancy angle
ΔV	Change in particle volume during cooling
E	Surface Energy
e	Void ratio
e_i	Void ratio at ith confining stress
e_{\max}	Maximum void ratio
e_{\min}	Minimum void ratio
e_{sk}	Sand void ratio in a rubber-sand mixture
f	Percolation exponent
$f_{c_{\text{cub}}}$	Cubical mortar specimen strength
$f_{c_{\text{cyl}}}$	Cylindrical mortar specimen strength
F_{elec}	Interparticle electrical force
g	Gravitational acceleration
G_{\max}	Small strain stiffness
G_s	Sand specific gravity
η	Orientation of the shear plane with respect to the σ_2 axis
h	Specimen height
h_o	Initial water height
h_i	Water height at the ith confining stress
ϕ	Angle of internal friction
ϕ_{cs}	Critical state friction angle
θ_i	Fourier phase angle
ϕ_u	Interparticle friction angle
θ_m	Angle of maximum stability
θ_r	Repose angle
K	Cooling particle compressibility
k	Ratio of cylindrical and cubical mortar strength
k_o	Horizontal earth pressure coefficient
L	Particle long axis

L_{\max}	Largest particle dimension
L_{\min}	Smallest particle dimension
L_{par}	Particle length parallel to the shear plane
L_{perp}	Particle length perpendicular to the shear plane
λ	Critical state slope in the e-p' space
M	Critical state strength parameter
M^*	Constrained modulus
μ	Poisson's ratio
n	Fractal proportionality constant
ν	Dilatancy coefficient
OCR	Overconsolidation ratio
$P(\lambda)$	Fractal line length
P_f	Oedometer side friction resistance
q	Deviator stress
ρ	Density
R_{dll}	Interparticle repulsive force
r_l	Radius of curvature of a particle corner
SF	Shape factor
S_s	Specific surface
σ	Normal stress
σ'_p	Mean stress in the polarization plane
t	Particles short axis
t_o	Interface shear strength
τ_f	Shear stress
V_d	Device volume
V_s	Shear wave velocity
V_{soft}	Rubber volume
V_{sp}	Specimen volume
V_{rigid}	Sand volume
V_{wo}	Reference water volume
V_{wi}	Water volume at the ith confining stress
W_s	Sand weight
ψ	Dilation angle

SUMMARY

TITLE: PARTICLE SHAPE AND STIFFNESS - EFFECTS ON SOIL BEHAVIOR -

Particle shape is evaluated on three scales corresponding to form, roundness and roughness. Shape at each of these scales uniquely influences material behavior. The shape of sand grains is largely formed as magma cools. Subsequent cleavage and abrasion change the roundness and roughness of particles. Published results indicate that particle shape influences several aspects of granular systems behavior including stiffness, strength, the evolution of strength anisotropy, dilation, and the development of strain localization.

The crushing of granite creates a particulate material with a unique angular shape. A wide range of experimental studies implemented as part of this research permit assembling a unique database of material parameters and comparing the behavior of several crushed and natural sands. In general, the low roundness of crushed sands leads to higher maximum void ratios, lower small strain stiffnesses, and higher critical state friction angles than more rounded natural sands. It also impacts mortar strength and workability.

Previous studies have emphasized size-controlled segregation. New experimental results show that differences in particle shape can also lead to segregation in a binary granular material. Round or spherical particles are more mobile than angular or flat particles. Then, the greater motion of round or spherical particles in a binary mixture subjected to horizontal or vertical vibration results in their segregation from their angular or flat neighbors.

Particle shape may change significantly with stress in the case of soft particles. Therefore, the presence of shape-deformable particles decreases the stiffness of binary rigid-soft particle mixtures. However, macro-scale measurements with rigid-soft mixtures show higher stiffness than would be expected by volume averaging techniques. A subsequent microscale study shows the formation of backbone chains made of the rigid particles, partially supported by the soft particles which prevent the buckling of the load-carrying chains.

CHAPTER I

INTRODUCTION - ORGANIZATION

Particulate materials are studied by geotechnical engineers, material scientists, physicists, and geologists. They are essential to several industries including chemical, food, agriculture, pharmaceutical, mining, energy, munitions, and electronics. The behavior of particulate materials is governed by the interaction of individual particles. While particle size plays a critical role, there is an increasing body of evidence that highlights the important affects of particle shape.

Particle shape has been studied sporadically by researchers in diverse fields throughout the 20th and into the 21st century. A literature review incorporating findings from each of these fields is the subject of Chapter 2.

The shape of crushed sands and its implications are studied in Chapter 3. To this end 40 Georgia crushed sands and 7 natural sands are assessed under the microscope and later tested for grain size distribution, maximum void ratio, shear wave velocity as a function of confinement, stiffness in confined compression, critical state parameters including critical state friction angle ϕ_{cs} , λ , and Γ and mortar strength and workability. Together these form a unique database which contains a wealth of information about the effect of shape on material properties.

Segregation leads to heterogeneous mixtures. The effect of particle shape on segregation is explained in Chapter 4. The literature produces no papers discussing segregation of particles due to horizontal and vertical vibration; which are likely to occur in a geotechnical engineering setting.

In geotechnical engineering applications, particles are generally assumed to be rigid with fixed shapes. However, engineers have recently begun using new soft-rigid mixtures. For instance, soft rubber particles from recycled tires are being used alone or with sand as lightweight fill, insulation beneath roads, and lightweight retaining wall backfill. The affect of soft particles of deformable shape on stiffness and force propagation is the subject of Chapter 5.

CHAPTER II
PARTICLE SHAPE
LITERATURE REIVEW

2.1 INTRODUCTION

Sands are granular media composed of individual particles. The interaction between particles determines the properties of the medium. Shape, along with mineralogy and size, is one of the major characteristics of an individual sand grain. Shape has been studied throughout the 20th century. Wadell (1932) developed characterization procedures to capture shape on multiple scales that are still in use today. Most of the research concerning the original shape of sand grains and the way that it changes with mechanical and chemical weathering can be traced to geologists in the 1960's and 70's who were working to determine the origin of sand grains from their current shape. The implications of shape on soil behavior is a line of research still in progress.

The purpose of this chapter is to elucidate the origin of shape, how it changes with mechanical and chemical weathering, the many scales that define shape, how it can be characterized and the connection between shape of sand particles and the microscale behavior observed.

2.2 SAND PARTICLE SHAPE

2.2.1 Formation

The formation of sand grains can be divided into the creation of the quartz crystal in cooling magma, weathering of the parent material, and release of the grains.

The bulk of all quartz sand particles originate from weathered coarse crystalline rocks, most commonly granite. The mineralogy and course fabric of granite suggests slow crystallization of siliceous magma. The crystals are part of a eutectic of quartz and feldspar which occurs at around 710°C after the larger feldspar particles have already formed. When the temperature

drops below 573°C, the quartz that has just formed, termed high quartz, goes through a bond angle transformation and becomes low quartz. The size and shape of sand grains are largely determined at the moment the eutectic quartz solidifies in cooling granite magma (Smalley 1966).

The ratio of long axis to short axis tends to be about 1.3 in quartz sand grains. This characteristic seems to stem from the cooling process as opposed to a weathering process (Smalley 1966). Evidence includes: (1) quartz has no pronounced tendency to fracture parallel to the C (elongated) axis, (2) elongation parallel to the C axis is not likely to be developed by differential abrasion, and (3) unbroken and unworn grains are elongated. The idea that the eccentric shape of quartz is somehow due to a metamorphic mechanism is also unlikely because the elongation of a this type of rock (schist for example) is typically much higher.

At least two plausible mechanisms for grain elongation during formation have been forwarded. The first considers the change of shape that occurs during the transformation from high β (stable above 1300° C and 35 kilobars) to low α (stable below 573° C and 1 kilobar) quartz. Nabarro (1940) uses elasticity theory to derive an equation relating the energy E in the cooling particle to its compressibility K, change in volume ΔV , and the long a and short b axis of an ellipse,

$$E = K \cdot \Delta V \cdot \frac{1}{3} \cdot f\left(\frac{b}{a}\right) \quad (2.1)$$

This equation shows that the energy E is least for a disk ($b/a \rightarrow 0$), greatest for a sphere ($b/a \rightarrow 1$), and that the most likely shape at the interface is an ellipse with three unequal dimensions.

The second explanation of particle elongation is given by Smalley (1966). When quartz cools from 800°C to 50°C the long (C) to short (A) axis ratio changes from 1.096 to 1.1. Also, during the phase transformation from high α to low β quartz there is a volume contraction to 86% of the original volume. The assumption is made that during cooling the C length remains constant

while contraction occurs about C axis. Stresses caused by this type of contraction would lead to a tensile stress parallel to the c axis, cause cracks parallel to this axis and lead to elongated grains.

2.2.2 Surface Features

The global shape of a sand grain is set during formation. However the surface texture can change markedly with mechanical and chemical weathering in geological time. Small particles which exhibit a much different shape than the parent particles may also be formed during weathering. The mechanisms of chemical weathering and the environments in which certain surface features are most likely to develop are summarized in Figure 2.1. The primary reference for this section is Margolis and Krinsley (1974). Information from other authors are cited in the text. It is important to highlight that while quartz is commonly perceived as a material that does not exhibit cleavage, more than 7 different forms of cleavage can develop (Margolis and Krinsley 1974).

Conchoidal fractures (Figure 2.2-a) occur as a result of uniform compression between two grains or one grain and a rough surface. The fracture is ideally dish shaped, but can exhibit varying degrees of irregularity. Lower energy fractures are closer to the ideal. Higher energy fractures tend to bend inward and exhibit a cup shape. The environment in which the grain resides can affect the number and dimensions of fractures. The environments most conducive to fracture include freshly weathered granite and glacial settings. Grain size also has a strong effect on conchoidal fracture. It occurs less often in smaller grains because smaller particles exhibit fewer imperfections. When fractures do occur, they take up a smaller proportion of the surface area. This is because the strength of a brittle material is governed by the stress at the tip of its most prominent crack.

The observed v-shaped patterns and grooves (Figure 2.2-b) are essentially notches cut into the outer layer of a quartz grain. When viewed under the electron microscope it becomes apparent that the notches are cut across several upturned parallel cleavage plates. The pits become shallower as they penetrate downward and finally vanish. This feature is characteristic of subaqueous abrasive action. It is most common in those subaqueous environments where

		ENVIRONMENT											
		<u>SUBAQUEOUS</u>			<u>EOLIAN</u>		<u>GLACIAL</u>			<u>REOLITH</u>			
		Turbulent Energy								Weathering			
		Low	Medium	High	Coastal	Tropical	Periglacial	Continental	Marine	Fluvial	Temperate	Tropical	Marine
1	Small blocks < 1mm												
2	Small conch. Fract. < 1mm												
3	Large blocks >1 mm												
4	Large conch. Fract. > 1mm												
5	Straight scratch												
6	Curved scratch												
7	Striations												
8	Step-like fract.												
9	Arc steps												
10	Meander ridges												
11	Vs												
12	Fract. Plates crack propog.												
13	Angular outline												
14	Round outline												
15	Low relief <.05 mm												
16	Medium relief												
17	High relief > 1 mm												
18	Oriented etch pits												
19	Irreg. pitted surface												
20	diagen. etch												
21	Smooth fract. surface												
22	Cryst. overgrowth												

Figure 2.1 Sand surface features and the environments that produce them. Darker boxes indicate greater prevalence (Margolis and Krinsley, 1974).

appreciable grain to grain impacts occur. As increasingly smaller grains are examined, the V-grooves become less common and are rarely seen in particles less than 300 microns in diameter.

Straight or slightly curved grooves are observed less often than their v-shaped counterparts. They are generally less than 25 microns in length and average about 1-5 microns in width. They are rarely found outside of subaqueous environment. Grooves are generally observed on grains larger than 400 to 500 microns in diameter, probably because smaller particles lack the momentum required for penetration.

The mechanism that forms grooves can be understood by considering metal abrasion. During polishing and grinding of metals small chips are propelled along the contact surface and are frequently present at the end of abrasive lines. In a similar manner, small chips break off grains during contact to form grooves and notches.

Upturned cleavage plates (Figure 2.2-c) are composed of a series of thin parallel plates oriented along traces of cleavage plates. These can be either continuous or not and are usually oriented at some angle to the grain surface which depends on the particle curvature. Plate relief ranges from several microns to less than one micron. Appearance can vary from sharp to jagged and undulating depending on the degree to which chemical action has affected the grain.

Upturned cleavage plates are usually formed by mechanical abrasion and are present when a grain is crushed. They are most common around the particle edges but can be found almost anywhere in the particle. Plates are present to some extent in all natural environments and are most common in large eolian grains, along coasts, and near glaciers.

Upturned cleavage plates play an important role in rounding sand grains in an eolian environment. Kuenen (1960) showed in wind machine simulations that plates are more concentrated at the edges of features and are rarely observed in the hollows. During abrasion the plates wear away. If this continues for enough time, the edges wear to the level of the depression and the particle become more spherical.

Chemical weathering is also important in the surface tomography of quartz grains. Its effect generally creates either etches or overgrowth. Etch types include both crystallographically-oriented pits and non-oriented etch patterns. Overgrowths tend to form a film around the grain.

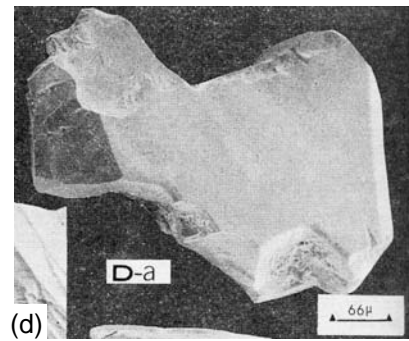
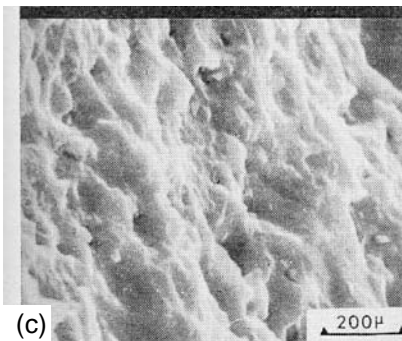
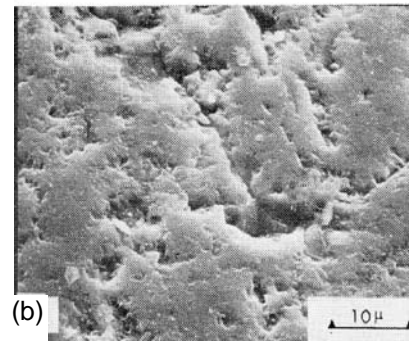
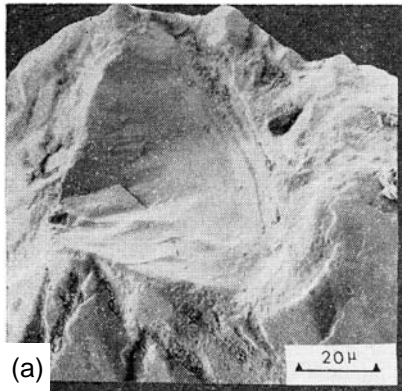


Figure 2.2 Mechanical weathering of quartz sands. (a) Conchoidal fracture, (b) v-shaped grooves, (c) upturned cleavage plates and (d) flat particle separated from a sand grain along a cleavage plane (Margolis and Krinsley 1974).

Together, these two chemical actions can modify or completely destroy mechanical surface features. Chemical weathering features can be difficult to distinguish from their mechanical counterparts. For instance, chemically precipitated ridges can resemble upturned cleavage plates, the difference being that those formed by chemical action are less crisp.

Although chemical features can be found in varying degrees in every location, specific features are usually associated with a particular environment. For instance, crystallographically-oriented pits are most often found in marine sands, non-oriented etch features are associated with sub-aerial weathering, oriented etch pits are found in seawater solutions, and aeolian sands acquire a gloss of precipitated silica.

Over an extended period of time, a sand grain will be subject to both chemical and mechanical action. These often produce competing surface features. Consider large sand grains in a desert environment. Chemical action produces a thin layer of precipitated silica which covers the grain. With the next strong wind upturned cleavage plates are formed on the surface. Eventually the surface texture will reflect a balance between mechanical and chemical weathering. Chemical weathering tends to dominate this balance in hot humid environment, whereas mechanical weathering plays a greater role in cold or dry climates.

2.2.3 Crushed Sand

Several factors contribute to the shape of crushed sand particles. First, the composition of the parent rock, including natural spacing, partings and mineralogy, is a major determining factor. Crushed quartz particles tend to be equidimensional because cleavage is rare (Krebs, 1961), whereas feldspar particles tend to be rectangular. Second, mode of fracture, including compression, in plane shear and out of plane shear affects crushed particle shape. Third, coordination number during crushing, and fourth, the ratio of grain size to product size influence crushed particle shape. The form of natural sands, on the other hand, is determined during formation while the roundness and roughness may be altered through weathering as discussed above.

2.3 CLAY PARTICLE SHAPE

2.3.1 Crystalline structure

The crystalline structure of a clay mineral is determined by the following four factors (Mitchell 1993):

- Sheet Type
- Unit Cell Order
- Bonding Mechanism
- Substitution

Clay minerals are made of two basic building blocks. The first is the silica tetrahedral, which is composed of one silicon atom surrounded by four oxygen atoms. These tetrahedra combine to form silica sheets. The second is the aluminum, or magnesium octahedral, which is composed of an Al or Mg atom surrounded by 8 oxygen atoms. Aluminum octahedra join to form gibbsite sheets, while magnesium octahedra combine to form brucite sheets. These silica, gibbsite and brucite sheets are stacked in a specific repeating order to form the clay mineral. The smallest repeating section is termed the unit cell. It can consist of one, two, three or four sheets.

The strength of the bond between unit cells can determine the thickness of a clay particle. Two or more unit cells may be bonded together in several different ways. Common mechanisms include hydrogen bonds, ionic bonds and van der Waals forces. The montmorillonite unit cell is composed of three sheets while kaolin unit cells can be more than one hundred times as thick because montmorillonite are primarily bonded by weak van der Waals forces which allow layers to separate, whereas kaolin unit cells are bonded by strong hydrogen bonds which keep layers together (Mitchell 1993).

Bond strength can also affect the form of the particle. Halloysite 7A (Figure 2.3), is the dehydrate form of halloysite 10A. The structure of halloysite (7A) is similar to kaolinite, but includes a water layer between each unit layer. In kaolin, the gibbsite sheet has a width of 8.93 angstroms, whereas unbounded gibbsite has a width of 8.62 angstroms, which implies that gibbsite must stretch to bond to the silica sheet. The bond between unit layers is weakened by the presence of water. This allows the gibbsite face in contact with the water to shrink back to

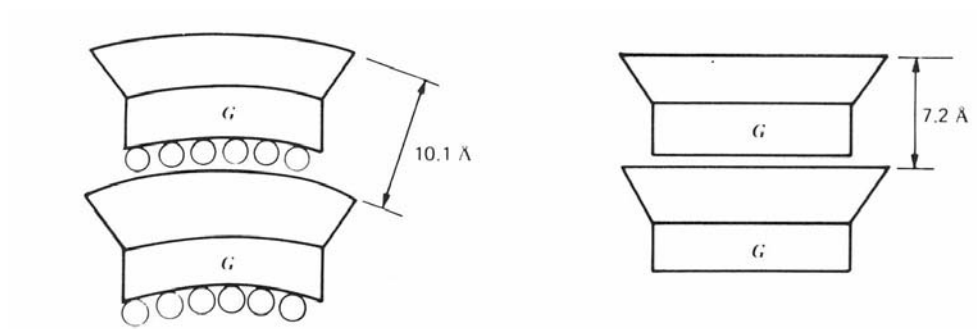


Figure 2.3 Schematic diagram of (left) Halloysite 10 Å and (right) halloysite 7 Å or kaolinite unit structure (Mitchell 1993).

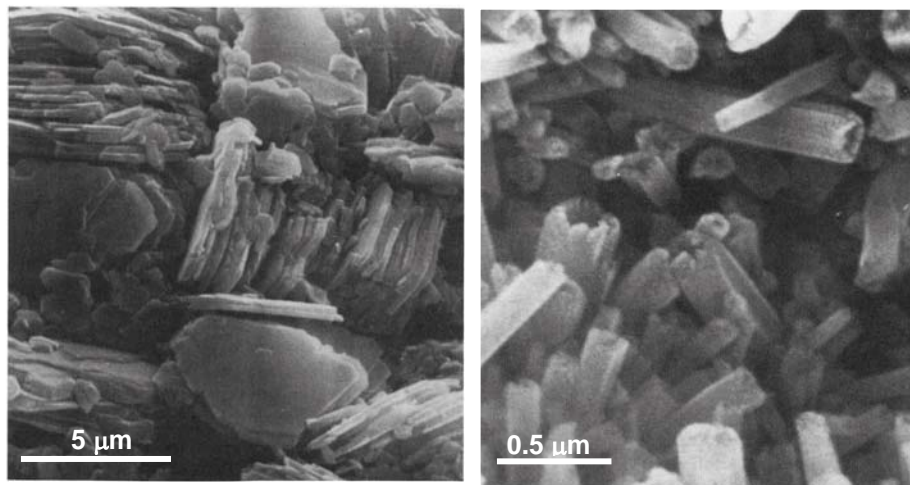


Figure 2.4 SEM images of kaolin (left) and halloysite particles (Mitchell 1993).

8.62 angstroms. Curvature results with the water face on the inside and the silica tetrahedral on the outside (Weaver 1989). Figure 2.4 shows electron photomicrographs of kaolin and halloysite.

Isomorphous substitution is also important in determining the shape of clay minerals. This phenomenon occurs when one cation takes the place of another. Common substitutions include Al and Mg taking the place of Si. The shape of montmorillonite is again a good example of the importance of this phenomenon. When a large number of Si atoms are substituted by Mg and Fe particles may be lath or needle shaped. This occurs because the larger substituting ions cause a directional strain in the material (Mitchell 1993).

Even when the crystalline structure is nearly identical, different formation processes can produce clay minerals which are geometrically diverse. Nagasawa and Miyazaki (1975) examined 57 halloysite samples from Japan. These were classified into the following four groups: (1) Those formed by hydrothermal alteration of a volcanic, pyroclastic or granite rocks (2) those formed by alteration of volcanic glass, (3) those formed by weathering of feldspar and (4) those formed by epidiagenesis of feldspar. Results of their study showed a strong correlation between morphology and mode of formation. Halloysite grown on feldspar grains or in the cracks of rocks exhibited a tubular form. Grains formed by replacement of volcanic glass or allophane sometimes formed as aggregates of very short tubes, creating a rounded shape.

2.4 CHARACTERIZATION

2.4.1 Internal Scales

Particle shape is captured through three independent relative scales (Barrett 1980):

- Form, which describes variations in the proportions of the particle
- Roundness, which describes variations at the corners superimposed on the particle
- Roughness, which describes characteristics superimposed on both corners and surfaces.

The independence of these descriptors means that one may vary markedly without necessarily affecting the others. This is illustrated by Figure 2.5. Shape can also be characterized through the Fourier method and, if the shape is self-similar, through fractal analysis.

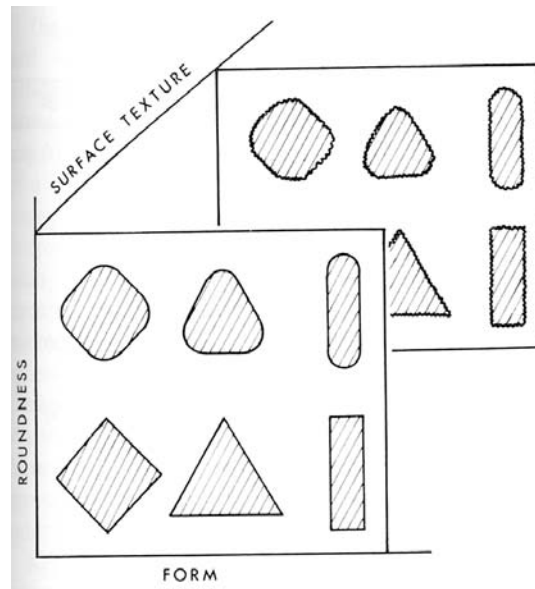


Figure 2.5 Diagram showing independence of form, roundness and roughness (Barrett 1980).

2.4.2 Form, Roundness and Roughness

Form. The form of a particle can be expressed in descriptive terms such as cubical, spherical, elliptical, elongated, flat, tubular, platey, lath like and needle. One way of quantifying form is through ratios of the lengths of the three orthogonal axes. Barrett (1980) lists at least 15 different parameters which have been defined from these ratios. One familiar parameter is the aspect ratio or elongation, which is the ratio of the long axis L to the intermediate axis B. Another is flatness, which is defined as the ratio of the intermediate, B, and short, t, axes.

Other mathematical descriptors of form include sphericity and eccentricity. Sphericity is defined by Wadell (1932) as the ratio of the particle volume to the volume of a circumscribing sphere. This definition is flawed because it included a measure of roundness. An improved definition of sphericity is the ratio of the surface area of the particle to the surface area of a sphere of equal volume (Santamarina et al. 2001). Eccentricity is defined as the ratio δ_p/R_p of an elliptical particle whose two dimensional outline has been expressed in polar coordinates as $R_p = \delta_p \cdot \cos(2\theta)$.

A new method of quantifying form is developed by Sukamran and Ashmawy (2001). This shape factor measures the deviation of a particle outline from that of a circle. The particle image is first sliced (similar to cutting a pie) into n sections. The outermost points on the slicing lines are connected to create an equivalent polygon. The orientations of the lines connecting points on the perimeter of the polygon are compared with the orientations on lines connecting the polygon created by slicing a circle. The angle which constitutes the difference in orientation α and the number of sampling points N are used to define the new shape factor as:

$$SF = \sum_{i=1}^n \left(\left| \frac{\alpha_i(\text{particle})}{\alpha_i(\text{flat_particle})} \right| \right) \cdot 100\% \quad (2.2)$$

$$SF = \sum_{i=1}^n \left(\left| \frac{\alpha_i(\text{particle})}{N \cdot 45 \cdot \text{deg}} \right| \right) \cdot 100\% \quad (2.3)$$

A comparison shows a correlation between this shape factor and Wadell's sphericity.

Roundness. Roundness can be assessed by averaging the radius of curvature of each corner r_i , and comparing it with the radius of the maximum inscribed circle of the particle Wadell (1932). The procedure is two dimensional but can be extended to three dimensions by using spheres instead of circles. The problem of recognizing what constitutes a corner introduces some subjectivity into the test.

Sukumaran and Ashmawy (2001) also develop a new parameter for measuring roundness. First, an equivalent polygon is constructed as described earlier. Each internal angle of the polygon β is measured and the sum of these angles is compared with the sum of the angles of the equivalent polygon of a circle. The angularity factor is defined as:

$$AF = \frac{\sum_{i=1}^n (\beta_i(\text{particle}) - 180 \cdot \text{deg})^2 - \sum_{i=1}^n (\beta_i(\text{particle}) - 180 \cdot \text{deg})^2}{3 \cdot 180^2 - \sum_{i=1}^n (\beta_i(\text{circle}) - 180 \cdot \text{deg})^2} \quad (2.4)$$

A comparison of the angularity factor with Wadell's roughness shows a correlation with substantial scatter, which the authors attribute to the subjectivity of the roundness parameter as defined by Wadell.

Roughness. Scale considerations play a critical role in the characterization of particle roughness. All surfaces are rough at some scale (Santamarina et al. 2001), therefore roughness must be characterized at the scale deemed relevant to the problem at hand.

2.4.3 Fourier and Fractal Characterization

Fourier analysis captures the shape of a particle at many different scales. This is accomplished by tracing the outline of a figure using one of the following equations (Bowman et al. 2001).

$$R(\theta) = a_0 + \sum_{n=1}^N (a_n \cdot \cos(n\theta) + b_n \cdot \sin(n\theta)) \quad (2.5)$$

$$x_m + iy_m = \sum_{n = \frac{-N}{2} + 1}^{\frac{N}{2}} (a_n + ib_n) \cdot \left(\cos\left(\frac{2 \cdot \pi \cdot n \cdot m}{M}\right) + i \cdot \sin\left(\frac{2 \cdot \pi \cdot n \cdot m}{M}\right) \right) \quad (2.6)$$

The first equation represents the traditional (R, θ) method, whereas the second represents the Fourier descriptor method. The descriptor method is used if the particle outline doubles back on itself so that two radii can be calculated for one θ . In these equations θ_i is the phase angle, and a_n and b_n are the coefficients for the i_{th} harmonic.

Different harmonics represent separate aspects of shape. Lower level harmonics capture shape on a global scale. Higher level harmonics characterize shape on increasingly smaller scales. Roundness is captured at a harmonics in the range of 10 and roughness is captured at much higher levels (Santamarina et al. 2001). Figure 2.6 shows the evolution of particle shape representation using a successively higher number of harmonics (Garboczi 2002). The Fourier method provides a wealth of information. It allows the outline of a grain to be reproduced so that the transition can be made from numeric to visual analysis. On the other hand the harmonic coefficients have not been reduced to a single form, roundness, or roughness parameter (Bowman et al 2001).

Fractal analysis is based on the concept that in a fractal system the measured property depends on the size of the unit of measurement. As the unit of measurement decreases, the measured property increases. Figure 2.7 illustrates this concept. In this diagram the unit

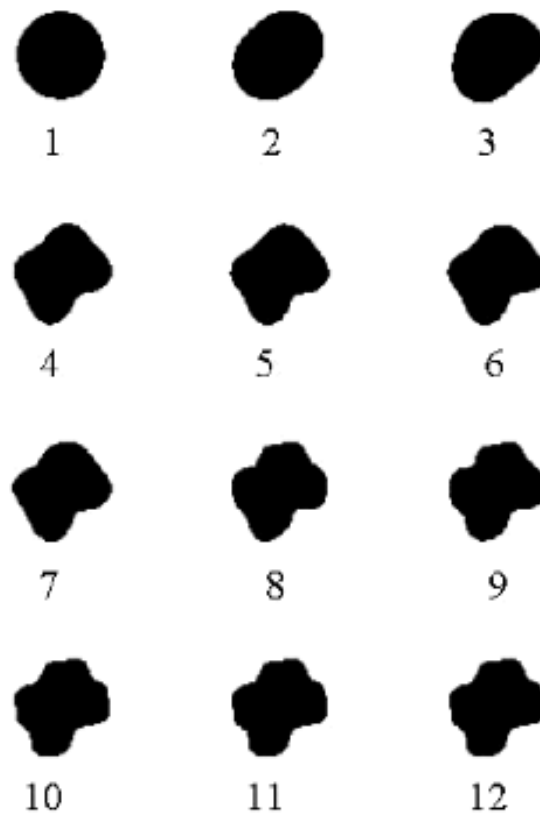


Figure 2.6 Fourier representation of shape using different numbers of harmonics (Garboczi 2002).

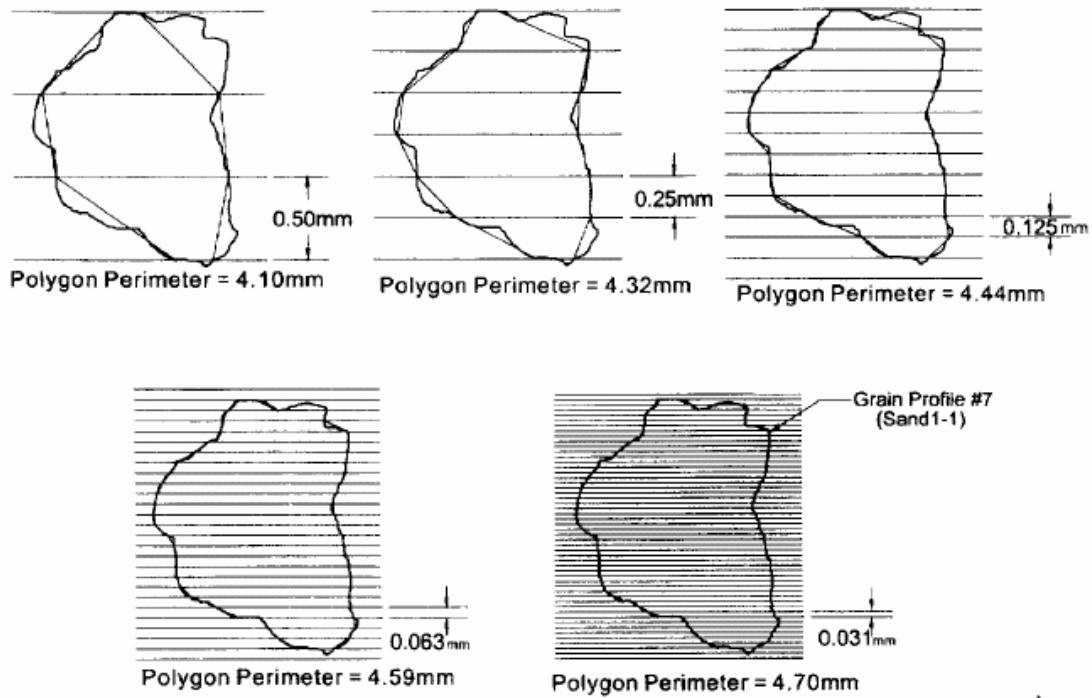


Figure 2.7 Fractal analysis of sand grains (Hyslip and Vallejo 1997).

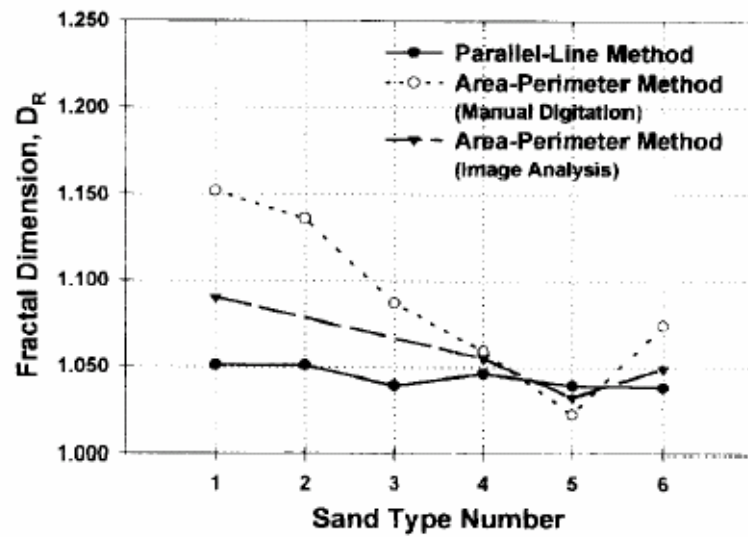


Figure 2.8 Fractal dimension versus sand roughness. Six sand samples (sand types 1-6) are examined ranging from rough (sand type 1) to smooth (sand type 6). (Hyslip and Vallejo 1997).

measurement is the distance between the parallel lines, and the measured property is the length of the polygon perimeter. The length of a fractal line $P(\lambda)$ can be approximated as a function of the unit measurement length λ , a proportionality constant n and the fractal dimension D_R through Equation 2.7.

$$P(\lambda) = n \cdot \lambda^{1-D_R} \quad (2.7)$$

Taking the logarithm of both sides yields a linear relation between $P(\lambda)$ and λ where D_R equals $1 - m$ (slope of the line). By incrementally decreasing λ and measuring the line length, the fractal dimension is obtained.

In order for this type of characterization to work, the property in question must exhibit self-similarity. Hyslip and Vallejo (1997) characterize sand grains as exhibiting bi-fractality, which meant that they considered both the structural and textural aspects of the particle to be fractal, but independent of one another. Surface asperities of many materials have been shown to exhibit self-affinity (Chaiai 2002). This characteristic makes fractal analysis of surface roughness plausible and several authors have observed a correlation between surface roughness and fractal dimension.

Figure 2.8 shows a graph of fractal dimension as a function of surface roughness. The six sand specimens considered are referred to as sand types one (roughest) through six (smoothest). The trend between fractal dimension and roughness is apparent. However, the authors of this study did not distinguish between textural and structural features. This led to some inconsistency in the relationship between fractal dimension and roughness for the smoother particles.

There are two major limitations to fractal analysis. The first, discussed above is the difficulty associated with determining the surface feature length range over which the particle is fractal. The second is the inability of the fractal dimension to relate to the form of the particle. This means that some other form of analysis is needed for complete characterization of the particle shape (Sukamaram and Ashmawy 2001).

2.5 AFFECTS OF PARTICLE SHAPE ON SOIL BEHAVIOR

2.5.1 Introduction

Coulomb's friction law relates the shear stress to the normal stress through the friction angle ϕ :

$$\tau_f = \sigma' \cdot \tan(\phi_\mu) \quad (2.8)$$

The friction angle ϕ is not a material constant, but is dependant on void ratio, fabric, and state of stress, among others. Taylor (1948) and others have separated the angle of internal friction into at least two components:

- The internal frictional component, which is a combination of rolling and sliding friction.
- The component of shearing against interlocked particles or dilatancy.

These two components can be quantified by considering the work required to shear a specimen (Taylor 1948).

$$\tau_f \delta x = \sigma'_n \cdot \mu \cdot \delta x + \sigma'_n \cdot \delta y \quad (2.9)$$

$$\tan(\phi) = \frac{\tau_f}{\sigma} \quad (2.10)$$

$$\tan(\phi) = \mu + \frac{\delta x}{\delta y} = \tan(\phi'_\mu) + \tan(\psi) \quad (2.11)$$

where ϕ'_μ is a physical angle related to both rolling and sliding friction, and ψ is the dilatancy coefficient which denotes the rate of dilatancy associated with shear deformation. The derivation of ψ is important in understanding the role of shape in shear strength.

2.5.2 Surface roughness and ϕ

There are at least two theories of friction. The first is the asperity theory which recognizes that all surfaces are rough at some scale, and the interaction of surface roughness causes friction. The second is the adhesion theory which states that because of surface roughness, the true contact area between two surfaces is very small. This implies very high stress at the contacts, plastic deformation, and subsequent adhesion (Santamarina et al. 2001).

The asperity theory predicts a constant relationship between frictional force and normal force which is independent of contact surface area. It also implies increased friction with increased roughness, because asperity interaction increases. The adhesion theory on the other hand predicts a relationship between frictional force and actual contact area. This implies an increase in friction as roughness decreases.

The effect of surface roughness on friction can be misleading. Mineral to mineral friction studies have shown that friction can increase when roughness decreases, as in the case of cold welding of highly polished metals. On the other hand, friction in particulate materials increases when interlocking between asperities occurs.

The length of the asperity determines whether the system behaves in an adhesion like or asperity like manner. Chiaia (2002) stated that at asperity scales below 10 – 100 μm the predictions of the adhesion theory seem to hold true. Chan and Page (1997) observe that the coefficient of friction increased as roughness increased in particles 150 μm in diameter with asperities much smaller than 100 microns. It is herein postulated that it is in fact the ratio of the asperity size to the particle size which determines which theory of friction best predicts experimental results.

To understand the predictions of adhesion theory in particulate material consider two smooth spheres in contact. Hertz (1881) shows that the contact area between the spheres increases with the cube root of normal force. Therefore the ratio of interface shear strength t_0 to normal stress p should decrease with increasing normal force. Assuming a perfectly smooth surface the coefficient of friction would tend to zero as the normal stress approaches an infinite value. However, all surfaces are rough at some scale and as increase in surface area describe by

Hertzian theory becomes less important, the role of asperities becomes more important and $\tan(\phi_\mu)$ decreases asymptotically toward the constant value α described by Amonton's Law.

$$\tan(\phi_\mu) = \frac{\tau_o}{P} + \alpha \quad (2.12)$$

Spherical glass particles interacting with a smooth wall (asperity height 1-10 μm) have been shown to act in this manner (Figure 2.9-a).

Adhesion theory can be used to predict a linear coefficient of friction in rough particles (Figure 2.9-b). Archard (1957) used a model of hertzian spheres with progressively smaller radii to obtain a linear relationship between normal force and real contact area. Because surface roughness has been shown to exhibit self affinity, this model presents a reasonable framework for understanding the linear relationship between normal and shear forces within the adhesion.

2.5.3 Angularity and ϕ

As angularity increases, the energy required for dilation and therefore the angle of internal friction increases due to particle interlocking. This affect is less pronounced at high confinement because (1) grain crushing reduces the influence of interlocking (Oda and Iwashita 1999) and (2) as confinement increases materials tend to contract rather than dilate. The effect of angularity and surface roughness is enhanced in dense rotationally frustrated packings (Figure 2.10). Particle rotation is a basic component of deformation within a shear band (Bardet 1994). Because of rotational frustration, localization is less likely to be observed in angular particles. When shear bands do form it is at higher strains and with a less pronounced drop in strength (Figure 2.11). Even without localization, friction is reduced due to rolling at contacts (Frye and Marone 2002). Mair et al. (2002) shows that the as angularity increases, the ratio of rolling to sliding contacts decreases leading to greater shearing resistance. Rotational frustration is more pronounced in denser packings (Santamarina and Cascante 1998). During shear, not all particles rotate in complementary directions (Figure 2.10). Rotation frustration increases as the total number of

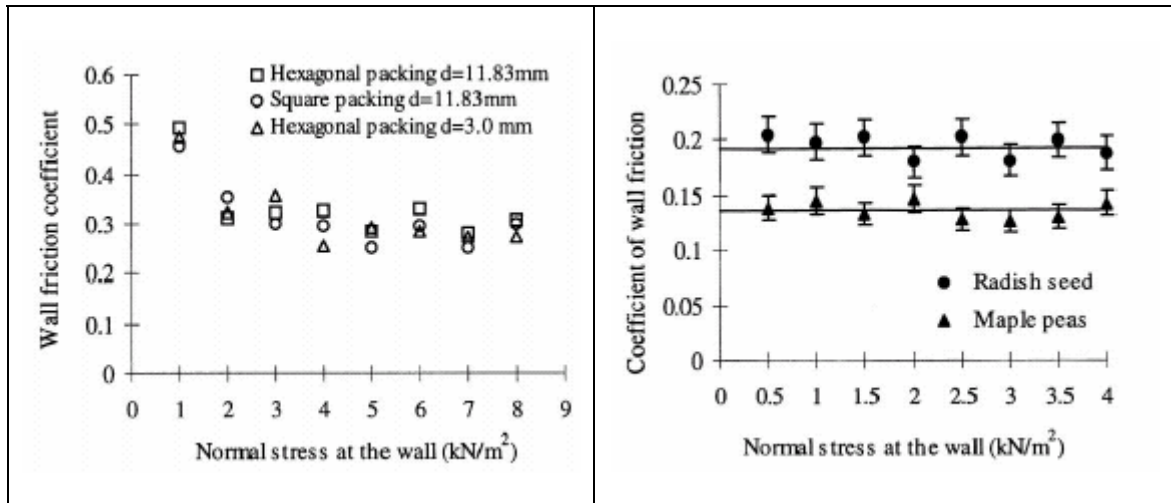


Figure 2.9 Coefficient of wall friction for smooth particles (left) and rough particles (right) interacting with a smooth wall (Abou-Chakra and Tuzun 1999).

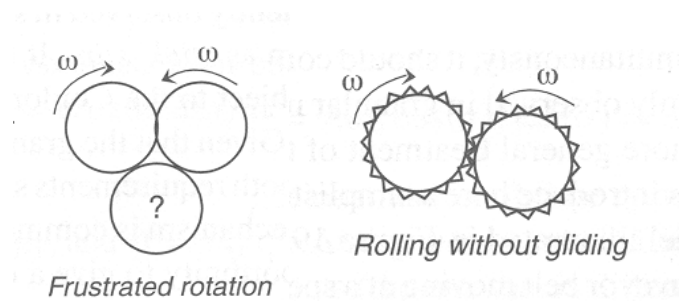


Figure 2.10 Surface roughness and rotational frustration (Duran 2000).

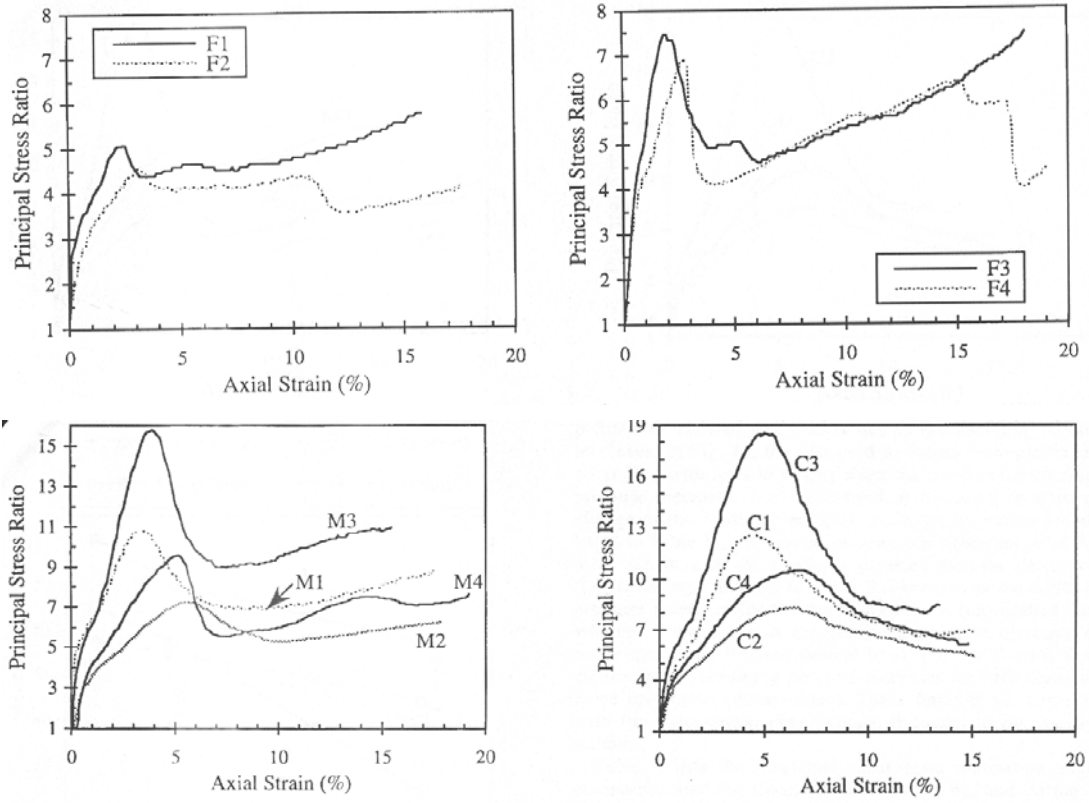


Figure 2.111 Effect of shape on shear band formation. C lines represents angular particles while M and F lines represent sub-angular to sub-rounded and smooth particles (Alshibli and Sture 2000). Notice that the drop in the principal stress ratio occurs at greater axial strains and is less marked in angular particles.

interparticle contacts, and therefore the number of contacts resisting rotation in a specific direction increases. This leads to increased rotational frustration.

2.5.4 Eccentricity and ϕ

Eccentricity is shown to strongly affect shear strength. Rothenburg and Bathurst (1993) shows that strength initially increases, peaks then decreases with increasing eccentricity (Figure 2.12a). This effect is in large part due to differences in (1) coordination number, (2) dilation, and (3) particle alignment between eccentrically and spherically shaped particle arrays. Coordination number, like friction angle, initially increases then decreases with increased eccentricity (Figure 2.12c). Because the energy required for particle rotation depends on the number of contacts increased coordination leads to rotational frustration and higher shear strength. Dilation of a random packing of eccentric particles follows the same trend as coordination number and friction angle (Figure 2.12-b). As eccentricity increases, initially particles must dilate more to displace during shear, however as eccentricity continues to increase particle alignment parallel to the direction of shear leads to a decrease in dilation and localization.

The affect of particle alignment is amplified when packing is not random. During sedimentation eccentric particles (most sand grains) are deposited with their long axes parallel to the bedding plane. This creates a situation where the strength of the particulate medium depends on the orientation of the grains with respect to the shear plane. Santamarina et al. (2001) shows that the dilation of aligned particles ($\tan \psi$) can be theoretically related to the slenderness of particles defined as the length of the particles parallel with L_{par} and perpendicular to L_{perp} the shear plane,

$$\tan(\psi) = \frac{L_{\text{perp.}}}{L_{\text{par.}}} \cdot \tan(30) \quad (2.133)$$

The orientation of the shear plane η with respect to the σ_2 axis is related to the angle of internal friction ϕ and the angle of dilation ψ by (Tatsuoka et al. 1990):

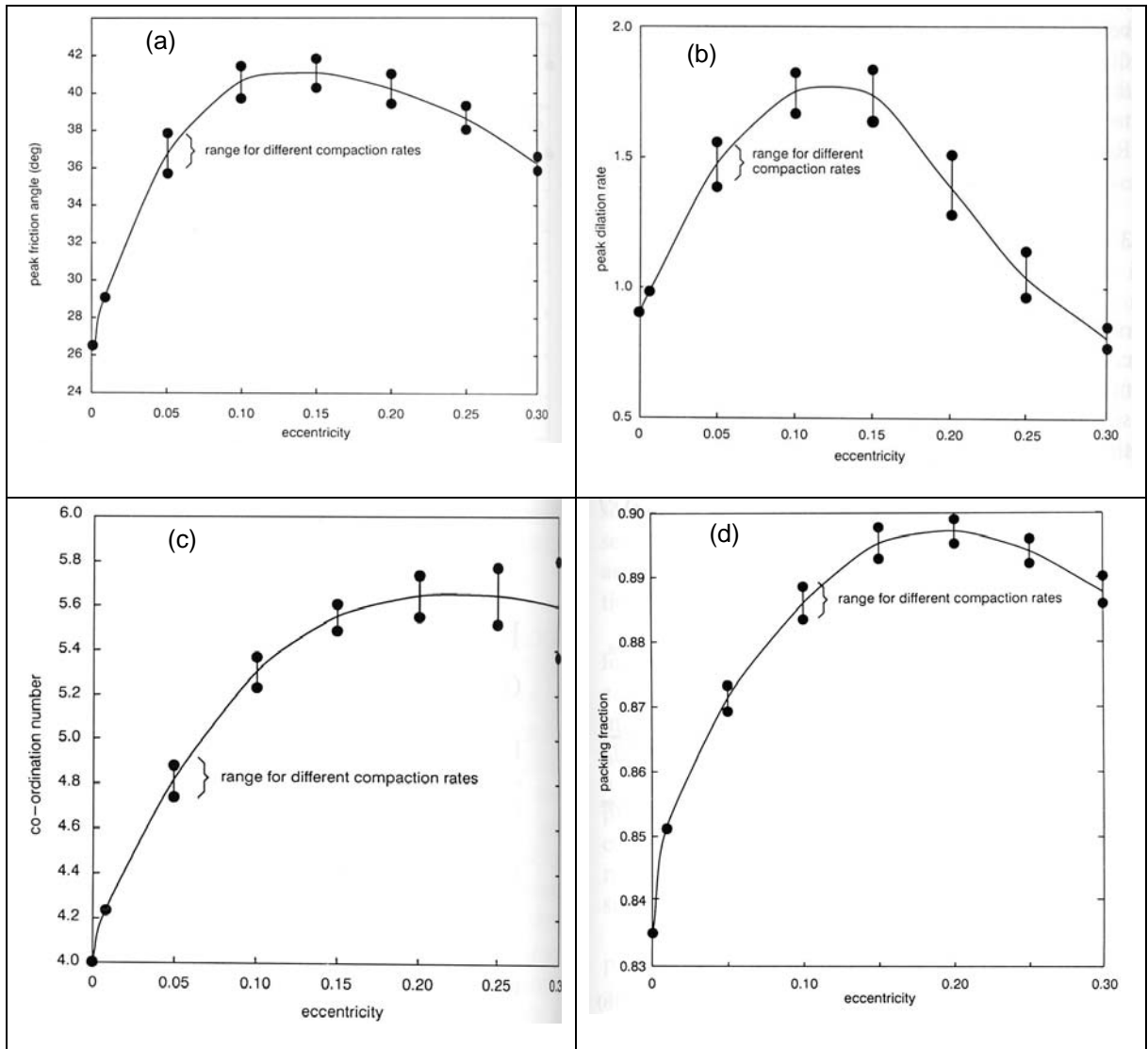


Figure 2.112 Effect of eccentricity on soil behavior. (a) Friction angle, (b) packing fraction, (c) coordination number and (d) peak dilation rate (Rothenburg and Bathurst 1993).

$$\frac{\pi}{4} + \frac{\psi}{2} \leq \eta \leq \frac{\pi}{4} + \frac{\phi}{2} \quad (2.14)$$

This indicates that the shear band for many sands will form at an angle near 60°. Experimental results showing angle of internal friction as a function of bedding angle of a sand are shown in Figure 2.13. Notice that a 30° bedding plane δ corresponds to a 60° shear plane angle η .

Eccentricity also leads to undrained strength anisotropy and post peak behavior in clays (Figure 2.14). The maximum undrained strength occurs when the clay particles are oriented parallel to the σ_1 axis as opposed to the σ_3 axis. This implies a separate mechanism of undrained strength anisotropy in clays (Oda 1999). Muller-Vonmoos and Loken (1989) states that the eccentricity of clay particles causes them to align with the shear plane; this leads to face to face alignment, increased double layer repulsion and decreased friction and post peak behavior.

2.6 OTHER AFFECTS OF SHAPE

Stiffness and Damping. At small strains, the stiffness of a soil is dependent on the nature of individual particle contacts (Santamarina and Cascante 1998). Both the total interparticle contact area and the nature of the contacts are important. The Hertz model of contact behavior shows that the stiffness of two spheres in contact is non-linear and rises with increasing force. Spheres with rough surfaces may have the same total contact area, but it is composed of many small asperities, which can be modeled as cones. The stiffness of a conical contact is lower than that of a spherical contact. As force between particles increases, the global spherical shape of the rough particles begins to have a greater influence on contact behavior than does the shape of the asperities, and the stiffness of the rough particle contact approaches that of a smooth particle. When many different sized asperities are present on particle surfaces only the largest are initially in contact, therefore actual contact area is lower than in the spherical case and stiffness is lower (Yimsiri and Soga 2000). This behavior is observed experimentally. Santamarina and Cascante (1998) show that spheres of equal composition, size and global shape exhibit lower small-strain stiffness if they are rougher (Figure 2.15).

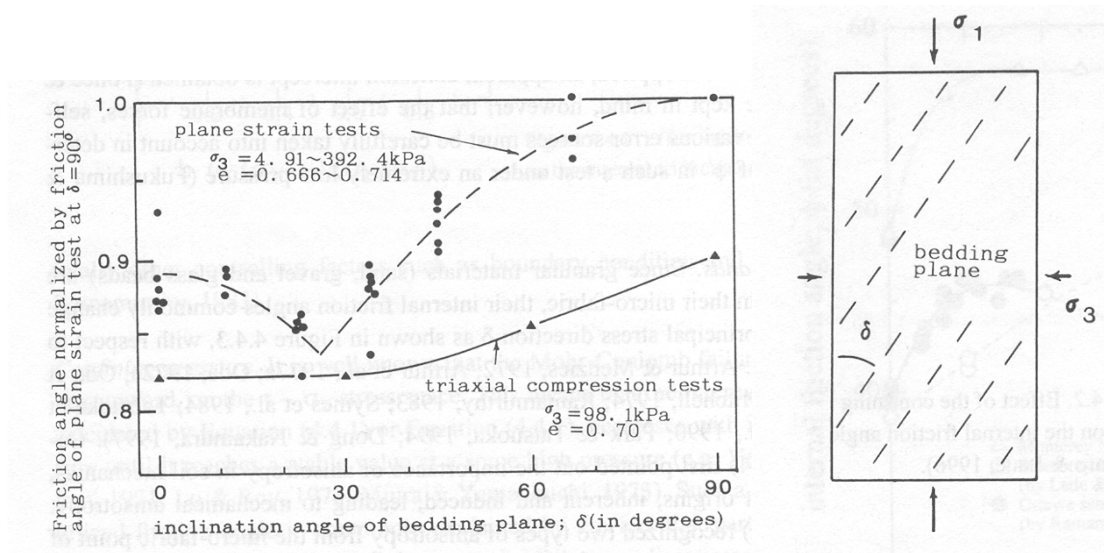


Figure 2.113 Friction angle versus bedding plane inclination angle in sands (Oda 1999).

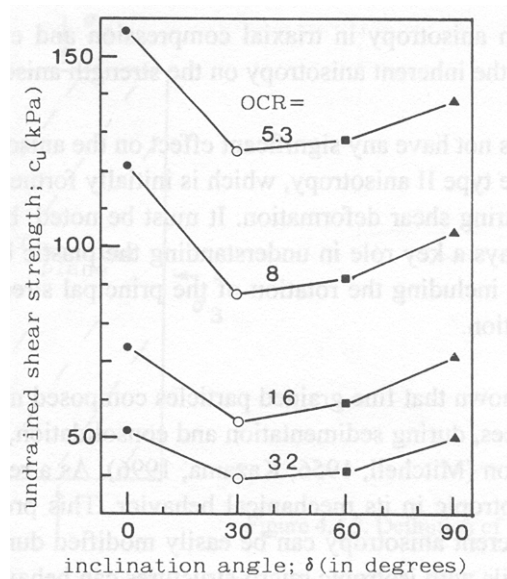


Figure 2.114 Undrained shear strength versus bedding plane inclination angle of clays (Oda 1999)

Furthermore, increased surface roughness decreases damping and makes it stress independent, similar to the response of a continuous medium. One possible reason for this is that asperities can penetrate adsorbed layers more easily than spherical contacts. This leads to decreased slippage and decreased damping. Another possible explanation is that roughness may alter the pressure distribution at the contacts so that the pressure at the edge of the contact is nonzero. This would lead to a decreased annulus of slippage and less damping.

Self Organization. Shape also plays an important role in self organization of particles. Villarruel et al. (2000) shows that under the right conditions inertial forces can be used to encourage assembly of highly eccentric particles into a very organized dense packing. In this experiment nylon rods are placed into a 1 meter high glass cylinder in the loosest possible configuration. The cylinder is then tapped 7000 times at a rate of two taps per second. The evolution of the packing with time is shown in Figure 2.16. The ordered state shown occurs because (1) rods are forced to align with the vertical walls to move relative to one another and fill the rather porous structure below and (2) the boundaries encourage a vertical orientation. This study also illustrates the potential effect of high aspect ratio on void ratio. High aspect ratio can increase the maximum void ratio as long particles bridge interparticle gaps. The maximum void ratio is 1.04 and 0.69 for nylon rods and monosized spheres. High aspect ratio can also decrease the minimum void ratio as particles align. The minimum void ratio of nylon rods and monosized spheres is 0.38 and 0.54 (Figure 2.16 a, b).

Shape can affect interparticle electrical forces in at least two ways. First, as the smallest particle dimension decreases specific surface S_s increases and the surface area A_s increase. The relative importance of electrical forces is a function of these variables as well as mass M , gravitational acceleration g , and interparticle repulsive R_{ddl} and attractive A_{tt} forces as in Equation 2.15.

$$\frac{F_{elec}}{W} = \frac{A_s \cdot (R_{ddl} - A_{tt})}{Mg} = S_s \cdot \frac{(R_{ddl} - A_{tt})}{g} \quad (2.15)$$

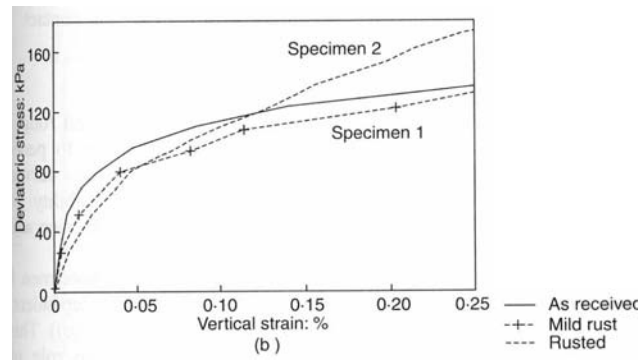


Figure 2.115 Influence of surface roughness on small strain stiffness (Santamarina and Cascante 1998).

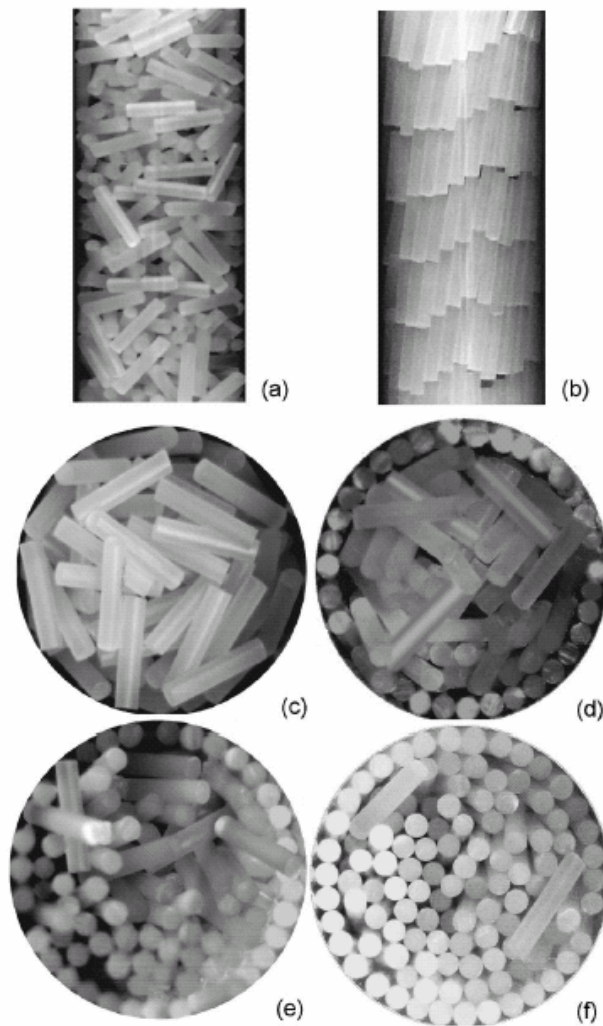


Figure 2.116 Evolution of structure of vibrated rod shaped particles with time. (a) initial fabric, (b) final arrangement, (c-f) pictures taken by stopping the test and carefully removing the top half of the particles at different stages of particle alignment (Villarruel et al. 2000).

Second, particle geometry can change the magnitude of the London-van der Waals attraction forces which are a function of separation distance of the atoms in each particle. Derivations of attraction forces between particles of different geometries are presented in Figure 2.17 (Tadmor 2001)

Rheology and Flow. Particle shape can affect rheological properties of suspensions. Small particle suspensions of anisotropic particles subject to low shear rates typically show a higher viscosity compared with those composed of spherical particles. This occurs because rotation of anisotropic particles causes greater perturbations of the flow streamlines than do isotropic particles. As the shear rate increases the effects of Brownian forces, which keep particle orientations random at low rates, are overcome by shear forces, which tend to align particles. Viscosity decreases and approaches that of isotropic particles. The suspension is referred to as shear thinning.

Shape affects the flow of sand. Baxter and Behringer (1989) use digital subtraction radiography to acquire density images of sands flowing through a funnel-like device made with two flat Plexiglas walls between which an incline leads to a spout. The flow of smooth rounded and rough faceted sands are compared. The density of smooth sands tends to be more homogeneous (Figure 2.18), than the faceted sand which exhibits distinct regions of low density (shown as black). These regions start at the center of the funnel just above the spout and propagate upward and outward like a wave during flow. A possible explanation for this behavior is the formation of internal arches in the rough sand. As the low density sand below the arch flows out of the funnel the arch collapses and another wider arch forms above it.

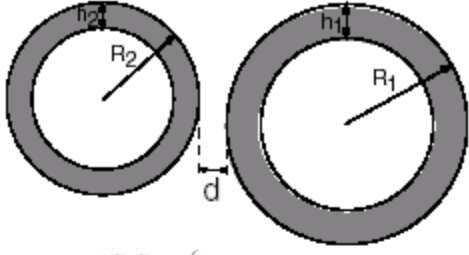

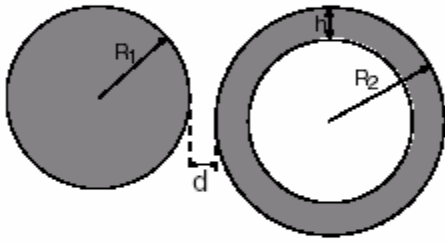
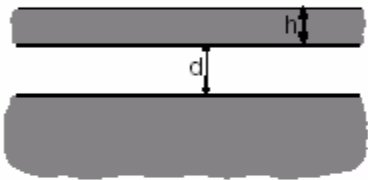
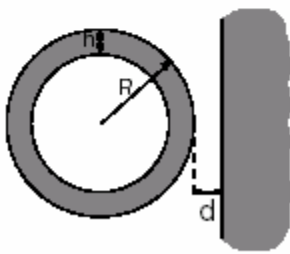
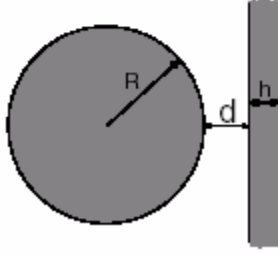
<p>Two spherical shells</p>  $E = -\frac{AR_1R_2}{6(R_1+R_2)} \left(\frac{1}{(d+h_1+h_2)} - \frac{1}{(d+h_2)} - \frac{1}{(d+h_1)} + \frac{1}{d} \right) - \frac{A}{6} \ln \left[\frac{d(d+h_1+h_2)}{(d+h_1)(d+h_2)} \right]$	<p>Two parallel walls</p>  $E = -\frac{A}{12\pi} \left(\frac{1}{d^2} + \frac{1}{(d+h_1+h_2)^2} - \frac{1}{(d+h_1)^2} - \frac{1}{(d+h_2)^2} \right)$ <p>(per unit area)</p>
<p>A sphere and a spherical shell</p>  $E = -\frac{AR_1R_2}{6(R_1+R_2)} \left(\frac{1}{d} - \frac{1}{(d+h)} \right) - \frac{A}{6} \ln \left[\frac{d}{(d+h)} \right]$	<p>Thin and a semi infinite walls</p>  $E = -\frac{A}{12\pi} \left(\frac{1}{d^2} - \frac{1}{(d+h)^2} \right)$ <p>(per unit area)</p>
<p>Spherical shell and semi-infinite wall</p>  $E = -\frac{AR}{6} \left(\frac{1}{d} - \frac{1}{(d+h)} \right) - \frac{A}{6} \ln \left[\frac{d}{(d+h)} \right]$	<p>A sphere and a wall</p>  $E = -\frac{AR}{6} \left(\frac{1}{d} - \frac{1}{(d+h)} \right) - \frac{A}{6} \ln \left(\frac{d}{d+h} \right)$

Figure 2.117 Particle shape and van der Waals interaction forces (Tadmor 2001).

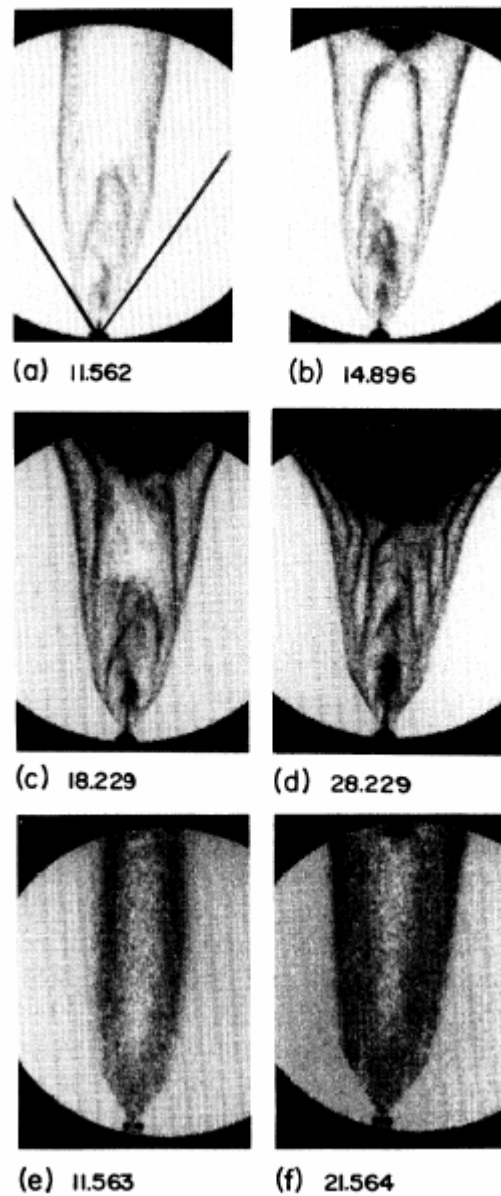


Figure 2.118 Flow of rough (a – d) and smooth (e-f) sand through a funnel like device. Dark regions correspond to low density. Arching in the rough sand leads to concentrations of low and high density (Baxter and Behringer 1989).

2.7 CONCLUSIONS

This review of historical and current research into particles shape, especially of sands addressed the origin of particle shape its characterization and known implications. Conclusions from this review include:

- Form is determined during crystallization. Mechanical and chemical weathering slowly change particle texture. Each type of particular surface features is characteristic of specific environments.
- Shape is manifest on several different scales relative to the particle size. Characterization generally seeks to describe shape on one of three relative scales which correspond to form, roundness and roughness
- Rough particles exhibit a linear coefficient of friction. Smooth particles display a non-linear coefficient which varies with contact area. Whether a particular surface behaves in a linear or non-linear manner depends on the relative length scales of the asperity height and particle diameter.
- Surface roughness and angularity couple with rotational frustration to increases the angle of internal friction and decreases the tendency and affects of localization.
- A small amount of eccentricity leads to increased coordination number and dilation. High eccentricity leads to particle alignment. Therefore shear strength initially increases, reaches a peak and then decreases with increasing eccentricity.
- Shape also affects stiffness, damping, self organization, electrical and capillary forces, suspension rheology and granular flow.

CHAPTER III

CRUSHED AND NATURAL SANDS

4.1 INTRODUCTION

The crushed stone industry in Georgia is the sixth largest in the nation and produces an estimated 467 million dollars of revenue annually (USGS, 2001). There are 83 quarries in Georgia. The number of quarries producing granite, limestone, marble and dolomite are 54, 15, 10, 2. Ten to twenty-five percent of the seventy six million metric tons of crushed stone produced each year in Georgia are crushed sand (USGS, 2001).

The goal of this chapter is to characterize the Georgia crushed sands and to contrast their microscale and macroscale based behaviors with those of an eclectic collection of natural sands selected to exhibit a variety of microscale qualities. Specimens include 39 crushed sands from Georgia (Figure 3.1) and five natural sands from the United States, one from Italy and one from Australia. Parameters tested include roundness, sphericity, particle size, maximum void ratio, critical state parameters, small strain stiffness, and mortar strength and workability. Tests are performed following standard procedures (Table 3.1).

4.2 MICROSCALE ANALYSIS

3.2.1 Particle Shape

Sphericity and roundness are determined in this study using the chart developed by Krumbein (1963). The procedure is as follows: A pinch of sand is placed on a Petri dish, which is set under a Leica MZ6 stereomicroscope. Light deflected from a reflective shield indirectly illuminates particles. Roughly 30 grains are studied at various magnifications. Representative grains are then selected and sphericity and roundness are determined from the chart (Figure 3.2, Figure 3.3). Note that Folk (1955) observes a variance of about 10% when many different students use the Powers chart to characterize the roundness of particles from the same vial of sand.

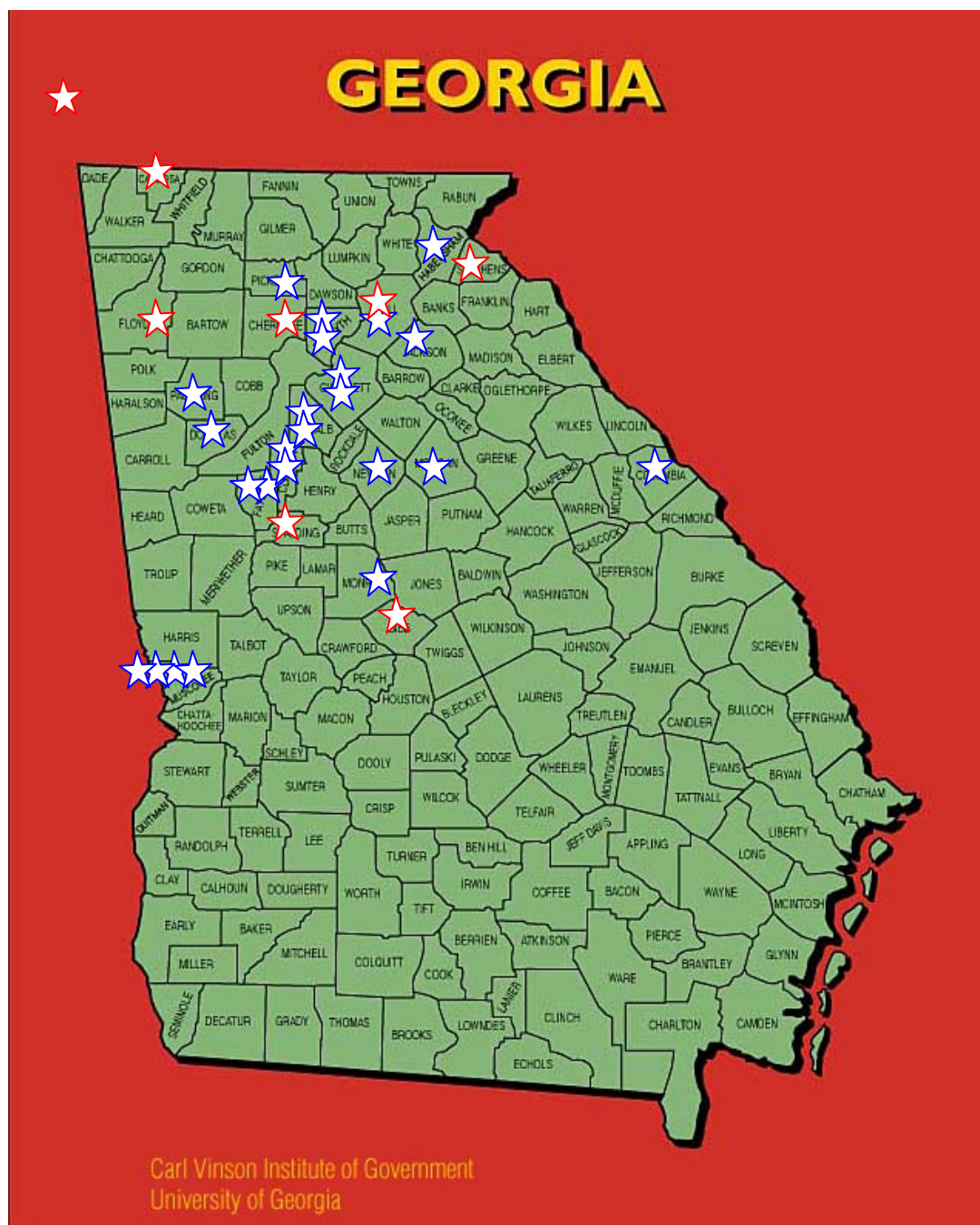


Figure 3.1 Quarry locations, 43 samples are tested from 32 quarries operated by five producers.

Table 3.1 Tests and standards. Modifications are discussed in the text.

Test	Method
Grain Size Distribution	ASTM C136, AASHTO T27
Maximum Void Ratio	ASTM D 4254
Shear Wave Velocity vs. Confinement	Santamarina and Yun, 2003
Critical State Parameters	Santamarina and Cho, 2001
Flow Test	GDT Method AASHTO M 152

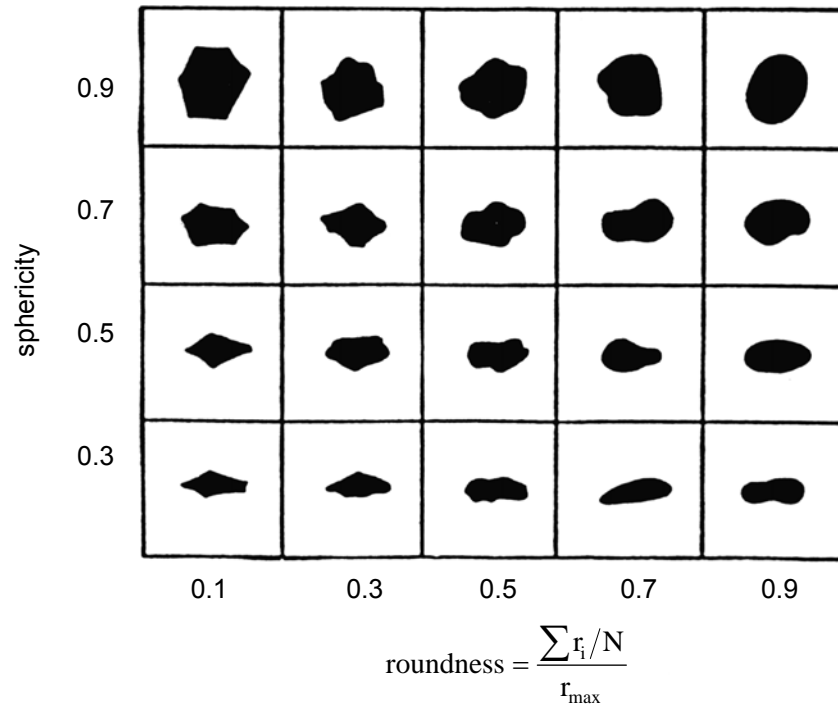
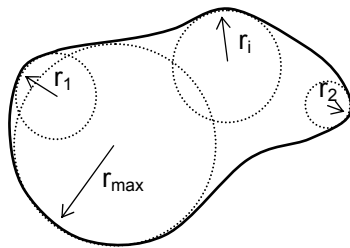


Figure 3.2 Chart used to characterize sphericity and roundness of particles (Krumbein and Sloss 1963).



Classification	<i>Roundness</i>
very angular	0.12-0.17
angular	0.17-0.25
subangular	0.25-0.35
subrounded	0.35-0.49
rounded	0.49-0.70
well rounded	0.70-1.00

Figure 3.3 Correlation between numerical roundness values and verbal descriptions used to classify particles (right). Roundness is defined as the radius of curvature of the corners divided by the radius of the maximum inscribed circle (left) (Powers, 1953).

Roughness is also determined for those particles that will be tested for shear wave velocity. A unique scale is created in which the particles of the roughest sample are arbitrarily assigned a roughness value of 3, Particles of the smoothest sample are assigned a value of 1 and all others are assigned an intermediate value according to their relative roughness.

Results and Analysis. The majority of the crushed granite particles exhibit similar shapes, their roundness values being near .25 and their sphericity values being about 0.8. However, the shape does vary with particle size. Smaller particles are more planar with sharp corners, while larger particles are rougher with more rounded corners (Figure 3.4). Crushed calcareous sands (limestone, dolomite, marble) are generally more rounded, elongated and rough than their granite counterparts. Natural sands exhibit a wide range of shapes with roundness ranging from very round 0.8 to subangular 0.3, sphericity ranging from 0.9 to 0.7 and surface texture ranging from very rough to smooth. Table 3.5 (end of chapter) presents shape values for both natural and crushed sands. Figure 3.5 shows extremes in shapes encountered in this study.

At least three mechanisms for the observed granite particles size-shape relationship are considered. First, the larger, rougher particles may be larger than the grain size of the parent material while smaller planar particles may be smaller than the grain size of the parent material. Intra-grain and Inter-grain fracture surfaces exhibit different shapes. Second, particle size plays an important role in the shape of natural sands due to the nature of brittle fracture. The stress at the root of the most prominent crack governs the strength of the material. Faults run throughout rock particles. Smaller particles are less likely to contain a major crack, and therefore are less likely to exhibit brittle fracture. In particles larger than 500 microns brittle fracture predominates over cleavage, but particles smaller than 50 microns are usually flat cleavage plates (Figure 2.2-d). The transition zone seems to occur at about 100 microns. Finally, Guimaraes (2002) observes that when Georgia granite coarse aggregate are fractured in compression, the resulting surface is covered by small and shallow vertical cracks with a teeth-like texture. The attrition between coarse aggregates with teeth-like surfaces generates a planar rock face and fine powder. Guimaraes (2002) indicates that this may be partially due to the influence of shear in fracture propagation.

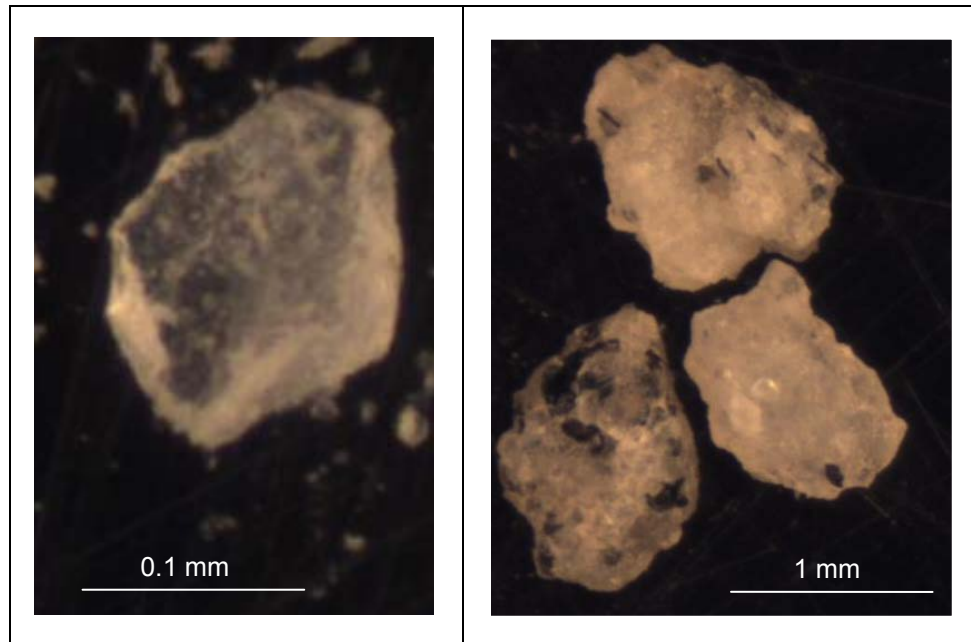


Figure 3.4 Shape of different sized particles from the same granite quarry. Smaller particles (left) tend to have planar faces and sharp corners, while larger particles (right) are more rough with less sharp corners.

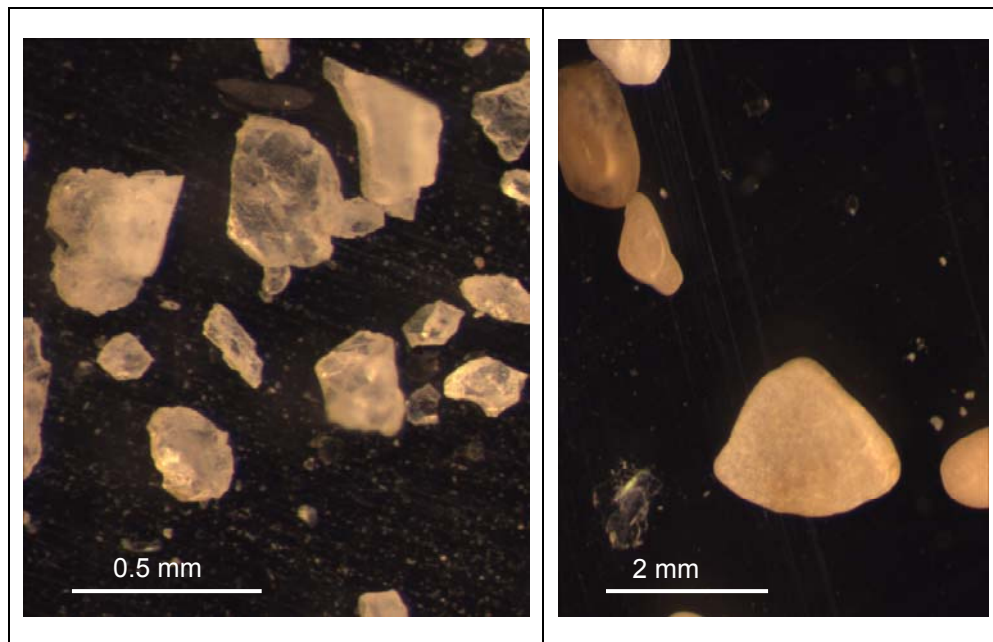


Figure 3.5 Shape extremes encountered in this study. The angular sand on the left is a crushed aggregate from Georgia, while the rounded sample on the right is a natural sand from Margaret River Australia.

The difference in shape between granite and calcareous sands is likely due to differences in cleavage properties and hardness between minerals. Krebs (1961) reports that granite particles are typically equidimensional because cleavage is less common. The Natural sands are generally less angular than the crushed sands due to the rounding tendencies of weathering as discussed in Chapter 1.

3.2.2 Grain Size Distribution

Crushed sands are manufactured to exhibit specific grain size distributions. Natural sands, on the other hand, come as-is and are generally less well graded than manufactured sands. Most of the crushed sands considered in this study are manufactured to meet state department of transportation specifications. Manufactured sand types are standard Georgia Department of Transportation concrete sand 10SM, high fines concrete sand 10FM, standard asphalt sands AW10 and W10, and high fines asphalt sands M10 and M810. Only that portion of the aggregate passing the #16 sieve is considered in this study.

The grain size distribution is determined in accordance with ASTM C136. One hundred fifteen grams of soil are separated using 8-inch sieves shaken by hand until the weight on each sieve changes less than 1% after 1 minute of shaking. Sieve numbers 20, 40, 60, 140 and 200 are used. The weight retained on each sieve is determined using a Denver scale accurate to 0.1 grams. Sands are split twice to homogenize the samples before returning them to their containers.

Results and analysis. The Grain size distributions of each crushed sand type fall within narrow bands (Figure 3.6). Several types of sands have very similar gradations. The gradations of the standard 10SM and high fines 10FM concrete sands are similar, with the high fines sand exhibiting an increase in percent passing the #200 sieve of less than 2%. Standard asphalt sands W10 and AW10 are similar in gradation to the concrete sands. High fines asphalt sands M10 and M810 contain significantly higher portions of particles passing the #200 sieve. Because the grain size distribution of most crushed sands fall within a few narrow bands, trends between gradation and macroscale properties discussed in section 3.3 show a limited number of points on the gradation axis.

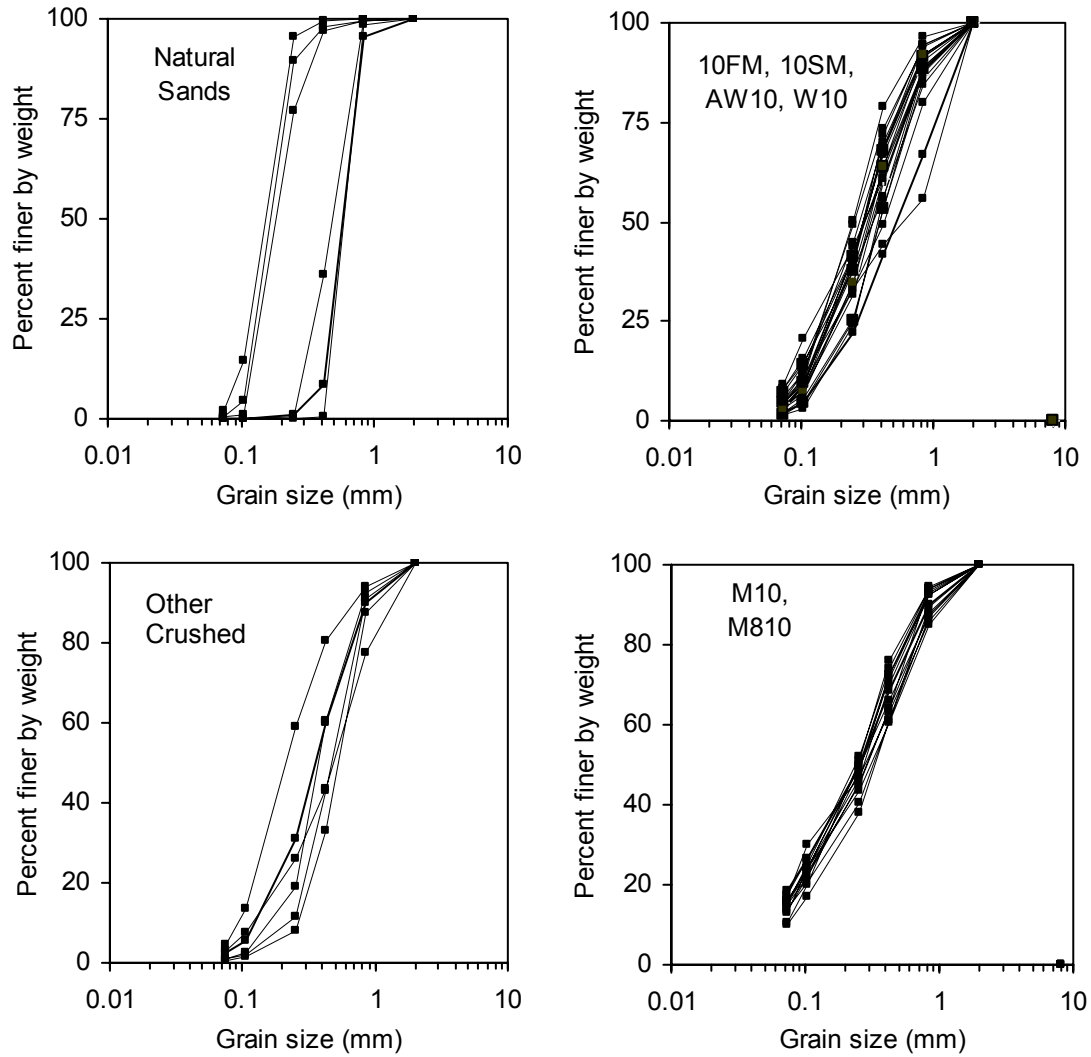


Figure 3.6 Grain Size distributions of sands used in this study. M10, M810 etc. are blend names used by the crushed stone industry, other refers to manufactured sands for which blend type is unknown or not standard. Most of the manufactured sands fall into two grain size distribution categories with lower or higher fines contents. Lower fines sands include 10FM, 10SM, W10 and AW10, while higher fines sands include M10 and M810 blends. Particles of a single natural sand show little size variation, but grain size does vary between specimens.

The natural sands from outside of Georgia are clean sands with uniformly sized particles, while those from inside Georgia have a broader grain size distribution. The sands generally fall into one of two size categories. The mean diameter of the larger grained sands is about 0.55 mm, while the mean diameter of the smaller grained sands is around 0.17 mm.

3.2.3 Microscale Parameters Comments

The shapes of crushed granites vary little between samples, but vary within a single sample according to particles size. In contrast, the shapes of natural sand particles vary markedly between samples, but vary little within a single sample. Crushed sand shape does vary between samples of different mineralogy. In addition, the variation in grain size distribution of crushed sands is mostly accounted for by the addition of particles passing the #200 sieve. However, the variation in grain size distribution of natural sands is mostly accounted for by different grain sizes. Because the natural and crushed sands vary at the microscale in different ways, when creating plots, which show the link between micro and macroscale it is often convenient to create separate plots; for the natural and the crushed sands.

4.3 MACROSCALE ANALYSIS

3.3.1 Maximum Void Ratio

Factors influencing maximum void ratio include the grain size distribution, roundness and slenderness ratio of the sand. A broader grain size distribution allows particles to pack more densely as smaller particles fill the voids between their larger neighbors. Particles that are more angular pack less tightly as sharp corners separate them. Increased particle slenderness, L_{\max}/L_{\min} , may decrease density as slender particles bridge gaps between grains and create large open voids. Each of the crushed granite samples contains some slender mica particles. The percentage of mica ranges from less than 1% to more than 25%.

The maximum void ratio is determined for twenty-seven crushed granites, four crushed limestones and nine natural sands in accordance with ASTM D 4254 methods A and C. Prior to testing sands are oven dried for 24 hours and the mold volume is water calibrated. Test method A

involves raining sand into a mold from a ½-inch spout positioned above the deposited soil. Several layers of loose sand are formed in the mold by slowly rotating the spout of the pouring device from the outer edge of the mold to the center in a circular manner. The tip of the spout is kept vertical ½ inch above the deposited sand and the layer height uniform. A straightedge is used to level the soil when the uppermost layer is between ½ and 1 inch above the top of the mold. The average of two tests determines the maximum void ratio if the difference between the tests is less than 1%. Otherwise, the procedure is repeated until constant values are attained. A specific gravity value of 2.65 is assumed in all calculations.

Test method C involves filling a 1000 ml graduated cylinder with 500 grams of sand and sealing it with a rubber stopper. The cylinder is inverted then quickly returned its original vertical position to create a loose fabric. The volume occupied by the sand is recorded and the procedure repeated until a consistent set of values is obtained.

Results and analysis. The maximum void ratios of each sample are presented in Table 3.5 (end of chapter). Figure 3.7 shows maximum void ratios obtained from test method A versus those obtained from test method C. There appears to be a linear correlation between the two with method A consistently producing higher values.

Figure 3.8 presents the measured maximum void ratios versus the coefficients of uniformity. Lines for different roundness are the empirical relationships developed by Youd (1973). This empirical relationship provides a convenient way to remove the effect of coefficient of uniformity and investigate the relationship between maximum void ratio and shape. According to these trends, roundness values between 0.21 and 0.49 are expected. These values are compared to the roundness values obtained in section 3.1.1 in Figure 3.9. Values determined using Krumbein's chart appear higher than those predicted with Youd equations.

Nineteen of the 27 crushed sands plot between the 0.20 and 0.25 roundness lines (Figure 3.8). Of the eight that plot outside of this range, four plot above, all of which are crushed granite. Those that plot above the 0.20 line are relatively high in mica, and the mica particles are relatively large so they can bridge their often-smaller more equidimensional neighbors. The specimen with the highest void ratio, (designated 1k9) is more than 25% mica and it is referred to

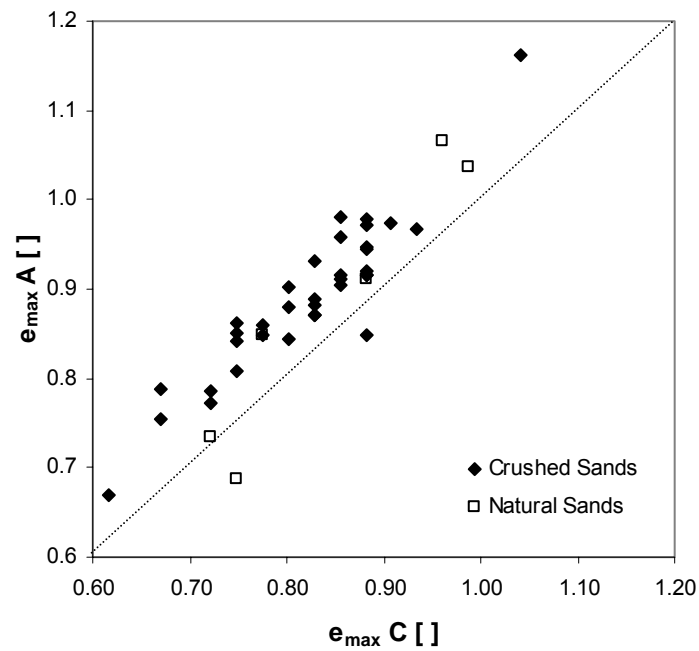


Figure 3.7 Maximum void ratio determined by raining sand into a mold (ASTM D 4254 method A) versus e_{\max} determined by inverting a graduated cylinder then quickly returning it to upright (ASTM D 4254 method C). There is a correlation between the values obtained from each method. Maximum void ratios determined from test method A are generally higher than those from test method C.

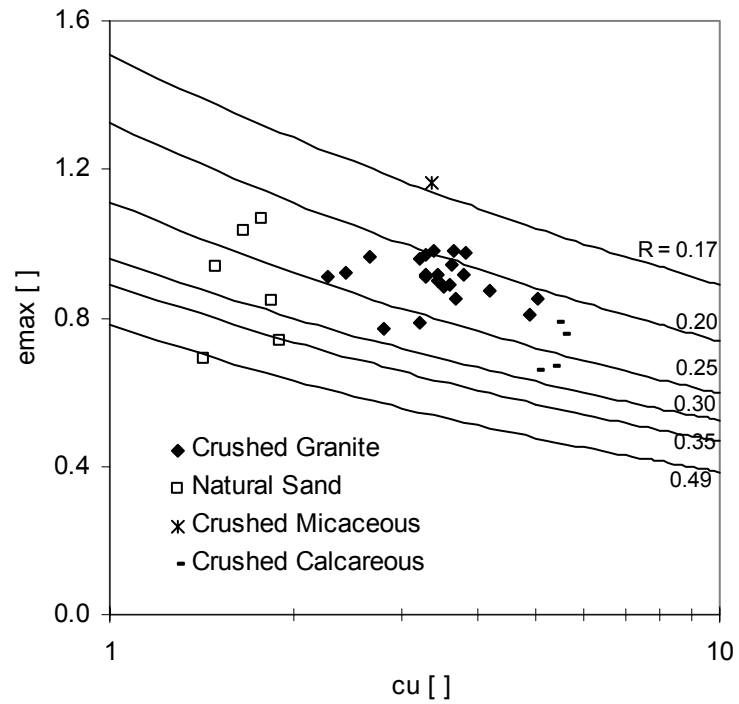


Figure 3.8 The value of e_{\max} as a function of coefficient of uniformity, C_u . Lines represent empirical relations between roundness R , e_{\max} and c_u (Youd, 1973). Youd roundness values are different from those used in this study (Figure 3.7). Nineteen of 27 crushed sand e_{\max} values fall between the 0.20 and 0.25 roundness lines. Natural sand e_{\max} values are much more variable.

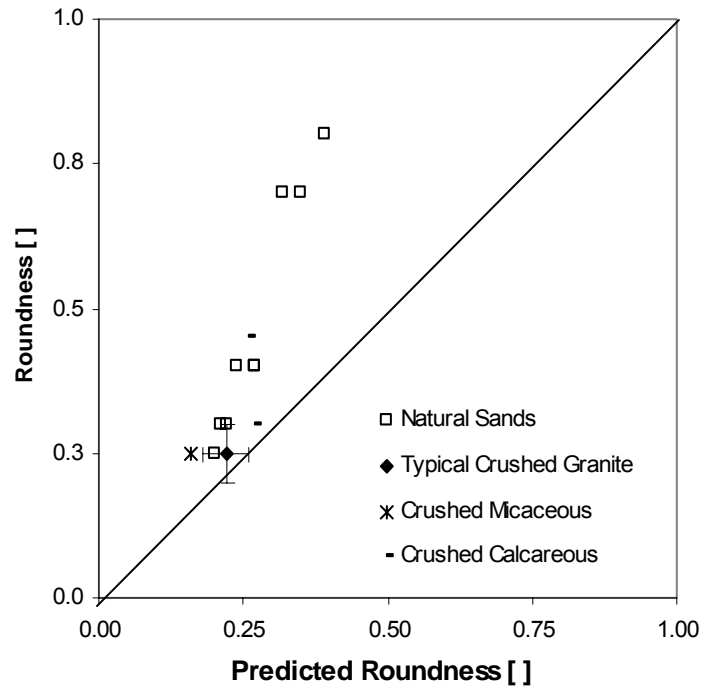


Figure 3.9 Relationship between roundness values determined using the chart in Figure 3.2, and roundness values predicted from e_{max} and c_u values using the empirical relations of Youd (1973).

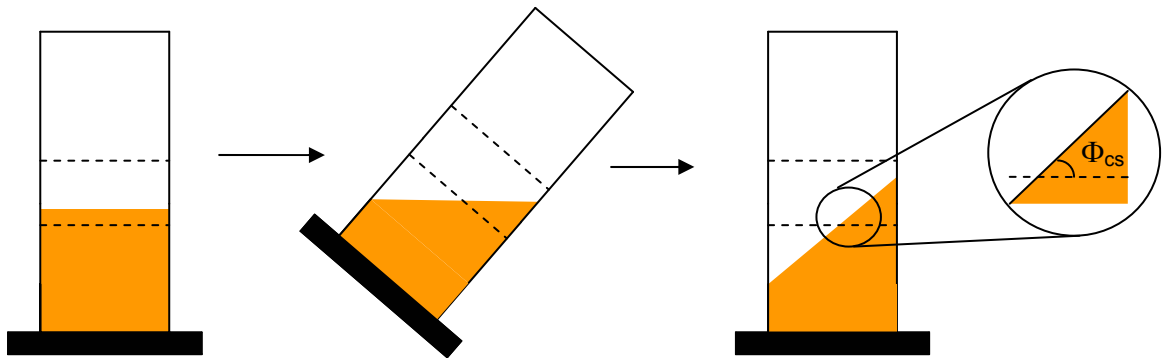


Figure 3.10 Use of Hele-Shaw cell to determine angle of repose (planar). The cell is rotated past 45° then returned to the upright position. The repose angle is determined in the center of the slope.

as micaceous sand throughout this document. Of the four samples which plot below the crushed sand trend, two are calcareous, they are both rounder than the crushed granites. One of these sands, (designated 2Z8) is composed of a mix of dolomite and limestone particles, which exhibit different shapes. Of the two crushed granites plotting below the trend, one is quite round for crushed granite and the other is composed of low sphericity particles with shapes resembling a rectangle. It is likely that particle alignment during deposition reduces the maximum measured void ratio.

3.3.2 Critical State Friction Angle

The critical state friction angle and the angle of repose share several characteristics. The critical state friction angle is related to the interparticle friction angle and the ability of particles to rotate (Cho, 2001) so is the angle of repose. Decreased roundness and increased roughness increase both angles through rotational frustration. Dilation and fabric rearrangement do not affect these two angles, as they do the angle of internal friction, because both occur at a statistically constant fabric and void ratio. However, unlike the critical state friction angle, a soil may exhibit several different angles of repose and the question arises as to which one should be used.

The angle of repose may be convex, concave or planar. The convex angle is created by raining sand onto a flat surface to create a pile, while the concave angle is the interior angle created by removing a plug from the center base of that sand pile, allowing the sand to exit. The planar angle of repose is created by rotating a Helle-Shaw cell past 45 degrees then returning it slowly to the upright position (Figure 3.10). A more detailed procedure is presented later in this section.

The planar angle is not a constant value. Jaeger et al. (1989) shows that if a sample with a slope equal to its angle of repose θ_r is tilted so that the slope increases, no movement is observed until the slope reaches a critical value θ_m , when an avalanche occurs. Equation 3.1 relates the difference between θ_r and θ_m , which is related to dilatancy δ .

$$\theta_r = \theta_m - \delta \quad (3.1)$$

Because of this affect the measured angle of repose oscillates between θ_m and θ_r with the former being the upper bound, the latter being the lower bound and the difference typically being a degree or two (D. A. Robinson and S. P. Friedman, 2002).

Two possible sources of error in measuring the planar angle of repose are (1) the tendency of the sand to segregate in the Helle-Shaw cell according to particles size and (2) the tendency of the measured angle to vary until a stable angle is reached after 2-3 rotations (Herrmann 1998). Segregation may be especially important in the crushed granite because of the size dependency of shape, and therefore the possibility that the repose angle varies with particle size.

The planar angle of repose of 34 sands are determined. Of these, 6 are natural sands, 24 are crushed granite and 4 are crushed calcareous sands. Planar results are compared with results of concave and convex tests performed on four of the specimens by Narsillio (2003) and critical state friction angles determined by triaxial tests of two of the sand types reported by Cho (2001). The planar friction angles of sands with fines contents greater than about 8% are not determined because they tend to stick together creating an uneven inconsistent angle.

The procedure recommended by Santamarina and Cho (2001) is used to determine the planar angle of repose. A Helle-Shaw cell is substituted for a graduated cylinder because of the extensive research into the angle of repose determined in this way. Prior to testing, sands are oven dried for 24 hours. They are allowed to cool in a sealed container. Sand is poured into the Helle-Shaw cell to a height just above the first of two lines. The device is rotated past 60 degrees, then slowly returned to the horizontal, taking to care to avoid bumps or jolts that may lead to an avalanche. A protractor is used to determine the angle between the horizontal line and the center section of the sand slope, which is the angle of repose. The procedure is repeated, changing the direction of rotation (right, left, right), until a steady angle is determined.

To measure the concave and convex angle of repose, Narsilio (2003) pours sand from a funnel to create a heap on a flat surface. A laser equipped to measure angles is shined across the heap surface to measure the convex angle. A small plug is then removed from the center of

the heap. Sand is allowed to flow until a stable internal angle is formed. This concave angle is then measured with the laser. The test is repeated five times for each specimen.

Results and analysis. Results of the angles of repose determined from the three different methods are presented in Figure 3.11. Only average values are shown, deviation from the mean is as high as 3 degrees. Angles of repose from highest to lowest value are concave, planar, convex and triaxial. The difference between concave and planar angles is about 8 degrees, planar and convex is about 1.5 degrees and convex and triaxial about 5 degrees. It is important to note that the angle of repose tests are all run on the same specimens, while triaxial test results are taken from results for sands with the same name. These sands may not have the same properties as the other specimens.

Planar angles of repose are plotted versus particle shape in Figure 3.12. Because crushed shapes show so little deviation, a typical value is shown. Decreased roundness clearly leads to increased angles of repose. Crushed calcareous sands exhibit higher friction angles at comparable roundness values than do crushed granite and natural sands.

The difference in angle of repose between planar and convex surfaces is most likely due to variation in the number and direction of particle contacts. Particles on the planar surface have a higher coordination number and contacts in more directions than particles on convex surfaces, which leads to greater stability. Particles resting on the concave surface form an arch shape. As the angle increases and particles begin to move toward the center it is possible that they form a compression ring and arching occurs increasing the angle of repose at which they are stable.

Roundness affects the angle of repose through rotational frustration. Particles that are more angular interlock and require greater activation energy to begin moving, which increases the angle of repose. Ellipticity leads to particle alignment, which decreases dilation. This leads to a smaller difference between the angle of repose and angle of maximum stability. Because the measured angle lies between the angle of repose and the maximum stability angle, the measured angle is likely to decrease.

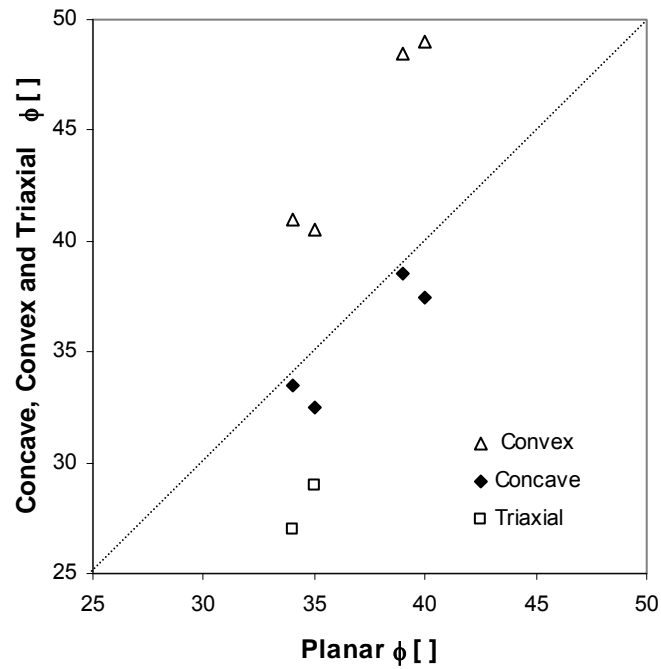


Figure 3.11 The Helle-Shaw cell (planar) angle of repose used to approximate the critical state friction angle versus angles of repose of a sand pile (convex), the cavity formed when sand drains from the center of a sand pile (concave) and the critical state friction angle from triaxial tests. Angles from highest to lowest are concave, planar, convex and triaxial. The same four samples are tested for planar, convex and concave (Narsillio, 2003) angles. Triaxial results are taken from Cho (2001).

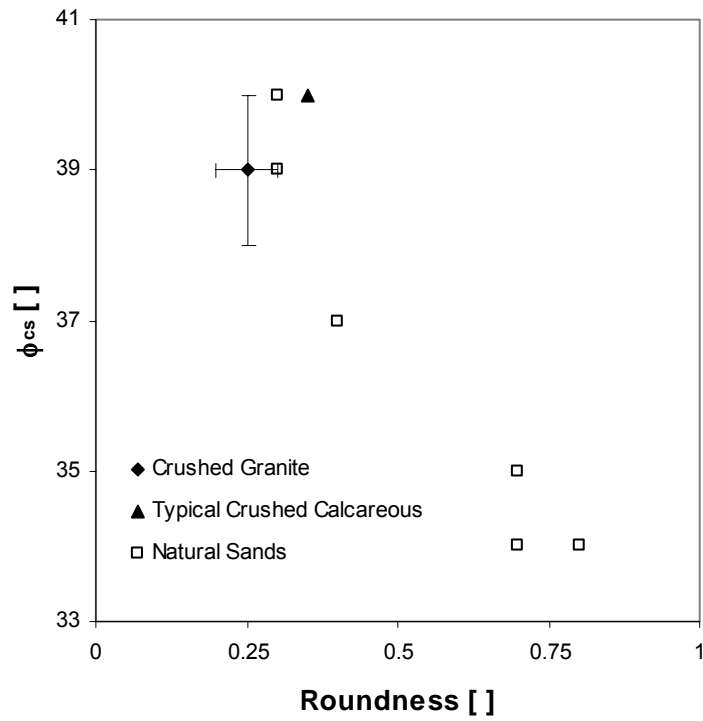


Figure 3.12 Critical state friction angle as a function of particle roundness. Because crushed sand shapes vary little between specimens, a typical roundness value for granite and calcareous sands is used. Lines represent the range of roundness and friction angles within which most samples fall.

3.3.3 Shear Wave Velocity versus Confinement

Shear wave propagation in particulate media is a contact dependent phenomenon. The change in shear wave velocity with effective stress can be modeled with a power relationship using α and β parameters according to $V_s = \alpha \sigma^\beta$. An empirical inverse relationship exists between α and β , which may be approximated as (Santamarina et al. 2001)

$$\beta = 0.36 - \frac{\alpha}{700} \quad (3.2)$$

It can be predicted that increasing surface roughness or decreasing roundness generally serves to reduce the stiffness at 1 kPa (α), and to increase the rate at which velocity increases with stress (β). Replacing a portion of the sand with silt has a similar effect. Preloading has the opposite affect; it generally increases α and decreases β .

Fifteen specimens are tested (seven natural sands, seven crushed granite and one crushed limestone–dolostone). A schematic of the test setup is displayed in Figure 3.13. Prior to testing, the heights of the mold, cap and bender elements are measured. The weight of the cap is determined and a 400 g sample of sand is weighed. Layers are created within the oedometer mold by pouring 60 cm³ through a 7 mm I.D funnel to create a single layer. The sand is placed by slowly rotating the funnel from the outside of the cell to the inside. Each layer is leveled then tamped with a 3.2 cm diameter tamper starting at the outside and moving toward the center in a circular motion. Tamping continues until no change in compaction is evident; the intent is to create the most dense specimen possible with this technique. Tapping with a rubber mallet five times per location at 90° intervals is used in addition to tamping to compact four of the crushed sands.

After the last layer is compacted, the cap is placed so that the bender elements are aligned vertically. Calipers are used to measure the distance from the top of the mold to the top of the cap at four locations. The vertical location of the bender element is determined using the average of these four distances and the cap thickness. The base plate bender element is connected to a

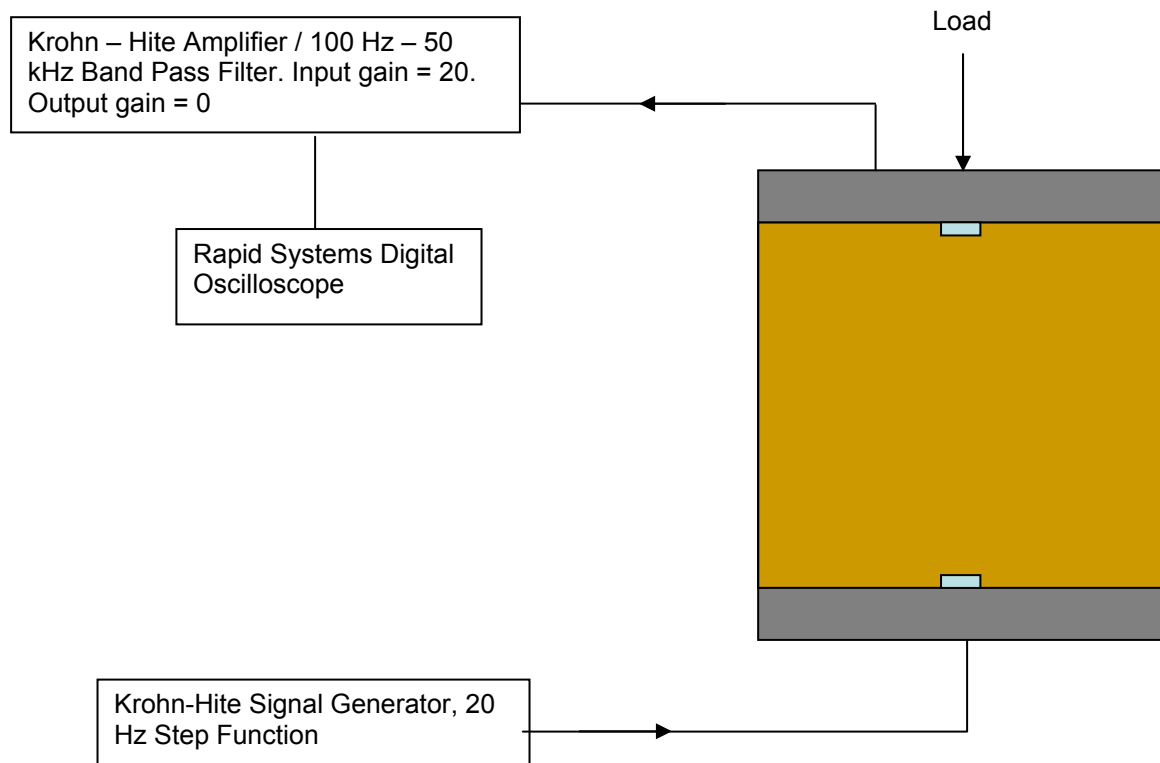


Figure 3.13 Simple schematic of shear wave velocity experimental setup. Diagram displays signal travel direction and instrument settings. Table 3.2 also displays instrumental settings.

Krohn - Hite model 1400 A signal generator while the top plate bender element is connected to a Krohn - Hite model 3944 amplifier/filter with coaxial cables (Figure 3.13). Both bender elements are covered with silver paint which is connected to ground wires. Equipment and settings are listed in Table 3.2.

Samples are loaded with 0, 6.9, 13.7, 2.8, 27.5, 11.2, and 110 N at 10-minute intervals then unloaded in the same manner. Dial gauge readings and shear wave signals are recorded at the completion of each load step.

Results and Analysis. Trends for α and β parameters are presented in Figures 3.14-16. The complete dataset is shown in Appendix A. Crushed sand shear wave parameter α is shown to increase with grain size while β decreases with both increasing grain size and fines content. Natural sands exhibit a different trend, α , decreases as roundness and roughness increase and is not a function of particle size. The α -coefficient is plotted against β -exponent for all sands in Figure 3.17. Results generally follow the trend expressed by Equation 3.8. Crushed micaceous and dolomite-limestone sands plot at one extreme with low α and high β values while angular beach sands plot at the other.

The observed relationship between D_{50} and shear wave velocity in crushed sands may be due to the relationship between size and shape. The angular, planar shapes of the smaller particles produce sharper contacts than the rounded rough shape of the larger particles. As discussed in Section 1.6, less stiff sharper contacts lead to decreased shear wave velocity.

The lower β values exhibited by sands with higher fines contents are related to the fabric of a sample with a broad grain size distribution. Smaller particles fill the voids between larger particles and avoid carrying load. Fewer load-carrying particles imply that each contact is at higher stress. Hertzian contact theory predicts a nonlinear stress-strain relationship, with stiffness increasing less quickly at higher stresses (Section 2.6). This leads to a lower β as small strain stiffness increases less quickly in soils that contain more high stress contacts.

The increase in α and decrease in β with decreasing roundness is due to the interplay between two competing mechanisms. As discussed previously the sharp contact of less round particles lead to a lower shear wave velocity, while preloading increases shear wave velocity.

Table 3.2 Instruments and settings used to determine shear wave velocity. Settings are constant unless otherwise noted. Figure 3.13 is a simple schematic of the experimental setup, which shows how each instrument is used.

Instrument	Model	Setting	Value
Oscilloscope	Rapid Systems R1016	Gain	Variable
		Number of Averages	50
Signal Generator	Krohn - Hite 1400 A	Frequency	20 HZ Step
Amplifier	Krohn - Hite 3944	Input Gain	20
		Output Gain	0
		Band Pass Filter	100 Hz - 50 kHz

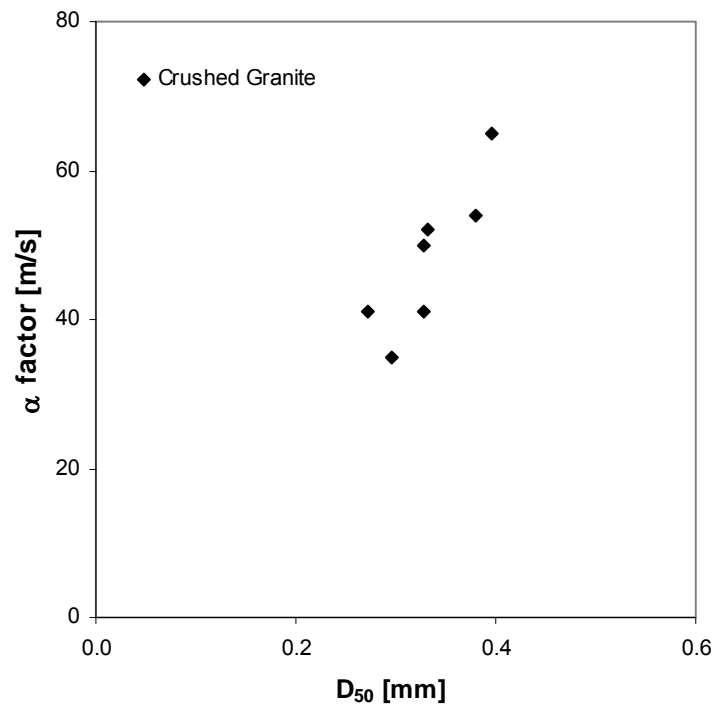


Figure 3.14 Shear wave parameter α as a function of mean crushed granite grain size D_{50} .

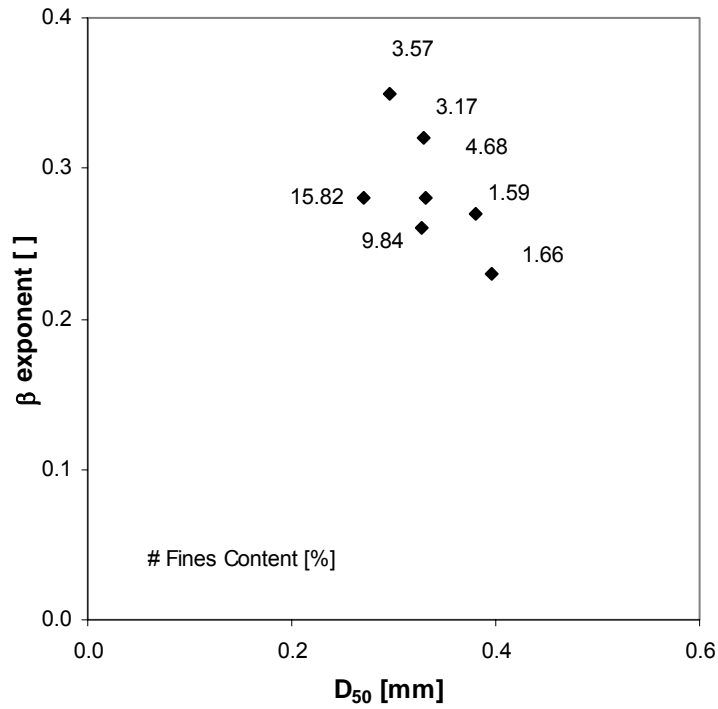


Figure 3.15 Shear wave parameter β as a function of crushed granite grain size and fines content.

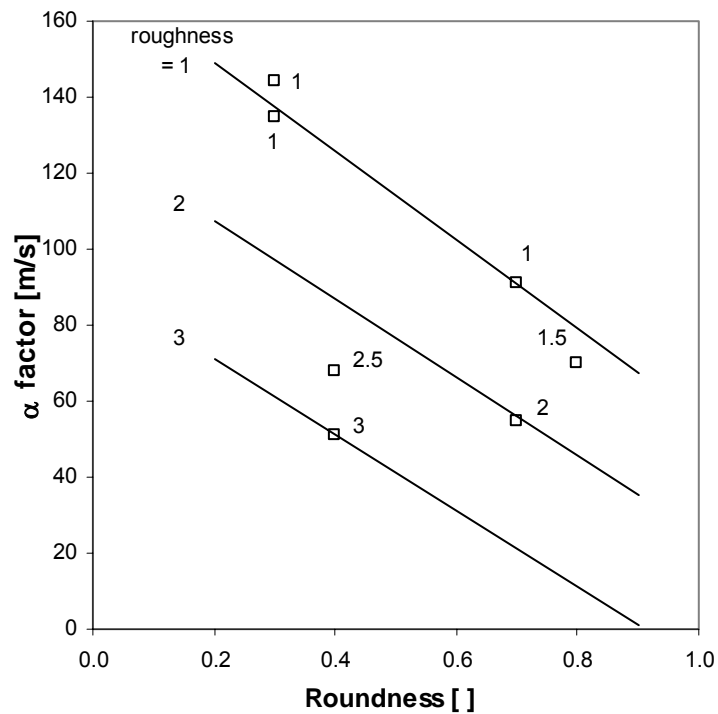


Figure 3.16 Shear wave parameter α as a function of natural sand roundness and roughness. Lines represent the two dimensional face of a three dimensional plane.

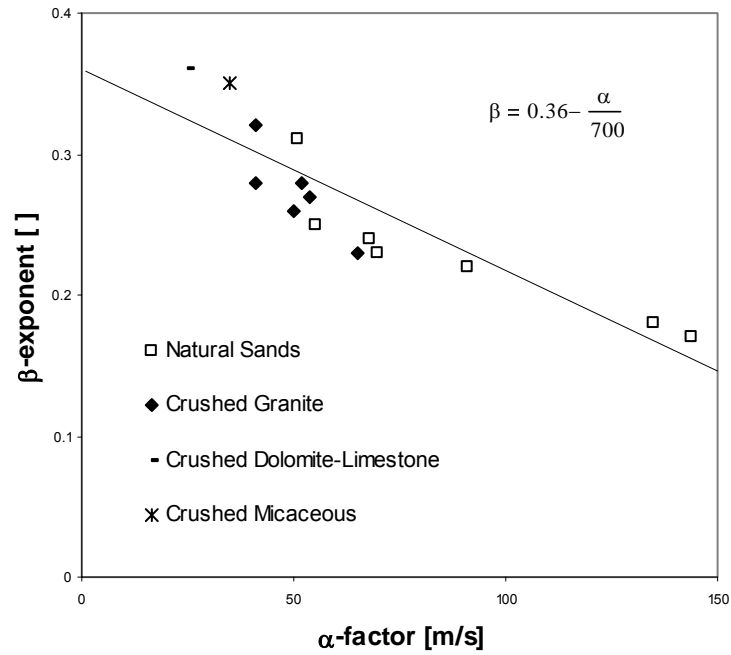


Figure 3.17 The Relationship between shear wave velocity parameters α and β . The line represents the relationship between α and β experimentally observed by Santamarina et al. (2001).

Tamping produces a significant vertical stress. A portion of this stress is transferred to the horizontal and locked in. The locked in stress creates a preloading condition, which is greater in angular sands because of interlocking particles. The change in contact nature due to preloading is more significant than the change due to the sharp angular contacts and shear wave velocity increases, α increases and β decreases, with increasing angularity.

Two factors contribute to the relatively high β and low α value observed in the calcareous sand. First, grain crushing allows considerable fabric rearrangement, which decreases void ratio and increases contact area with stress. Second, the shear modulus of the dolomite-limestone sand may be lower than the shear modulus of the crushed granite. Both lead to lower α and higher β values. Crushed micaceous sand behaves similarly. Low stiffness caused by the shape of mica particles decreases α . Bridging leads to a more open, less stable fabric which allows the number of contacts and the void ratio to change rapidly with stress leading to a higher β .

Crushed sands generally exhibit lower α and higher β values because (1) the sharp edges of their fractured shapes produce contacts which are less stiff than the more rounded natural sand contacts and (2) the presence of fines reduces shear wave velocity.

3.3.4 Critical State Parameters

The critical state is defined as the volume-stress state at which soil continues to shear at constant volume. In this state, particle rotations (which cause the soil to loosen) and force chain collapses (which cause the soil to densify) are balanced (Santamarina 2002). Critical state theory postulates that, a unique line, termed the critical state line, exists in the e - p' - q space, and represents the ultimate state of the particulate material in drained and undrained tests.

The critical state line is characterized by three parameters M , λ and Γ . M is the strength parameter relating shear and confining stress at failure, Γ is the void ratio when the soil fails at 1 kPa and λ is related to the effect increased confining stress has on void ratio. These are the slope in the p' - q space and the slope and intercept in the e - p' space.

Cho and Santamarina (2003) demonstrate that the critical state parameters may be related to soil index properties (Table 3.3) and/or particle shape. Both the strength parameter M

Table 3.3 One-to-one correlation among soil index properties and critical state parameters – Trends (Cho and Santamarina 2003).

Parameters	C_u	e_{max}	e_{min}	I_e	\underline{M}	λ	Γ
D_{50}	n	W^*	n	n	n	n	W^*
C_u		W	n	S	W	W	n
e_{max}			S	S	W	W	S
e_{min}				n	n	n	S
I_e					W	W	W
M						n	W
λ							W

Notation: S strong ($r^2 \geq 0.5$); W weak ($0.5 > r^2 \geq 0.2$); n none ($r^2 < 0.2$); * inverse correlation, i.e., if one increases the other decreases.

and the intercept Γ are shown to increase as roundness and sphericity decrease. There is a strong correlation between maximum and minimum void ratio and Γ . However, there is a weak correlation between λ and both particle shape and soil index properties.

Critical state values are typically obtained through analysis of a series of drained triaxial tests. Santamarina and Cho (2001) propose a simplified method used in this study. Results are compared with triaxial data for the same soils and are found to be reliable. One limitation of the simplified test method is that sands with moderate or high fines content can not be tested. Staley (2002) uses a similar method to investigate critical state parameter values.

Seven natural sands and two crushed sands are tested following the procedure outlined by Santamarina and Cho (2001). Materials used in the setup include a vacuum pump, 1.5 inch ID thin latex membrane, two Plexiglas caps, two O-rings, a graduated cylinder, a porous stone, and a 4.6 mm I.D. transparent Teflon tube (Figure 3.18). Prior to testing the volume of the empty device which includes the Plexiglas caps, porous stone, membrane, o-rings and a predetermined length of tubing, is determined by submerging them in a graduated cylinder. The soil is boiled in water for five minutes to remove air. Additional water is de-aired using a Nold De-Aerator. The soil is submerged in the deaired water then spooned into the membrane to a height roughly twice the specimen diameter. The vacuum is activated to allow water to fill the Teflon tubing to a predetermined height, then the Plexiglas cap is placed atop the soil and secured with an o-ring.

The test procedure is as follows: The specimen is kneaded, then rolled between the hands to produce a homogeneous sample in the loosest possible state. The device is then placed vertically atop a notched table so that the tubing runs through the notch. A 5 kPa vacuum pressure is applied while axially compressing the specimen to a strain of 40%, making sure that the specimen remains vertical. Before releasing the specimen the height of the water in the Teflon tubing is recorded. The entire procedure is repeated at confining pressures of 10, 15, 20, 30, 45 and 60 kPa. To determine a reference void ratio, the specimen is kneaded, rolled and exposed to a confining pressure of 40 kPa, then submerged in a graduated cylinder to determine the volume of the combined device and soil. Finally, the soil is removed from the device, oven dried and weighed.

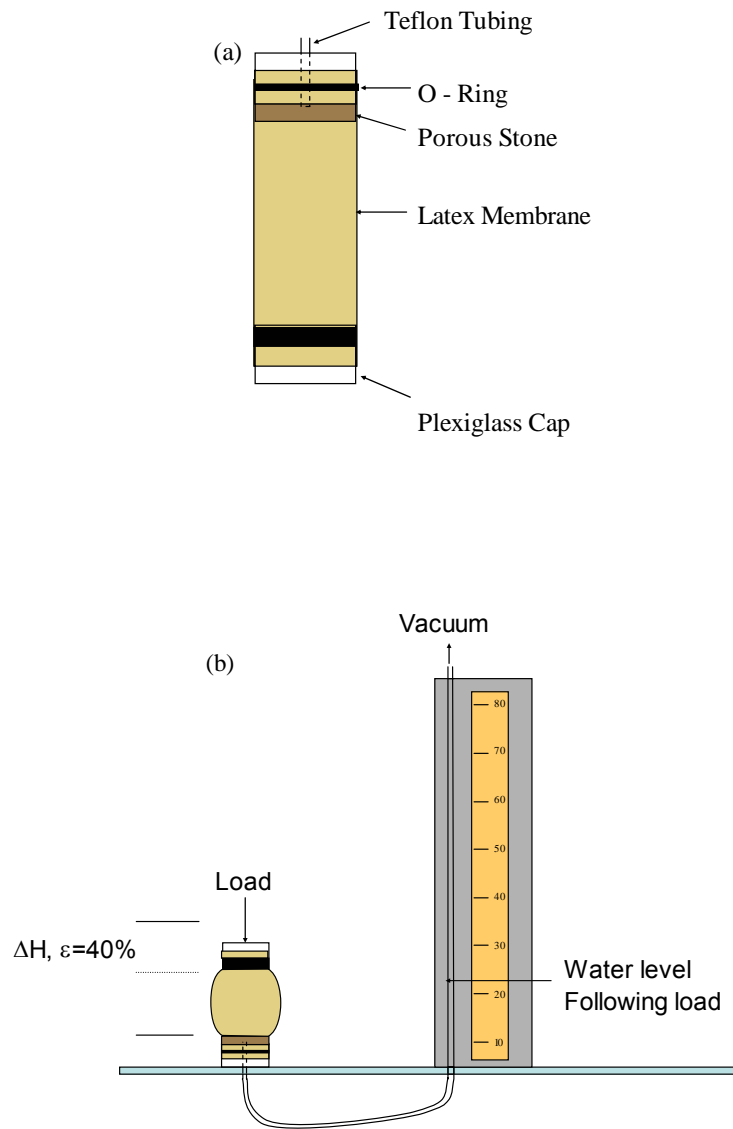


Figure 3.18 Simplified critical state apparatus. (a) Description of parts and (b) apparatus following applied load. Vacuum pressures of 5, 10, 20, 30, 45 and 60 are applied. Load magnitude is not measured; sands are loaded until strains reach about 40%. All samples are dilative during shear.

Data reduction and error analysis. The effective confining stress is corrected for membrane stiffness as

$$\sigma'_3 = \sigma'_c + \sigma'_m \quad (3.3)$$

where σ'_m is the stress required to laterally strain only the membrane in a manner similar to that which it undergoes during testing, σ'_c is the confining stress corresponding to the vacuum pressure, and σ'_3 is the corrected confining stress.

The principal and deviator stresses, p and q , can be written in terms of the confining stress and the critical state friction angle, ϕ_{cs} according to the following equations.

$$p' = \sigma'_3 \cdot \left[\frac{(3 - \sin(\phi_{cs}))}{3(1 - \sin(\phi_{cs}))} \right] \quad (3.4)$$

$$q = \sigma'_3 \cdot \left[\frac{(2 \sin(\phi_{cs}))}{(1 - \sin(\phi_{cs}))} \right] \quad (3.5)$$

The strength parameter M is defined as the ratio of q to p' at critical state. Dividing Equation 3.5 by Equation 3.4 gives equation 3.6 which is only valid for triaxial compression.

$$M = \frac{q}{p'} = \frac{6 \cdot \sin(\phi_{cs})}{3 - \sin(\phi_{cs})} \quad (3.6)$$

The specimen volume V_{sp} is determined by subtracting the device volume measured before the test V_d from the total volume measured during the test V_t . The reference water volume in the specimen V_{wo} is then determined by subtracting the volume of the dried soil V_s from the specimen volume V_{sp} . From the reference water volume, Equation 3.7 is used to determine the water volume at any confining stress is

$$V_{wi} = V_{wo} + (h_o - h_i) \cdot A_t \quad (3.7)$$

where h_o is the height of the water recorded when determining the reference volume, h_i and V_{wi} are the height and volume at the i^{th} confining stress, and A_t is the cross sectional area of the tubing. The final step is to compute the void ratio at each confining pressure according to the Equation 3.8.

$$e_i = \frac{(V_{wi} \cdot G_s \cdot \gamma_w)}{W_s} \quad (3.8)$$

An error analysis of the procedure is completed using the parameter values and standard uncertainties as shown in Table 3.4. Mathematical calculations are shown in Mathgram 3.1. The graduated cylinder, which is used to determine the volume of the apparatus has lines every two milliliters, while the graduated cylinder used to determine the volume of the apparatus and soil has lines every 5 ml. Volume precisions of 0.5 ml and 1 ml for the two cylinders are used in the calculation. The scale is accurate to 0.1 grams and specific gravity values are assumed to be with .02 grams per cubic centimeter. The analysis shows that the relative standard uncertainty of the void ratio measurement is about .05 or 5%.

Results and analysis. Results are displayed in Table 3.5 (end of chapter). No strong correlation is observed between λ or Γ and any microscale soil indexes or shape. There is a weak correlation between λ and Γ in the natural sands (Figure 3.19). M is a function of the critical state friction angle. The relationship between f_{cs} and soil indexes and shape is discussed in Section 3.3.2.

Localization may have caused error in the critical state parameter values reported herein. Roughly 50% of the sands show visible localization. When it is observed, the test is repeated with the sand in a looser state to reduce localization. Even when localization is not observed it may affect results as shown by Klotz and Coop (2002) (Figure 3.20). They use local and global measurements of void ratio to determine the critical state parameters of two sands, and infer localization when local strains differ from global strains. All samples reported localize before 30% strain and localization begins earliest and is most prevalent in the sample tested at 50 kPa, which is within the range of confining pressures used in this testing regimen. Another reason to consider

Table 3.4 Values used to establish the uncertainty in critical state parameters determined using the simplified method. Typical values are used, they do not represent the results of a single test.

	Description	Value	Standard Uncertainty	Relative Standard Uncertainty U_x/x
V_{total}	Volume measured during the test	135 ml	1 ml	.0074
V_{app}	Volume of latex membrane, caps, o-rings and tubing	65 ml	.5 ml	.0077
M_{sand}	Mass of the sand	105 gm	. 1 gm	.00095
G_s	Estimated specific gravity	2.65	.02	.0075
e (Mathgram 3.1)	Void ratio	.85	.053	.06
Γ (Mathgram 3.1)	Intercept of e-p' CS line	0.82	.051	.06

Mathgram 3.1 Error analysis of simplified critical state test. Assumed values are listed first, followed by equations, calculations and results.

Constants

$V_{total} := 135\text{mL}$	$\Delta V_{total} := 1\text{mL}$	$G_s := 2.65$	$p'_i := 23.1 \cdot 10^3$
$M_{sand} := 105\text{gm}$	$\Delta M_{sand} := .1\text{gm}$	$\Delta G_s := .02$	$p'_f := 123.6 \cdot 10^3$
$V_{app} := 65\text{mL}$	$\Delta V_{app} := 0.5\text{mL}$	$e_o := .85$	

Equations

$$\Delta Y(x) = \left| \left(\frac{d}{dX} Y \right) \cdot \Delta X \right| \quad (1)$$

$$e = \frac{V_{void}}{V_{solid}} \quad (2)$$

$$V_{void} = V_{total} - V_{sand} - V_{apparatus} \quad (3)$$

$$V_{solid} = \frac{M_{sand}}{G_s} \cdot \frac{\text{mL}}{\text{gm}} \quad (4)$$

$$\Delta \Gamma = \Delta e_i \quad (5)$$

$$\lambda = \frac{e_f - e_i}{\log(p'_f) - \log(p'_i)} \quad (6)$$

Substituting (2), (3) and (4) into (1)

$$\Delta e(V_{total}, V_{app}, M_{sand}, G_s) = \left| \left(\frac{d}{dV_{total}} e \right) \cdot \Delta V_{total} \right| + \left| \left(\frac{d}{dV_{app}} e \right) \cdot \Delta V_{app} \right| + \left| \left(\frac{d}{dM_{sand}} e \right) \cdot \Delta M_{sand} \right| + \left| \left(\frac{d}{dG_s} e \right) \cdot \Delta G_s \right| \dots$$

$$\Delta e = 0.053$$

$$\frac{\Delta e}{e_o} = 0.062$$

From Equation 5:

$$\Delta \Gamma = 0.053$$

$$\frac{\Delta \Gamma}{\Gamma} = .062$$

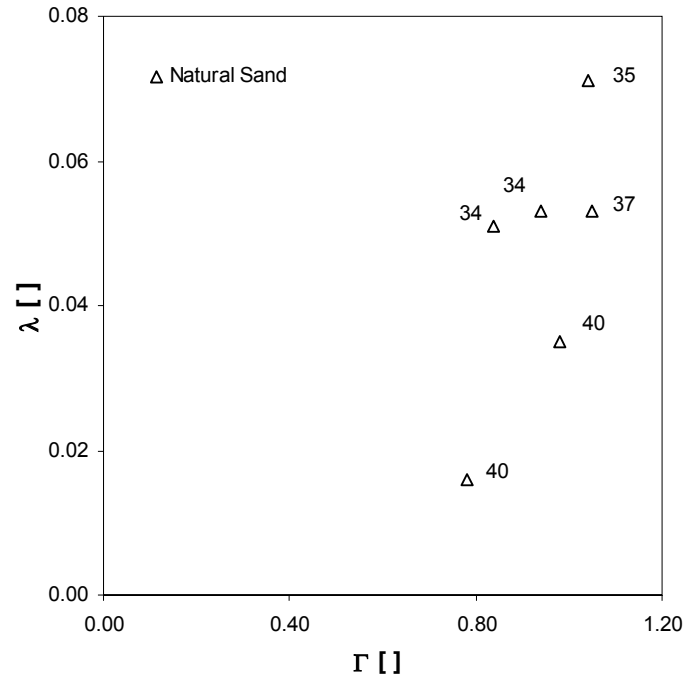


Figure 3.19 Critical state parameter λ as a function of Γ for natural sands. Numbers next to symbols represent the specimen critical state friction angle.

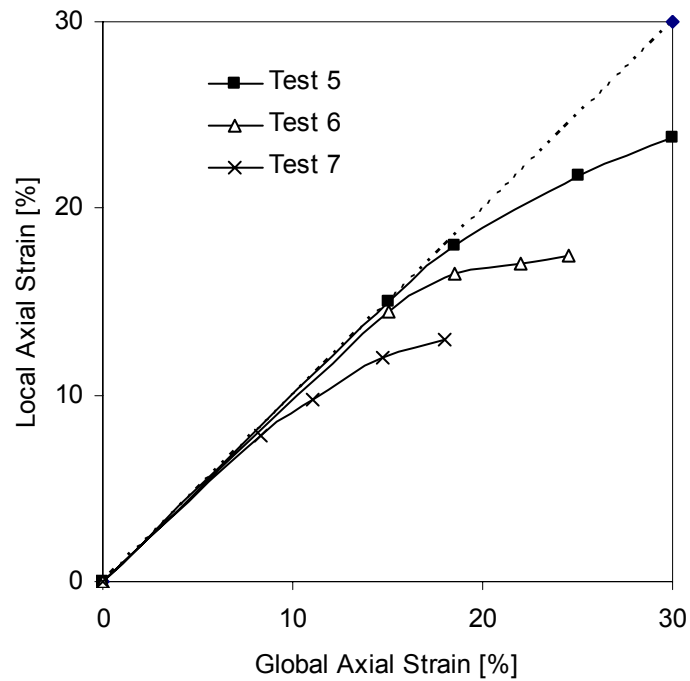


Figure 3.20 Localization identified by comparing local and global strains. Test 7 which exhibits the greatest localization is performed on a loose sand at a confining pressure within the range used in this study. The strain level for localization is much lower than the strain level used in performing simplified critical state tests. (Klotz and Coop, 2002).

localization is that all samples tested are dilative. Dilative drained triaxial tests are prone to localization.

Localization may have been more prevalent in this study than in the studies reported by Santamarina and Cho (2001) and Staley (2002) because of the range of confining pressures used. Santamarina and Cho (2001) use a confining pressure range of 0-120 kPa, while Staley (2002) uses confining pressures of 0-150 kPa. A range of 0-60 kPa is used in this study. Higher confining pressures reduce the tendency to localization.

3.3.5 Flow Test / Compressive strength

Factors influencing the strength of concrete include the water cement ratio, air entrainment, cement type, aggregate, mixing water, admixtures, curing conditions, time, humidity, temperature and testing conditions. Workability is also a function of several variables, which include water content, cement content, aggregate characteristics and admixtures (Mehta and Monteiro 1993). Of these, only aggregate characteristics are varied in this study.

Aggregate properties, which affect workability and/or strength, include particle size, shape, surface texture, gradation and mineralogy. In low water-cement ratio mortars, strength decreases as the maximum coarse aggregate size increases because a weaker paste-aggregate transition zone is formed (Mehta and Monteiro 1993). This effect should not be significant in this study because of the relatively high water cement ratio used and because only fine aggregate is present. As the maximum coarse aggregate size decreases, workability also decreases, because increased particle specific surface requires more paste to coat particles, which leaves less to fill voids. Again, the trend may be different when only fine aggregate is present. More angular particles increase strength and decrease workability. The decrease in workability can be related to increased specific surface and interlocking of angular particles. The strength difference between angular and round particles is most significant in the first few weeks, and diminishes with time. Mehta and Monteiro (1993) propose that the early increase in strength is due to a better physical bond between mortar and rough particles. At later stages as chemical bonding takes place the influence of physical bonding is reduced, as is the strength difference. Alford and Poole (1979) give three explanations for the increase in strength with angularity. First, angular

aggregates have more nodal points at which micro cracking may develop; this type of cracking increases the mortar's resistance to catastrophic crack propagation. Second angular aggregate interlocking leads to an increase in strength. Finally, the energy to cause stable fracture is equal to the energy required to form new surface. Angular aggregates exhibit a greater surface area and thus the energy required to form new surface is higher.

Research addressing the influence of grain size distribution on strength and workability has produced conflicting results. Kronlof (1994) shows that the addition of fine sand and silt to a cement paste increases workability and strength while decreasing porosity. The improvements in mortar properties are largest when fines are irregularly shaped and silt sized. Kronlof relates these effects to improved packing. Data from Bonavetti and Irassar (1994), on the other hand, shows that replacing a portion of the natural sand with granite stone dust in a mortar causes decreased workability. Early strength increases when dust content is less than 10% and decreases when dust content is greater than 10%. Limestone and quartz dust increase strength at all compositions tested. The decrease in workability is proposed to be due to the greater specific surface of the dust, while the increase in early strength is due to increased hydration. Greater hydration leads to a higher gel-space ratio and therefore decreased capillary porosity, which has been shown to increase strength. The discrepancy between these two studies may be due to the presence of coarse aggregate in the first study and not in the second, which would have affected the grain size distribution and the packing. It may also be due to the use of a different shapes very fine aggregate and sand in the second study. The replacement of natural sand with similar sized crushed sand rather than stone dust may have produced similar results.

Strength values reported herein are not converted to equivalent cylindrical strengths. De Larrard et al. (1994) reports that a typical value of $k_{cc} = f_{c_{cyl}} / f_{c_{cubic}}$ is about 0.82. However, values range from 0.71 to 0.94 for standard concretes. An experimental study of the conversion ratio is recommended if strengths are to be converted.

Ten crushed sands and six natural sands are used to prepare mortar, which is tested for workability and strength. The test procedure follows closely the Draft Flow Test compiled by the

Georgia Crushed Stone Association and provided by Eric Ownby (personal communication 2003), but modified to accommodate strength as well as workability testing.

To prepare the mortar (Figure 3.21), water is first poured into a mixing bowl then cement is slowly added while mixing (30 s). Mixing continues as sand is added (30 s) and for 30 seconds more. The bowl is removed from the mixer, the sides are scraped with the metal spatula (15 s), and the bowl is covered. The mortar is then allowed to set (75 s), after which mixing continues for 60 seconds.

The flow test is performed next. The flow table is modified from AASHTO M152, C clamps are used to attach the table to a solid base. The flow mold is filled to mid-height with mortar, which is tamped 20 times with only enough pressure to ensure the mold is uniformly filled. The mold is then filled just above full height and the upper layer of mortar is tamped 20 times. Mortar above the mold is scraped away using a sawing motion with a straightedge. The flow table is wiped clean and dry. The mold is removed and the table is dropped 10 times at a frequency of 100 Hz (60 s). Calipers are used to measure the distance from the edge of the table to the mortar at four locations 90° apart (30 s).

Then, three cubical molds coated with mold release are filled to mid-height with mortar, which is tamped ten times. The mold is then filled above full height, tamped 10 more times then vibrated for two minutes on a vibratory table. Excess mortar is scraped away with a straightedge and the mold is placed in an airtight container. After 24 hours the samples are removed from the mold and placed in a lime-water bath to cure (lime mixed with water at saturation). After 14 days, a hydraulic compression tester is used to axially load the samples at a rate of 2000 lb per minute to failure.

Results and analysis. Results of tests using natural sands are plotted in Figure 3.22. Flow values increase with increasing particle size and roundness. Strength also increases with particle size and may decrease with increasing sphericity. Sands with higher flow values also tend to exhibit higher strength.

Crushed granite results are plotted in Figure 3.23. Samples can be divided into higher fines (>13%) sands and lower fines (<5%) sands. The higher fines sands are stronger and flow

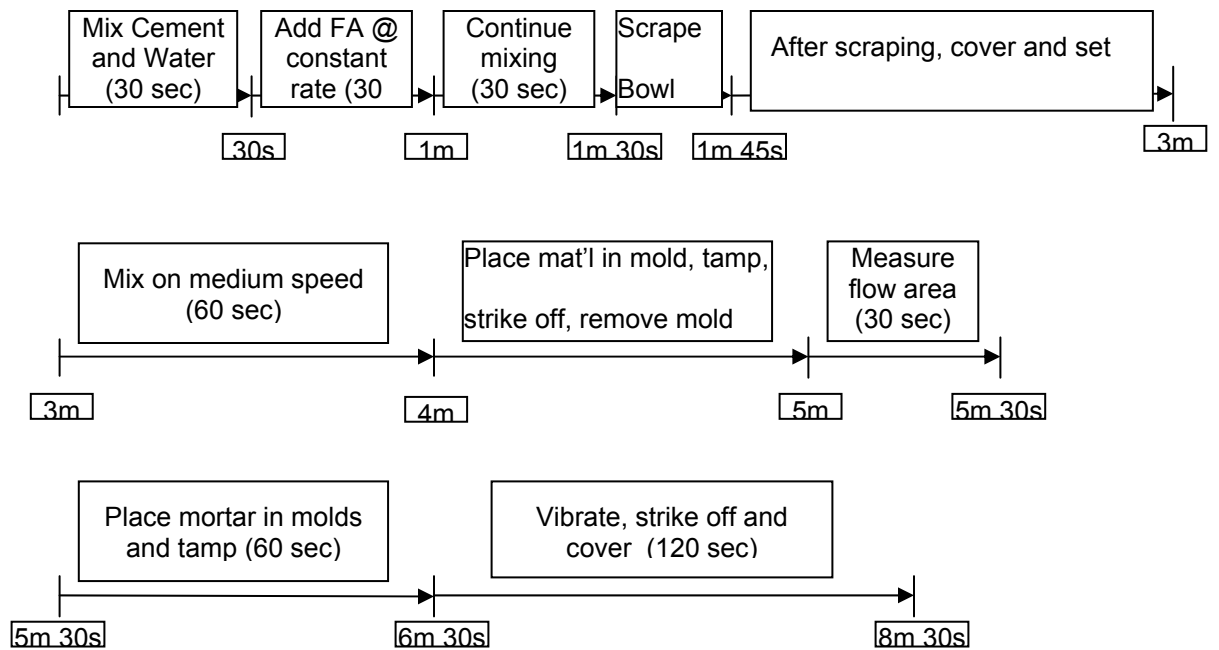


Figure 3.21 Schedule followed in performing the flow test and preparing cubical samples for strength testing. Details in the text.

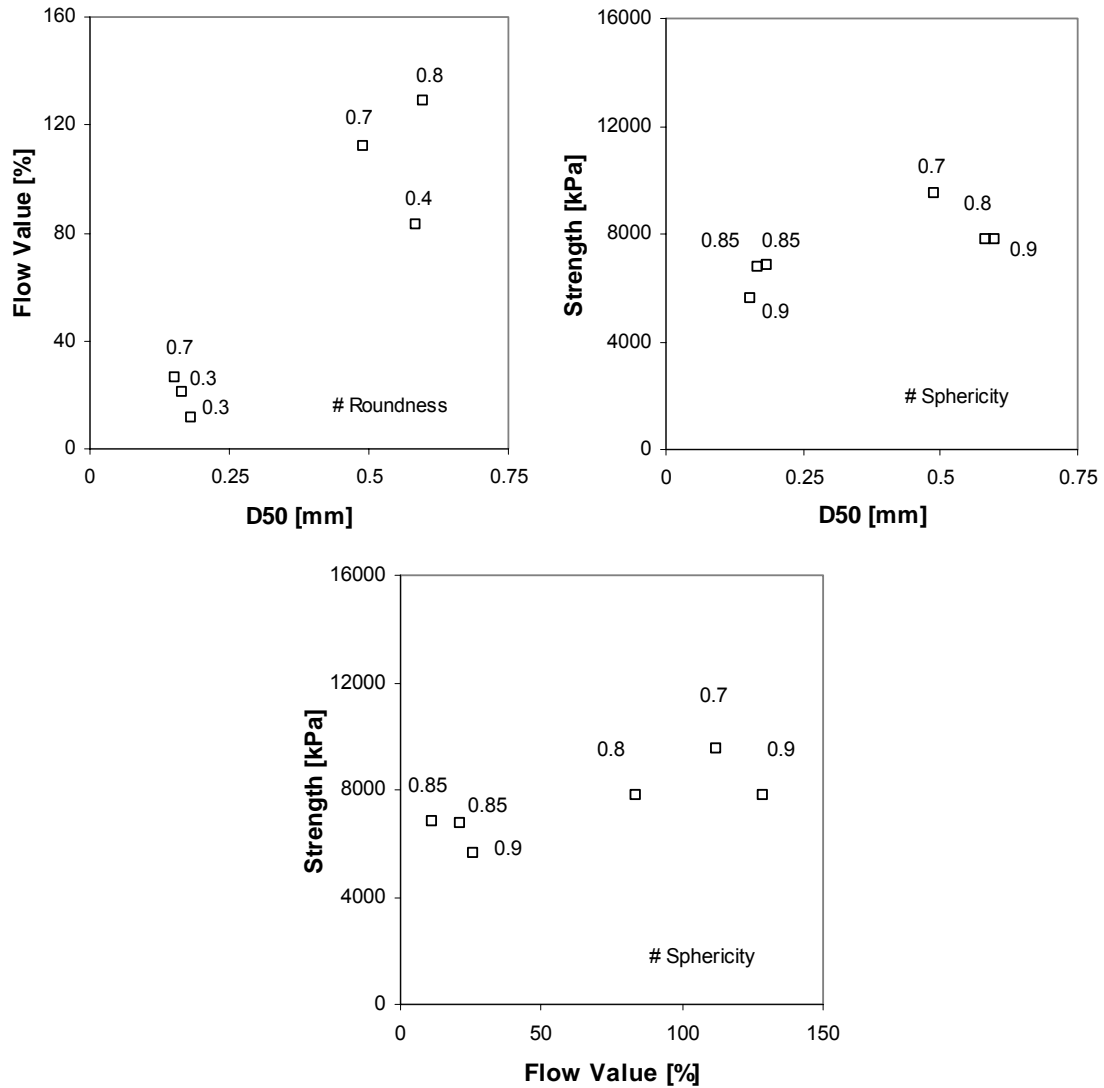


Figure 3.22 Strength and workability of natural sand mortars. (top left) Flow as a function of particle size and roundness, (top right) strength as a function of particle size and sphericity and (bottom) strength as a function of flow value.

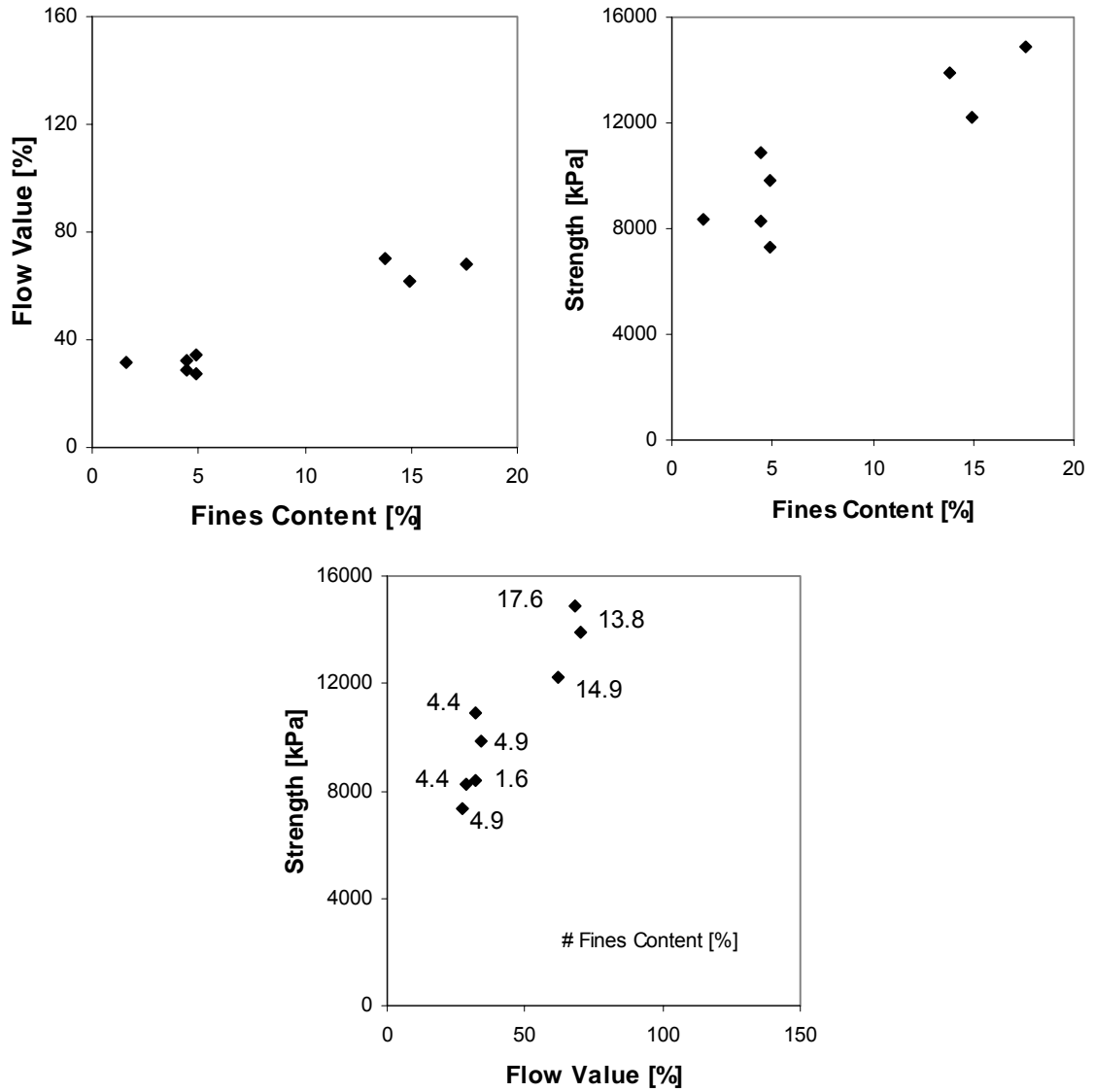


Figure 3.23 Strength and workability of crushed granites. (top left) Flow as a function of fines content, (top right) strength as a function of fines content and (bottom) strength as a function of flow value.

more easily than the lower fines sands. As with natural sands, strength increases with increasing flow.

Figure 3.24 presents data from all samples. Strength is shown to increase with fines content and particle diameter. Flow also increases with particle diameter. The slope of the strength-flow trend is higher for crushed than natural sands.

Capillary forces decrease with increasing particle diameter, leading to increased flowability with larger grain size. Also, larger particle size in natural sands decreases the specific surface of the aggregate. This means that less paste is required to coat aggregate particles; and more paste remains in the voids to promote flow. It is unclear why a correlation is observed between grain size and strength.

High fines content in crushed sands decreases the permeability of the fresh mortar. During the flow test, pore pressures build up as the table is dropped. The effective stress inside the mortar decreases and particles may lose contact. This allows particles to move more freely and flow increases. Fines content may increase strength by increasing the packing density of the mortar, or by increasing hydration, thereby decreasing porosity for capillary action. These results show that for the sands considered, flow is correlated to strength.

4.4 CONCLUSIONS

- The shape of Georgia crushed granites is size dependent. Larger grains exhibit uneven surface texture and comparatively rounded corners. Smaller grains have planar sides and angular corners.
- The shape of natural sands varies markedly, from very round and spherical to angular and non-spherical.
- The maximum void ratio depends on the coefficient of uniformity and particle shape.
- Lower roundness values in crushed sands lead to higher maximum void ratios, higher critical state friction angles, lower small strain stiffness values, and increased mortar strength.

- Increased fines content leads to increased workability and strength in the tested sands and conditions.
- The value of flow is correlated with mortar strength for the sands and conditions tested. The strength of a sand exhibiting a given flow value is higher for crushed sands than for natural sands.

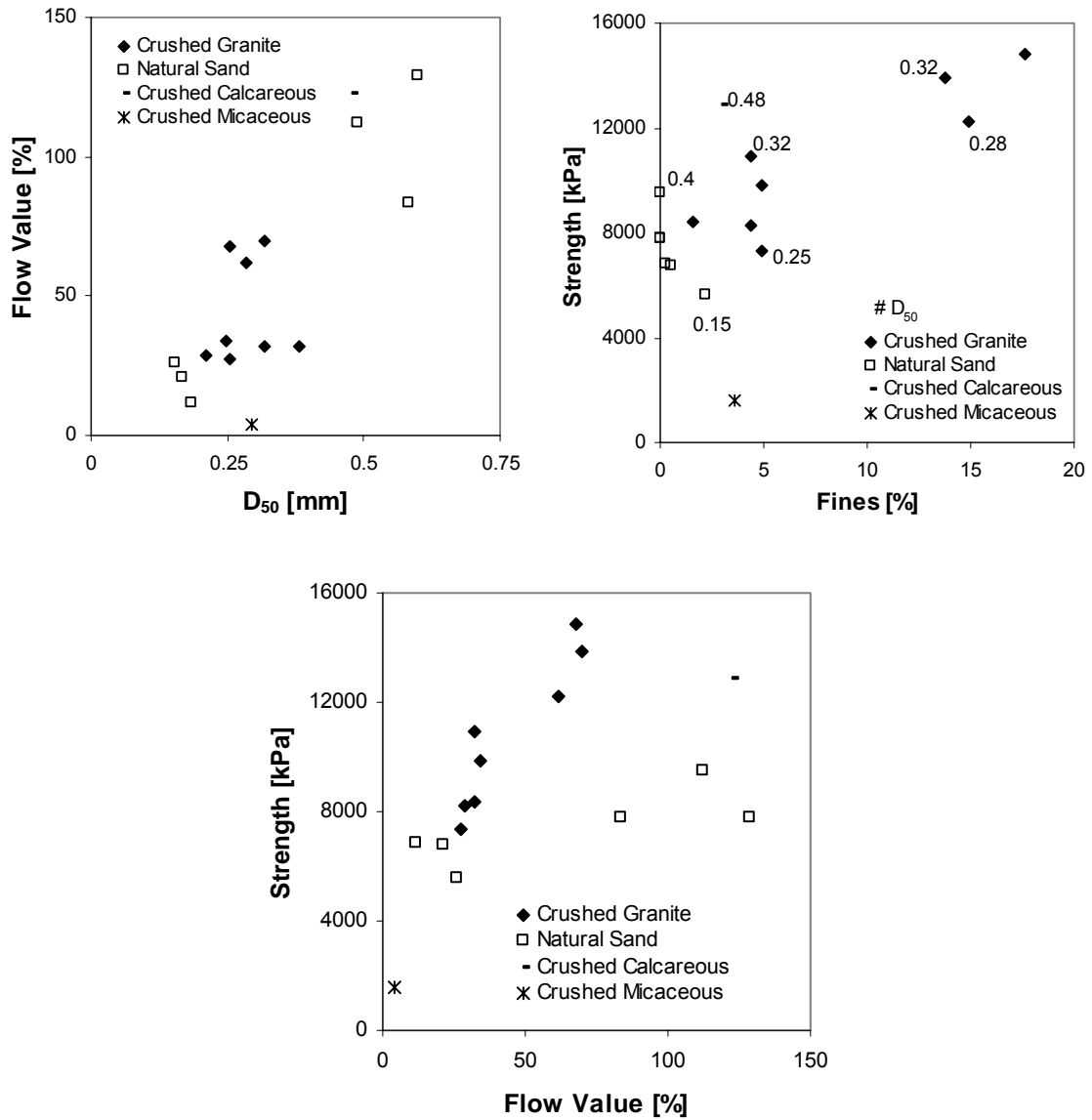


Figure 3.24 Strength and workability of all specimens. (top left) Flow as a function of particle size (top right) strength as a function of fines content and (bottom) strength as a function of flow value.

Table 3.5 Experimental results – Complete Dataset for specimens used in at least one macroscale test (Critical state friction angle, critical state parameters, shear wave velocity, mortar strength and workability). The table is in two parts; gradation, shape and void ratio results are listed on the first page and critical state, shear wave velocity, mortar and other results are listed on the second page.

Sand	Gradation			Shape			Void Ratio	
	D ₅₀ [mm]	C _u	Fines [%]	Sphere.	Round.	Rough.	Youd Round.	e _{max}
1K9	0.30	3.4	3.57	0.8	0.25	n/a	0.17	1.16
1O2	0.25	2.9	4.90	0.8	0.25	n/a	n/a	.83*
1O6	0.21	2.8	4.40	0.7	0.3	n/a	0.27	0.77
2L6	0.28	n/a	14.93	0.8	0.25	n/a	n/a	0.84
2Z8	0.48	5.0	2.97	0.75	0.45	n/a	0.27	0.66
3C7	0.26	n/a	17.62	0.8	0.25	n/a	n/a	0.85
3P3	0.27	n/a	15.82	0.7	0.2	n/a	n/a	0.95
5U1	0.32	n/a	13.81	0.7	0.3	n/a	n/a	0.84
5Z9	0.40	3.6	1.66	0.8	0.3	n/a	0.21	0.89
6A2	0.33	5.5	9.84	0.6	0.1	n/a	n/a	0.93
6F5	0.25	3.3	4.92	0.8	0.25	n/a	0.21	0.91
6H1	0.33	3.8	4.68	0.8	0.2	n/a	0.19	0.97
7U7	0.30	3.2	4.35	0.8	0.2	n/a	0.27	0.79
8B8	0.32	3.7	4.42	0.8	0.25	n/a	0.22	0.85
8M8	0.38	3.3	1.59	0.7	0.2	n/a	0.2	0.97
9F1	0.33	3.5	3.17	0.7	0.2	n/a	0.21	0.90
9C1	0.52	2.3	0.70	0.9	0.5	3	0.24	0.91
Jekyll Island	0.17	1.7	0.52	0.85	0.3	1	0.22	1.04
Nevada	0.15	1.8	2.20	0.9	0.7	2	0.32	0.85
Ottawa	0.60	1.4	0.00	0.9	0.8	1.5	0.39	0.69
Margaret River	0.49	1.9	0.00	0.7	0.7	1	0.35	0.74
Ponte Vedra	0.18	1.8	0.26	0.85	0.3	1	0.21	1.07
Ticino	0.58	1.5	0.00	0.8	0.4	2.5	0.27	.99*

Table 3.5 Continued.

Sand	Critical State			V_s		Mortar		Other	
	ϕ_{cs} [deg]	λ	Γ	α [m/s]	β	Flow [%]	Strength [psi]	Type	Minerology
1K9	39	n/a	n/a	35	0.35	4.0	230	10SM	Granite
1O2	38	n/a	n/a	n/a	n/a	34.1	1426	10SM	Granite Gneiss
1O6	38	n/a	n/a	n/a	n/a	28.7	1196	#10	Granite
2L6	n/a	n/a	n/a	n/a	n/a	33.1	1774	M10	Granite Gneiss/amphib.
2Z8	41	n/a	n/a	25	0.36	122.6	1867	n/a	Dolomite/Limestone
3C7	n/a	n/a	n/a	n/a	n/a	67.9	2154	M810	Granite/Granite Gneiss
3P3	n/a	n/a	n/a	41	0.28	n/a	n/a	M10	Granite Gneiss/amphib.
5U1	n/a	n/a	n/a	n/a	n/a	69.9	2014	M10	Granite
5Z9	38	n/a	n/a	65	0.23	n/a	n/a	10SM	Granite
6A2	n/a	n/a	n/a	50	0.26	n/a	n/a	M810	Granite Gneiss
6F5	39	n/a	n/a	n/a	n/a	27.6	1064	W10	Granite Gneiss/amphib.
6H1	38	n/a	n/a	52	0.28	n/a	n/a	10SM	Granite
7U7	37	0.064	1.06	n/a	n/a	n/a	n/a	10SM	Granite
8B8	38	n/a	n/a	n/a	n/a	32.1	1580	AW10	Granite
8M8	40	0.138	1.16	54	0.27	31.9	1216	W10	Granite Gneiss/amphib.
9F1	36	n/a	n/a	41	0.32	n/a	n/a	W10	Granite Gneiss/amphib.
9C1	39	0.067	1.06	51	0.31	n/a	n/a	Natural	n/a
Jekyll Island	40	0.035	0.98	135	0.18	21.1	983	Natural	Quartz
Nevada	35	0.071	1.04	55	0.25	26.1	812	Natural	Quartz
Ottawa	34	0.053	0.94	70	0.23	129.0	1126	Natural	Quartz
Margaret River	34	0.051	0.84	91	0.22	112.3	1382	Natural	Quartz
Ponte Vedra	39	0.016	0.78	144	0.17	11.4	992	Natural	Quartz
Ticino	37	0.053	1.05	68	0.24	83.3	1132	Natural	Quartz/Feldspar

CHAPTER IV

SHAPE BASED SEGREGATION

4.1 INTRODUCTION

Segregation in granular materials leads to heterogeneous materials and weak layers. This can contribute to strain localization and premature failure. On the other hand, segregation is useful and beneficial in materials processing, where particles exhibiting different properties need to be separated. A fundamental understanding of segregation mechanisms is necessary to promote or to hinder segregation.

Size-based segregation has been reported extensively. Shape-based segregation is a less well known. This study is a first step toward a microscale understanding of shape-based segregation in soils.

4.2 LITERATURE REVIEW

Shape-based segregation is typically studied using a rotating cylinder. It has been observed that the shape of the particle leads to different dynamic angles of repose. This occurs in particles of different form e.g., hemispheric versus rod-like (Khosropour et al. 2000), roundness and roughness e.g., sand versus glass beads (Zek et al. 1994). In a binary mixture, regions develop where the concentration of one constituent is greater than the other. Because of differences in dynamic angles of repose, as the cylinder turns, low angle particles slide to the valleys and high angle particles move to the mounds (Figure 4.1). Rough boundaries (cylinder caps) exacerbate this process by leading to higher mounds near boundaries because the dynamic friction angle between the boundary and the high angle constituent may be higher than the dynamic friction angle between particles.

There are at least four classes of shape separation methods (Furuuchi and Gotoh 1992): (1) particle velocity on a tilted surface, (2) the time particles take to pass through a mesh aperture, (3) adhesion to a solid surface and (4) settling velocity in a liquid.

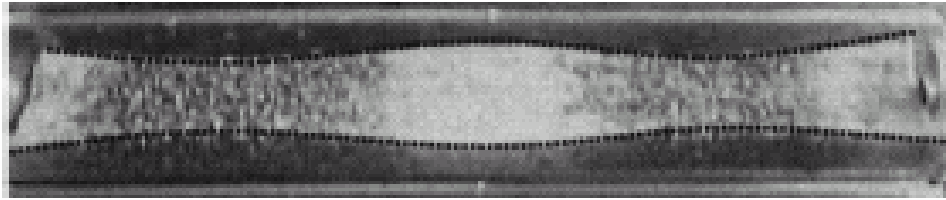


Figure 4.25 Segregation of disk (split peas) and rod (rice) shaped particles in a rotating cylinder. The lines represent the surface heights of particles along the length of the glass cylinder. Notice that the light colored rice forms a mound, while the dark colored peas form a valley as the particles segregate (Khosropour et al., 2000).

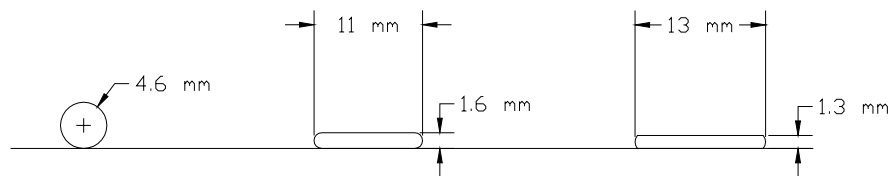


Figure 4.26 Profile view of lead particles. Original spherical shape (left), Particles flattened using 1.5 mm spacers (middle), and particles flattened using 1.2 mm spacers (right).

Particles are segregated on a tilted surface by the flatness of their sides. Round particles are more mobile and will roll, while flat particles will slide slowly, leading to good separation. This method does not separate well a binary mixture of particles in which particles slide at different rates. Small jumps during sliding reduce the difference in velocity due to particle shape. Devices that have been developed to separate particles by rolling include the tilted rotating disk, tilted rotating cylinder, tilted vibrating trough, and tilted chute (Furuuchi and Gotoh 1992).

A mixture of particles with different shapes may also be separated with a mesh aperture. For example, particles could transverse a stack of uniform sieves. Elongated particles pass through the sieves more slowly than do round particles. If the particles are cylindrical, the rate they pass through the sieve is inversely proportional to the cube of the particle length-to-diameter ratio. The mesh aperture technique has the advantage of being able to separate both spherical-elongate and elongate-elongate mixes. Devices developed using this concept include the tilted vibrating screen, vibrated stacked screens and rotating cylindrical sieve (Furuuchi and Gotoh 1992).

Particles of differing shapes may also be separated by differences in adhesion. Consider, for example, suction applied to the inside of a rotating drum with small surface holes. Particles are placed on the surface of the drum. Spherical particles plug the holes more completely, which causes them to adhere more tightly to the drum surface. As the drum rotates, irregular particles are released early and fall into one bin, while spherical particles release later into another bin. Fine particles of differing shapes may also be separated by their adhesion to a rotating drum, however, the presence of holes and suction pressure may not be needed.

Finally, particles of different shape may be separated by differences in settling velocity. The terminal velocity of a particle falling through a liquid is a function of the drag coefficient, which depends on shape. An elongated particle with the same volume as a spherical particle will settle more slowly than a spherical particle. One device, which makes use of this concept, consists of a weir followed by four bins. After crossing the weir, spherical particles will settle into one of the bins closest to the weir, while elongated particles will settle into a bin farther downstream.

4.3 FUNDAMENTAL STUDY

The goal of this exploratory study is to determine whether particles of different shape segregate when subject to horizontal and vertical vibration, to determine the circumstances that promote shape based segregation and to study microscale processes that promote shape-based segregation.

3.3.1 Procedure

Lead spheres, 2.3 mm in diameter, are compressed between two flat steel plates. Spacers (1.2 and 1.5 mm thick) are placed between the lead spheres to produce particles of uniform thickness (Figure 4.2). Flattened particles are painted white and unflattened round particles are painted black. Particles of varying aspect ratios are placed on a smooth flat paper surface to determine the rolling/sliding tendency. One side of the planar surface is raised until the particles begin to move (Figure 4.3). Rolling/sliding tendency is recorded. The procedure is repeated with light vibration at a frequency of 2 Hz.

Several segregation techniques are employed. First, a 3 part round to 1 part flat mixture of particles is placed inside a clear Plexiglas 1 inch inside diameter tube, with rubber end caps. The tube is rotated about its long axis at 30 rpm and particle interactions are recorded. Second, the same mixture is placed inside a transparent rectangular box and tilted, alternating direction, at about 45° so that the top layer flows from one end of the box to the other. Finally, the sand is placed in a 41x41x48 mm transparent box and vibrated horizontally at about 3 Hz and an amplitude of 50 mm so that the top half of the mixture moves while the bottom half remains stationary relative to the box (Figure 4.4). The horizontal vibration direction is switched periodically (x-x, y-y) so that shearing takes place in both directions. The box is then filled with clear gelatin, which is cooled and allowed to stiffen. Layers of particles are removed one at a time to determine the ratio of round to flat particles at each depth.

3.3.2 Results and Analysis

Sliding and rolling. Whether particles roll or slide down an incline plane depends on the inclination of the surface, the aspect ratio of the particle and the level and frequency of vibration.

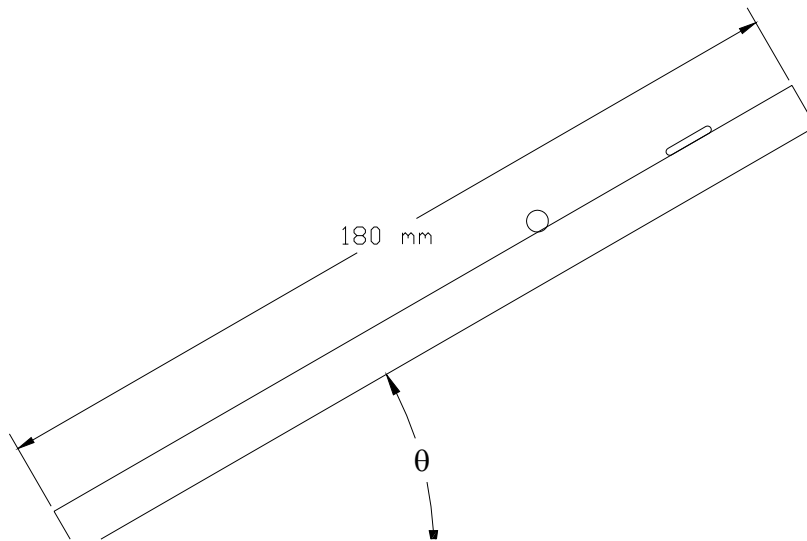


Figure 4.27 Method used to investigate rolling and sliding tendencies of different particles. A planar, paper covered, Plexiglas sheet is rotated from the horizontal and particle motions are recorded.

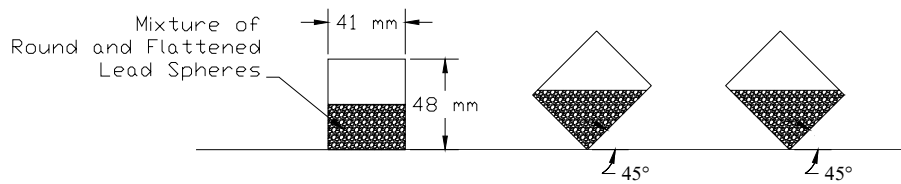


Figure 4.28 Spherical and flattened particles are segregated by tilting the transparent box at 45°.

When no vibration is imposed, round particles begin rolling at low plane inclinations. Flat particles remain stationary until the inclination of the plane is relatively steep. When movement begins, the particles slide for a few inches then begin rolling oriented in the same manner as a rolling penny. When vibration is imposed, flat particles begin sliding at lower planar inclinations than without vibration, and continue to slide the full length of the plane.

The observed phenomena may be explained by considering the force required to start particle movement, and the force required to keep the particle moving. Very little force is required to start round particles rolling and to keep them rolling therefore the inclination is low. More force is required for a flat particle to overcome static friction, to begin rolling. Sliding particles require more force to continue moving than rolling particles, so if there is enough force present to start the particle rolling it will preferentially roll rather than slide. In this system the force required to overcome static friction is higher than the force required to start the particle rolling so no particles slide the entire length of the plane. Vibration has the effect of cyclically lessening the normal force on the particle and therefore lessening the static friction and allowing the particles to begin sliding.

Segregation. Mixtures of round and flat particles segregate when tilted from side to side or vibrated horizontally. During tilting or vibration, a shear layer is formed above which particles move and below which particles are stationary relative to the container. Three distinct bands form in the container. The lower band, located below the shear zone, remains in its original well-mixed state. The intermediate band is composed almost entirely of flat particles and is located just above the shear band. The upper band is primarily composed of round particles (Figure 4.5).

There are at least two possible reasons for the observed behavior. First, as demonstrated by the experiment with the inclined plane, sliding requires more energy than rolling. During tilting or vibration, particles randomly move from top to bottom. Flat particles stay at the base of the moving layer while round particles move out of it because the imposed energy at that layer is greater than the required rolling energy but less than the required sliding energy. Second, flat particles have been shown to align at a shear plane. It is possible that particles align when the flat

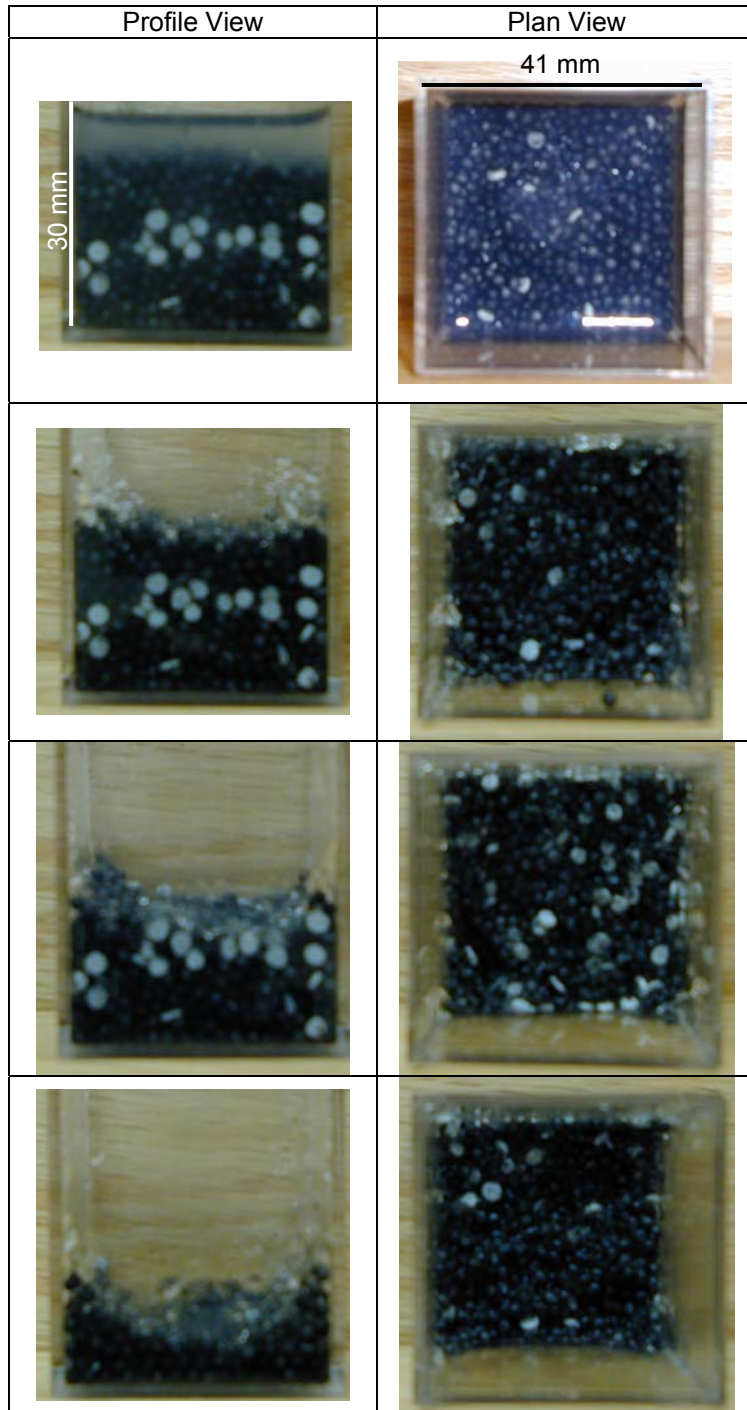


Figure 4.29 Segregation of round (black) and flat (white) lead particles. Photos are in sets with the photo on the left representing the profile view and the photo on the right representing the plan view as each layer is removed. The particle mixture is 3 parts round to 1 part flat. The mixture is vibrated at a frequency of 3 Hz and an amplitude of 50 mm for 3 minutes. During vibration the top half of the particles are in motion while the bottom section remains static relative to the container. The spherical particles are 2.3 mm in diameter. The long axis to short axis ratio of the flat particles is about 2. The container is LxWxH 41x41x48 mm.

particles come in contact with the shear plane and remain there as round particles move above them.

4.4 SANDS

The purpose of this section is to determine: (1) whether sands of differing shapes will segregate when subjected to horizontal and vertical vibration, and (2) if they do segregate, why segregation occurs.

Two sands are employed, round Ottawa 20-30 and angular crushed granite from Georgia (Figure 4.6). Eight-inch standard sieves are used to separate the crushed sand fraction passing the #20 sieve and retained on the #40 sieve. The Ottawa sand is dyed green and the crushed sand is dyed red using food dye so that segregation may be visually observed. Sands are combined at a mass ratio of ten parts Ottawa to one part crushed Granite and placed into a clear 41x41x48 mm plastic box.

To promote segregation by horizontal vibration, the sand mixture is vibrated at a frequency of 3 Hz and amplitude of 15 mm (Figure 4.7). The vibration causes the sands in the upper half of the container to move while those in the lower half remain stationary relative to the container.

Vertical vibration is also used to segregate the sands. The sands are vibrated using a modified four-inch speaker cone. The speaker is attached to a Krohn-Hite model 7500 amplifier, which is connected to an HP model 200 A B Oscilloscope. The box is filled with 52 cm³ of sand and is vibrated at frequencies ranging from 20 to 300 Hz. The vibration causes the box to shift from the center of the speaker so that the vibration direction passes through a point about 10mm from the center of the box.

3.4.1 Results and Analysis

The horizontal vibration of sand mixtures produces segregated specimens similar to those observed when the round and flat particles are horizontally vibrated. The round Ottawa sand forms the upper layer while the irregular crushed sand forms the lower layer above the shear plane. As with the lead particles of different shape, the round particles most likely remain

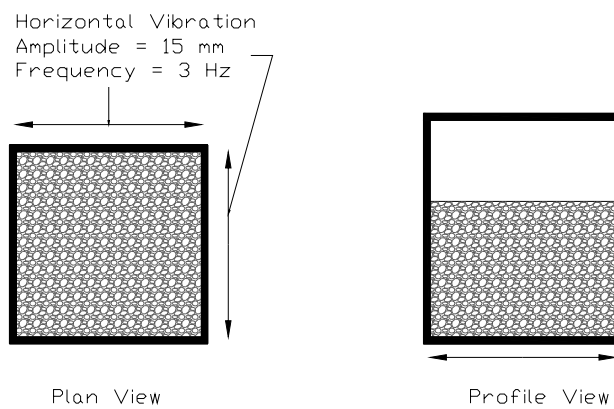


Figure 4.30 Mixture of round and angular particles segregated by horizontal vibration at an amplitude of 15 mm and a frequency of 3 Hz. Vibrational direction is switched periodically from right to left in the figure to top to bottom.

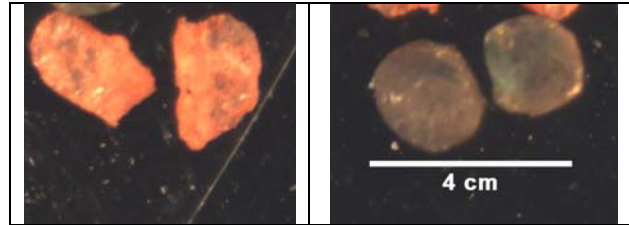


Figure 4.31 Sands segregated through horizontal and vertical vibration. Georgia crushed granite (left) and Ottawa sand (right). Particles all pass the #20 sieve and are retained on the #40 sieve.

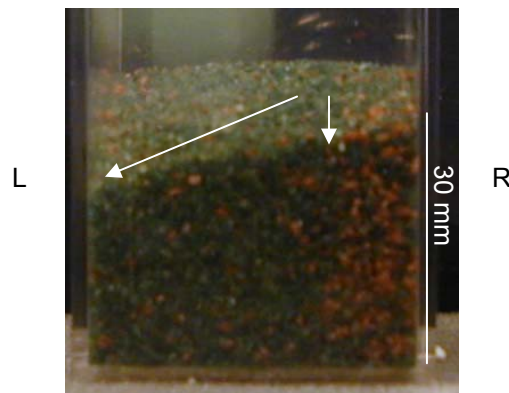


Figure 4.32 Segregation of angular (lighter color) and round (darker color) particles during convective flow. The ratio of round to angular particles is 10:1. Vertical vibration is applied at 122 Hz using a modified 4 inch speaker. An HP model 200 Oscilloscope is used to create the signal at an amplitude of 15 volts. A Krohn-Hite model 7500 amplifier is used to amplify the signal with the gain set at 15. During vibration the sand container is allowed to move so that the center of the speaker is about 10 mm from the center of the base of the container.

on top because of their greater mobility. While the irregularly shaped particles are more likely to be found at the base of the moving layer because of the greater force required to move them.

Vertical vibration at a constant frequency and amplitude produces one of three behaviors. First, individual sand grains do not move significantly relative to one another and fabric remains constant. Second, the top layer of sand particles moves and fabric rearrangement takes place in that region, while the lower layers remain static relative to the sides of the container. Third, convective flow occurs.

The first two scenarios, constant fabric and fabric changes without convection, do not produce segregation. However, sand segregates during convective flow. As discussed earlier, round particles will move by sliding/jumping if subjected to vertical vibration and a small inclination angle. However, they will roll at higher inclination angles. Flat particles, on the other hand, require a much greater inclination angle to begin rolling. Segregation occurs when the surface inclination is high enough that round particles roll, but low enough that flat particles do not. Convection circulates particles so that a continuous supply of round particles roll to one side of the cube while flat particles slide along the current.

The conditions for segregation exist when: (1) a convective current transports particles from one face of the cube B (back) to the opposite face F (front), and when (2) a significant slope perpendicular to the convection direction allows round particles to roll from the high corner B-R (back-right) on the first face to the low opposite corner on the second face F-L (front-left), Figure 4.8).

4.5 CONCLUSIONS

- Segregation of monolayers on inclined planes demonstrates the underlying mechanism for shape-based segregation: rotational freedom.
- Particles of different shape may segregate when subjected to horizontal excitation. Rounder particles rotate more freely and move to the top of the dynamic layer. Angular particles however, rotate less freely and move to the base of the dynamic layer.
- Different shaped sand particles segregate due to vertical vibration when convective flow occurs and a difference in surface height exists which allows some particles to roll while others follow with the convective current.

CHAPTER V

MIXTURES OF RIGID AND SOFT PARTICLES

5.1 INTRODUCTION

Chains made of “primary” particles carry most of the load transferred through granular materials. The role of secondary particles is to prevent the buckling of these chains. It is hypothesized that mixtures of hard and soft particles may show surprisingly good performance due to the self-assignment of different roles. In this study, rigid-soft particle mixtures are subjected to confined compression. Stress strain and shear wave data are recorded. A photo-elastic study with rigid and soft particles is used to model microscale behavior.

Rubber and mineral particles are selected because of their very different properties (Figure 5.1). The rubber particle strength and stiffness is much lower than that of the sand particles. Rubber recovers from large deformations when stress is removed. Rubber particles also have a greater damping capacity than sand particles. (Feng and Sutter 2001). Typical rubber and sand properties are summarized in Table 5.1. The sand and rubber particles in this study also differ in size. The mean grain size of the sand is 0.35 mm, about 4 times larger than the mean grain size of the rubber particles (Figure 5.2).

Two mechanisms control strains in granular materials (Lambe and Whitman 1979): (1) Distortion of individual particles (which is quite significant in rubber) and (2) relative motion between particles as the result of sliding or rolling. These are seldom independent of one another. A small amount of deformation allows particles to move past one another and cause a previously stable array of particles to collapse. Compared to rubber particles, sand particles can be considered perfectly rigid, leading to a sand matrix which is much stiffer than a rubber or rubber-sand particle matrix. When $e_{\text{sand}} < e_{\text{max}}$ a stable sand matrix is formed and a sizable increase in material stiffness is expected.

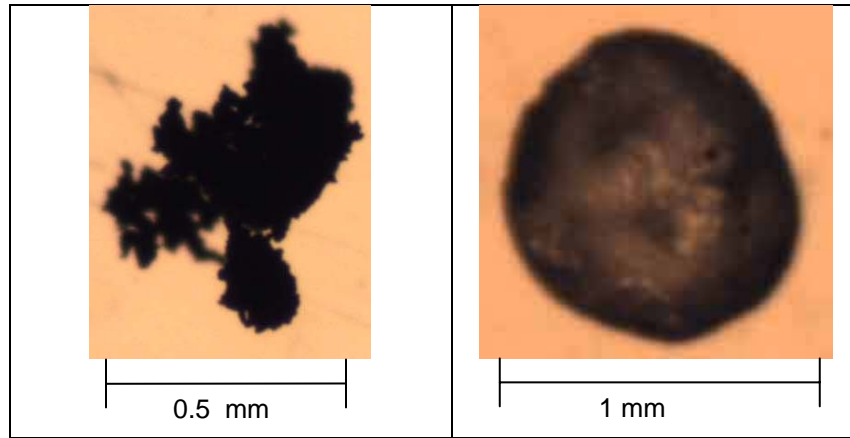


Figure 5.1 Photograph of a crumb rubber (left) and Ottawa sand (right) particles. Photographs are of particles of the same composition, but larger size than the particles used in this study.

Table 5.1 Basic properties of rubber from pneumatic tires and Quartz (Beatty 1980, Santamarina et al. 2001).

Material Properties	Rubber	Quartz
Specific Gravity []	1.15	2.65
Shear Modulus [MPa]	1	$29 \cdot 10^3$
Poisson's Ratio []	.49	.31

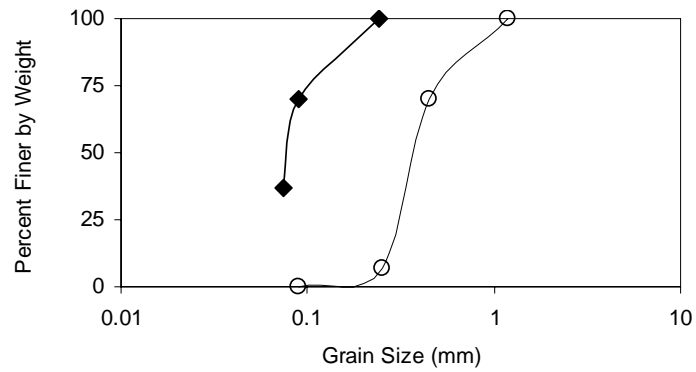


Figure 5.2 Grain size distribution of Ottawa sand and rubber particles determined using sieve analysis.

Table 5.2 Theoretical shear wave velocity exponent β values for different contact types (Santamarina et al. 2001).

Contact type	Comments	Theoretical b value []
Ideal solid		0
Cemented soil	Below transition stress	0
Hertzian contact	Elastic spherical particles	1/3
Cone-to-plane contact	Rough or angular particles	1/2
Spherical particles with contact yield		1/2
Contacts varying with DLVO forces		Variable (.6 – 1)

5.2 BRIEF REVIEW OF V_s AND G_{max}

The small strain shear stiffness, G_{mas} , is a constant fabric phenomenon, which is controlled by the nature of interparticle contacts (Santamarina et al. 2001). In practice, shear wave velocity is generally measured then converted to stiffness as:

$$V_s = \sqrt{\frac{G}{\rho}} \quad (5.1)$$

G_{max} is used throughout this chapter because the different materials being tested have very different densities.

At the microscale, G_{max} is dependent on several factors including the material properties of the individual particles (G_m and v_m), the packing arrangement and the interparticle contact type. The shear wave velocity measured in this study is a macroscale phenomenon because the shear wavelength is much greater than the internal scale of the system and travels through the specimen as a continuum.

Fabric and contact behavior change with stress, so does G_{max} . Empirical power relations between G_{max} and effective stress properly match the data.

$$G_{max} = A \cdot \sigma^b \quad (5.2)$$

In this equation the A-coefficient captures the stiffness at 1 kPa, while the b-exponent captures the sensitivity of stiffness to effective stress. Theoretical values of the b-exponent have been derived for different interparticle contact types; these values are shown in Table 5.2. Fabric changes, in particular, and changes in the number of interparticle contacts, have also been shown to influence the b parameter (Santamarina and Aloufi 1999).

5.3 RUBBER-SAND MIXTURES --- LITERATURE REVIEW

Engineering properties of sand-rubber mixtures are shown in Table 5.3. These results show that the addition of rubber particles ($D_{soft} / D_{rigid} = 10$) to sand decreases permeability, the

minimum void ratio, and both stiffness and friction angle, however it increases the maximum void ratio.

Lee et al. (1999) uses finite element analysis and data from a built retaining wall, which uses tire shreds as backfill, to investigate the mechanical feasibility of using tire shreds as a lightweight backfill. Results of the investigation show significantly greater settlement behind the tire shred wall than a gravel wall, but significantly less horizontal earth pressure.

Feng and Sutter (2000) study the dynamic properties of sand-rubber. The mixtures they study involve ~3.4 mm rubber particles and ~ 0.72 mm Ottawa sand particles. Mixes of ~ 25, 50, 75 and 100 percent rubber are tested. Results are presented in Figure 5.3. In this figure, shear modulus values are divided by a function of the overconsolidation ratio and the confining stress to the $\frac{1}{2}$ power. It is similar to solving for A assuming that b is equal to 0.5 (Equation 5.2), taking into account OCR. Notice the similarity of the shape of the resultant curve to the A-coefficient curve in Figure 5.9.

Environmental effects of using sand-rubber mixtures in a lightweight fill application are investigated by Liu et al. (2000), who compile results from several different studies. These results are presented in Table 5.4. Two metals, Iron and Magnesium, are raised to levels higher than the drinking water standards near some waste tire sites. These contaminants presumably arise from steel that is not completely separated from the rubber when the tires are recycled. Results of the compiled tests combined with the safe long term use in America of rubber in car tires lead to the conclusion of Liu et al. (2000) that the use of sand-rubber in lightweight fill applications is environmentally safe.

Salgado et al. (2000) report the properties of a mixture of Ottawa sand with silt sized quartz particles. They define the skeletal void ratio as the void ratio of the sand.

$$e_{sk} = \frac{1 + e}{1 - f} - 1 \quad (5.3)$$

Table 5.3 Mechanical properties of rubber-sand mixtures. $D_{\text{rigid}} / D_{\text{soft}}$ is roughly 0.1. Permeability values are determined at 150 kPa. Modulus of elasticity, friction angle and cohesion intercept values are determined from consolidated drained triaxial tests (Masad et al. 1996). Friction angle values are reinterpreted from the shear stress – normal stress plot, using the assumption that the cohesion intercept is zero.

	Ottawa Sand	50/50 Blend	Rubber particles
Specific gravity	2.65	1.86	1.07
Minimum void ratio	0.47	0.36	0.6
Maximum void ratio	0.7	0.82	1.36
Permeability, k at 150 kPa [cm/sec]	$2.55 \cdot 10^{-3}$	$2.4 \cdot 10^{-3}$	$1.9 \cdot 10^{-3}$
Modulus of elasticity [kPa]	70,000	15,000	1900
Friction angle [deg]	45	4*	9*

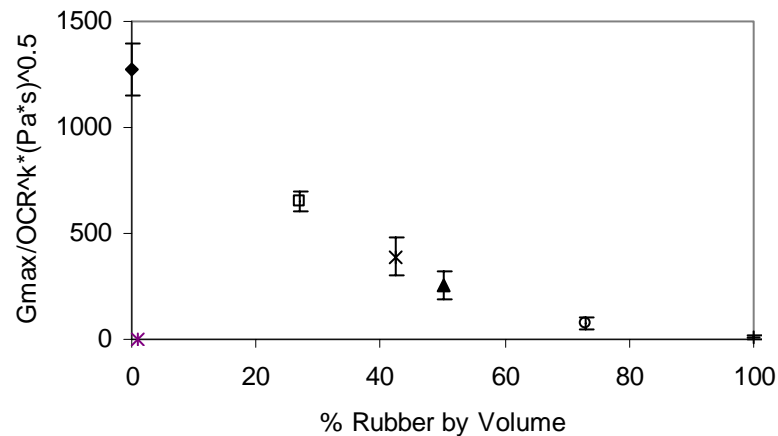


Figure 5.3 G_{max} of sand-rubber mixtures tested in the resonant column device (Feng and Sutter 2000). Tests are performed using effective stresses between 69 and 483 kPa. Bars represent the range of reported values. G_{max} is divided by a number that is a function of the overconsolidation ratio OCR, a parameter related to the soil index k , and the confining pressure raised to the 0.5 power. A similar plot could be created by solving for A in equation 5.2 assuming b equals 0.5, and plotting the value against the % rubber or sand (see Figure 1.5). $D_{\text{rigid}} / D_{\text{soft}}$ is roughly 0.2.

Table 5.4 Compilation of data from several studies which measure water contaminant levels near tire shred fill sites (Liu et al. 2000). Numbers in bold represent higher than maximum contaminant levels. Only Fe and Mg levels were observed above maximum contaminant levels. Standards for these minerals are aesthetic rather than health related.

Field Study (unit: mg/L)							
	Maximum contaminant level	Secondary maximum contaminant level	Minnesota ground water sample	Wisconsin DOT	Tire pond ground water, Connecticut	Tire pond surface- water, Connecticut	University of Maine
Al	-	0.05~.2	1.8	-	-	-	0.2
Ba	2	-	1.93	0.69	-	-	0.045
Ca	0.005	-	36.6	-	-	-	-
Cd	0.1	-	0.032	-	-	-	<0.005
Cr	1.3	-	0.35	-	-	-	0.013
Fe	0.015	-	5.8	0.004	55.2	1.83	<0.1
Pd	-	0.05	0.23	0.015	-	-	0.057
Mg	0.002	-	6.2	-	-	-	18.3
Mn	0.1	-	-	3.2	-	-	0.294
Ni	-	0.1	-	-	0.673	<0.04	-
Zn	-	-	-	2.1	0.27	0.03	<0.01

When this void ratio exceeds the maximum void ratio of the sand, skeletal particles are, on average, not in contact, and mechanical properties are no longer controlled by the sand.

The study shows that G_{max} decreases as silt sized quartz particle content increases from 0 to 20%. For instance, at a confining pressure of 100 kPa, G_{max} values decline from 89 to 75, 66, 46, and 42 Mpa as silt fraction increases from 0 to 5, 10, 15, and 20% fines. Two explanations are presented for the observed behavior. First, fines are positioned in the sand matrix in such a way that they do not have well developed contacts, and second, even when well developed contacts exist, silt particles are more free to move laterally during shear reducing measured velocity.

Santamarina and Aloufi (1999) report an experiment in a true triaxial cell, which shows the effect of contact number on stiffness. Sand is placed in a true triaxial cell, where stress is relaxed in one direction until some interparticle contact is lost. Stress is then reapplied in that direction. As the number of contacts increases, stiffness increases rapidly and a b value of $b=0.62$ is observed. This value is well above the b -exponent value of 0.33, which occurs when contact number is more stable.

5.4 EXPERIMENTAL DESIGN

5.4.1 Dimensional Analysis – Scale Effects

A dimensional analysis is performed using Buckingham's π theorem. Table 5.5 presents those ratios deemed most meaningful, their significance and values. The ratio between the diameter of the rigid particle divided by the diameter of the soft particle D_{rigid}/D_{soft} is about 4 in this study. Therefore, smaller soft particles fill the voids between larger rigid particles. The volume of stiff particles divided by the total solids volume V_{rigid}/V_{soft} , hints on fabric control. At very low volume fractions, the rigid particles are essentially inclusions in a soft particle matrix and the influence of the rigid particles on material behavior is minimal. The converse occurs at high sand fractions. At some intermediate value, which also depends on the void ratio and state of stress,

Table 5.5 Salient ratios --- Significance.

Ratio	Value	Significance
$\frac{D_{\text{rigid}}}{D_{\text{soft}}}$	4	When > 1 void filling may occur.
$\frac{V_{\text{rigid}}}{V_{\text{soft}}}$	Varies 0-1	When the ratio is very low, rigid particles are dispersed within a soft particle matrix. When the ratio is close to one soft particles are dispersed within a rigid particle matrix. Intermediate values represent a transition region.
$\frac{E_{\text{rigid}}}{E_{\text{soft}}}$	$29 \cdot 10^3$	If >> 1, rigid particle contacts determine the stiffness of the material above the rigid particle percolation threshold.

the percolation threshold is crossed. Near the percolation threshold the system is self-similar which implies lack of a characteristic internal scale and specimen-size dependent material properties (Santamarina et al. 2001). Measured values increase exponentially with increasing rigid particle contact number. This occurs when mixture proportions are adjusted to increase rigid particle volume fraction or when applied load lowers void ratio.

One boundary effect is side friction between the sand-rubber mixture and the walls of the oedometer cylinder. This causes a reduction in effective stress with depth within the cylinder. An equilibrium analysis related by Kezdi (1980), can be implemented to relate the side frictional resistance P_f to the specimen height h , wall-soil coefficient of friction f , Poisson's ratio μ and base dimension d .

$$P_f = 4 \cdot \frac{h \cdot f}{d \left(\frac{1}{\mu} - 1 \right) + h \cdot f} \quad (5.4)$$

This correction is not made in this study because errors are expected to be less than 5%.

5.4.2 Procedure

The procedure used is the same as the one described in Section 3.3.3 with the exception that only tamping is used to compact the mixture. The initial experimental regimen includes testing at sand fractions of 0, 0.2, 0.4, 0.6, 0.8 and 1; at vertical effective stresses of 1, 10, 19, 36, 70, 140, 279 and 556 kPa. The region with the greatest variation, between sand fractions of 0.6 and 1.0 is studied further.

The effective stress value that is used to calculate A and b parameters is the mean stress in the polarization plane σ'_p . It may be calculated from the applied vertical effective stress σ'_v and the k_0 value of the mixture.

$$\sigma'_p = \sigma'_v \left(\frac{1 + k_0}{2} \right) \quad (5.5)$$

The value of k_o is similar to $1-\sin\phi$ for normally consolidated material.. When the effective stress in the polarization plane is substituted for the vertical effective stress at 0% rubber, the A value increases from 58.3 to 63.7 kPa, a change of 8.5%.

Using vertical effective stress instead of mean stress in the polarization plane does not change the computed b-exponent; however, it does change the A-coefficient. For this reason, b-values determined herein will be compared with other theoretical and empirical values, whereas A-values will not.

Electronic devices and settings are summarized in Table 5.6. An oedometer cell specially equipped with bender elements is selected for this study (Figure 5.4).

5.5 STIFFNESS RESULTS AND ANALYSIS

5.5.1 Results

Selected data are presented herein; the complete data set is captured in Appendix A (shear wave amplitude versus time, strain versus stress and G_{mas} versus stress in both linear and log-log scales). Figure 5.5 shows oedometer data for both 60% and 100% sand on the same plot for contrast. Figure 5.6 presents typical time series during loading and unloading for the same mixtures. Figure 5.7 shows selected G_{max} – effective stress plots. Best fit lines shown in the figures are used to determine A-coefficient (Figure 5.9) and b-exponent (Figure 5.10) for each mixture. And Figure 5.8 shows the summary G_{max} -vs- σ_v' trends. There appear to be two well-defined behavior regions and a transition zone in between. Specimens composed of 90% or more sand (sand-like) exhibit relatively high shear moduli, which increase with stress in a similar manner to one another. Specimens with less than 20% sand (rubber-like) exhibit low shear moduli, which also increase with stress in a manner similar to one another. Specimens in the transition region, 40%-80% do not exhibit either sand-like or rubber-like behavior and the shear modulus increases much more with stress in some specimens than others.

Table 5.6 Instruments and settings used to determine shear wave velocity. Settings are constant unless otherwise noted. Figure 3.13 is a simple schematic of the experimental setup, which shows how each instrument is used.

Instrument	Model	Setting	Value
Oscilloscope	Rapid Systems R1016	Gain	Variable
		Number of Averages	50
Signal Generator	Krohn - Hite 1400 A	Frequency	20 HZ Step
Amplifier	Krohn - Hite 3944	Input Gain	20
		Output Gain	0
		Band Pass Filter	100 Hz - 50 kHz

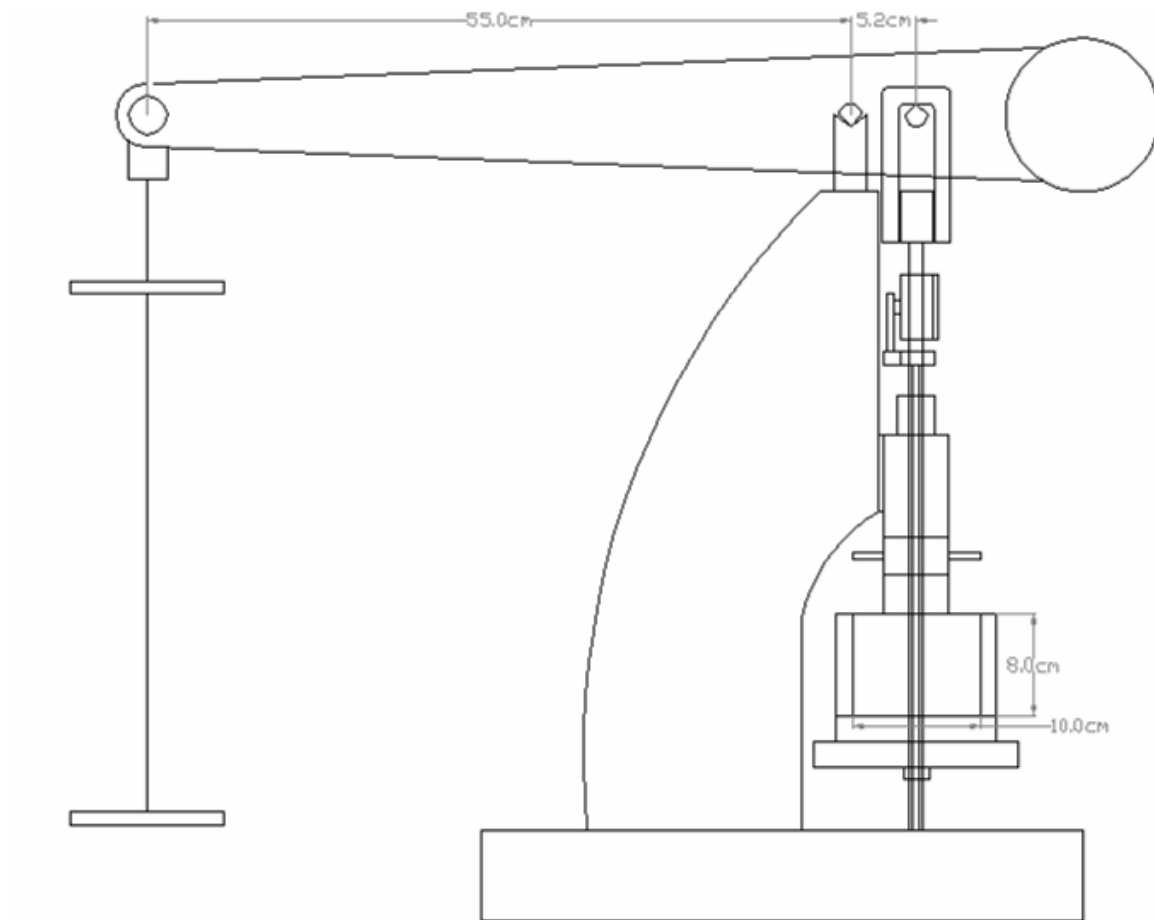


Figure 5.4 Sketch of oedometer used to determine stiffness. Cap and baseplate are fitted with bender elements.

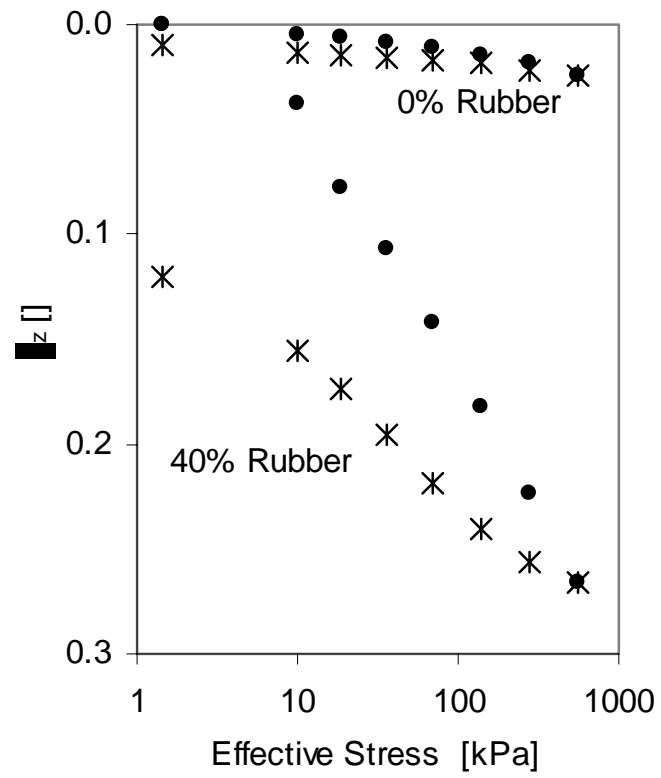


Figure 5.5 Strain as a function of vertical effective stress.

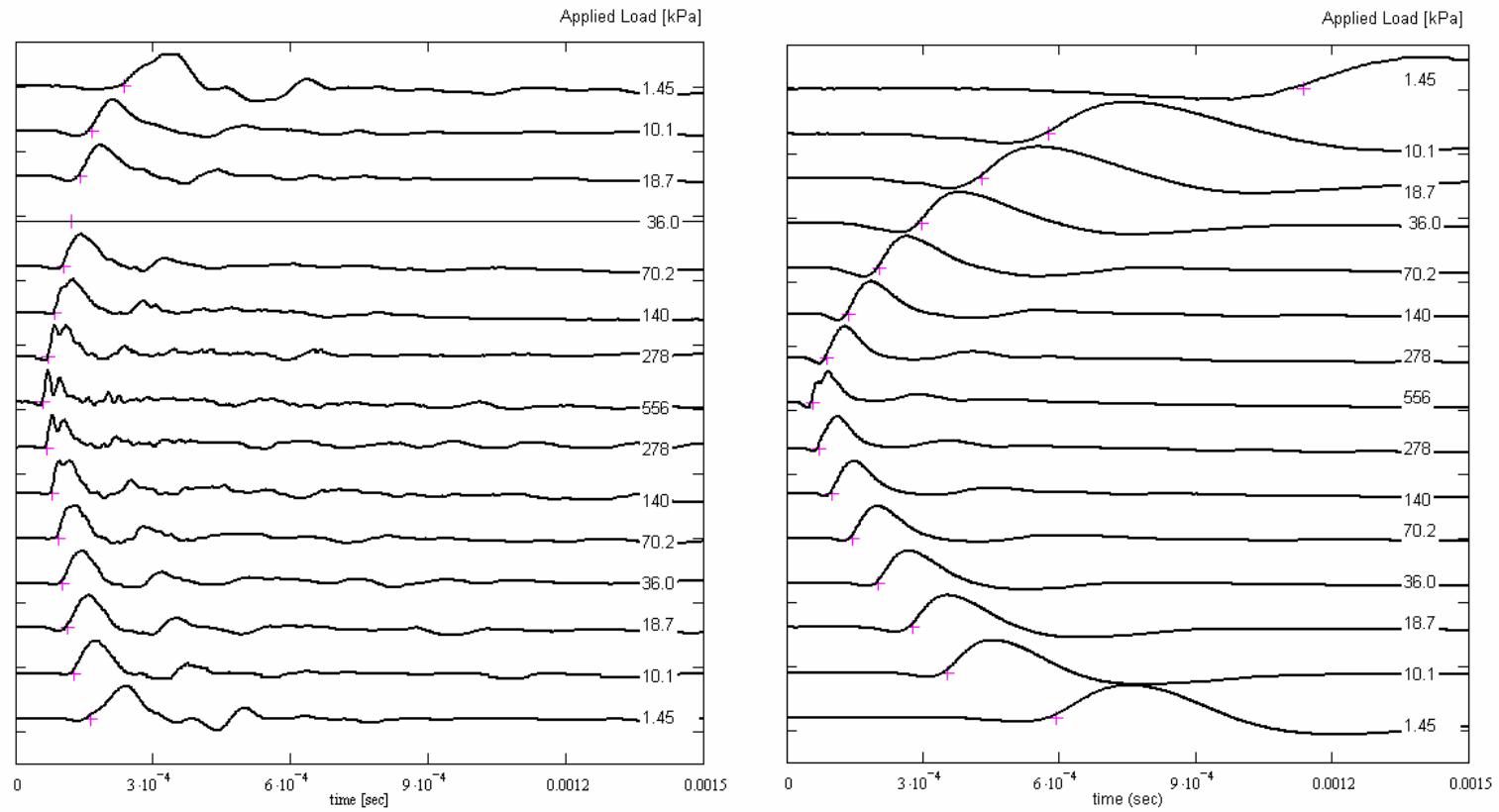


Figure 5.6 Shear wave signals collected at different confining pressures. Amplitudes are normalized with respect to the peak amplitude to create the plot. (+) markers indicate the arrival times used to calculate shear wave velocity. Signals are for 100% sand (left) and 60% sand, 40% rubber (right).

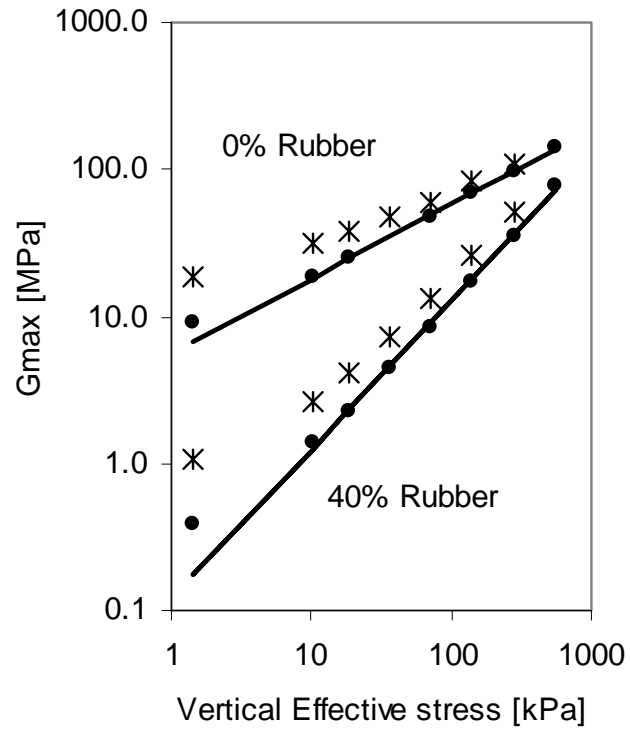


Figure 5.7 Selected plot of Gmax vs. vertical effective stress plotted in log-log form. The lines in the plot represent Gmax as calculated from the equation $G_{\max} = A\sigma^b$, where A and b are determined experimentally.

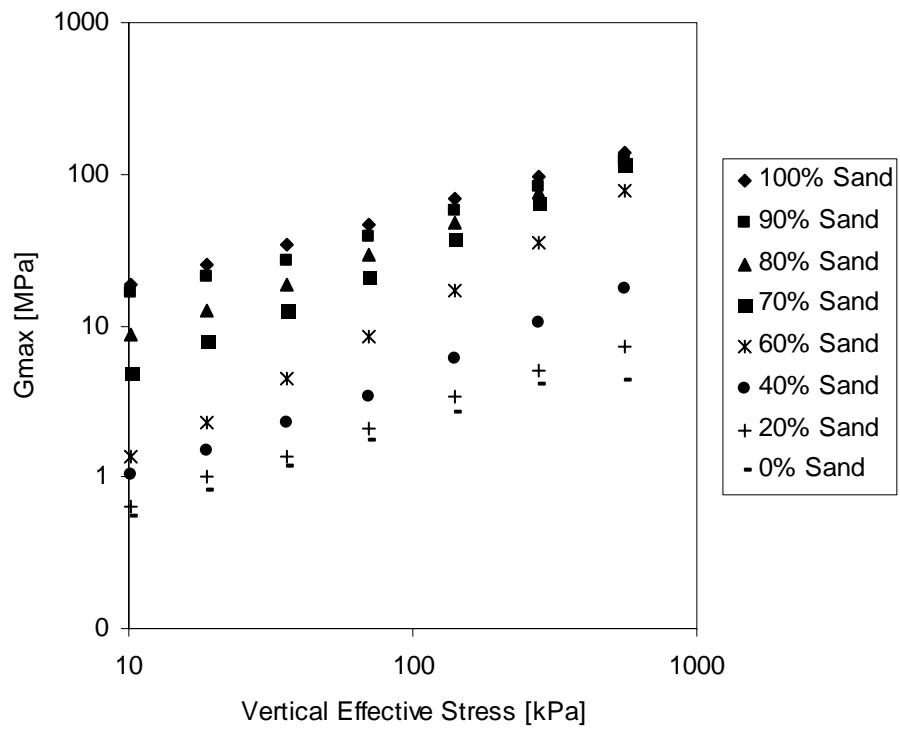


Figure 5.8 G_{max} as a function of vertical effective stress during loading for each sand fraction in the sand-rubber mixture.

Figure 5.9 plots the corresponding A and b parameters for different sand fractions. The lines on the G_{\max} versus effective stress plots in appendix A are created using the A and b parameters shown in Figure 5.9. The figure shows that the b-exponent is about the same when the specimen is composed primarily of sand or primarily of rubber. However b increases when the sand fraction approaches 0.6. The A parameter, on the other hand, remains relatively constant at sand fractions below 0.6, and it rises quickly as the sand fraction exceeds 0.6.

Figure 5.10 is a plot of the oedometer constraint modulus M^* versus effective stress for each specimen. The slope of the stress strain curve is calculated at each loading step so that the modulus at each loading step is captured. The behavior as shown in Figure 5.10 can be divided into two regions: Sand fractions below 80% where M^* resembles the M^* of the 100% rubber sample, and above 90% sand where M^* more closely resembles that of 100% sand sample.

Figure 5.11 shows plots of G_{\max} versus sand fraction at different effective stresses. This figure suggests that the percolation threshold occurs at lower sand fractions as stress increases.

5.6 ANALYSIS

The number and nature of rigid particle contacts determines the stiffness of the mixture. The A-coefficient is related to the contact behavior at 1 kPa, while the b-exponent is related to the change in contacts with stress.

In binary mixtures of spherical rigid particles of different size, particles pack most densely when the ratio of large particles to small particles is about 0.6 as shown in figure 5.12. This occurs because the void space between the large particles is similar to the volume of small particles at this mixing ratio and the smaller particles fill the voids between the larger particles. Rubber particles are not spherical (Figure 5.1), therefore, at low stresses the rubber forms a loose fabric which separates sand particles. However, at higher stresses rubber particles deform and act more like the small particles of Figure 5.11 by filling the voids between their rigid neighbors. This allows sand particles to come in contact (Figure 5.12) and G_{\max} increases rapidly.

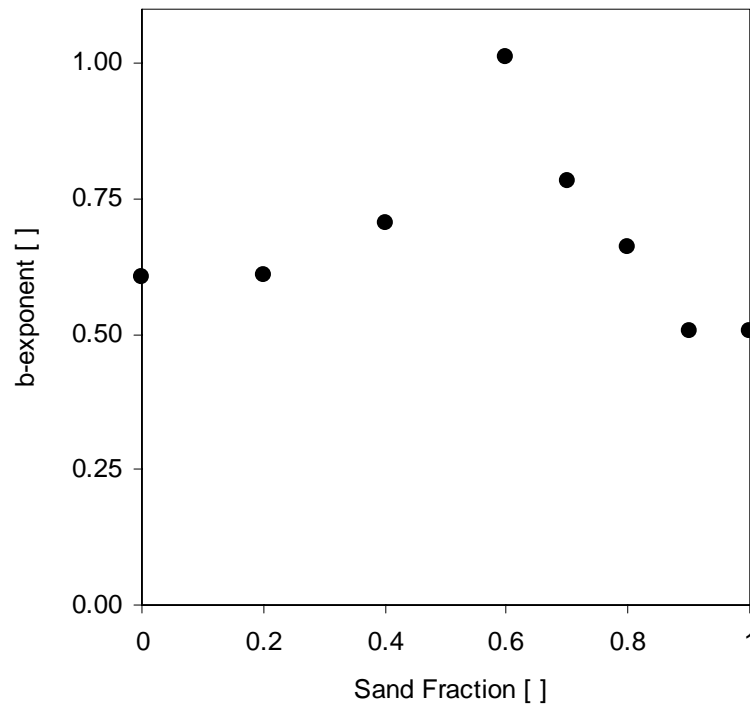
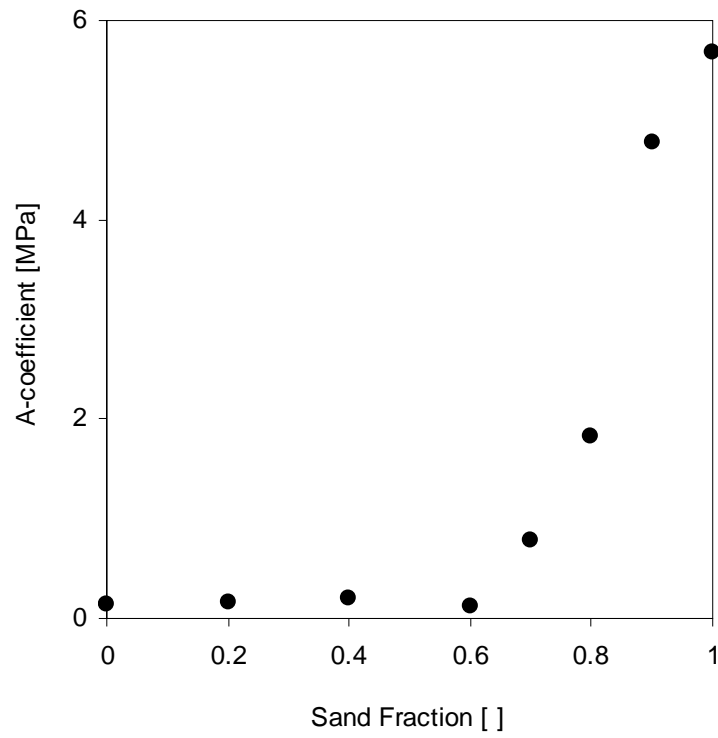


Figure 5.9 A-coefficient and b-exponent used to model small strain stiffness; plotted as a function of sand fraction.

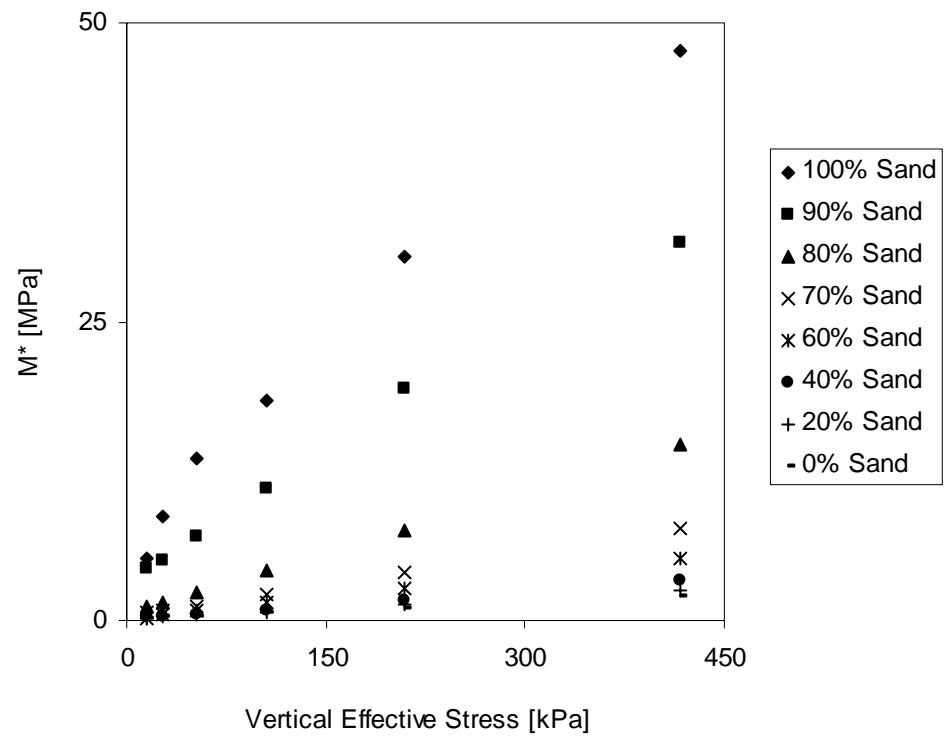


Figure 5.10 Constraint modulus as a function of confining pressure for several rigid-soft mixtures. M^* is calculated at each stress increment by dividing the average stress by the strain over the loading increment.

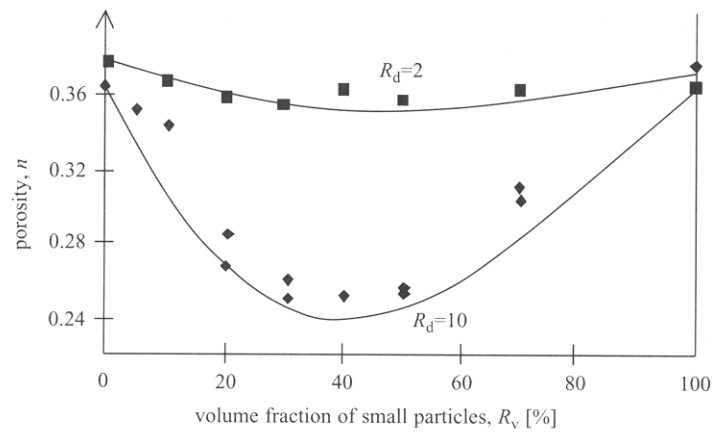


Figure 5.11 Porosity of a binary mixture of large and small particles as a function of volume fraction of small particles (Guyon, Oger and Plona 1987).

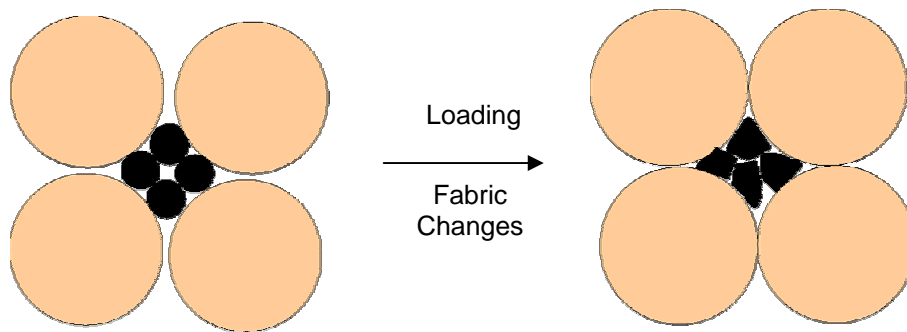


Figure 5.12 Increase in sand particle contact with increasing effective stress.

Because this effect is most prevalent at a sand fraction of 0.6, the b-exponent is highest for this sand fraction and for sand fractions near 0.6. It is important to note that this behavior would be different when the $D_{\text{rigid}}/D_{\text{soft}}$ ratio is less than or equal to 1 because void filling would not occur.

Research has shown that near the percolation threshold the properties of a granular elastic system change as (Feng, 1995)

$$G_{\text{max}} = c(p - p_c)^f \quad (5.6)$$

Where p , in this case, would be the sand fraction and p_c would be the sand fraction at the percolation threshold. The specific value of p_c , the proportionality constant c , and the exponent f , are system dependent. Two dimensional estimates for granular systems have placed f between 3.1 and 3.8, while an experimental three dimensional study places f at 3.8 (Feng 1985). Therefore, relatively small changes in p and p_c can cause a large change in measured G_{max} . Data in Figure 5.13 show that the percolation threshold occurs at lower sand fractions at higher stresses. The b-exponent of mixtures near the percolation threshold are unusually high because of this phenomenon.

Stiffness in confined compression is a function of the stiffness of individual particles and force chain buckling (Section 5.1). These two factors are seldom independent of one another. When soft particles are part of the load-carrying skeleton, they deform extensively. When the load-carrying skeleton consists of rigid sand particles, the constraint modulus of the mixture increases dramatically; as occurs at a sand fraction of 0.9 (Figure 5.10). One way to estimate whether a rigid particle skeleton is present is by considering the void ratio of only the sand particles (skeletal void ratio). When the skeletal void ratio is less than or equal to the maximum void ratio of the sand, a stable sand skeleton is expected. This is illustrated by Figures 5.14. Both M and G_{max} are good indicators of whether a stable skeleton is present.

5.7 PHOTOELASTIC STUDY

Photoelasticity is used to gain further insight into the interaction between small, soft and large, stiff particles and the role of this interaction in force propagation and stiffness. The

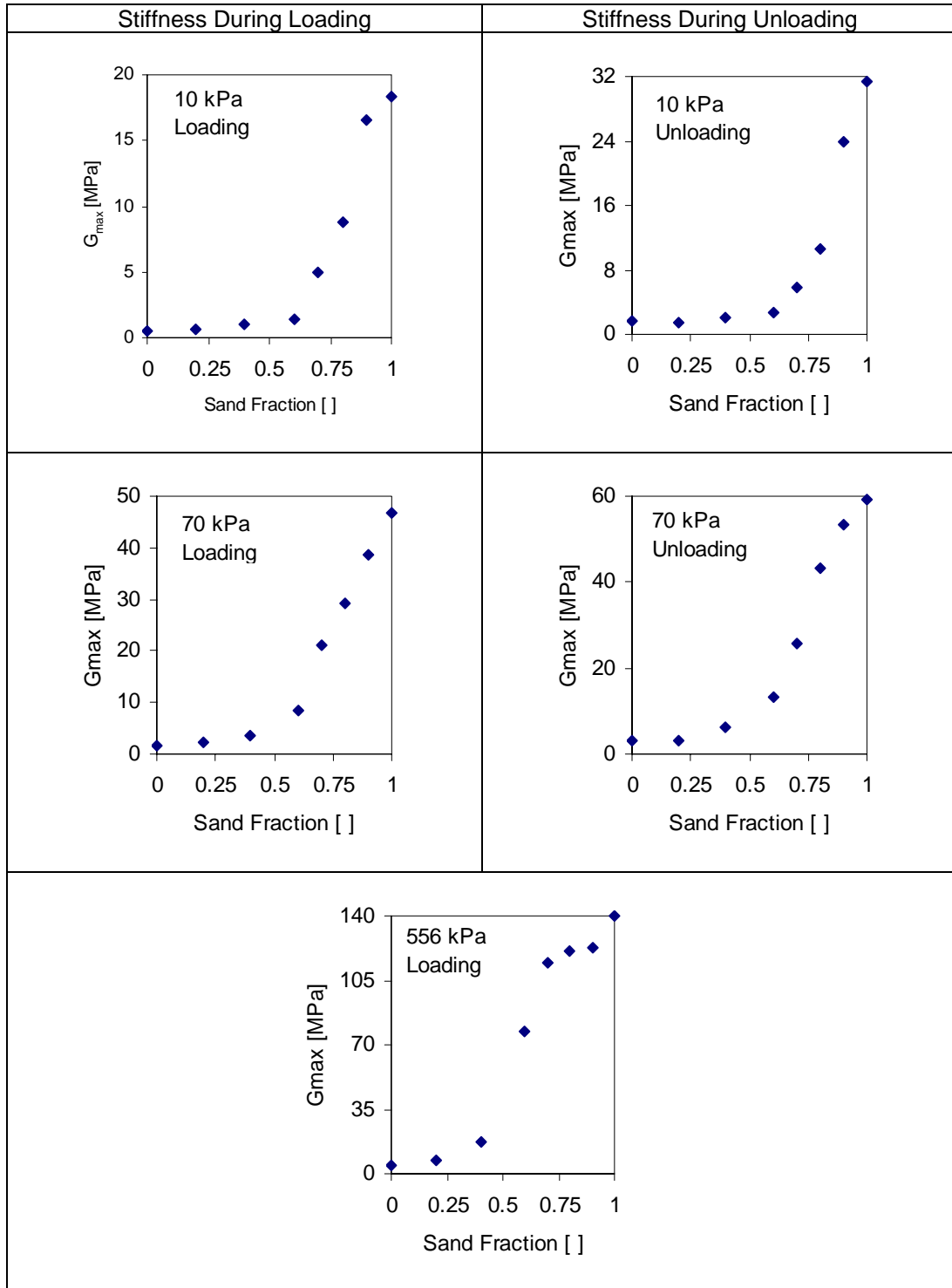


Figure 5.13 G_{\max} at different loading levels. Near the percolation threshold, the change in G_{\max} with stress follows a power relationship. As stress increases, soft particles deform, allowing rigid particles to move closer to one another and form a percolating network at lower sand fractions.

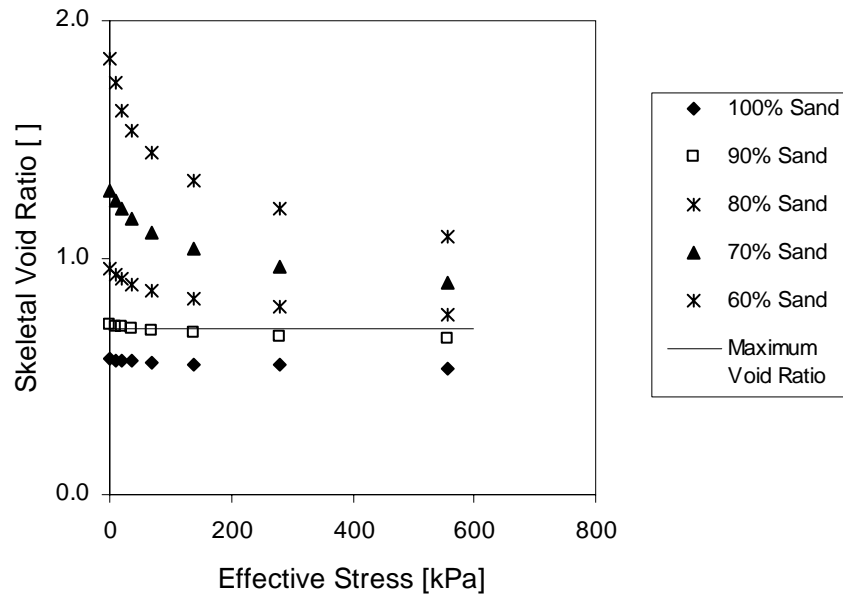


Figure 5.14 Skeletal void ratio as a function of effective stress for several sand fractions.

photoelastic disks used herein are polymer materials, which are birefringent under strain. Therefore it is possible to characterize the stresses field within each particle using a polariscope. Near the contacts, stresses are non-uniform and produce a series of light and dark bands or fringes. The band density increases with contact force (Geng et al. 2001).

Stiff particles are represented by 12.6 mm diameter stiff photoelastic disks, while soft particles are represented by 9.3 mm rubber cylinders. Both particle types are 12.6 mm thick. Three sets of tests are performed in which the number of rubber particles is increased from 29 to 56 to 79, while the number of photoelastic disks remains constant at 118.

Particles are placed one at a time in a 166 mm square by 13 mm thick plexiglass box in a fairly uniform packing (Figure 5.15). Boundaries are made of photoelastic material as well. Load is applied using pneumatic pressure fed through a Bellofram air cylinder mounted on the load frame. Load magnitude is determined using a Fairchild test gauge. The load is transferred from the pneumatic cylinder to the particles using a photoelastic block with several layers of foam attached at the end in contact with the particles to distribute the load more evenly (Figure 5.16). Two fluorescent lamps produce light, which passes through a diffuser, a polarizer, the disks and a second polarizer. Photos of each level of loading are taken with a digital camera.

During each test, the load is slowly applied until stress bands in the photoelastic disks become clear. A picture is taken, then the front polarizer is rotated 90° to change the orientation of light that passes through the polarizer and another picture is taken. The load is removed and a small rod is thrust into the matrix 3-4 times to randomize the fabric and the procedure is repeated. Three to four fabrics are tested at each mixture ratio.

5.7.1 Results and Analysis

Typical photographs are presented in Figure 5.17. The numbers of load-free rigid particles in the array and the numbers of soft-rigid particle contacts that visibly transfer load are determined. When the number of load-free rigid particles is high, the load is being transferred through fewer rigid particles. When the number of load transferring rigid-soft contacts is low, rigid particles primarily carry the load. In this case, large distinct force chains are observed. However,

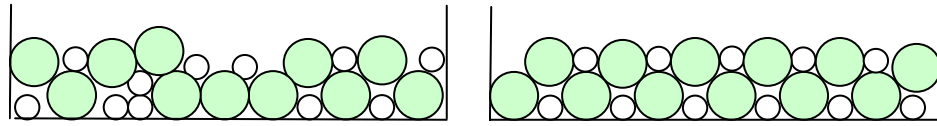


Figure 5.15 First two layers of a disordered (left) and ordered (right) packing. Particles are more evenly spaced in an ordered packing.

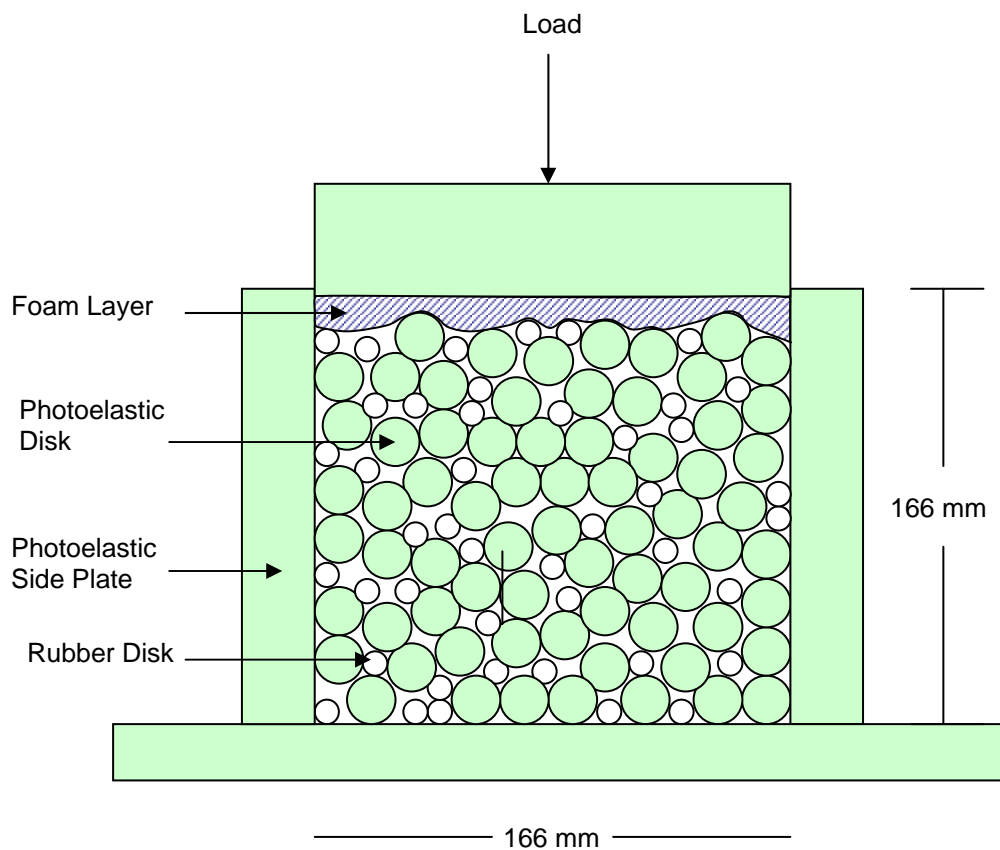


Figure 5.16 Simple Schematic of the photoelastic setup. The Load is applied using a Bellofram air cylinder mounted on a load frame. The Load magnitude is determined using a Fairchild guage. Photoelastic disks represent stiff particles while rubber disks represent soft particles.

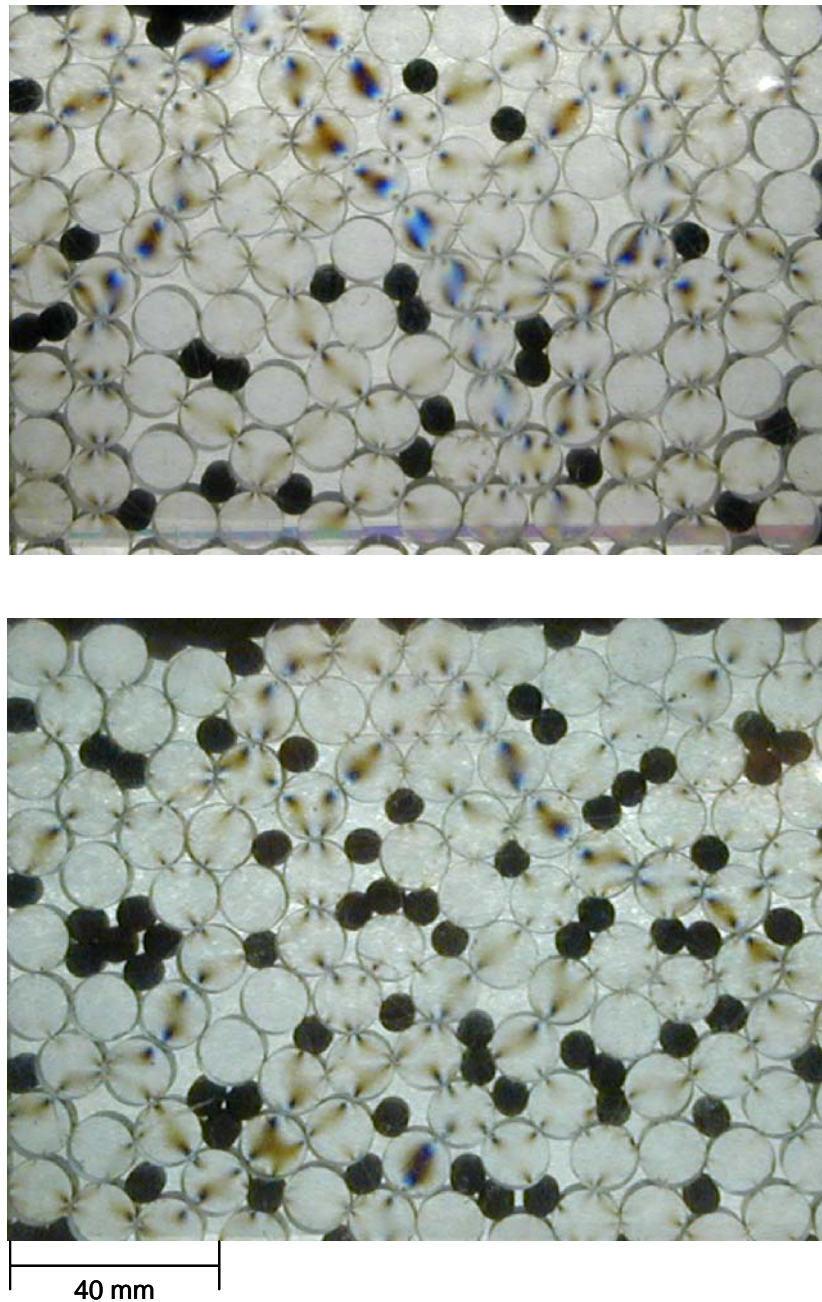


Figure 5.17 Typical photoelastic results. Soft particles appear as dark circles (top). Mixture of 29 soft and 119 rigid particles. Notice the high number of particles with no dark lines caused by stress. Several large chains carry most of the load while many particles do not contribute. Mixture of 56 soft and 119 rigid particles (bottom). Notice the high number of dark (soft) particles causing stress in their rigid neighbors. The high number of soft particles leaves few paths made of rigid particles only. This causes a more even distribution of load among particles and fewer vertical force chains.

when more rigid and soft particles transfer force, the load is more dispersed, and force chains are less distinct.

Using these two criteria, the nature of force chains in different packings may be determined. Table 5.7 presents results from this investigation. The initial packing, in which the soft particles are evenly spaced within the rigid particle matrix, is termed ordered. Subsequent packings, in which rubber particles are randomly distributed through the rigid particle matrix, are termed disordered. In ordered packings, large distinct force chains form more readily at lower rubber contents, whereas the chains are less distinct at higher rubber contents. The converse occurs in disordered packings; chains are less distinct at low rubber contents and are larger and more distinct at high rubber contents.

The prevalence of force chains and the amount of load each chain carries depends on the number of viable rigid particle paths. When there are many rigid particle paths, there are many chains of small numbers of particles, as is the case in a random packing with few soft particles. When there are few viable rigid particle paths, all the force is transferred through those paths, so a few large force chains carry the entire load. This happens when there are few soft particles in an ordered packing or many soft particles in a disordered packing.

In the ordered packing with many soft particles there are no continuous rigid particle paths and some of the force must pass through the soft particles. When this happens soft particles deform, transferring the load to their neighbors, and large force chains become less apparent as the entire matrix carries the load.

Force chains cannot exist without supporting particles which keep the chains from buckling. Although the rubber particles are generally not primary members of the force chains, they appear to be as likely as their rigid counterparts to be supporting members.

5.8 CONCLUSIONS

- Three factors that influence the stiffness of a binary mixture of soft and rigid particles are the dimensionless ratios $D_{\text{rigid}} / D_{\text{soft}}$, $V_{\text{rigid}} / V_{\text{total}}$, and the state of stress.
- Soft particles in a rigid-soft matrix tend to channel and support force chains. If there are very many or very few rigid particle force paths, force chains disappear as force propagates somewhat evenly through the medium.
- Three distinct small strain stiffness regions exist: (1) rigid particle-like, (2) soft particle-like, and (3) a transition. The ratio of stiff to soft particles at which the transition occurs marks the percolation threshold. Above the percolation threshold stiffness increases rapidly with increasing sand fraction until the behavior is sand-like at high sand fractions.
- This rigid particle fraction at which the percolation threshold exists decreases with increased stress as small soft particles deform and fill the voids between larger, stiff particles.
- Near the percolation threshold stiffness increases rapidly with stress leading to unusually high b values as the number of rigid particle contacts increases rapidly with stress and soft particle deformation.
- The oedometer stiffness is controlled by the void ratio of the sand fraction. Considering the rubber particles as voids, when the void ratio is higher than the maximum void ratio, stiffness declines markedly. When the void ratio is at or below the maximum void ratio, a stable sand skeleton is formed and stiffness is sand-like.

Table 5.7 Photoelastic results. Rigid particles which do not cause visible force in neighboring photoelastic particles (no force), and rigid particles visibly stressed are used to quantify the nature of force chains. Greater numbers of un-stressed rigid particles, and fewer numbers of load transferring soft particles implies that the load is primarily transferred by a small number of large rigid force chains. In contrast, less unstressed rigid particles and more load transferring soft particles implies a diffused load which is transferred through many small chains. Packings in which soft particles are uniformly spaced are termed ordered, other packings are termed disordered.

	Photoelastic Disks	Rubber Particles	No Force Particles [%]	Load Carrying Rubber [%]
<i>Ordered</i>				
Low	118	29	26	28
Medium	118	56	20	43
High	118	79	16	54
<i>Disordered</i>				
Low	118	29	20	41
Medium	118	56	24	32
High	118	79	25	29

CHAPTER VI

CONCLUSIONS

Particle shape occurs on many scales relative to the particle diameter, but is most commonly characterized on three independent scales corresponding to form, roundness and roughness. The global shape, or form, of a sand particle is determined during formation, and is later affected by weathering. Weathering mechanisms are related to cleavage, which is rare. Weathering changes roundness and roughness, yet changes in form through weathering are less common. The roughness of the particle is environmentally determined as specific surface textures are characteristic of specific environments.

Eccentricity is a measure of particle form and it is influential in the angle of internal friction, strength anisotropy, coordination number, and dilation. Low roundness values lead to rotational frustration and interlocking which lead to an increase in the observed angle of repose and a decrease in localization and shear band formation. Particle roughness leads to increased damping, rotational frustration and decreased soil stiffness. Shape also influences the flow of granular materials, self-organization, the magnitude of electrical and capillary forces and rheology. Because of the broad influence of shape on material behavior, shape should be considered whenever soil is classified.

The shape and behavior of the crushed granite sands vary little between producer and quarry. However, shape and behavior vary by particle size. Because of their angular shape, crushed sands generally exhibit higher maximum void ratios at the same coefficient of uniformity, higher critical state friction angles, and lower small strain stiffnesses than round natural sands.

The addition of fines increases workability as measured by the flow test for the materials and conditions considered in this study. This is most likely due to a decrease in mortar permeability as fines content increases, leading to increased pore pressure during shear. At 14 days, higher fines content sands exhibit higher strength than their counterparts which contain fewer fine particles. The creation of a complementary database to the one developed in chapter three, which is compiled from the literature review, is recommended.

Particles of differing form or angularity will segregate when subjected to vibration. This appears to occur because of the greater mobility of round particles. Nevertheless, the study of shape-based segregation is still in its infancy.

The presence of soft, shape-changing particles alters soil behavior. Mixtures of rigid-soft particles in which the soft particles are smaller than the rigid particles can render altered force chains.

The constraint modulus is low (rubber-like) at most sand fractions, but exhibits a large increase between sand fractions of 80% and 90%. Below 90% sand, the void ratios of the sand fraction are higher than the maximum void ratio for Ottawa sand. At 90% sand and above, the void ratio is at or below the maximum void ratio of Ottawa sand and a load carrying sand skeleton is formed.

The small strain stiffness sand-rubber mixtures falls into one of two categories. At low stiff particle fractions, the stiffness is low (rubber like). At high stiff particle fractions the stiffness is high (sand like). The transition region begins at the stiff particle percolation threshold, above which stiffness increases rapidly with sand fraction at a specific confinement, until sand-like behavior is observed. This occurs because the numbers of stiff particle contacts, which control the stiffness of the mixture, increase rapidly near the percolation threshold. As confinement increases, the percolation threshold occurs at lower sand fractions because small, soft particles deform and fill the voids between larger, stiff particles so that more stiff particles are in contact. Sand-rubber mixtures may be designed to exhibit a desired stiffness at a particular confinement.

APPENDIX A COMPLETE SHEAR WAVE VELOCITY RESULTS

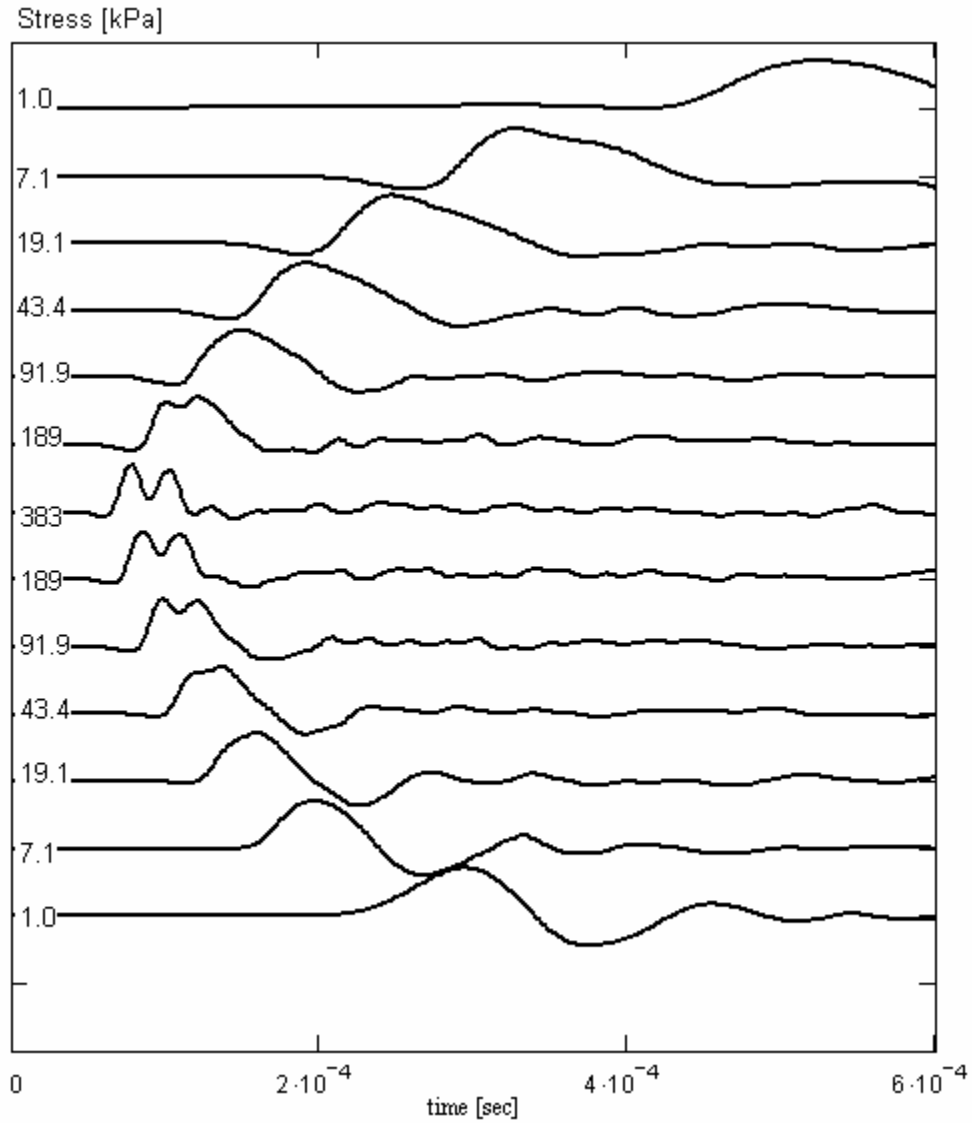


Figure A.1 Shear wave amplitude as a function of time for 1K9 sand. The output signal is normalized to the maximum signal amplitude. Step function signals are generated with a Krohn-Hite model 1400 A signal generator at 20 Hz and variable amplitude. Output signals are band pass filtered (100 Hz to 50 kHz) and amplified (input gain 20 output gain 0) using a Krohn-Hite model 3944 amplifier-filter. Signals are collected using a Rapid-Systems digital oscilloscope. Stresses displayed at the left represent the state of stress on the polarization plane.

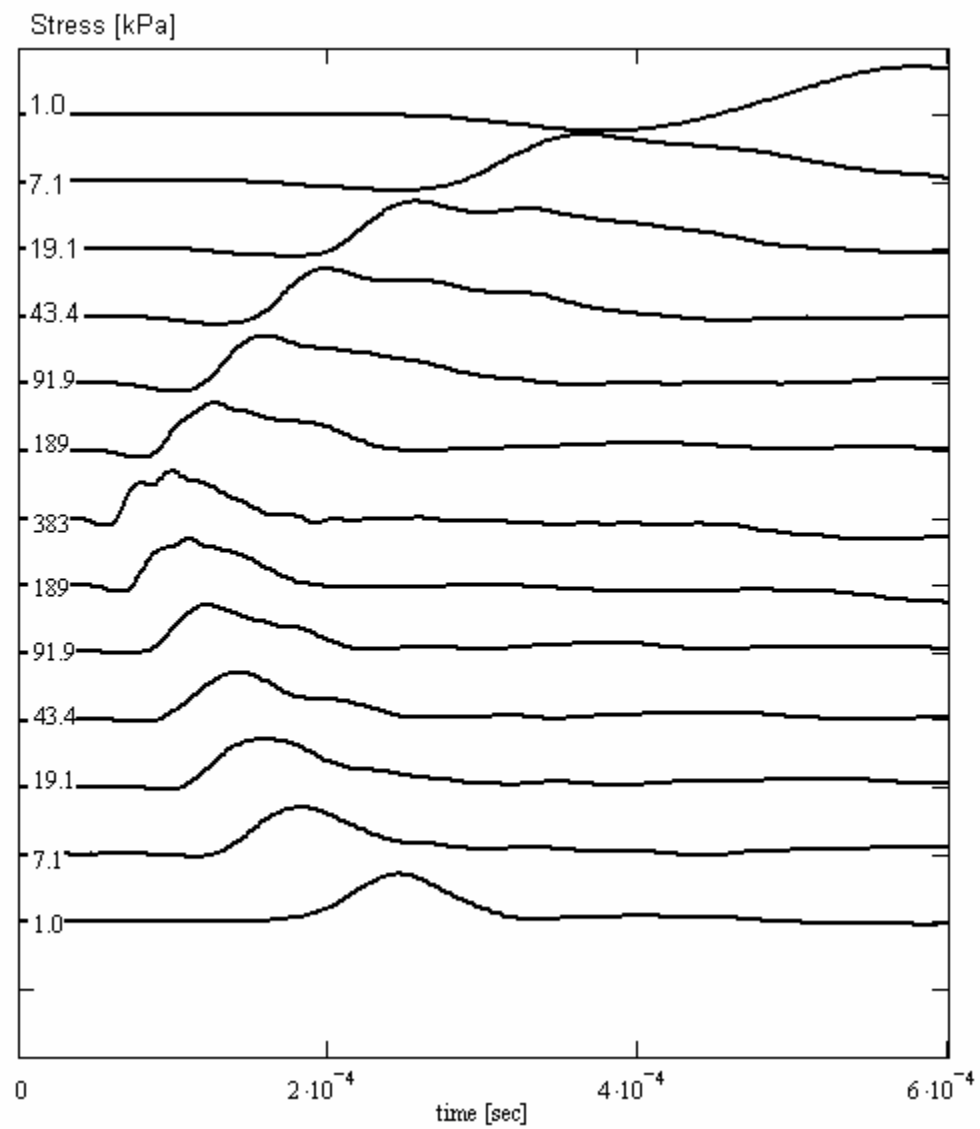


Figure A.2 Shear wave amplitude as a function of time for 2Z8 sand. See figure A.1 for details.

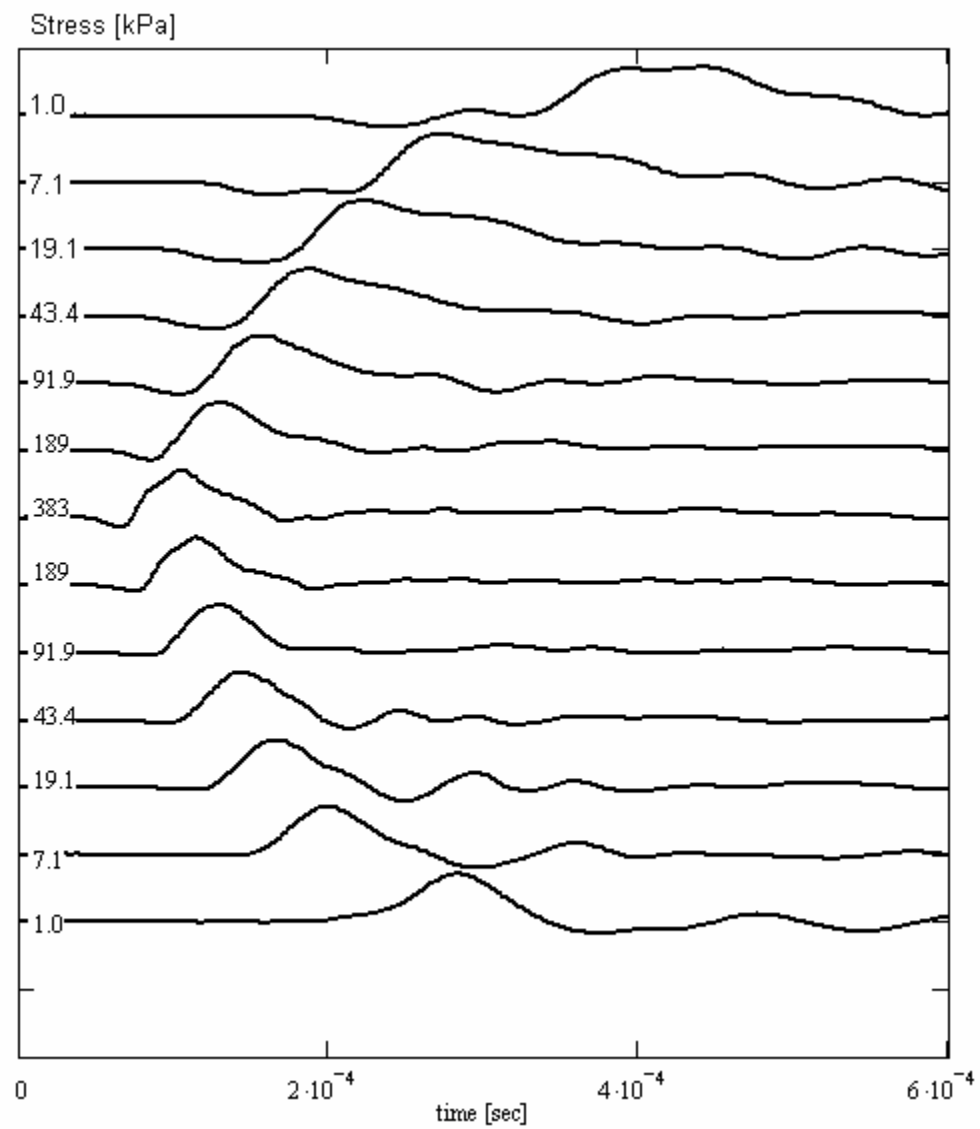


Figure A.3 Shear wave amplitude as a function of time for 3P3 sand. See figure A.1 for details.

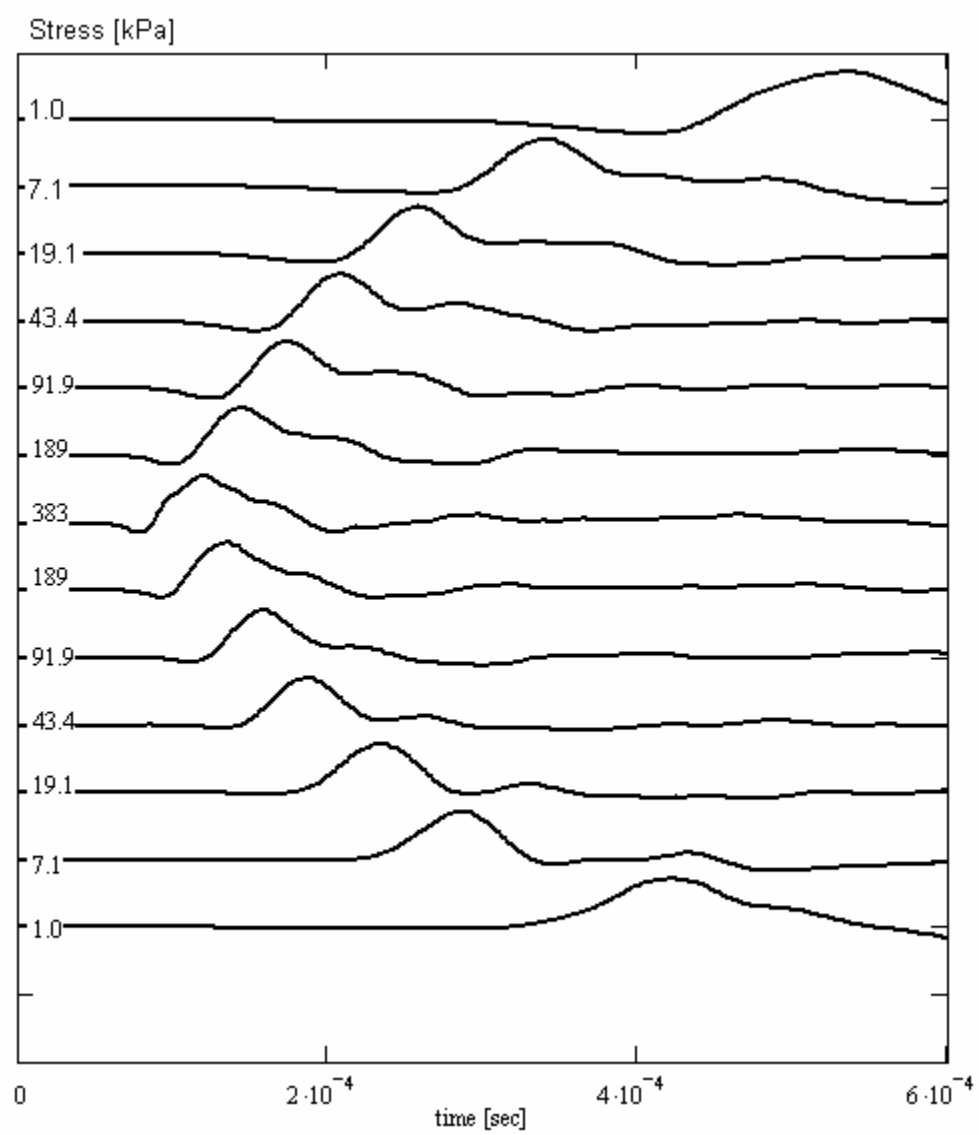


Figure A.4 Shear wave amplitude as a function of time for 5Z9 sand. See figure A.1 for details.

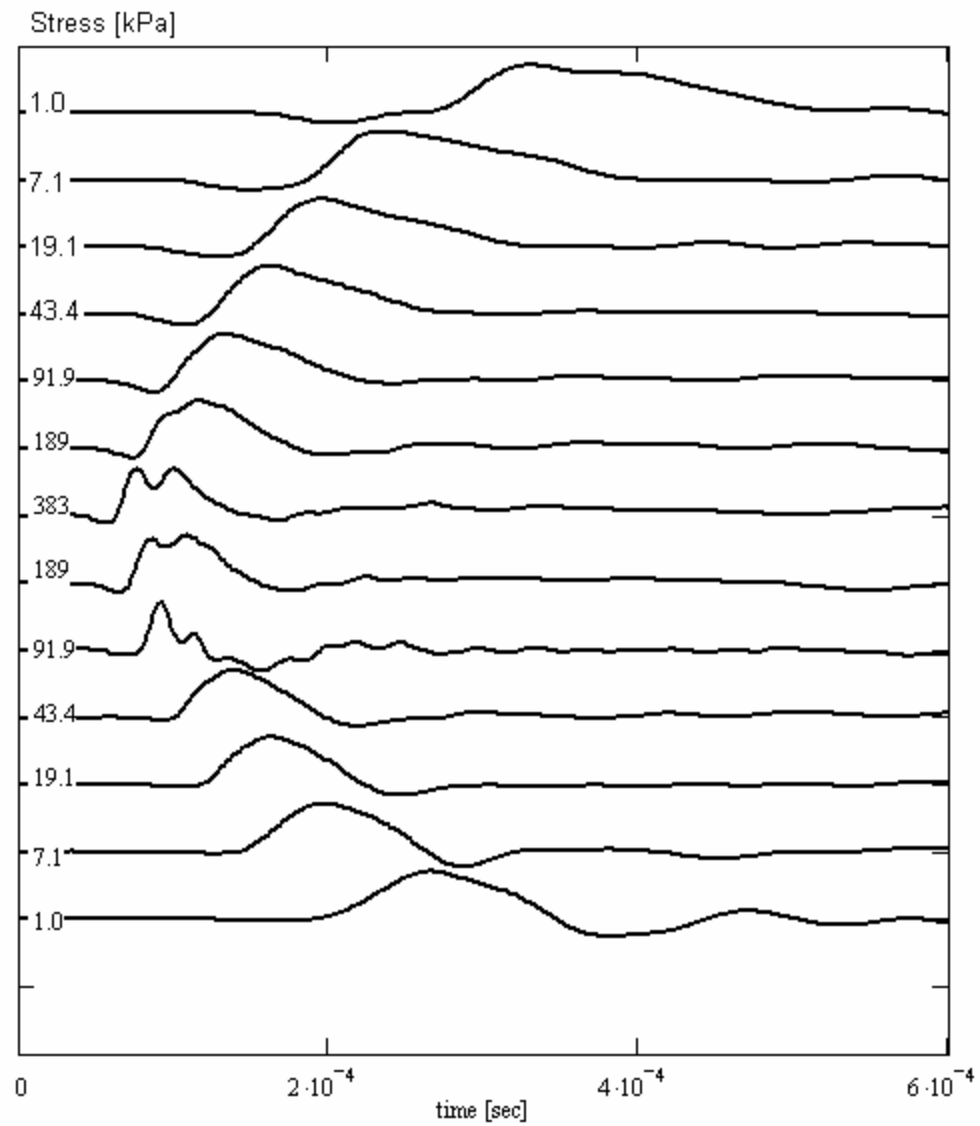


Figure A.5 Shear wave amplitude as a function of time for 6A2 sand. See figure A.1 for details.

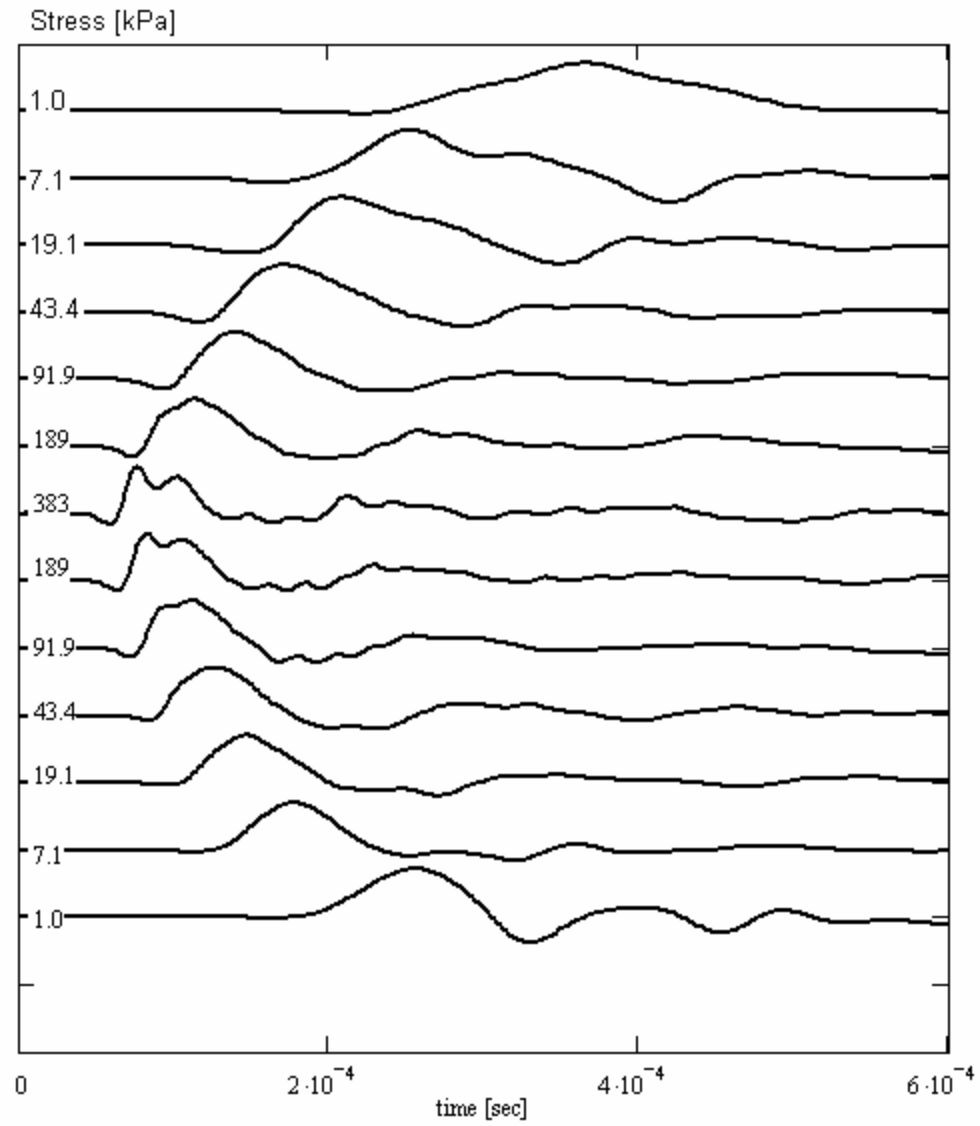


Figure A.6 Shear wave amplitude as a function of time for 6H1 sand. See figure A.1 for details.

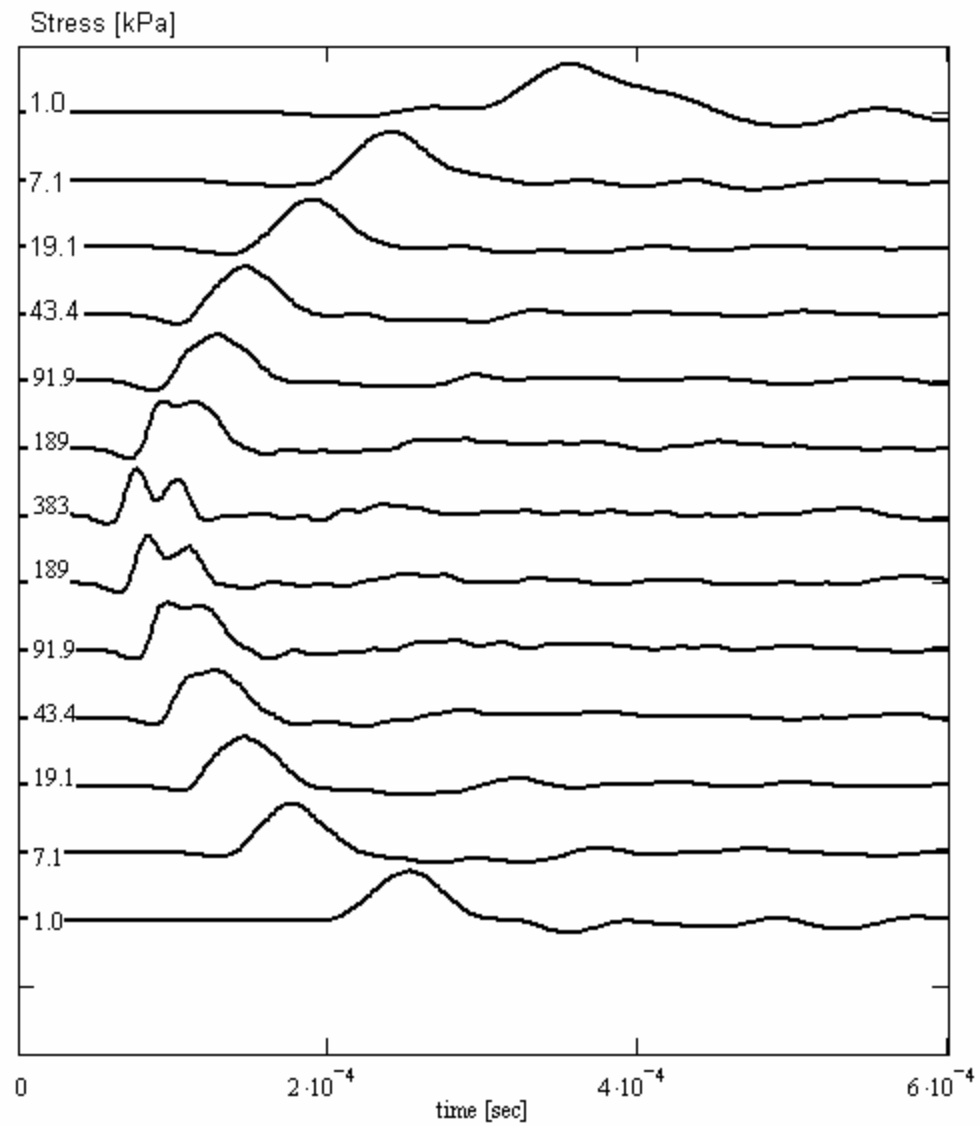


Figure A.7 Shear wave amplitude as a function of time for 8M8 sand. See figure A.1 for details.

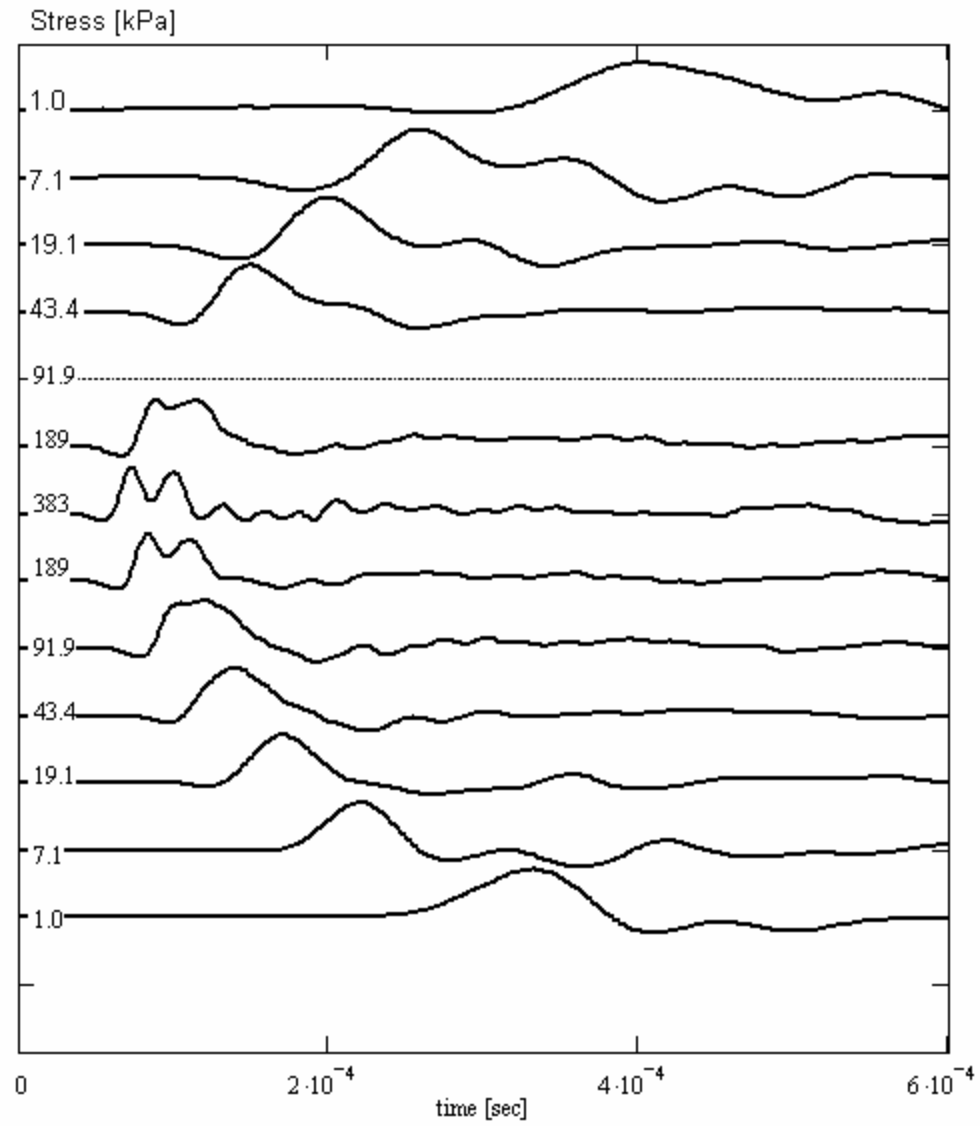


Figure A.8 Shear wave amplitude as a function of time for 9C1 sand. See figure A.1 for details.

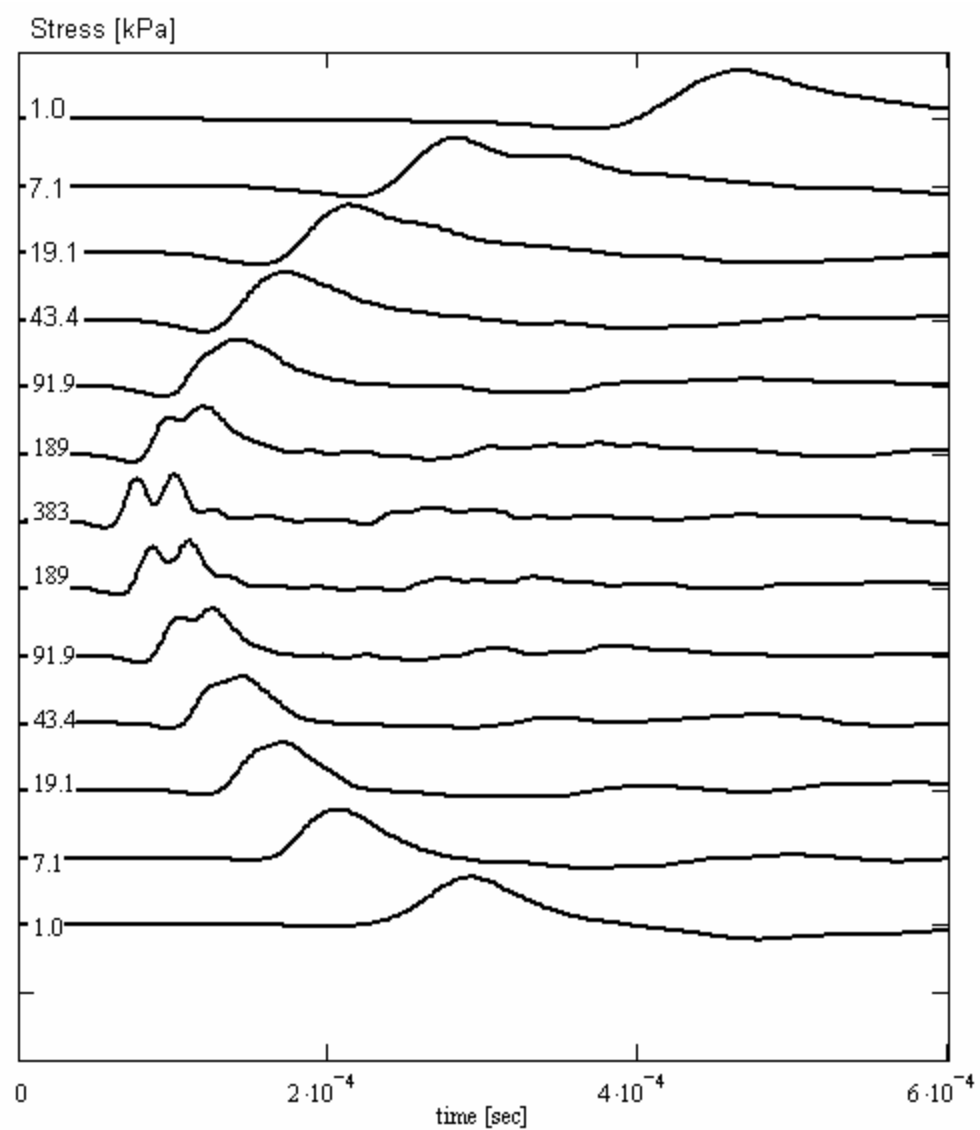


Figure A.9 Shear wave amplitude as a function of time for 9F1 sand. See figure A.1 for details.

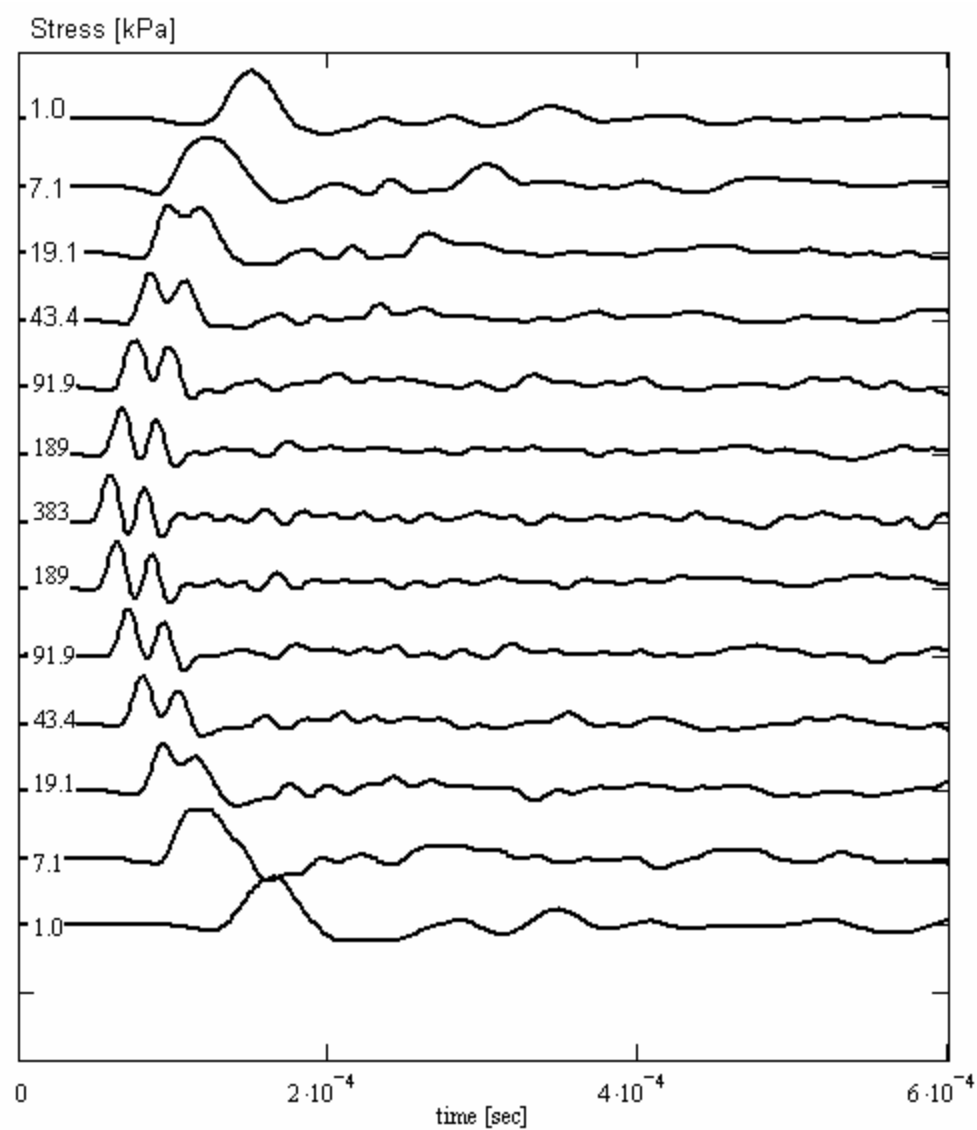


Figure A.10 Shear wave amplitude as a function of time for Jekyll Island sand. See figure A.1 for details.

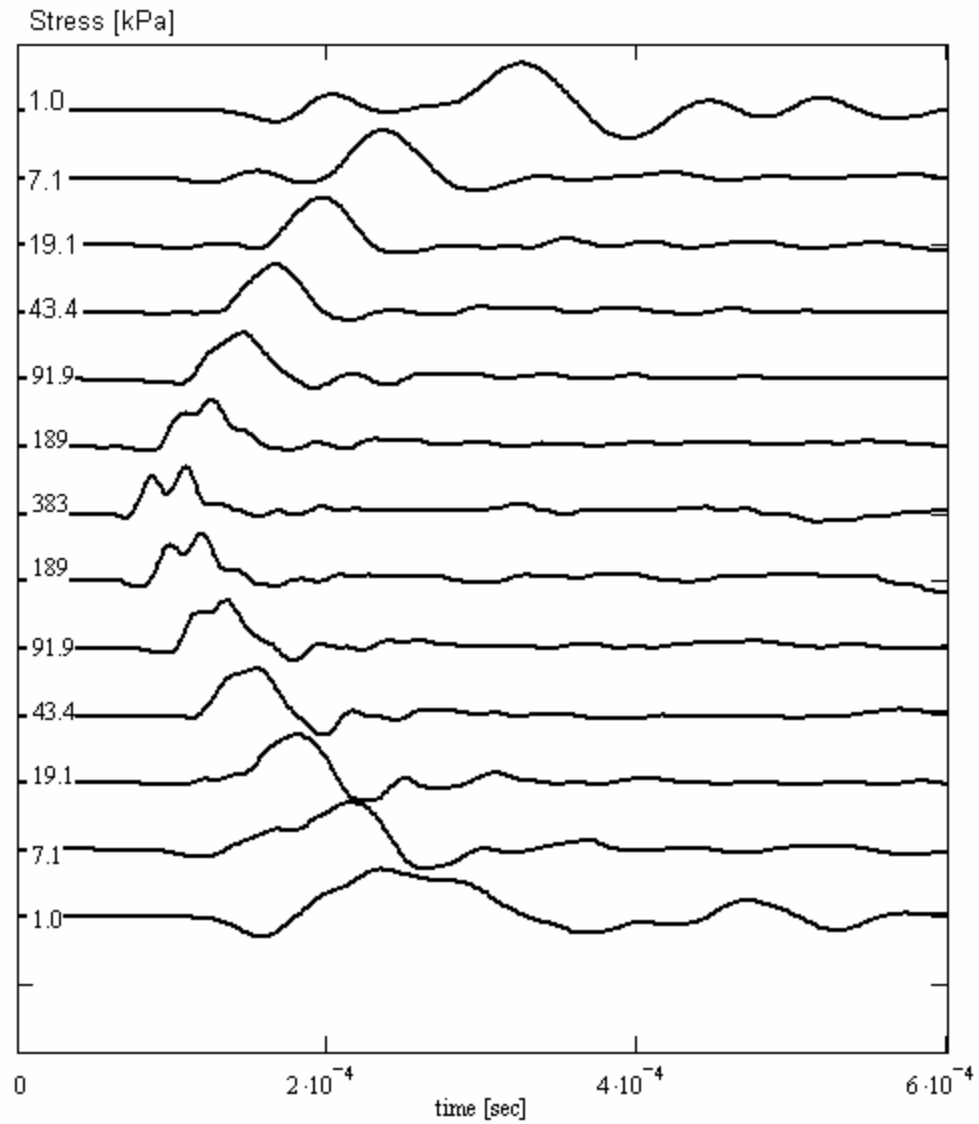


Figure A.11 Shear wave amplitude as a function of time for Nevada sand. See figure A.1 for details.

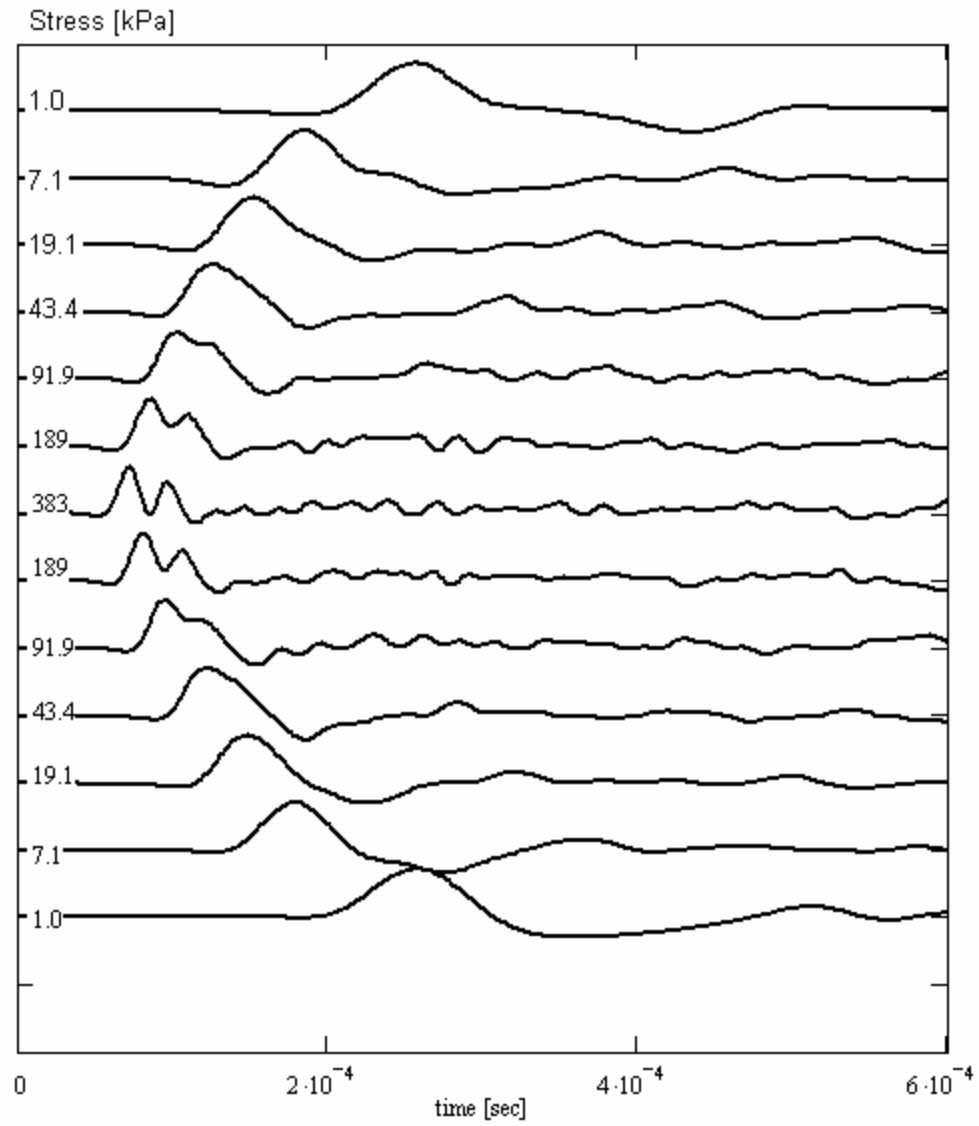


Figure A.12 Shear wave amplitude as a function of time for Ottawa sand. See figure A.1 for details.

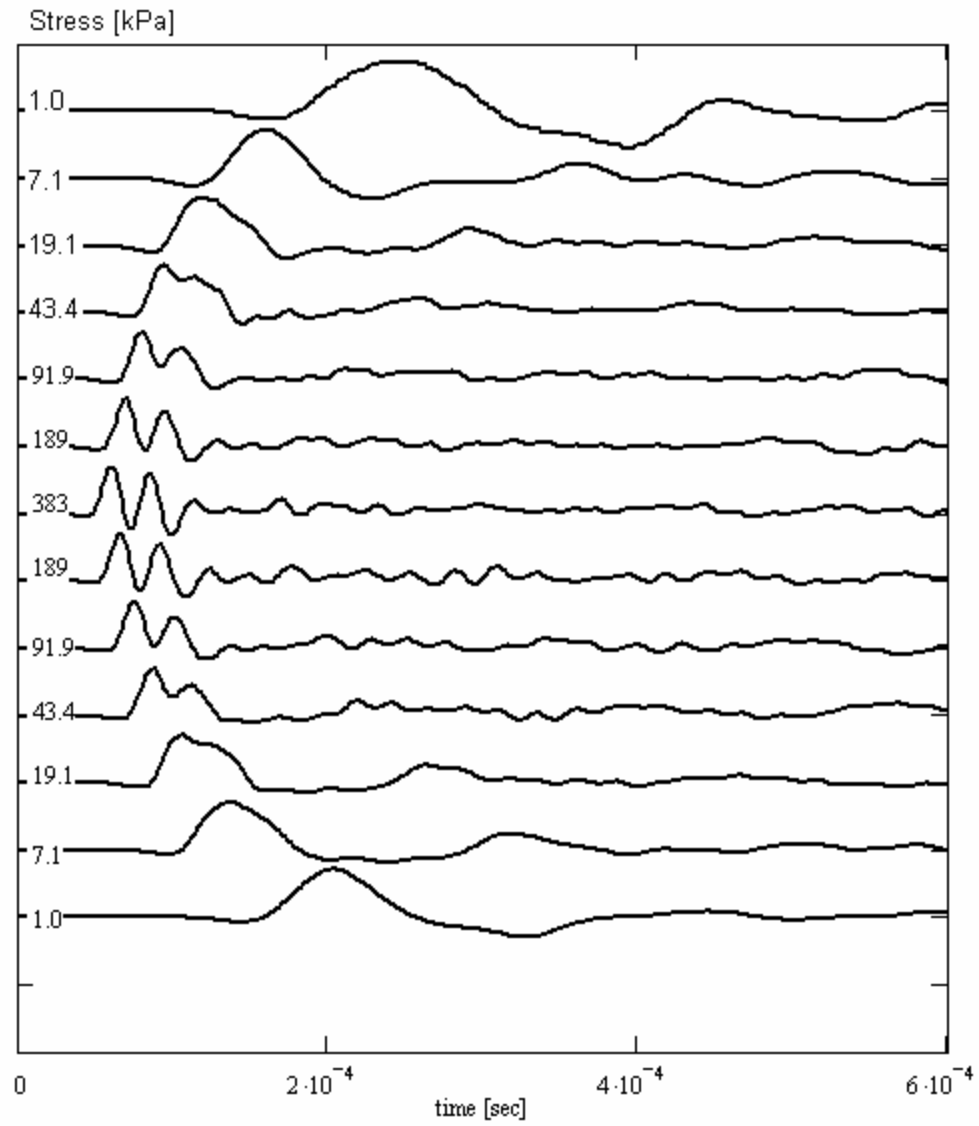


Figure A.13 Shear wave amplitude as a function of time for Margaret River sand. See figure A.1 for details.

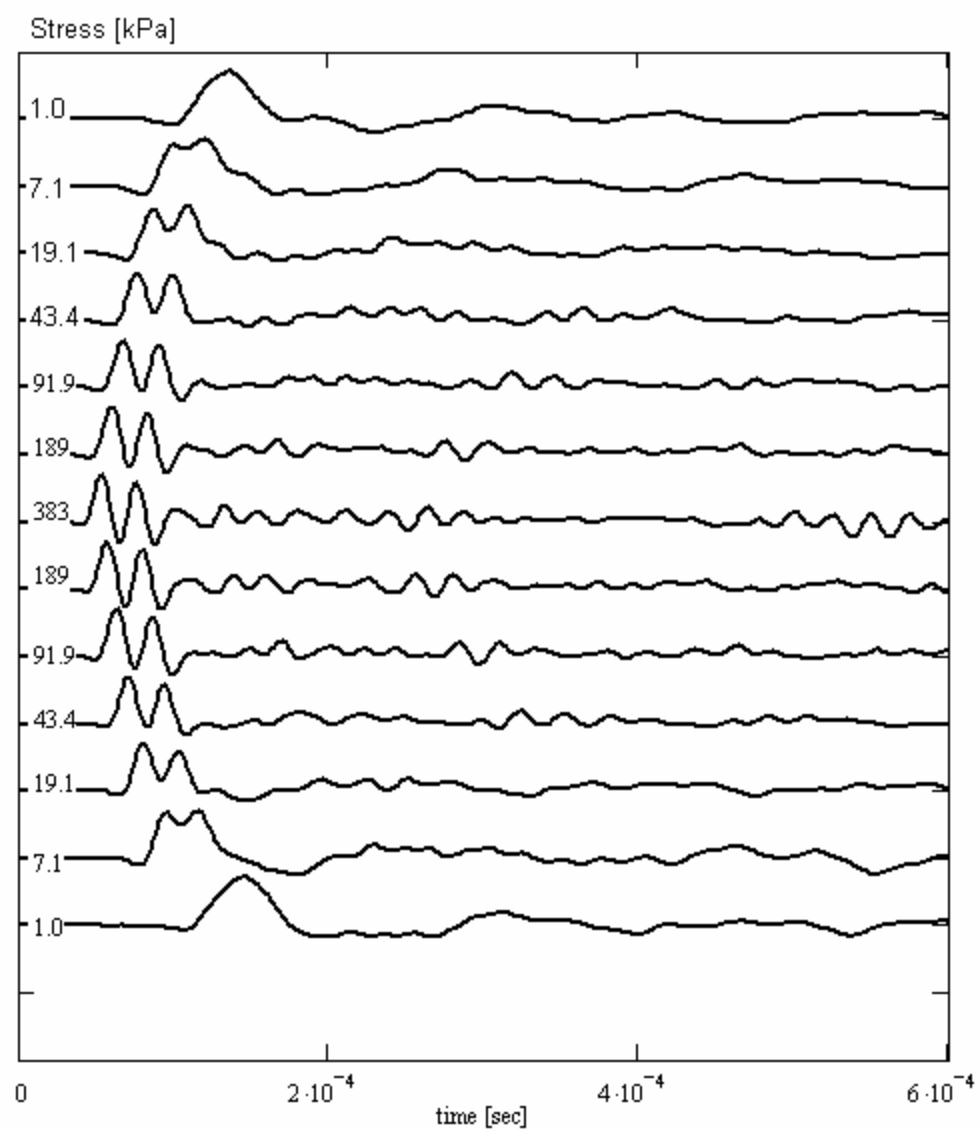


Figure A.14 Shear wave amplitude as a function of time for Ponte Vedra sand. See figure A.1 for details.

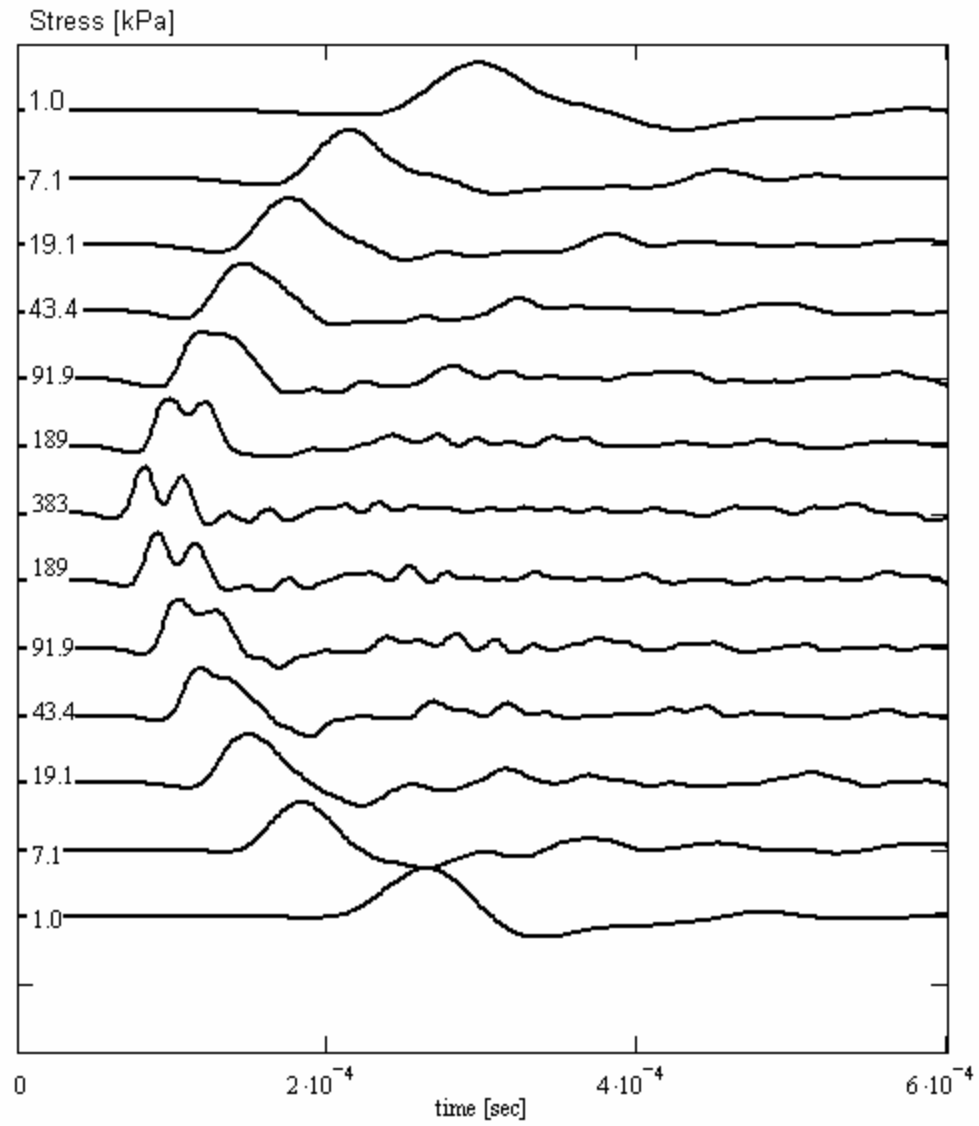


Figure A.15 Shear wave amplitude as a function of time for Ticino sand. See figure A.1 for details.

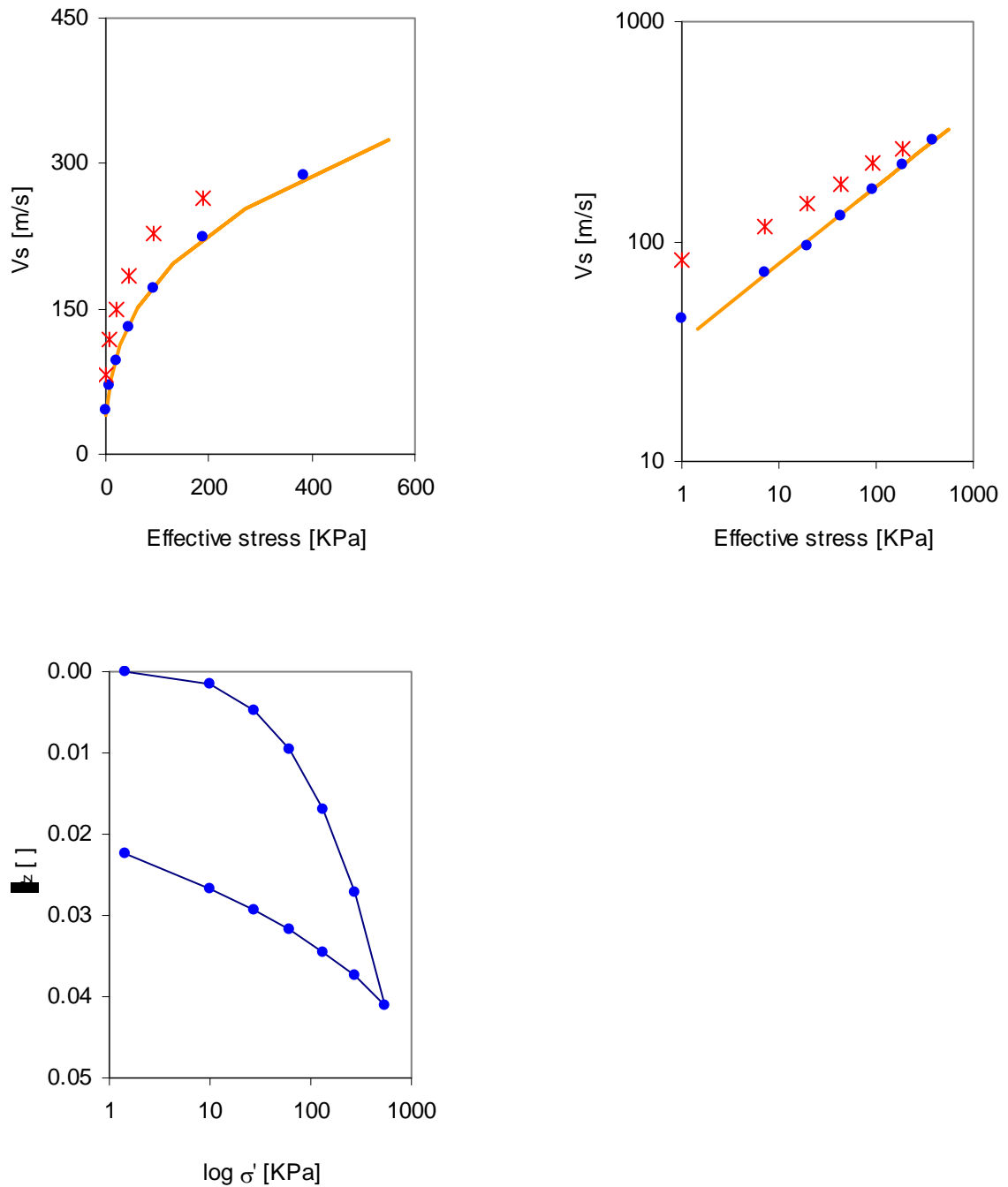


Figure A.16 Shear wave velocity and stiffness in confined compression of 1K9 sand. Shear wave velocities are computed using travel times from figures A.1 – A.15. Effective stress in the top two figures represents stress in the polarization plane, whereas stress in the lower figure is vertical effective stress. A time increment between load steps of 10 minutes is used.

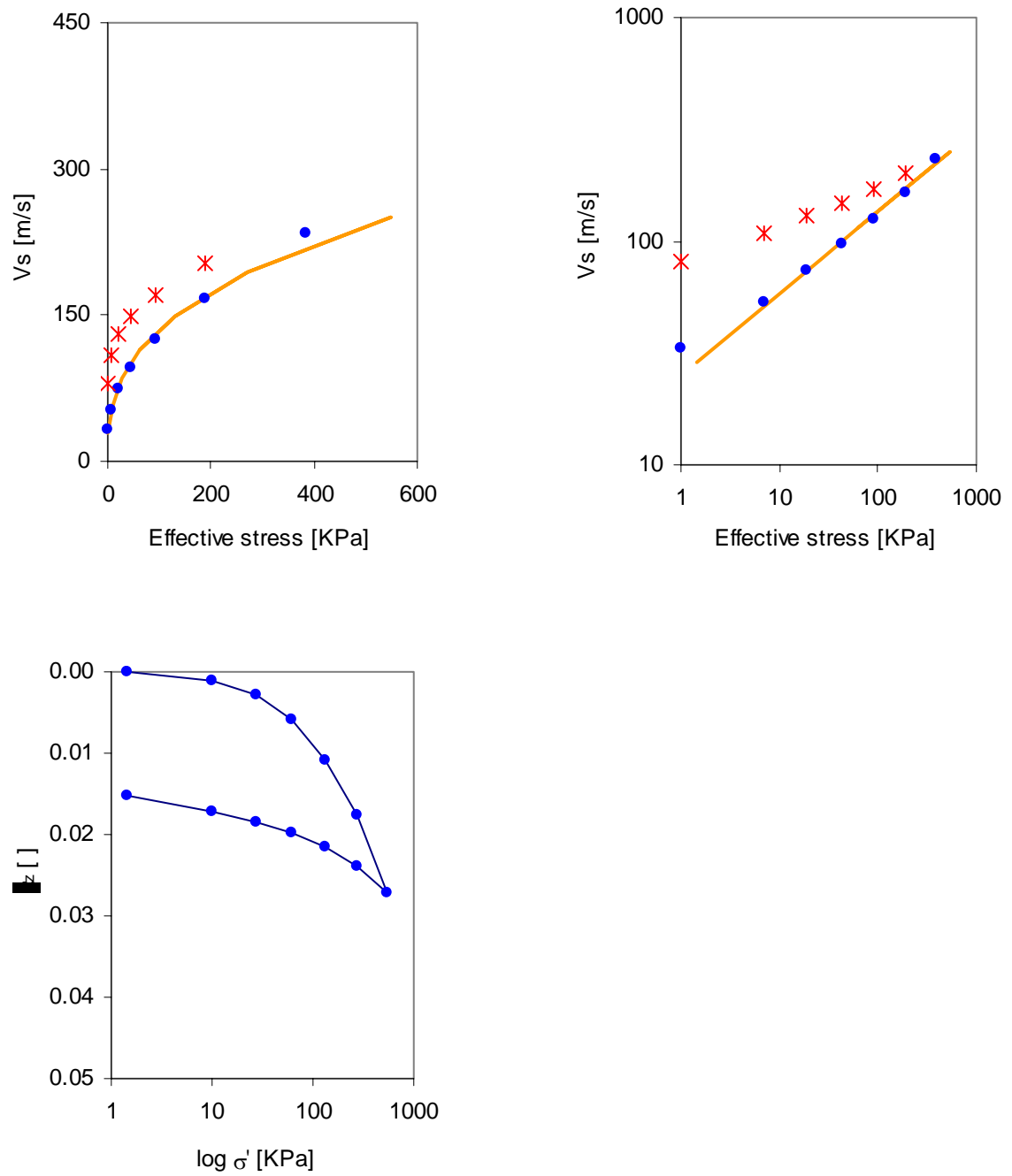


Figure A.17 Shear wave velocity and stiffness in confined compression of 2Z8 sand. See figure A.16 for details.

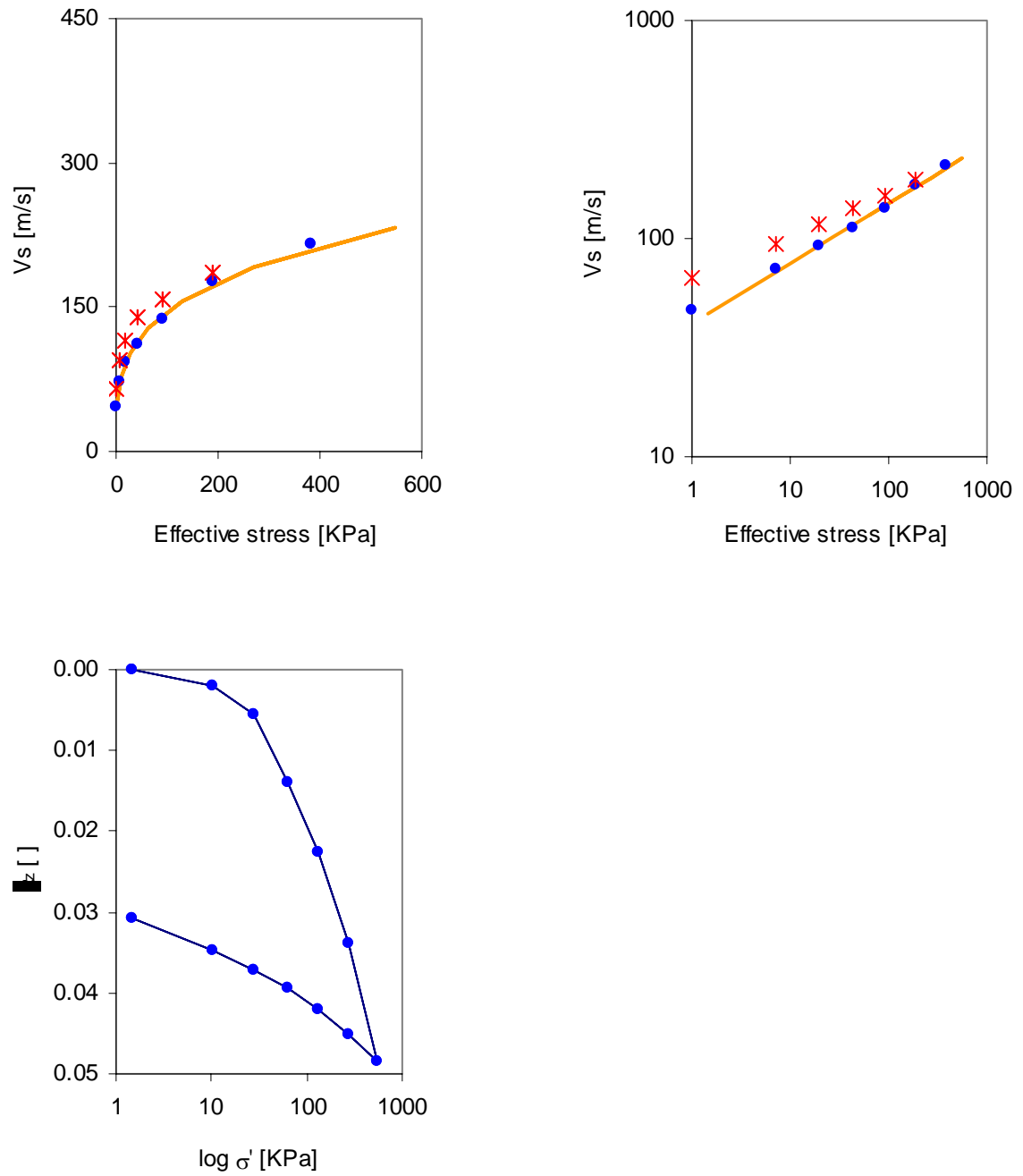


Figure A.18 Shear wave velocity and stiffness in confined compression of 3P3 sand. See figure A.16 for details.

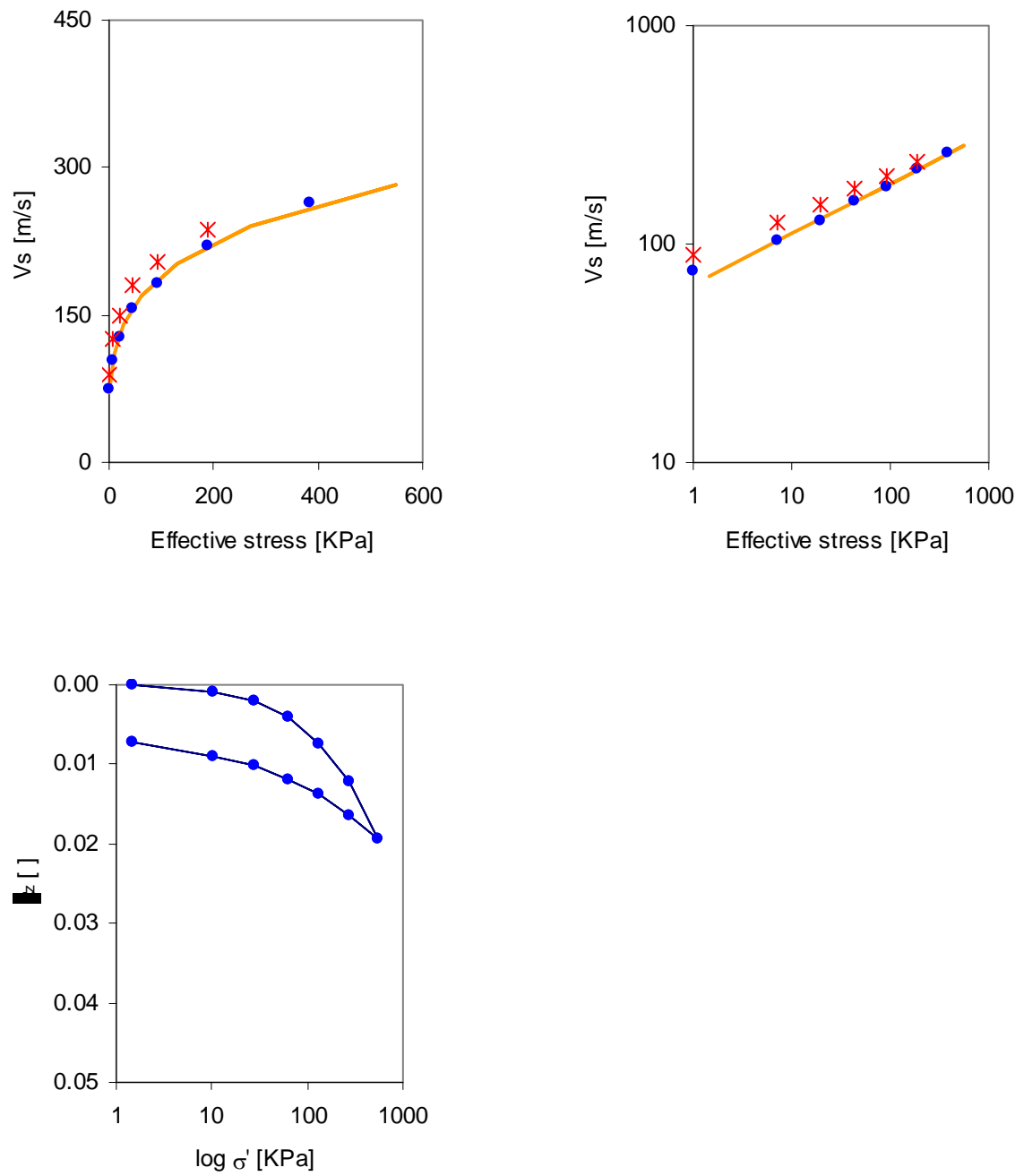


Figure A.19 Shear wave velocity and stiffness in confined compression of 5Z9 sand. See figure A.16 for details.

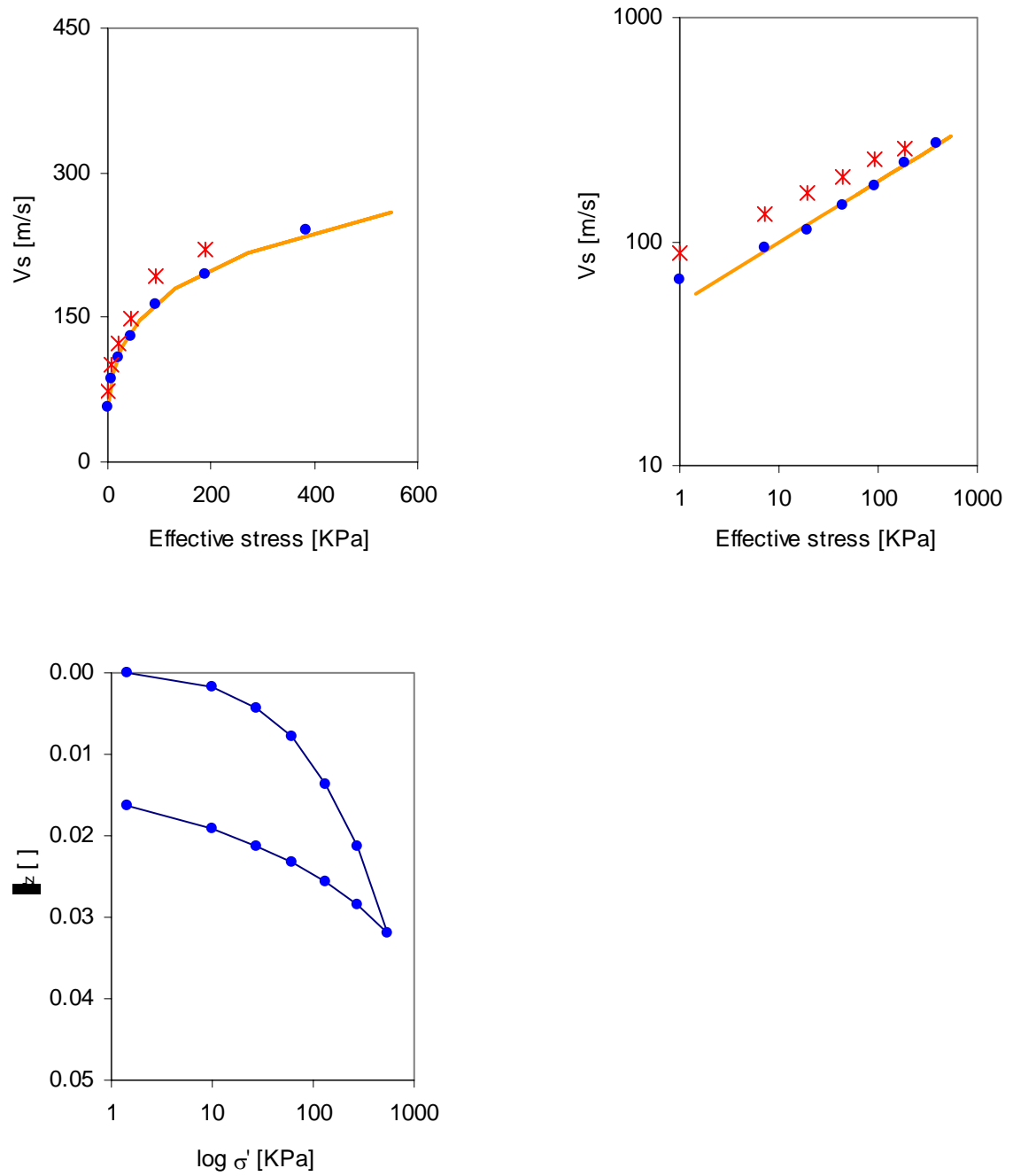


Figure A.20 Shear wave velocity and stiffness in confined compression of 6A2 sand. See figure A.16 for details.

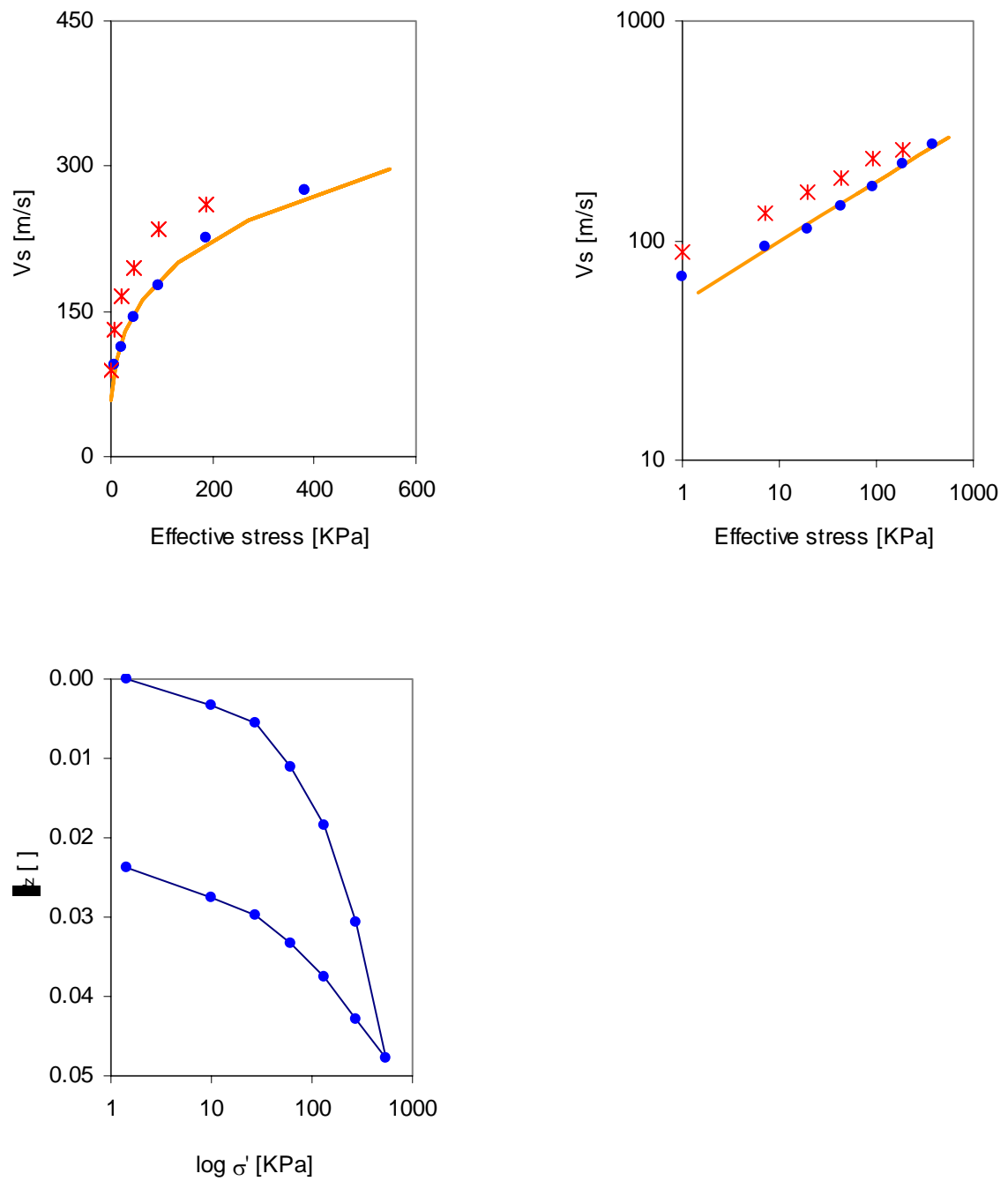


Figure A.21 Shear wave velocity and stiffness in confined compression of 6H1 sand. See figure A.16 for details.

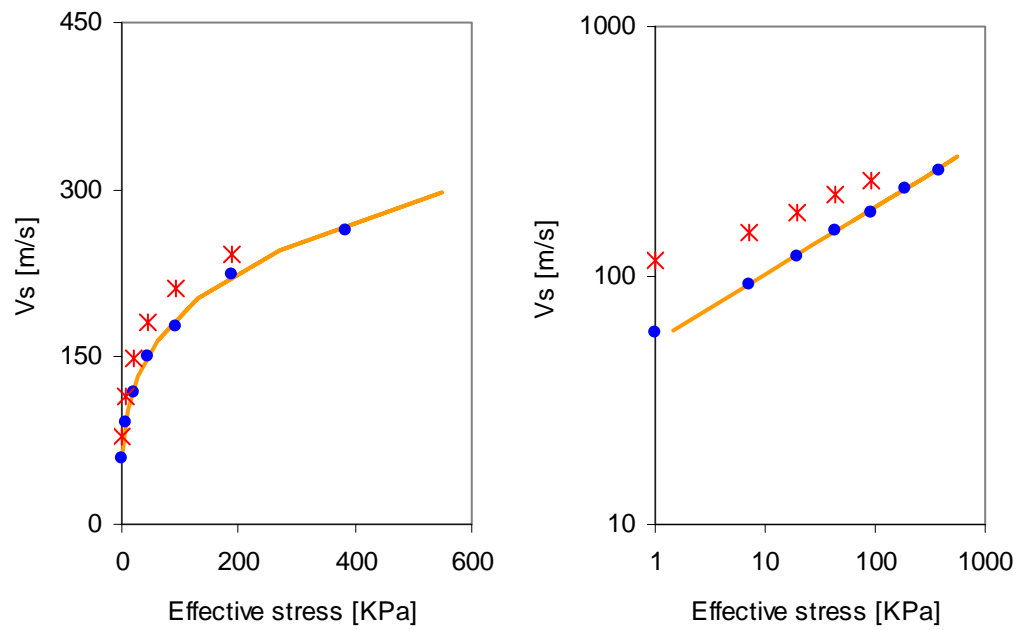


Figure A.22 Shear wave velocity as a function of stress for 8M8 sand. Stiffness data is not presented because of an erroneous dial gauge reading. See figure A.16 for details.

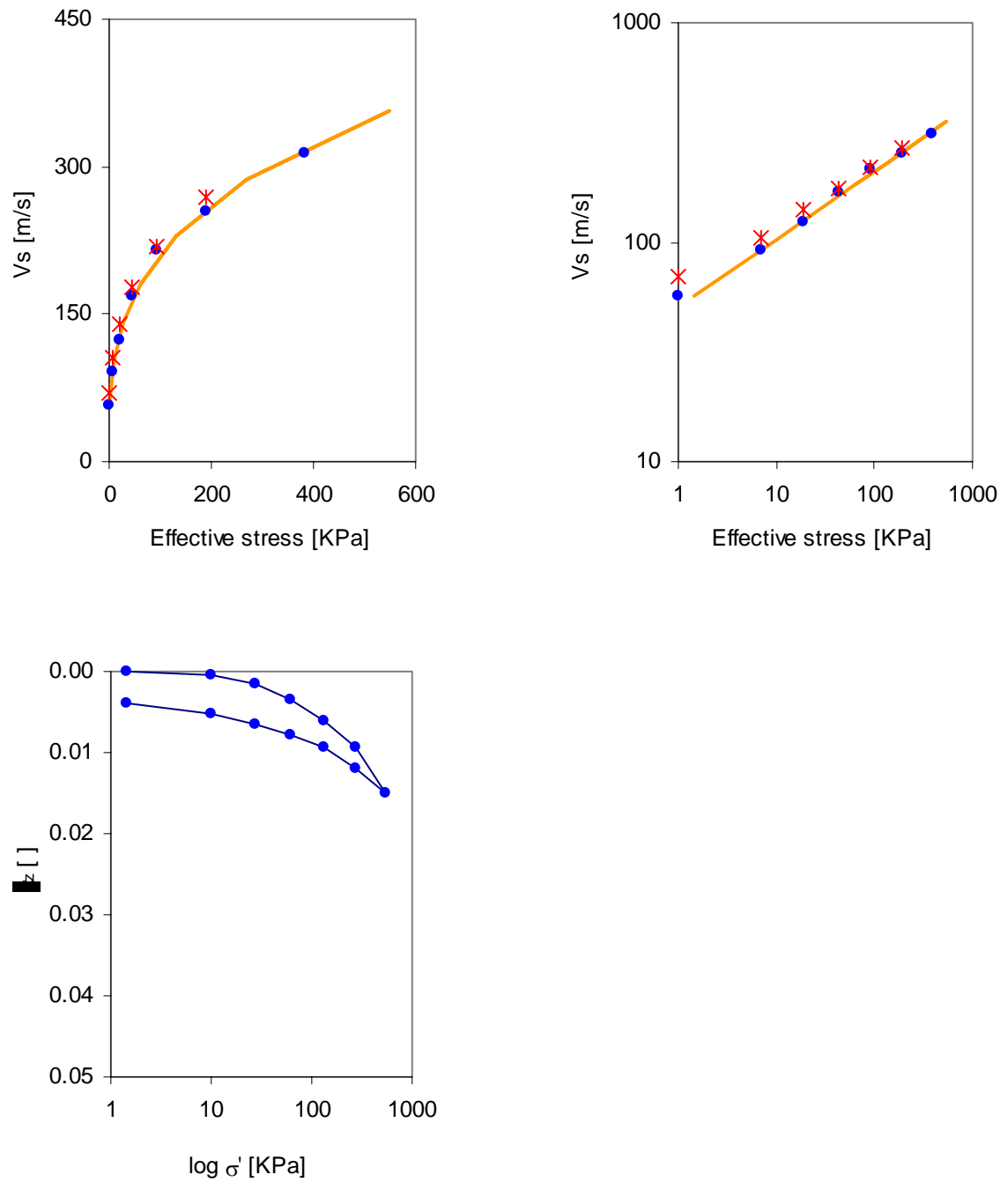


Figure A.23 Shear wave velocity and stiffness in confined compression of 9C1 sand. See figure A.16 for details.

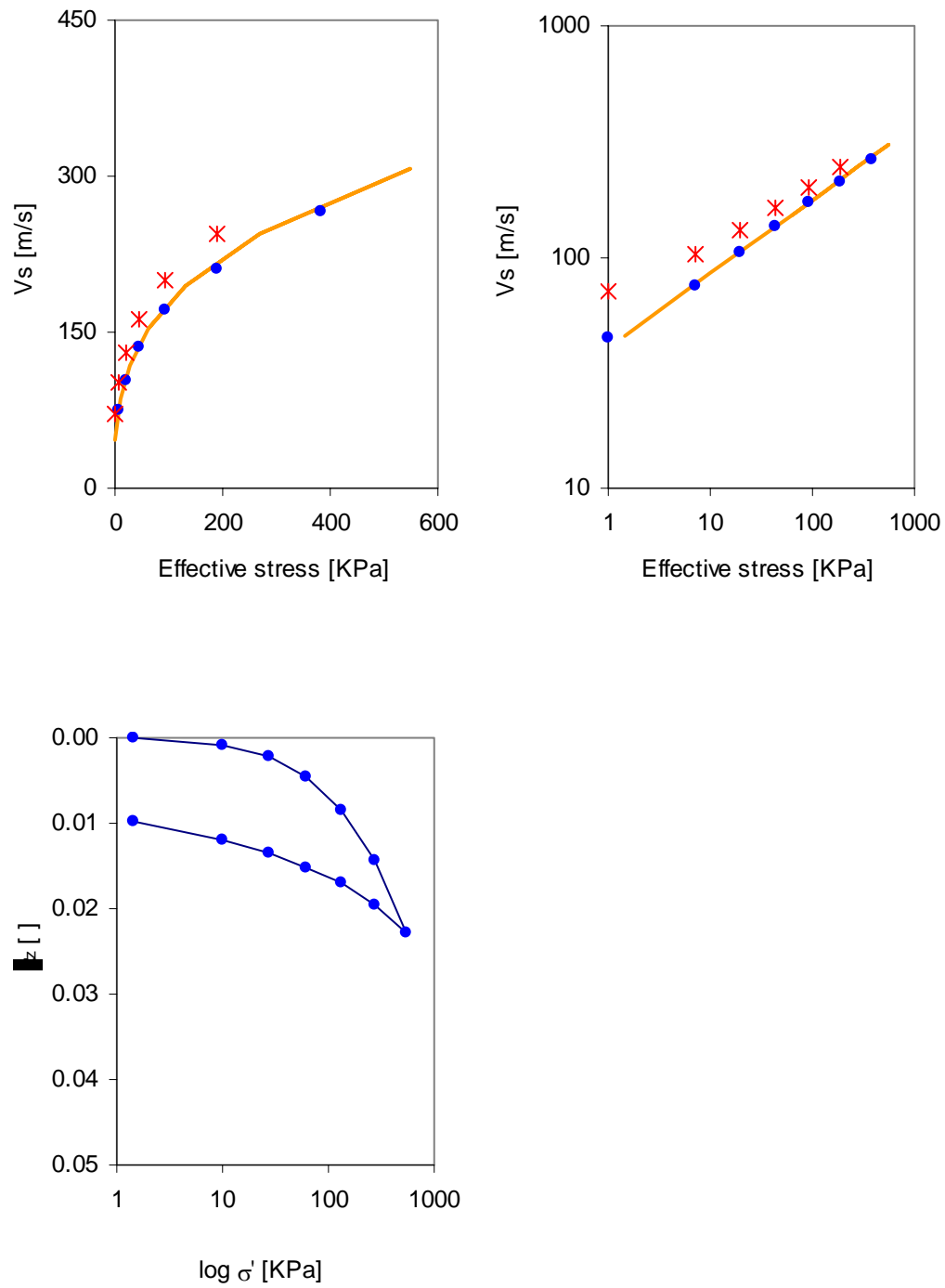


Figure A.24 Shear wave velocity and stiffness in confined compression of 9F1 sand. See figure A.16 for details.

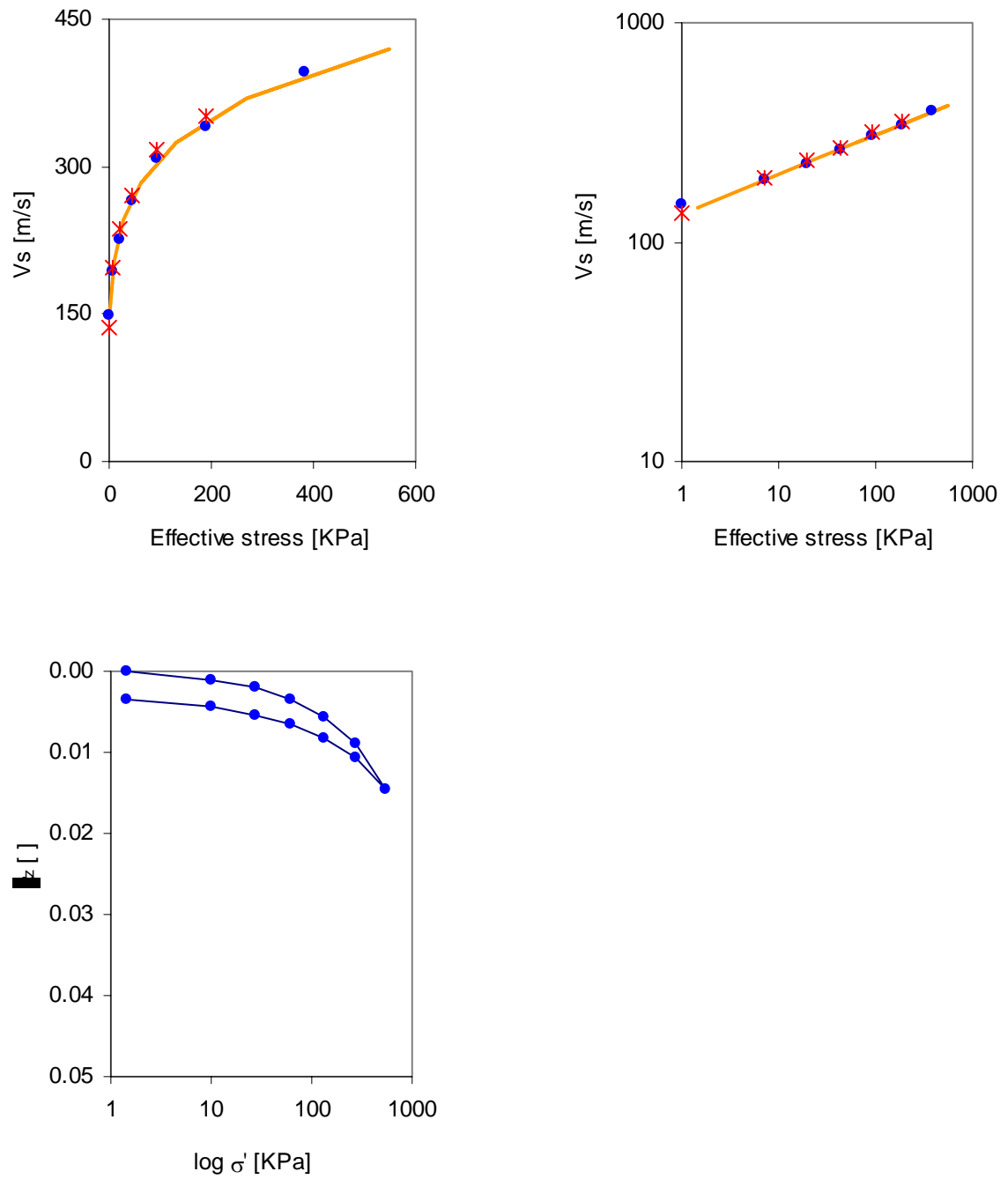


Figure A.25 Shear wave velocity and stiffness in confined compression of Jekyll Island sand. See figure A.16 for details.

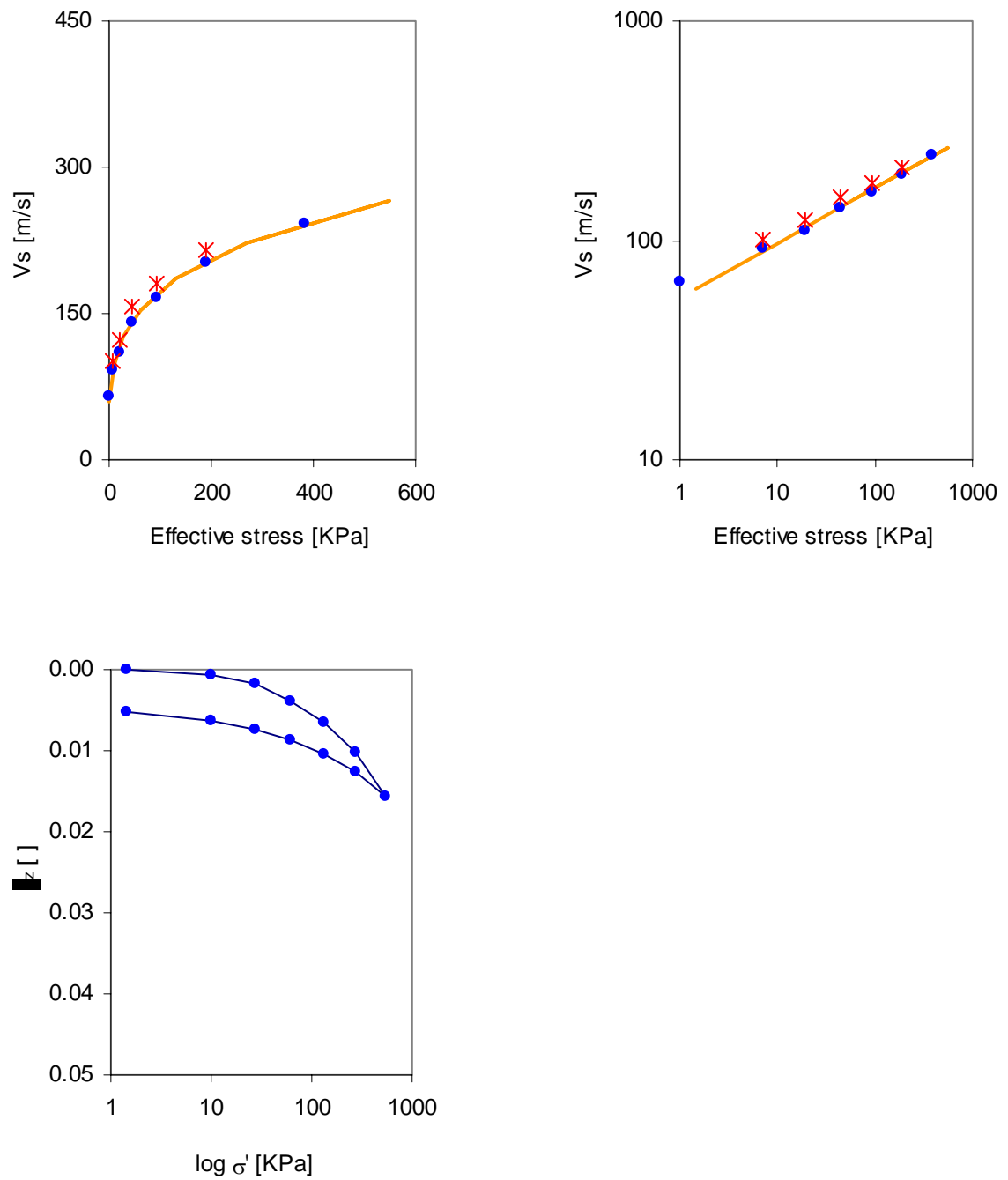


Figure A.26 Shear wave velocity and stiffness in confined compression of Nevada sand. See figure A.16 for details.

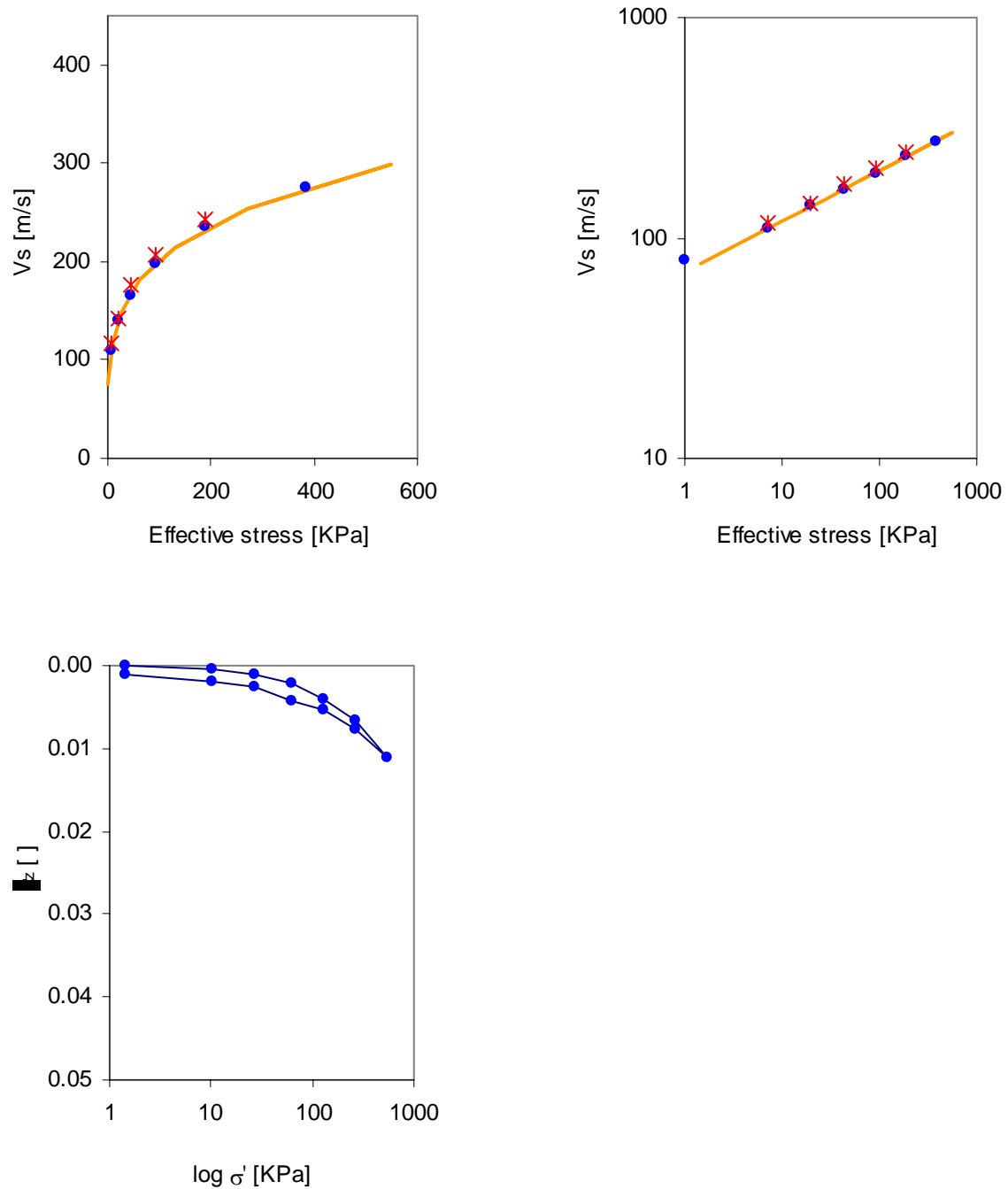


Figure A.27 Shear wave velocity and stiffness in confined compression of Ottawa sand. See figure A.16 for details.

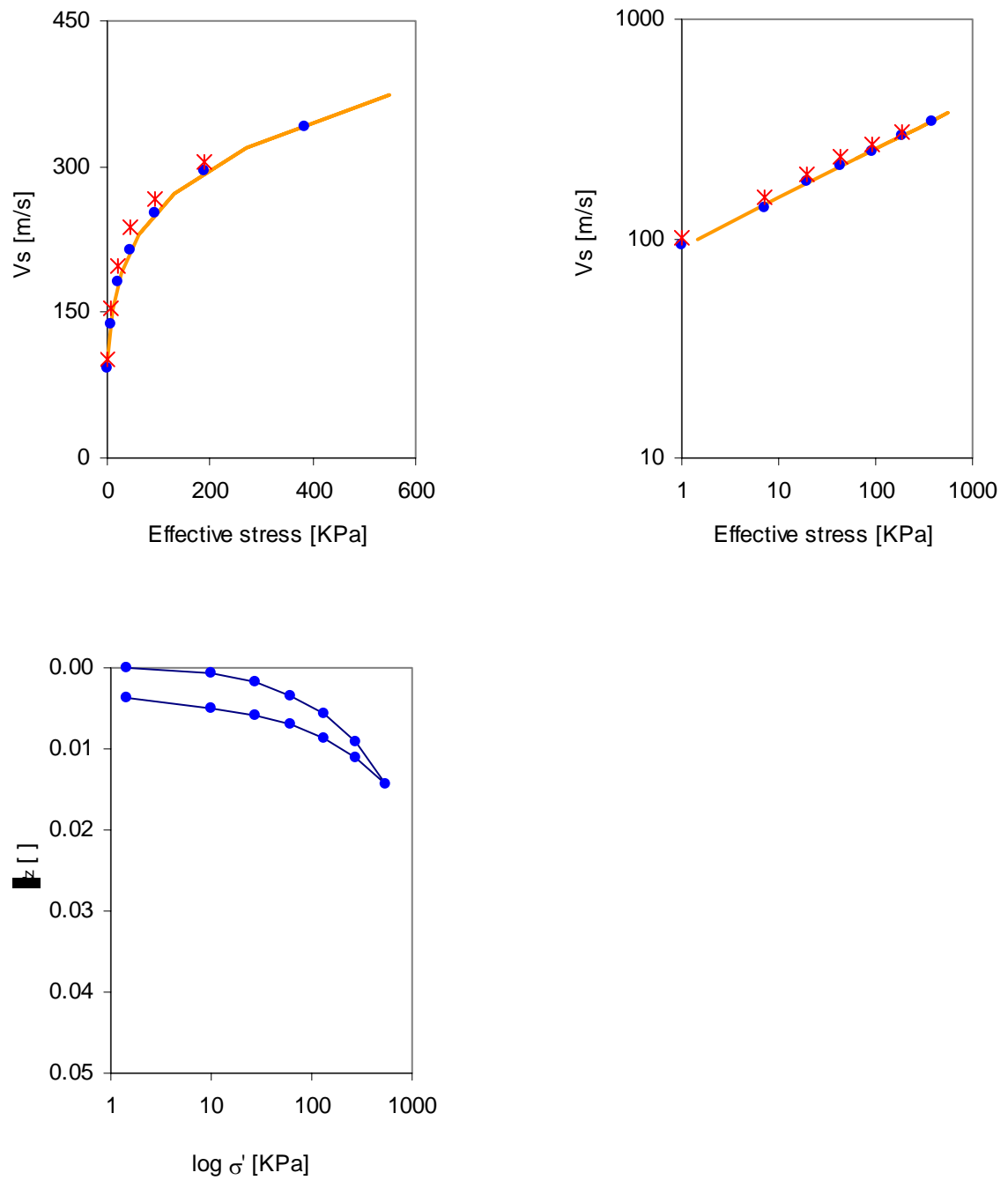


Figure A.28 Shear wave velocity and stiffness in confined compression of Margaret River sand. See figure A.16 for details.

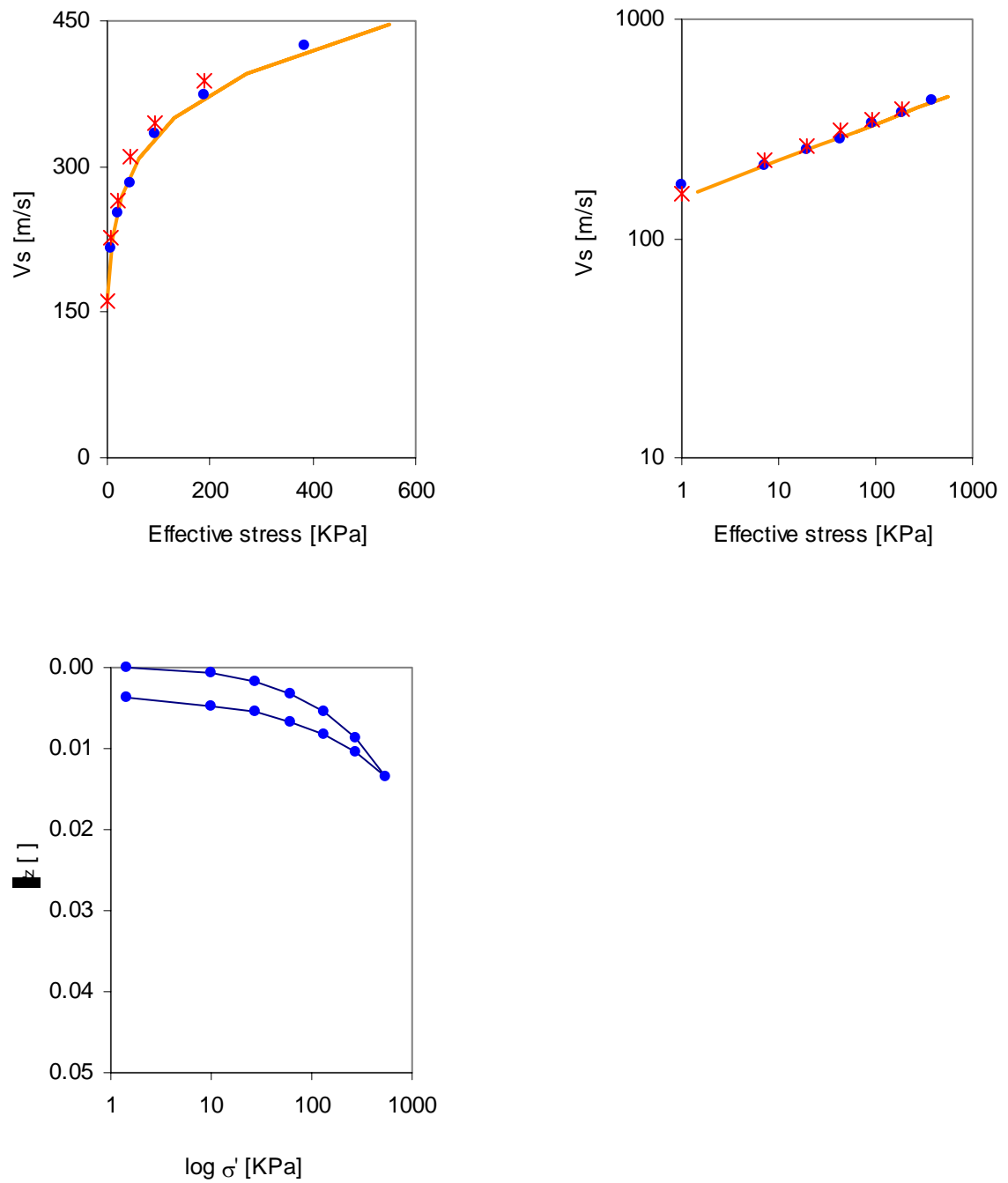


Figure A.29 Shear wave velocity and stiffness in confined compression of Ponte Vedra sand. See figure A.16 for details.

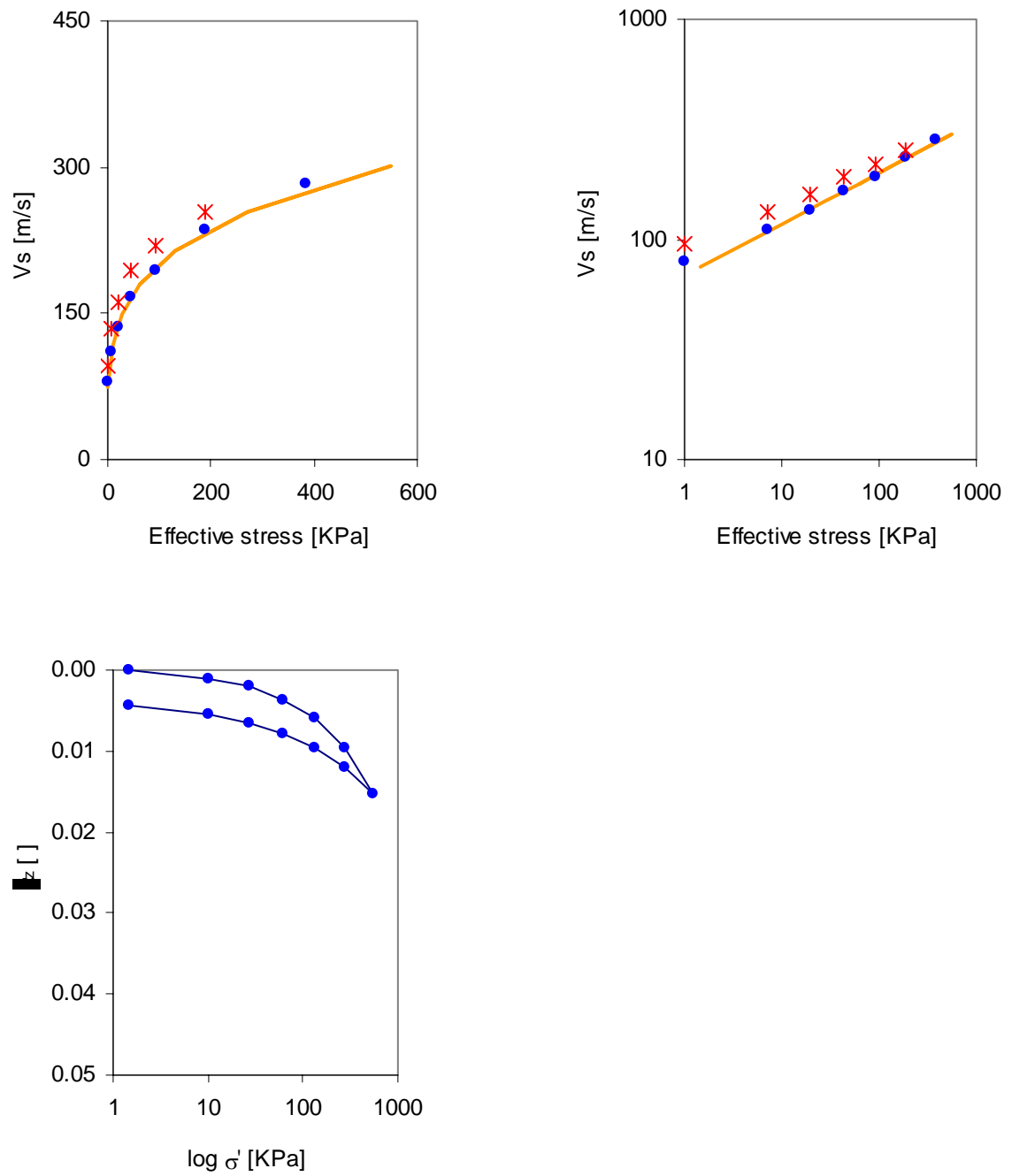


Figure A.30 Shear wave velocity and stiffness in confined compression of Ticino sand. See figure A.16 for details.

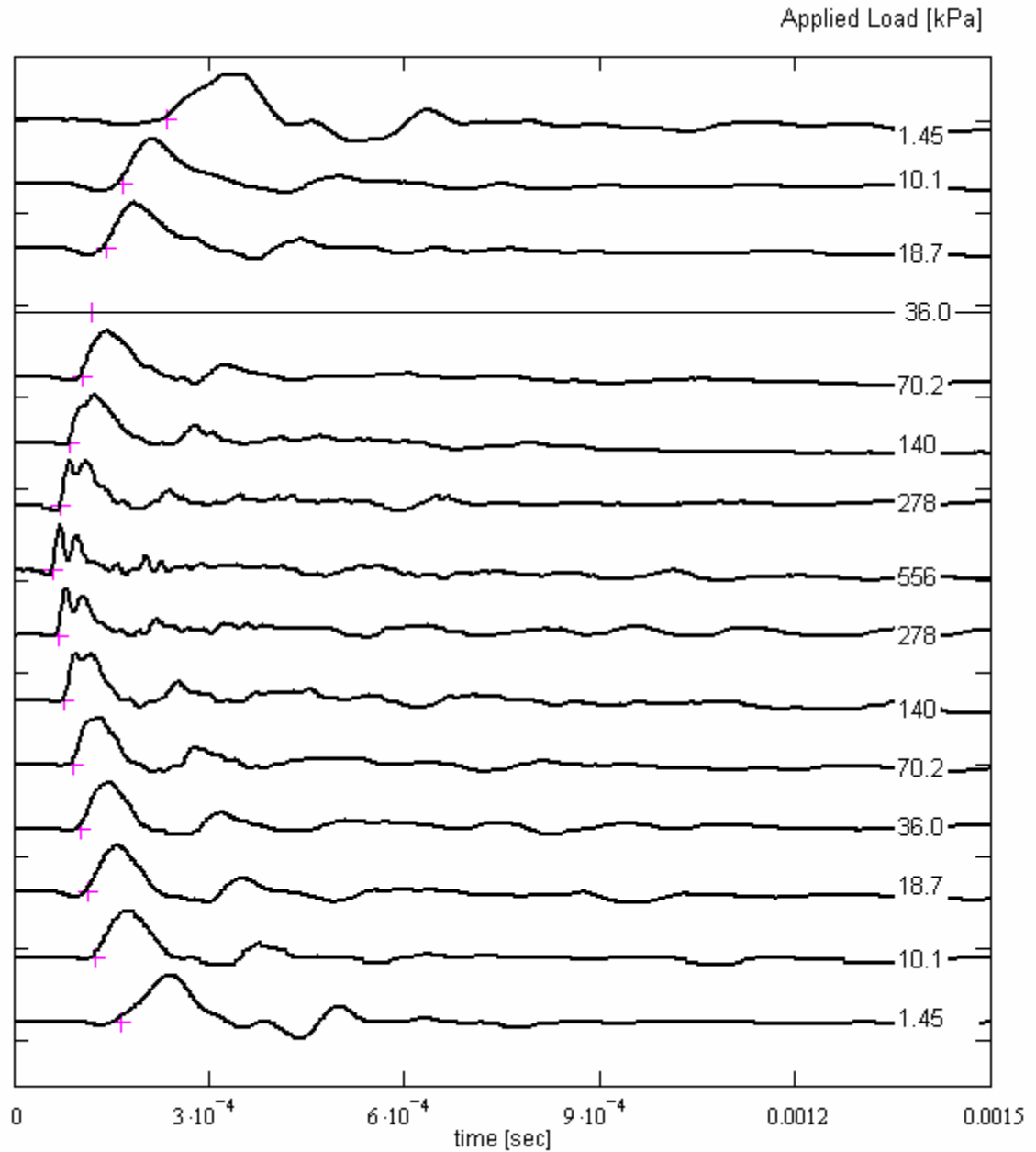


Figure A.31 Shear wave amplitude as a function of time for Ottawa 70-80 sand. The output signal is normalized to the maximum signal amplitude. Step function signals are generated with a Krohn-Hite model 1400 A signal generator at 20 Hz and variable amplitude. Output signals are band pass filtered (100 Hz to 50 kHz) and amplified (input gain 20 output gain 0) using a Krohn-Hite model 3944 amplifier-filter. Signals are collected using a Rapid-Systems digital oscilloscope. Stresses displayed represent the applied vertical stress.

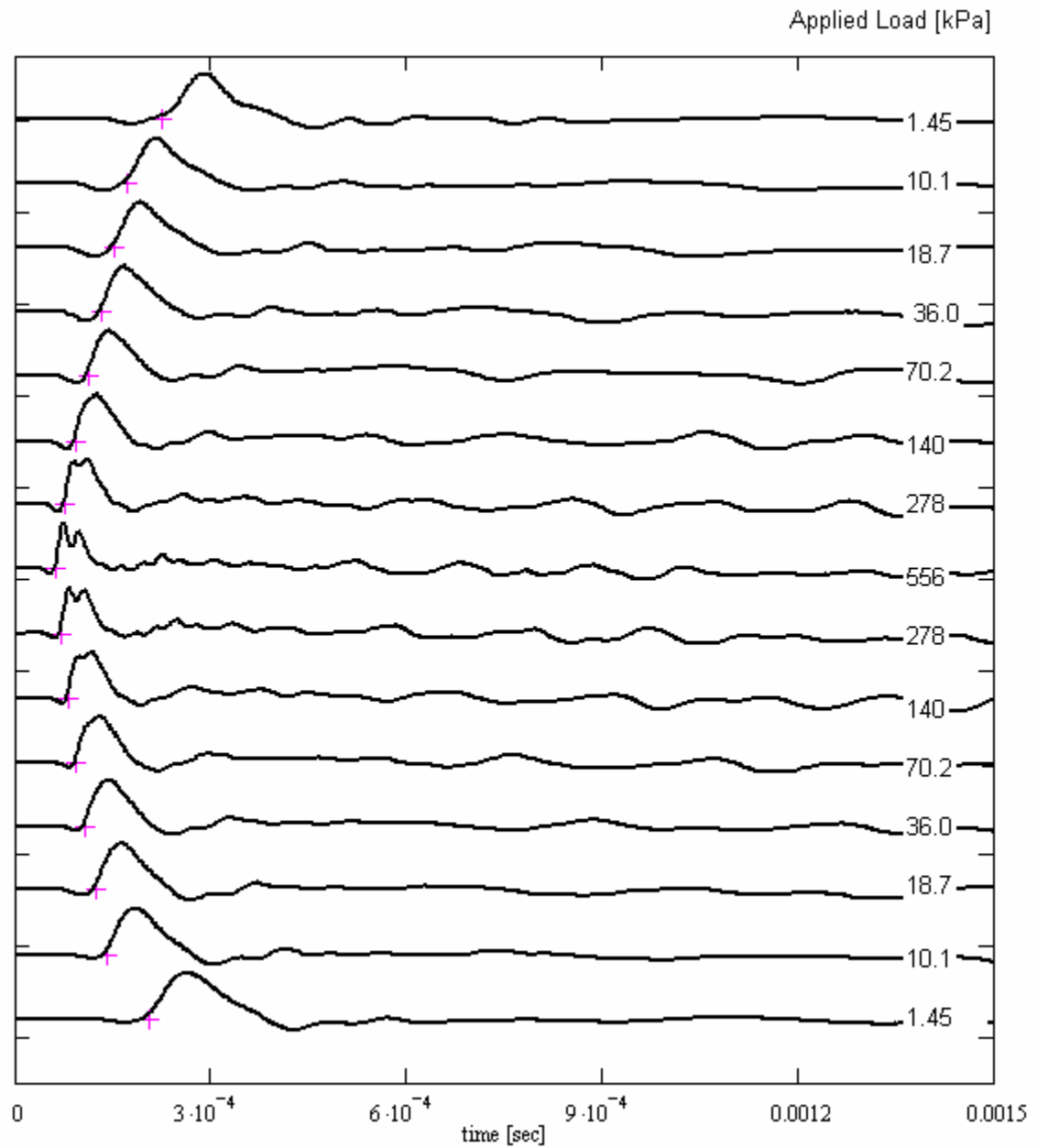


Figure A.32 Shear wave amplitude as a function of time for a 90% sand 10% rubber by volume mixture. See figure A.31 for details.

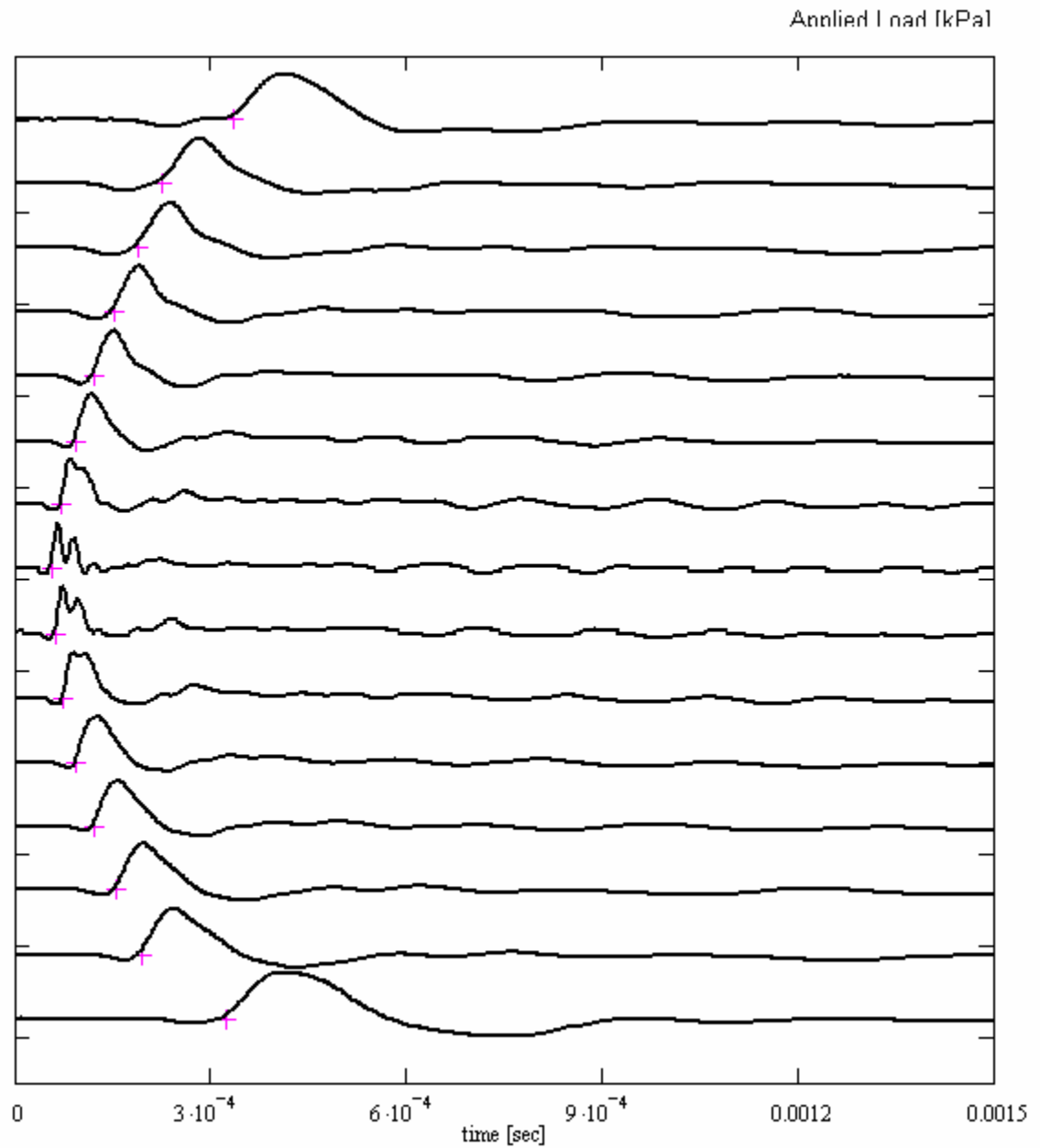


Figure A.33 Shear wave amplitude as a function of time for a 80% sand 20% rubber by volume mixture. See figure A.31 for details.

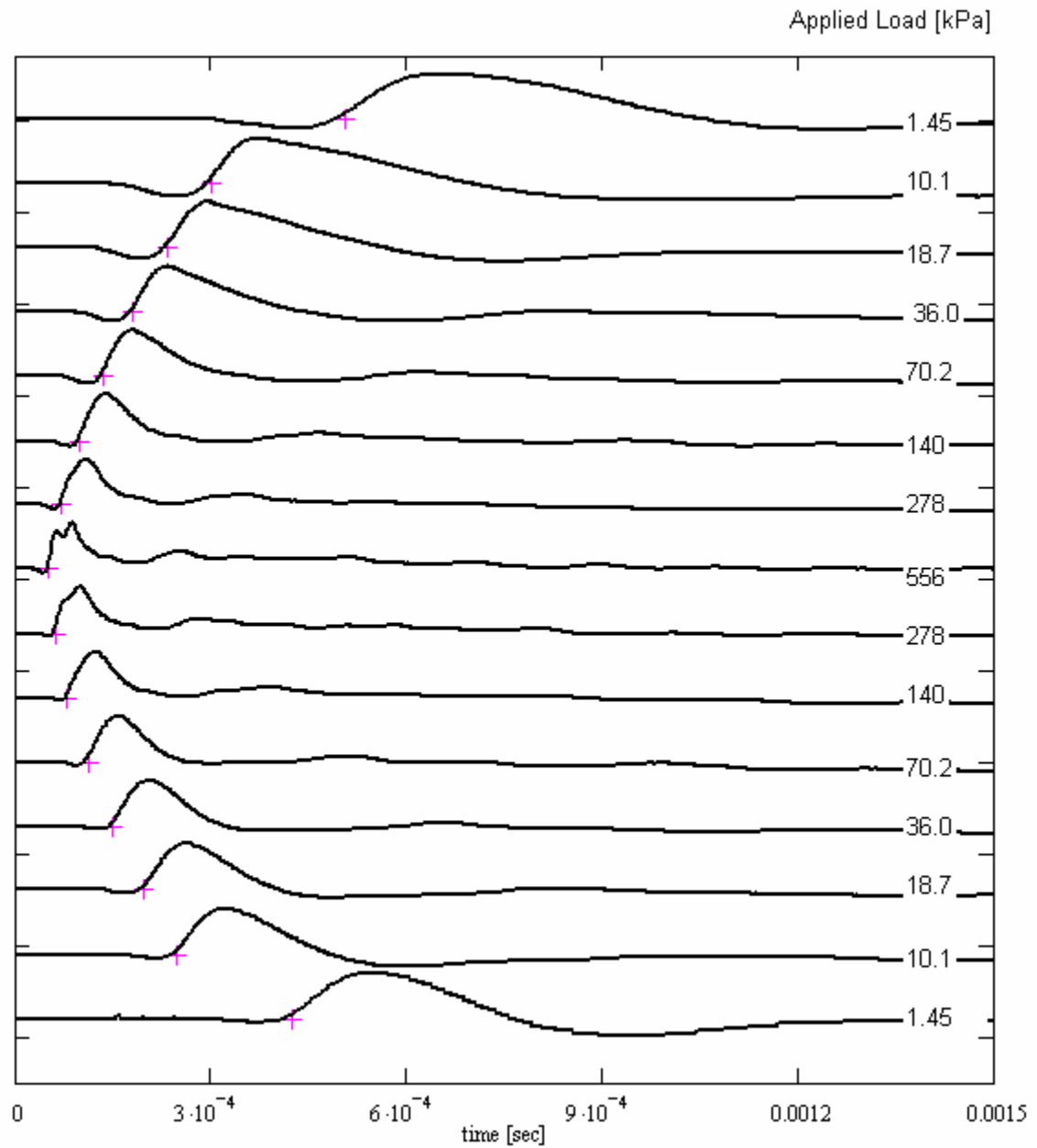


Figure A.34 Shear wave amplitude as a function of time for a 70% sand 30% rubber by volume mixture. See figure A.31 for details.

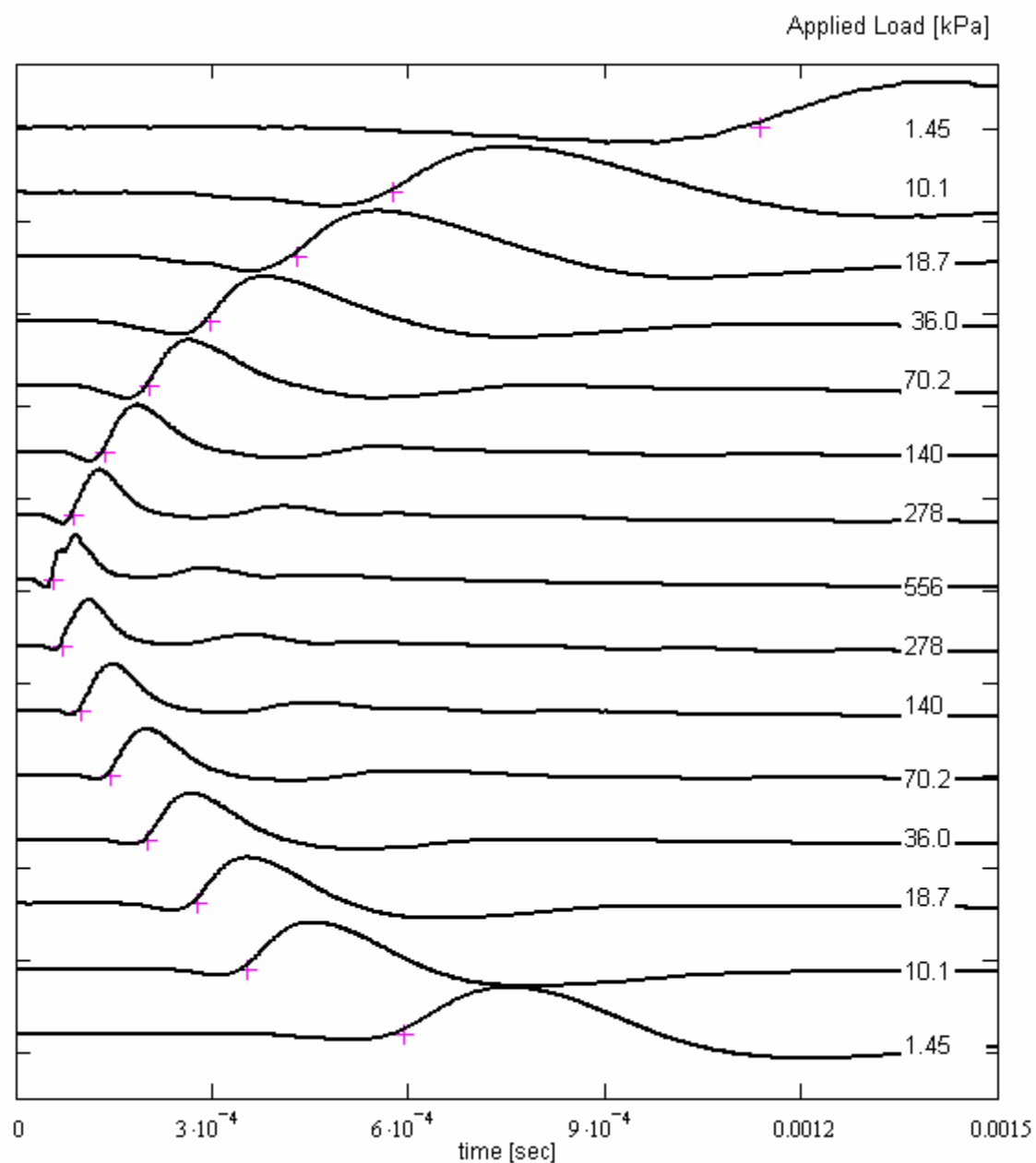


Figure A.35 Shear wave amplitude as a function of time for a 60% sand 40% rubber by volume mixture. See figure A.31 for details.

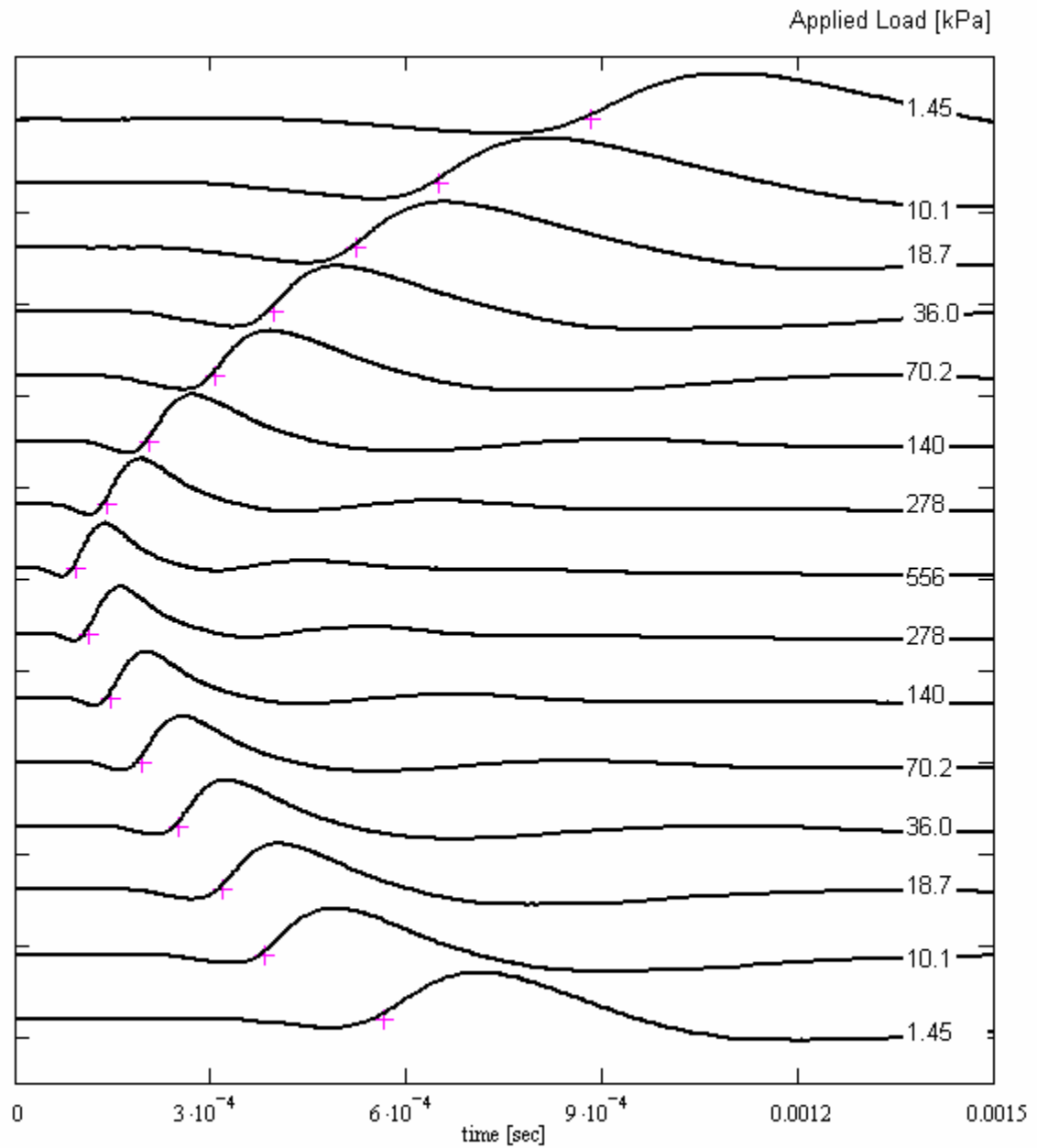


Figure A.36 Shear wave amplitude as a function of time for a 40% sand 60% rubber by volume mixture. See figure A.31 for details.

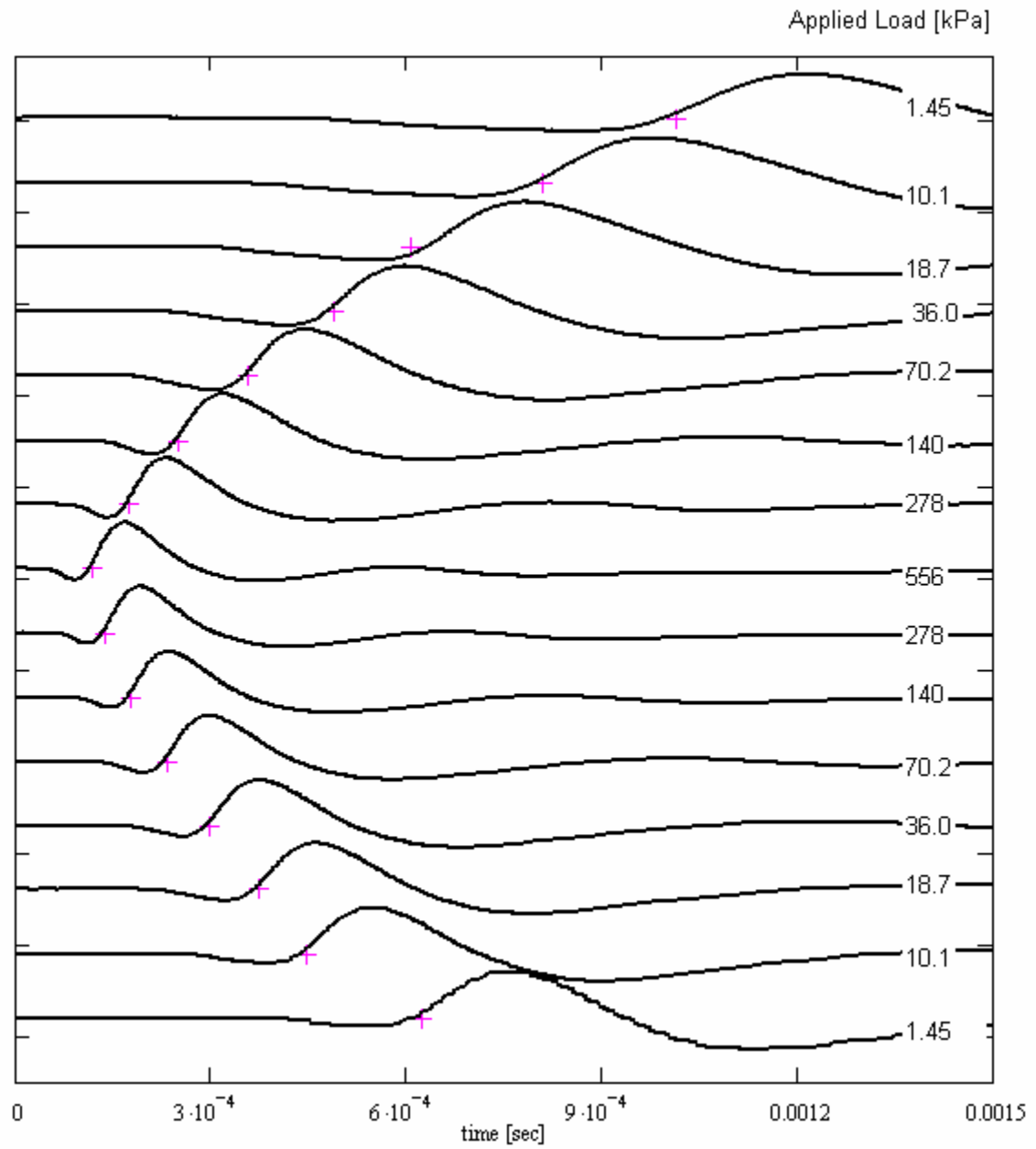


Figure A.37 Shear wave amplitude as a function of time for a 20% sand 80% rubber by volume mixture. See figure A.31 for details.

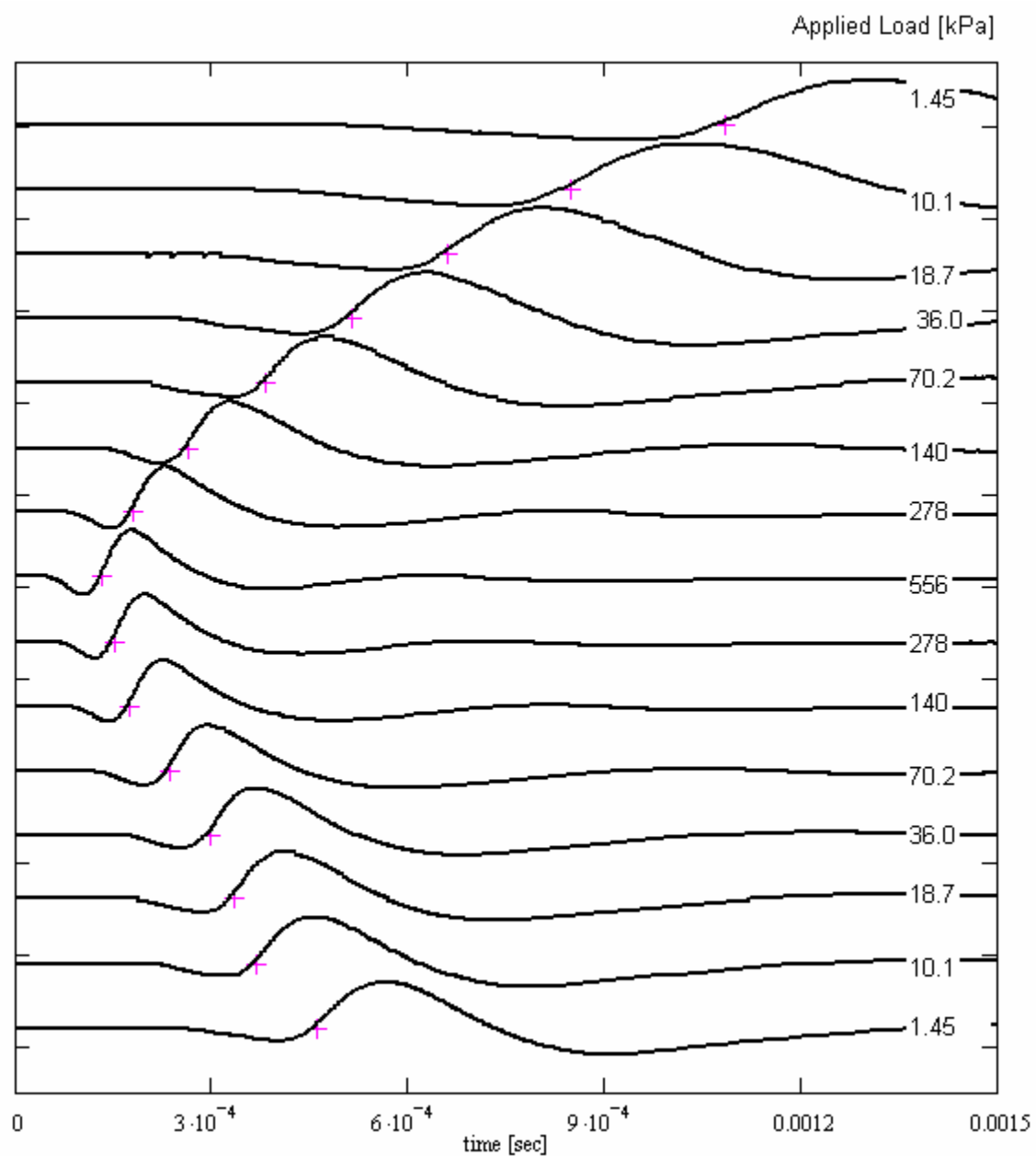


Figure A.38 Shear wave amplitude as a function of time for rubber particles. See figure A.31 for details.

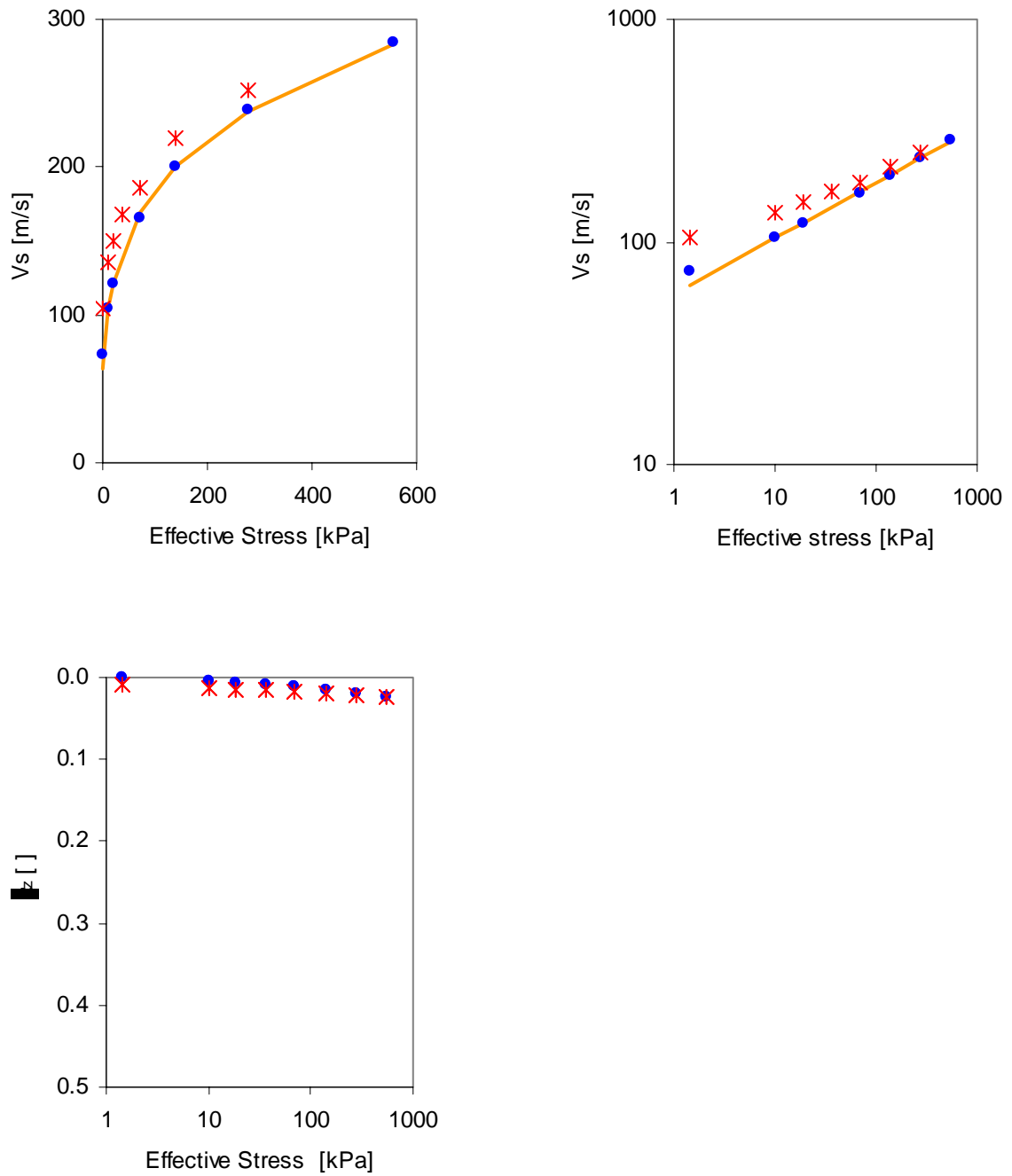


Figure A.39 Shear wave velocity and stiffness in confined compression of Ottawa 70-80 sand. Shear wave velocity and stiffness values are determined simultaneously using an oedometer cell equipped with bender elements. Input is a step function at 20 Hz. Time between load increments is 10 minutes. Mean particle diameters of sand grains and rubber particles are roughly 0.36 and 0.09 mm.

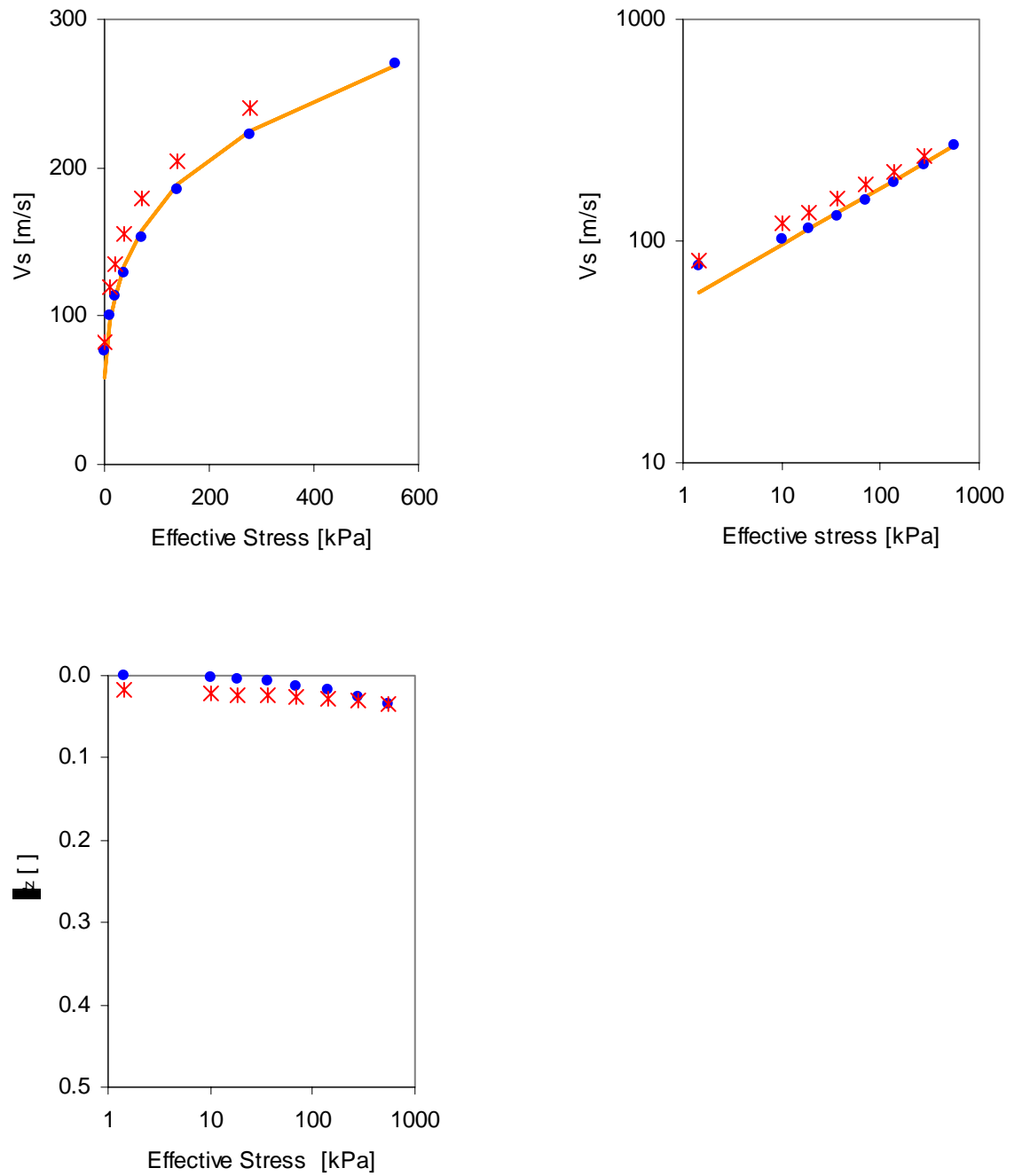


Figure A.40 Shear wave velocity and stiffness in confined compression of a 90% sand 10% rubber by volume mixture. See figure A.39 for details.

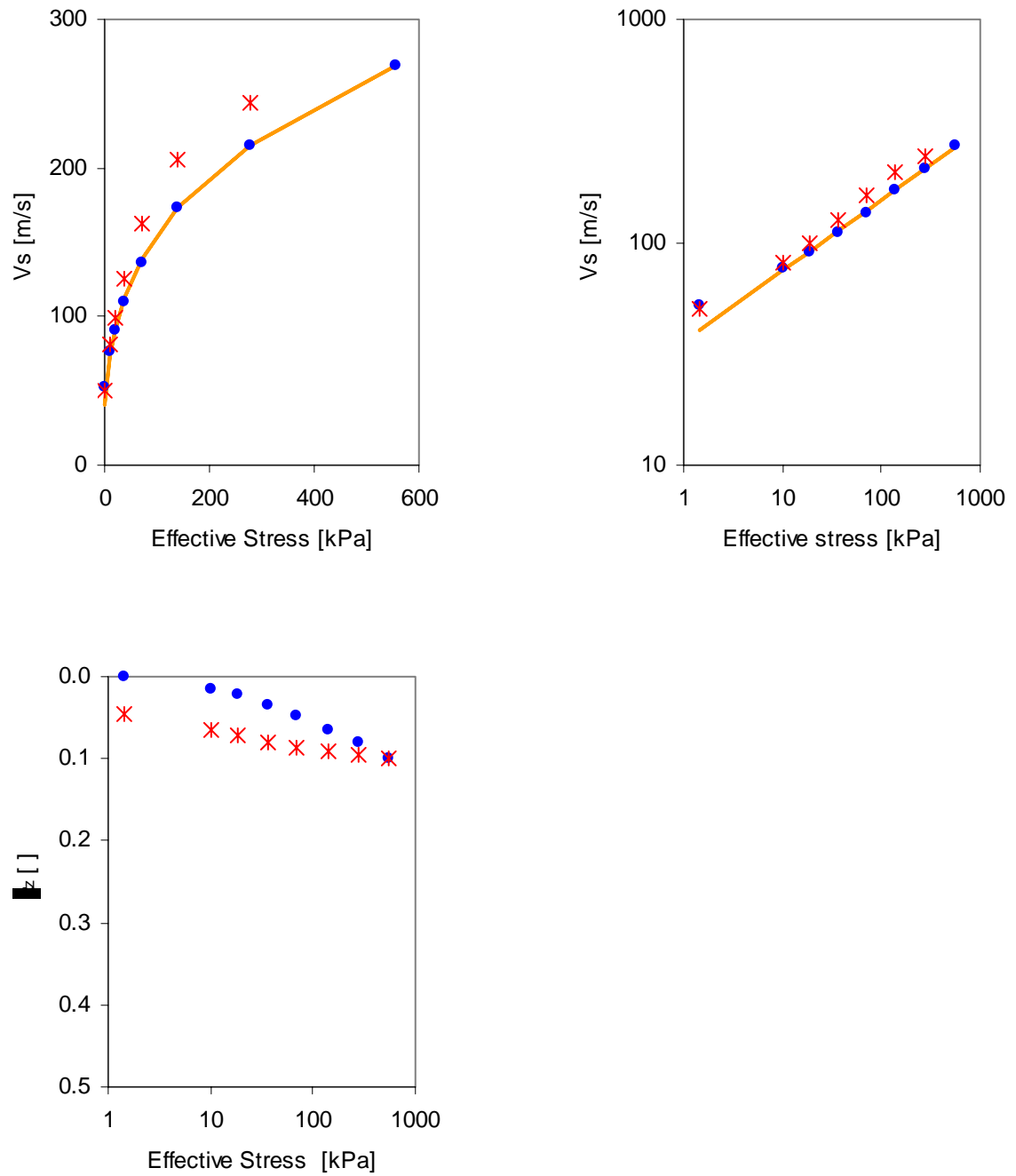


Figure A.41 Shear wave velocity and stiffness in confined compression of a 80% sand 20% rubber by volume mixture. See figure A.39 for details.

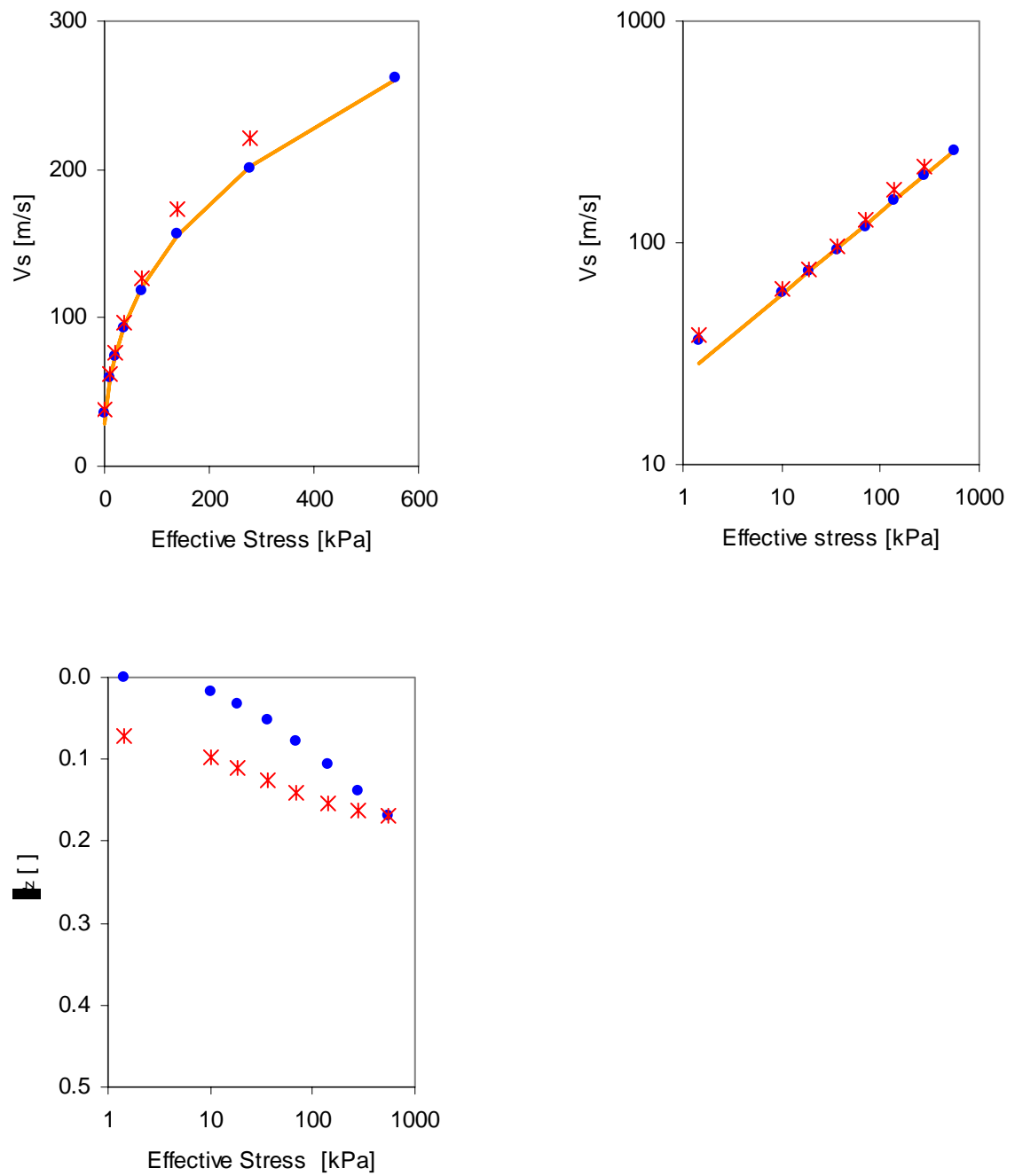


Figure A.42 Shear wave velocity and stiffness in confined compression of a 70% sand 30% rubber by volume mixture. See figure A.39 for details.

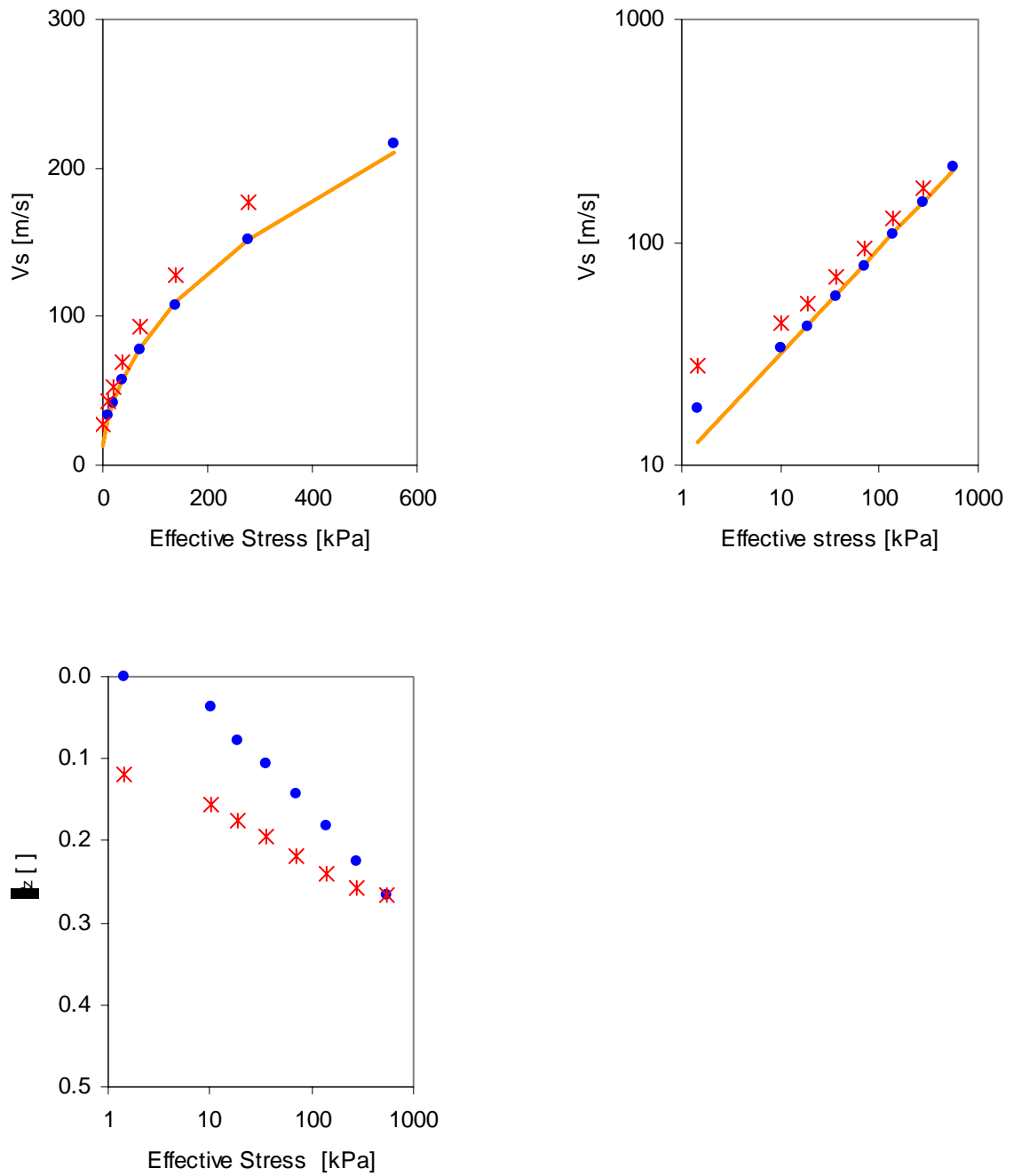


Figure A.43 Shear wave velocity and stiffness in confined compression of a 60% sand 40% rubber by volume mixture. See figure A.39 for details.

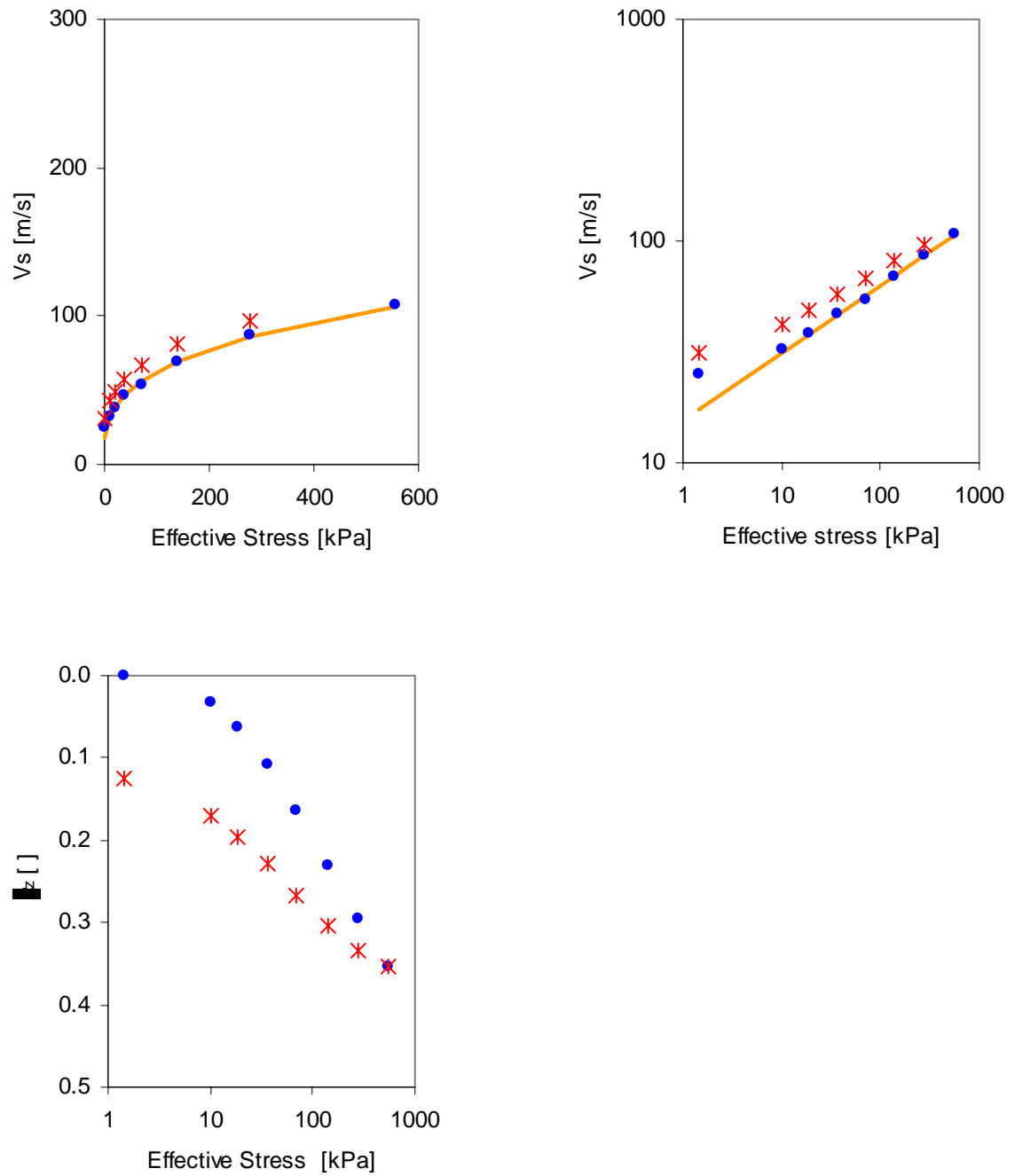


Figure A.44 Shear wave velocity and stiffness in confined compression of a 40% sand 60% rubber by volume mixture. See figure A.39 for details.

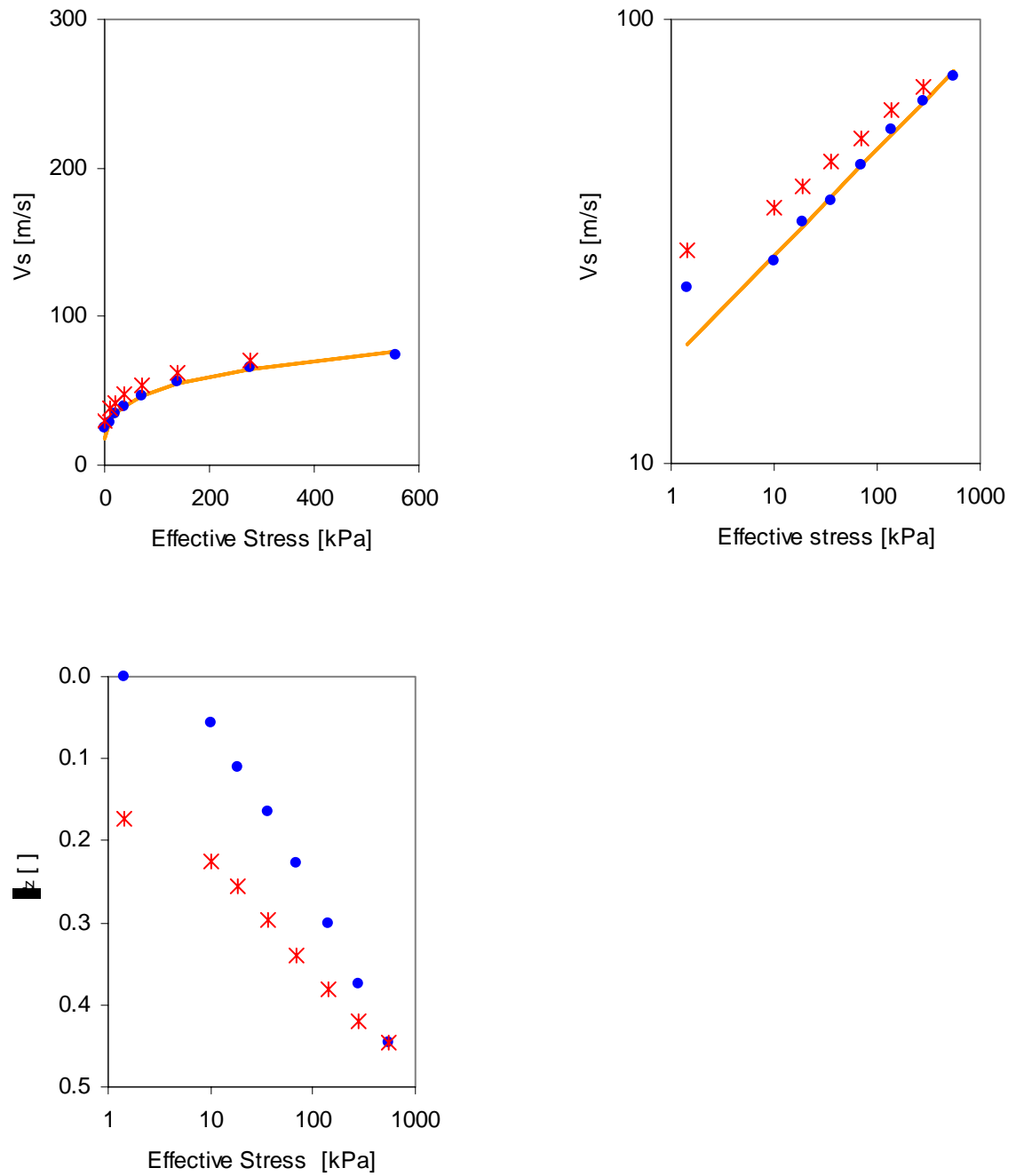


Figure A.45 Shear wave velocity and stiffness in confined compression of a 20% sand 80% rubber by volume mixture. See figure A.39 for details.

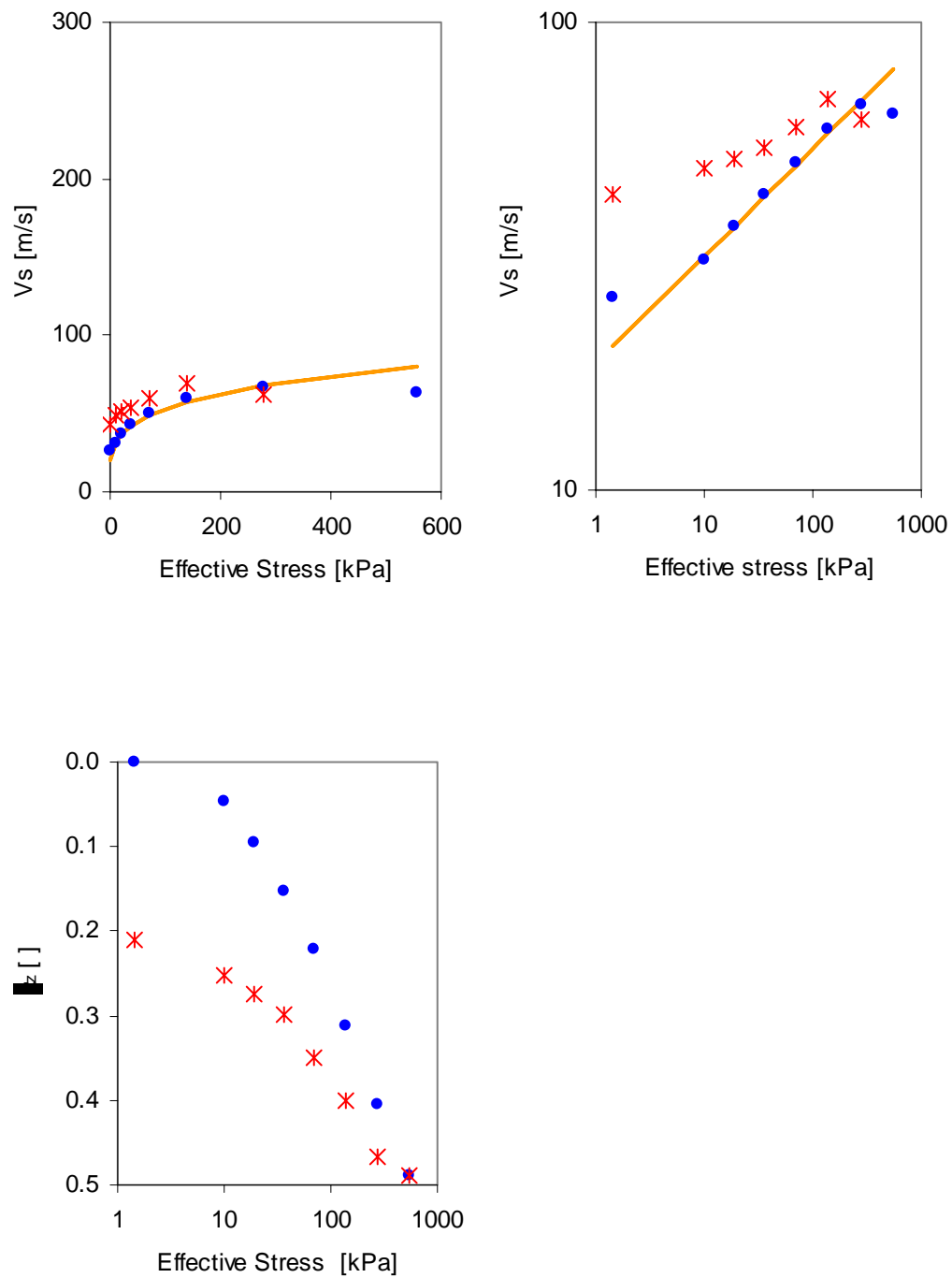


Figure A.46 Shear wave velocity and stiffness in confined compression of rubber particles. See figure A.39 for details.

REFERENCES

- Abou-Chakra, H. and Tüzün, U. (1999), Coefficient of friction of binary granular mixtures in contact with a smooth wall, *Chemical Engineering Science*, vol. 54, pp. 5901-5912.
- Ahmed, I. (1993), Laboratory study on the properties of rubber-soils, Report No. FHWA/IN/JHRP-93/4, Purdue University, West Lafayette, Indiana, 347 pages.
- Alford, N. and Poole, A. (1979), Effect of shape and surface texture on the fracture toughness of mortars, *Cement and Concrete Research*, vol. 9, no. 5, pp. 583-589.
- Alshibli, K. A. and Sture, S. (2000), Shear band formation in plane strain experiments of sand, *Journal of Geotechnical and Geoenvironmental Engineering*, vol.126, no. 6, pp. 495-503.
- Archard, J. F. (1957), Elastic deformation and the laws of friction, *Proceedings of the Royal Society of London A*, vol. 243, no. 1233, pp. 190-205.
- Bardet, J. P. (1994), Observations on the effects of particle rotations on the failure of idealized granular materials, *Mechanics of Materials*, vol. 18 n 2, pp. 159-182.
- Barrett, P. J. (1980), The shape of rock particles, a critical review, *Sedimentology*, vol. 27, no. 3, pp. 291-303.
- Baxter, G. W. and Behringer, R. P. (1989), Pattern formation in flowing sand, *Physical review letters*, vol. 62, no. 24, pp. 2825 – 2829.
- Beatty, J. R. (1980), Physical properties of rubber compounds, Chapter 10, *Mechanics of Pneumatic Tires*, USDOT, 930 pages.
- Bergman, D. J. (2002), Exact relations between critical exponents for elastic stiffness and electrical conductivity, *Physical Review E*, 65, pp. 026124-026131.
- Bonavetti, V. L. and Irassar, E. F. (1994), The effect of stone dust content in sand, *Cement and Concrete Research*, vol. 24, no. 3, pp. 580-590.
- Bowman, E. T., Soga, K. and Drummond, W. (2001), Particle shape characterization using fourier descriptor analysis, *Geotechnique*, vol. 51, no. 6, pp. 545-554.
- Cecich, V., Gonzales, L., Hoisaeter, A., Williams, J. and Reddy, K. (1996) Use of shredded tires as lightweight backfill material for retaining structures, *Waste Management & Research*, vol. 14, no. 5, pp. 433-451.
- Chan, C. Y. and Page, W. P. (1997), Particle fractal and load effects on internal friction in powders, *Powder Technology*, vol. 90, pp. 259-266.
- Chiaia, C. (2002), On the sliding instabilities at rough surfaces, *Journal of the Mechanics and Physics of Solids*, vol. 50, no. 4, pp. 895-924.
- Cho, G. C. (2001), Saturation effects and post-liquefaction shear strength, Ph.D. Thesis, Georgia Institute of Technology, 294 pages.
- Cho, G.C. and Santamarina, J.C. (2003), Microscale particle characteristics and soil index properties, Available from the authors, pp. 1-13.

Cooke, M. H., Stephens, D. J. and Bridgwater, J. (1976), Powder Mixing – A Literature Review, *Powder Technology*, vol. 15, no. 1, pp 1-20.

De Larrard, F., Belloc, A., Renwez, and Boulay, C. (1994), Is the cube test suitable for high performance concrete, *Materials and Structures* vol. 27, no. 174, pp 580-583.

Donald, M. B. and Roseman, B. (1962), Mechanisms in a horizontal drum mixer, *British Chemical Engineering*, vol. 7, pp. 749-753.

Duran, J. (2000), *Sands, Powders and Grains*, Springer, New York, 214 pages.

Feng, S. (1985), Percolation properties of granular elastic networks in two dimensions, *Physical Review B*, vol. 32, no. 1, pp. 510-513.

Feng, Z. Y. and Sutter, K. G. (2000), Dynamic properties of granulated rubber sand mixtures, *Geotechnical Testing Journal*, vol. 23, no. 3, pp. 338-344.

Frye, K. M. and Marone, C. (2002), The effect of particle dimensionality on granular friction in laboratory shear zones, *Geophysical Research Letters*, vol. 29, no. 19, pp. 22-1 – 22-4.

Folk, R. L. (1955), Student operator error in determination of roundness, sphericity and grain size, *Journal of Sedimentary Petrology*, vol. 25, no. 4, pp. 297-301.

Forsyth, A. J., Hutton, S. R., Rhodes, M. J. and Osborne, C. F. (2001), Effect of applied interparticle force on the static and dynamic angles of repose of spherical granular material, *Physical Review E*, vol. 63, no. 3, pp. 0313021-0313025.

Furuuchi, M. and Gotoh K. (1992) Shape separation of particles, *Powder Technology*, vol. 73, no. 1, pp 1-9.

Garboczi, E. J. (2002), Three-dimensional mathematical analysis of particle shape using x-ray tomography and spherical harmonics: Application to aggregates used in concrete, *Cement and Concrete Research*, vol. 32, no.10, pp. 1621-1638.

Geng J., Howell D., Longhi E., Behringer R., Reydellet G., Vanel L., Clement E. and Luding S. (2001) Footprints in the sand: The reponse of a granular material to perturbations, *Physical Review Letters*, vol. 87, no. 3, pp. 355061-355064.

Gray, W. A. (1968), *The Packing of Solid Particles*, Chapman and Hall, London, 134 pages.

Guimaraes, M. (2002) Crushed stone fines and ion removal from clay slurries, Ph.D. Thesis, Georgia Institute of Technology, pp. 52-82.

Guyon, E., Oger, L. and Plona T. J. (1987) Transport properties in sintered porous media composed of two particle sizes, *Journal of Applied Physics D: Applied Physics*, vol. 20, no. 12, pp. 1637-1644.

Hawkins, A. E. (1993), *The shape of powder particle outlines*, John Wiley and Sons, New York, 150 pages.

Hyslip, J. P. and Vallejo, L. E. (1997), Fractal analysis of the roughness and size distribution of granular materials, *Engineering Geology*, vol. 48, no. 3-4, pp. 231-244.

Jaeger, H. M. Liu, C. and Nagel S. (1989), Relaxation at the angle of repose, *Physical Review Letters*, 62, pp. 40-43.

- Kezdi, A. (1980), *Handbook of Soil Mechanics, Volume 2, Soil Testing*, Elsevier, New York, 258 pages.
- Khosropour, R., Valachovic, E. and Lincoln, B. (2000), Flow and pattern formation in a binary mixture of rotating granular materials, *Physical Review E*, vol. 62, no.1, pp. 807-812.
- Klotz, E. U. and Coop, M. R. (2002), On the identification of critical state lines for sands, *Geotechnical Testing Journal*, vol. 25, no. 3, pp. 289 – 302.
- Kronlof, A. (1994), Effect of very fine aggregate on concrete strength, *Materials and Structures*, vol 27, no. 165, pp. 15-25.
- Krumbein, W. C., and Sloss, L. L. (1963), *Stratigraphy and Sedimentation*, Second Edition, W. H. Freeman and Company, San Francisco, 660 pages.
- Kuenen, H. (1960), Experimental abrasion 4: eolian action, *Journal of Geology*, vol. 68 no. 4, pp. 427-428.
- Lambe, T. W. and Whitman, R. V. (1969), *Soil Mechanics*, John Wiley and Sons, New York, 553 pages.
- Lee, J. H., Salgado R., Bernal, A. and Lovell, C. W. (1999), Shredded tires and rubber-sand as lightweight backfill, *Journal of Geotechnical and Geoenvironmental Engineering*, vol. 125, no.2, pp. 132-141.
- Liu H.S., Mead J. L., and Stacer R. G. (2000), Environmental effects of recycled rubber in light-fill applications, *Rubber Chemistry and Technology*, vol. 73, no. 3, pp. 551-564.
- Mair, K., Frye, K. M. and Maronez, C. (2002), Influence of grain characteristics on the friction of granular shear zones, *Journal of Geophysical Research*, vol. 107 no. B10, pp. 4-1 - 4-9.
- Margolis, S.V. and Krinsley, D.H. (1974), Processes of formation and environmental occurrence of microfeatures on dentrital quartz grains, *American Journal of Science.*, vol. 274, pp. 449-465.
- Masad, E., Taha, R., Ho, C. and Papagionnakis, T. (1996), Engineering properties of tire/soil mixtures as a lightweight fill material, *Geotechnical Testing Journal*, vol. 19, No. 3, pp 297-304.
- McLane, M. (1995), *Sedimentology*, Oxford University Press, New York, NY, 423 pages.
- Mehta, P. K. and Monteiro, P. J. M. (1993), *Concrete Microstructure, Properties and Materials*, Second Edition, McGraw-Hill, New York, 548 pages.
- Mirghasemi, A. A., Rothenburg, L. and Matyas, E. L. (2002), Influence of particle shape on engineering properties of two-dimensional polygon-shaped particles, *Geotechnique*, vol. 52., no. 3, pp. 209-217.
- Mitchell, J. K. (1993), *Fundamentals of soil behavior*, Second Edition, John Wiley & Sons, New York, 437 pages.
- Muller-Vonmoos, M. and Loken, T. (1989), The shearing behavior of clays, *Applied Clay Science*, vol. 4, pp. 125-141.
- Nabarro, F. R. N. (1940), The strains produced by precipitation in alloys, *Proceedings of the Royal Society of London A*, vol. 175, no. 963, pp. 519-538.
- Narsilio, G. A. (2003), Personal Communication.

- Nagasawa, N and Miyazaki, S. (1975), Mineralogical properties of halloysite as related to its genesis, *Proceedings of the International Clay Conference*, vol.1, Wilmette, pp. 257-265.
- Oda, M. (1977), Coordination number and its relation to shear strength of granular materials, *Soils and Foundations*, vol.17, pp. 29-42.
- Oda, M. (1999) Internal friction of granular soil, *Mechanics of Granular Materials*, Eds. M. Oda and K. Iwashita, Balkema, Rotterdam, pp. 276-283.
- Olsen, James L. and Edward G. Rippie, (1964) *J. Pharmaceutical Sci.* 53, 147.
- Powers, M. C. (1953), A new roundness scale for sedimentary particles, *Journal of Sedimentary Petrology*, vol. 23, no. 2, pp. 117-119.
- Pettijohn, F. J., Potter, E. P. and Siever, R. S. (1972), *Sand and Sandstone*, Springer-Verlag, Berlin, 618 pages.
- Robinson, D. A. and Friedman, S. P. (2002), Observations of the effects of particle shape and size distribution on the avalanching of granular materials *Physica A*, vol. 311, no. 1-2, pp. 97-110.
- Rothenburg, L. and Bathurst, R. J. (1993), Influence of particle eccentricity on micromechanical behavior of granular materials, *Mechanics of Materials*, vol. 16, no. 1-2, pp. 141-152.
- Sacks, M. D. (2003), Characterization of the State of Dispersion, Fine Particle Technology Course Notes.
- Salgado, R., Bandini, P. and Karim, A. (2000), Shear strength and stiffness of silty sand, *Journal of Geotechnical and Geoenvironmental Engineering*, vol. 126, no. 5, pp. 451-462.
- Santamarina, J. C. (2001) Soil Behavior at the Microscale: Particle Forces, *Proc. Symp. Soil Behavior and Soft Ground Construction, in honor of Charles C. Ladd*, pp. 1-32.
- Santamarina, J. C. and Aloufi, M. (1999), Small strain stiffness: A micromechanical experimental study, *Proceedings of the Pre-failure Deformation Characteristics of Geomaterials*, IST99, Ed. by M Jamiolkowski, R. Lancellotta and D. Lo Presti, Torino, Italy, pp. 438-451.
- Santamarina, C. and Cascante, G. (1998), Effect of surface roughness on wave propagation parameters, *Geotechnique*, vol. 48, no. 1, pp. 129-136.
- Santamarina, J. C. and Cascante, G. (1996), Stress anisotropy and wave propagation – A micromechanical view, *Canadian Geotechnical Journal*, vol. 33, no. 5, pp. 770-782.
- Santamarina, J. C. and Cho, G. C. (2001), Determination of critical state parameters in sandy soils – simple procedure *ASTM Geotechnical Testing Journal*, vol. 24, no. 2, pp. 185-192.
- Santamarina, J. C., Klein, K. A., Wang, Y. H. and Prenke, E. (2002), Specific surface: determination and relevance, *Canadian Geotechnical Journal*, vol. 39, no. 1, pp. 233-241.
- Santamarina, J. C., Klein, K. A. and Fam M. A. (2001), *Soils and Waves*, Wiley, West Sussex, 488 pages.
- Shinohara, K., Oida, M. and Golman B. (2000), Effect of particle shape on angle of internal friction by triaxial compression test, *Powder Technology*, vol.107, no. 1, pp. 131-136.
- Smalley, J. J. (1966), Formation of quartz sand, *Nature*, vol. 211, pp. 476-479.

- Sukumaran, B. and Ashmawy, A. K. (2001), Quantitative characterization of the geometry of discrete particles, *Geotechnique*, vol. 51, no. 76, pp. 19-627.
- Tadmor, R. (2001), The London-van der Waals attraction energies between objects of various geometries, *Journal of Physics: Condensed Matter*, vol. 13, no. 9, pp. 195-202.
- Taylor, D. W. (1948), *Fundamentals of Soil Mechanics*, John Wiley and Sons, New York, 699 pages.
- Tobita, Y. and Oda, M. (1999), Friction based deformation and strength behaviors of granular soils, *Mechanics of Granular Materials*, Eds. M. Oda and K. Iwashita, Balkema, Rotterdam, pp. 50-55.
- USGS (2001), Minerals Yearbook volume II – Area Reports: Domestic, The Mineral Industry of Georgia, USGS Minerals Information Center, Reston, Va, 6 pages.
- Villarruel, F. X., Lauderdale, B. E., Mueth, D. E. and Jaeger, H. M. (2000), Compaction of rods: relaxation and ordering in vibrated, anisotropic granular material, *Physical Review E*, vol. 61, no. 6, pp. 6914-6921.
- Wadell, H. (1932), Volume, Shape, and Roundness of Rock Particles, *Journal of Geology*, vol. 40, pp. 443–451.
- Wadell H. (1933), Sphericity and Roundness of Rock Particles, *Journal of Geology*, vol. 41, pp. 310–331.
- Weaver, C. E. (1989), *Clays, Muds, and Shales*, Elsevier, New York, 819 pages.
- Yimsiri, S., and Soga, K. (2000), Micromechanics-based stress-strain behaviour of soils at small strains, *Geotechnique*, vol. 50, no. 5, pp. 559-571.
- Youd, T. L. (1973), Factors controlling maximum and minimum densities of sands, *ASTM-STP #523, Relative density involving cohesionless soils*, Eds. E.T. Selig and R.S. Ladd, pp. 98-112.
- Yousuff, M. and Page, N. W. (1993), Particle material, morphology and load effects on internal friction in powders, *Powder Technol.*, vol. 76, pp. 155-164.
- Zik, O., Levine, D., Lipson, S. G., Shtrikman, S. and Stavans, J. (1994), Rotationally induced segregation of granular materials, *Physical Review Letters*, vol. 73, no. 5, pp. 644 – 649.